STATUS OF THESIS

| Title of thesis | CHARACTERIZATION OF FLOW STRUCTURES IN THE CYLINDER OF A GDI ENGINE USING STEREOSCOPIC-TIME RESOLVED PIV AND POD |
|---|---|

I MOHAMMED ABD EL MOTLEB KOTB EL ADAWY

hereby allow my thesis to be placed at the Information Resource Center (IRC) of Universiti Teknologi PETRONAS (UTP) with the following conditions:

1. The thesis becomes the property of UTP
2. The IRC of UTP may make copies of the thesis for academic purposes only.
3. This thesis is classified as

☐ Confidential

☑ Non-confidential

If this thesis is confidential, please state the reason:

_____

_____

The contents of the thesis will remain confidential for _____ years.

Remarks on disclosure:

_____

_____

Endorsed by

_____ _____

Signature of Author Signature of Supervisor

Permanent address: Name of Supervisor

Alexandria University, Faculty of Engineering, Alexandria, Egypt

Prof. Dr. Morgan R. Heikal

Date: _____ Date: _____

UNIVERSITI TEKNOLOGI PETRONAS

# CHARACTERIZATION OF FLOW STRUCTURES IN THE CYLINDER OF A GDI ENGINE USING STEREOSCOPIC-TIME RESOLVED PIV AND POD

By

MOHAMMED ABD EL MOTLEB KOTB EL ADAWY

The undersigned certify that they have read, and recommend to the Postgraduate Studies Programme for acceptance of this thesis for the fulfillment of the requirements for the degree stated.

Signature: _____

Main Supervisor: Prof. Dr. Morgan R. Heikal

Signature: _____

Co-Supervisor: Prof. Dr. Abdul Rashid Bin Abdul Aziz

Signature: _____

Head of Department: AP. Dr. Puteri Sri Melor Binti Megat Yusoff

Date: _____

# CHARACTERIZATION OF FLOW STRUCTURES IN THE CYLINDER OF A GDI ENGINE USING STEREOSCOPIC-TIME RESOLVED PIV AND POD

by

MOHAMMED ABD EL MOTLEB KOTB EL ADAWY

A Thesis

Submitted to the Postgraduate Studies Programme

as a Requirement for the Degree of

DOCTOR OF PHILOSOPHY

MECHANICAL ENGINEERING

UNIVERSITI TEKNOLOGI PETRONAS

BANDAR SERI ISKANDAR,

PERAK

APRIL 2019

DECLARATION OF THESIS

| Title of thesis | CHARACTERIZATION OF FLOW STRUCTURES IN THE CYLINDER OF A GDI ENGINE USING STEREOSCOPIC-TIME RESOLVED PIV AND POD |
|---|---|

I MOHAMMED ABD EL MOTLEB KOTB EL ADAWY

hereby declare that the thesis is based on my original work except for quotations and citations which have been duly acknowledged. I also declare that it has not been previously or concurrently submitted for any other degree at UTP or other institutions.

Witnessed by

| | |
|---|---|
| Signature of Author | Signature of Supervisor |
| Permanent address:<br>Alexandria University,<br>Faculty of Engineering,<br>Alexandria, Egypt | Name of Supervisor<br>Prof. Dr. Morgan R. Heikal |
| Date: | Date: |

# DEDICATION

*I dedicate this thesis to my parents, my wife and my cute daughters "Malak" and "Lojin"*

ACKNOWLEDGEMENTS

First and foremost, I would like to thank Almighty ALLAH for granting me the capability, strength and knowledge to proceed successfully my research work.

I wish to express my utmost thanks to my supervisor, Prof. Dr. Morgan Heikal for his support, encouragement and supervision throughout the project. I highly respect his expertise and enthusiasm. This work would have been impossible without his encouragement and support. I would like also to extend my special thanks to my co-supervisor Prof. Dr. A. Rashid A. Aziz. His constant help and support were much appreciated.

It is with immense gratitude to acknowledge the friendship and support from all my fellow researchers of the Center for Automotive Research and Electric Mobility (CAREM) in Mechanical Engineering Department, Universiti Teknologi PETRONAS.

I cannot fail also to acknowledge financial and technical support provided by Ricardo Consulting Engineers throughout the course of this study.

There are others whose names do not appear on this list but who have contributed directly or in directly to my study. Their help and encouragement will always be cherished.

Finally, I would like to take this opportunity to thank my family for their constant affection, care and support.

# ABSTRACT

There is a growing need for better understanding of the processes which control the combustion in modern gasoline direct injection (GDI) engines. Large-scale intake-generated flow structures such as swirl and tumble are known to have a significant effect on the combustion behavior and have been widely studied by the automotive research community. Traditionally, the standard tools available to assess the in-cylinder flow behavior inside an engine are either steady-state flow rigs or research engines with optical access. Steady-state flow rigs are used to evaluate the bulk motion using some integral parameters such as flow coefficient, discharge coefficient and tumble ratio. Whilst the optical engines are used to simulate detailed in-cylinder flow conditions. However, optical engines have several issues including limited optical access, cycle-to-cycle variability and limited range of operating engine speeds. Therefore, a joint project between the Universiti Teknologi PETRONAS (UTP) and Ricardo UK LTD to combine the advantages of steady-state flow rig and the level of details of optical measurements was proposed. The principle aim of this project was to carry out comprehensive in-cylinder flow measurements and to validate Ricardo VECTIS CFD simulation. Therefore, a steady-state flow rig was used to measure full field velocity vector maps using a stereoscopic time-resolved particle image velocimetry technique (Stereo-PIV). The in-cylinder flow behavior was investigated in the vertical tumble plane at different experimental conditions including; the effect of valve lift, measurement plane and pressure difference across the air intake valves. The focus of this work was totally on tumble measurements, as modern GDI engines are considered as tumble-dominated engines. The results revealed that, the effect of the pressure difference across the air intake valves on the flow structure was negligible compared to the effect of valve lift. Moreover, increasing the valve lift and pressure difference led to high velocities which in-turn increased the strength of the air motion and therefore enhanced the turbulent kinetic energy (TKE) and tumble ratio (TR). Furthermore, the predictions of the Ricardo VECTIS CFD simulation were in agreement with the

velocity vector fields acquired from the PIV measurements. Phase-dependent and phase-invariant POD techniques were then utilized to extract the most energetic structures and investigating the in-cylinder flow variation and evolution considering the effect of valve lift and pressure difference.

Furthermore, high-speed time-resolved PIV measurements were carried out to chronicle the spatial and temporal evolution of air/fuel-spray interaction considering the effect of injection pressure and pressure difference across the intake valves. The Mie scattering images and the instantaneous velocity vector fields before, during and after the injection event illustrated that, the intake generated-tumble motion had a significant effect on the fuel spray distortion and distribution inside the cylinder. It was concluded that the combination of the flow rig as a qualitative tool and the high-speed time-resolved particle image velocimetry and proper orthogonal decomposition as quantitative tools offer a new detailed insight into in-cylinder flows and mixture preparation and hence can inform engine combustion optimization.

# ABSTRAK

Baru-baru ini, terdapat permintaan yang semakin meningkat dalam memahami proses-proses yang mengawal pembakaran dengan lebih baik terutamanya, dalam enjin suntikan langsung (GDI) petrol moden. Struktur aliran masuk yang besar seperti putaran dan jatuh dikenal pasti mempunyai kesan yang signifikan terhadap tingkah laku pembakaran dan telah dikaji secara meluas oleh industri penyelidikan automatik. Secara tradisinya, alatan-alatan standard yang tersedia digunakan untuk menilai tingkah laku aliran silinder di dalam enjin sama ada rig aliran keadaan mantap atau enjin penyelidikan dengan akses optik. Rig aliran keadaan stabil digunakan untuk menilai gerakan pukal dengan menggunakan beberapa parameter penting seperti pekali aliran, pekali pelepasan dan nisbah tumble. Manakaia enjin optik digunakan untuk mensimulasikan keadaan aliran silinder sebenar. Walaupun merupakan cara yang paling tepat, enjin optik mempunyai beberapa isu termasuk akses optik yang terhad, variasi antara kitaran dan kelajuan enjin operasi yang terhad. Oleh itu, satu projek bersama antara Universiti Teknologi PETRONAS (UTP) dan Ricardo UK LTD untuk menggabungkan cara kualitatif rig aliran keadaan mantap dan cara kuantitatif ukuran optik telah dicadangkan. Tujuan utama projek ini adalah untuk menjalankan pengukuran aliran silinder yang komprehensif dan untuk mengesahkan simulasi Ricardo VECTIS CFD. Oleh itu, pelantar aliran keadaan mantap (FEV) telah diubahsuai untuk menyediakan akses keterlihatan lengkap untuk aliran dalam silinder dan dengan itu, ukuran halaju medan sepenuhnya diperoleh dengan menggunakan zarah teknik (Stereoscopic Time-Resolved Particle Image Velocimetry) (Stereo-PIV). Reaksi aliran dalam silinder diselidiki dalam satah ‘Tumble’ tegak dalam keadaan eksperimen yang berbeza termasuk; ‘Valve lift’, satah pengukuran dan perbezaan tekanan di seluruh injap pengangkut udara. Kerja ini lebih bertumpukan kepada pengukuran jatuh, kerana enjin GDI moden dianggap sebagai mesin yang dikuasai ‘tumble’. Keputusan menunjukkan bahawa, kesan perbezaan tekanan di seluruh ‘Air intake valve’ ke atas struktur aliran diabaikan berbanding kesan ‘valve lift’. Selain itu, peningkatan valve

dan perbezaan tekanan membawa kepada kadar aliran yang lebih tinggi ke dalam silinder dengan halaju tinggi yang meningkat di-seterusnya kekuatan gerakan udara dan seterusnya meningkatkan tenaga kinetik gelora (TKE) dan nisbah 'tumble' (TR). Halaju lebih tinggi yang dihasilkan pada 'Mid-valve-plane' meningkatkan gerakan udara secara keseluruhan di dalam silinder dari segi TKE dan TR yang lebih tinggi berbanding dengan pesawat lain. Tambahan pula, hasil simulasi Ricardo Vectis CFD bagi aliran silinder pada 'tumble plane' tegak pusat adalah selaras dengan medan vector halaju yang diambil dari pengukuran PIV. Kedua-dua teknik POD iaitv 'phase-dependent' 'phase-invarient' digunakan untuk mendapatkan struktur yang paling bertenaga dan menyiasat Perubahan dalam silinder aliran dan evolusi memikirkan kesan daripada 'valve lift' dan perbezaan tekanan. Tambahan pula, kelajuan tinggi masa diselesaikan ukuran PIV telah dijalankan untuk chronicle evolusi ruang dan masa campuran udara / bahan api memikirkan kesan daripada tekanan suntikan dan perbezaan tekanan merentasi 'intake valve'. Imej Mie yang tersebar dan medan vektor serta-merta sebelum, semasa dan selepas peristiwa suntikan menunjukkan bahawa, 'intake generated tumble' yang dihasilkan telah memberi kesan yang besar kepada penyelewengan dan pengedaran semburan bahan api di dalam silinder.Kesimpulannya, gabungan rig aliran sebagai alat kualitatif dan 'time-resolved particle image velocimetry' dan 'proper orthogonal decomposition' yang tepat sebagai alat kuantitatif dapat memberikan kefahaman terperinci bar uke dalam aliran silinder dan penyediaan campuran dan dapat digunakan sebagai alat penyelidikan enjin.

TABLE OF CONTENT

LIST OF FIGURES

LIST OF TABLES

# LIST OF ABBREVIATIONS

| | |
|---|---|
| 2C | Two Velocity Components |
| 2D | Two Dimensional |
| 3C | Three Velocity Components |
| 3D | Three Dimensional |
| ASOI | After Start of Injection |
| ATDC | After Top Dead Center |
| CCD | Charged Coupled Device |
| CCV | Cycle-to-Cycle Variability |
| CFD | Computational Fluid Dynamics |
| CI | Compression Ignition |
| CO | Carbon Monoxide |
| $CO_2$ | Carbon Dioxide |
| COV | Coefficient of Variation |
| DC | Direct Current |
| DNS | Direct Numerical Simulations |
| EGR | Exhaust Gas Recirculation |
| EOI | End of Injection |
| FOV | Field of View |
| GDI | Gasoline Direct Injection |
| HC | Unburned Hydrocarbons |
| HGA | Harmonic Generation Assembly |
| HWA | Hot Wire Anemometry |
| IA | Interrogation Area |
| ICE | Internal Combustion Engine |
| IMF | Image Model Fit |
| ISD | Inner Seat Diameter |
| ISM | Impulse Swirl Meter |
| KE | Kinetic Energy |
| LDA | Laser Doppler Anemometry |

| | |
|---|---|
| LES | Large Eddy Simulations |
| LSP | Laser Speckle Photography |
| Nd: YAG | Neodymium Doped Yttrium Aluminum Garnet |
| Nd: YLF | Neodymium Doped Yttrium Aluminum Fluoride |
| $NO_x$ | Oxides of Nitrogen |
| PDA | Phase Doppler Anemometry |
| PFI | Port Fuel Injection |
| PIV | Particle Image Velocimetry |
| PLIF | Planar Laser Induced Fluorescence |
| POD | Proper Orthogonal Decomposition |
| RANS | Reynolds-Averaged Navier Stokes |
| RMS | Root Mean Square |
| rpm | Revolution Per Minute |
| SI | Spark Ignition |
| SNR | Signal to Noise Ratio |
| SOI | Start of Injection |
| SR | Swirl Ratio |
| TKE | Turbulent Kinetic Energy |
| TR | Tumble Ratio |
| TR-SPIV | Time-Resolved Stereoscopic Particle Image Velocimetry |
| VFAM | Viscous Flow Air Meter |
| VVT | Variable Valve Timing |

LIST OF SYMBOLS

| | |
|---|---|
| $\| . \|$ | $L^2$-norm |
| $\beta_m$ | Eigenvector index $m$ |
| $C_m^{(k)}$ | POD coefficient for input snapshot number k and mode number $m$ |
| $L_V$ | Valve lift |
| $r_p$ | Radius of the recommended seeding particles |
| $A_V$ | Orifice area between valve head and seat |
| $A_{seat}$ | Inner seat area |
| $C_d$ | Discharge coefficient |
| $C_f$ | Flow coefficient |
| $D_{cyl}$ | Cylinder bore diameter |
| $D_{seat}$ | Inner seat diameter of the intake valve |
| $P_1$ | Air pressure upstream of the valve |
| $P_2$ | Air pressure downstream of the valve |
| $R_{MFL}$ | Mean paddle wheel radius |
| $S_P$ | Mean piston speed |
| $T_1$ | Air temperature upstream of the valve |
| $V^{(k)}$ | Velocity field $k$ |
| $\dot{V}$ | Volume flow rate |
| $\langle V \rangle$ | Ensemble-averaged velocity field |
| $V_o$ | Velocity head |
| $f_{max}$ | Maximum frequency of flow oscillations |
| $f_u$ | Maximum frequency of the particles can follow |
| $\dot{m}$ | Measured mass flow rate |
| $u_{i,j}^{(k)}$ | Velocity component at grid point $(i, j)$ in velocity field $k$ in X axis |
| $v_{i,j}^{(k)}$ | Velocity component at grid point $(i, j)$ in velocity field $k$ in Y axis |
| $\lambda_m$ | Eigenvalue index $m$ |
| $\rho_{air}$ | Air density |

| | |
|---|---|
| $\rho_{cyl}$ | Air density inside the cylinder |
| $\varphi_m$ | POD mode index $m$ |
| $\Delta P$ | Pressure drop across the intake valves |
| $\Delta t$ | Time between laser pulses |
| $TR_1$ | Tumble ratio based on angular momentum |
| $TR_2$ | Tumble ratio based on vorticity |
| $C$ | Spatial correlation matrix |
| $Cs$ | Flow velocity under isentropic conditions |
| $G$ | Torque measured by impulse meter |
| $I, J$ | Number of total grid points in the snapshot |
| $K$ | Total number of input snapshots |
| $KE_m$ | Kinetic energy captured by POD mode $m$ |
| $M$ | The total number of POD modes |
| $N$ | Paddle wheel speed |
| $P$ | Pressure |
| $Q$ | Measured air volume flow rate |
| $R$ | Gas constant |
| $T$ | Temperature |
| $i, j$ | Index of the grid points in the snapshot |
| $k$ | Isentropic exponent for air (1.4) |
| $k$ | Input snapshot number index |
| $ke_m$ | Energy fraction captured by POD mode $m$ |
| $m$ | POD mode index |
| $n$ | Number of intake valves |
| $\rho s$ | Air density under isentropic conditions |

# CHAPTER 1

# INTRODUCTION

## 1.1 Research Motivation

Motor vehicles are considered to be one of the major sources of outdoor air pollution [1, 2]. This is by exposing a huge sector of populations to different types of harmful emissions such as carbon monoxide (CO), unburned hydrocarbons (HC) and oxides of nitrogen ($NO_x$). The exposure to these harmful emissions is associated with a range of serious and chronic diseases i.e. lung cancer and cerebrovascular disease which in worst cases lead to early death [3]. In addition, many of pollutants are not associated only with adverse health outcomes, but also are implicated in climate changes [4]. It is divided into short-lived pollutants which are chemically active gases and aerosols such as carbon monoxide and nitrogen oxides and long-lived greenhouse gas (carbon dioxide). Therefore, to meet the lower vehicle emissions legislations, two parallel actions have been set up by the automotive industry. Firstly, the development of new combustion systems such as, variable valve timing (VVT) [2], multi-stage turbocharging and gasoline direct injection (GDI) [5]. Secondly, vehicle emission standards are set by the regulatory bodies of Europe, Japan and USA. Table 1.1 shows the past, present and future European emission standards for spark ignition (SI) engines with continuing tendency for reducing the emissions.

Table 1.1: European emission standards for spark ignition engines [6]

| **EURO 5-6 SPARK IGNITION EMISSION LIMITS** | | | | | | | | | | |
|---|---|---|---|---|---|---|---|---|---|---|
| **Emissions** | **Unit** | **PC M, LDT N1 CL 1** | | | **LDT N1 CL 2** | | | **LDT N1 CL3, N2** | | |
| | | **Euro 5a** | **Euro 6b** | **Euro 6c** | **Euro 5a** | **Euro 6b** | **Euro 6c** | **Euro 5a** | **Euro 6b** | **Euro 6c** |
| **THC** | **mg/Km** | 100 | 100 | 100 | 130 | 130 | 130 | 160 | 160 | 160 |
| **NMHC** | | 68 | 68 | 68 | 90 | 90 | 90 | 108 | 108 | 108 |
| **NOx** | | 60 | 60 | 60 | 75 | 75 | 75 | 82 | 82 | 82 |
| **CO** | | 1.000 | 1.000 | 1.000 | 1.810 | 1.810 | 1.810 | 2.270 | 2.270 | 2.270 |
| **PM** | | 5,0 | 4,5 | 4,5 | 5,0 | 4,5 | 4,5 | 5,0 | 4,5 | 4,5 |

## 1.2 Background

In the last century, internal combustion engines (ICE) have been widely developed by the automotive industry for powering light and heavy-duty vehicles. Even though engine design and technology have improved considerably, research is still continuing as the issues of air pollution and market competitive have become increasingly important. With the recent regulations and standards for exhaust emissions and fuel consumption there is, more than ever, a need for an accurate control of the in-cylinder combustion process. It is generally accepted that the in-cylinder flow structures formed during the intake stroke have a significant influence on the mixing process and hence the combustion behavior of internal combustion engines. The significance of in-cylinder flow structures is mainly reflected in large eddy formation and its subsequent break down into turbulence kinetic energy, as shown in Figure 1.1.

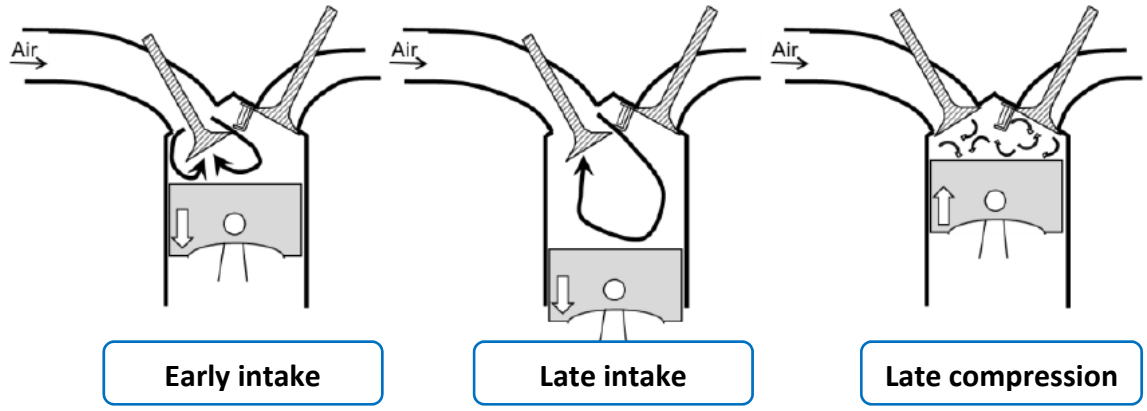


Figure 1.1: The evolution of in-cylinder tumble flow

In-cylinder flow structures can be divided into two main forms of large-scale motions (coherent structures), swirl and tumble. Swirl is the in-cylinder flow where the flow rotational axis is parallel to the cylinder axis and usually denoted for compression ignition (CI) engines. Tumble is the flow with an axis perpendicular to that of the cylinder, as shown in Figure 1.2.

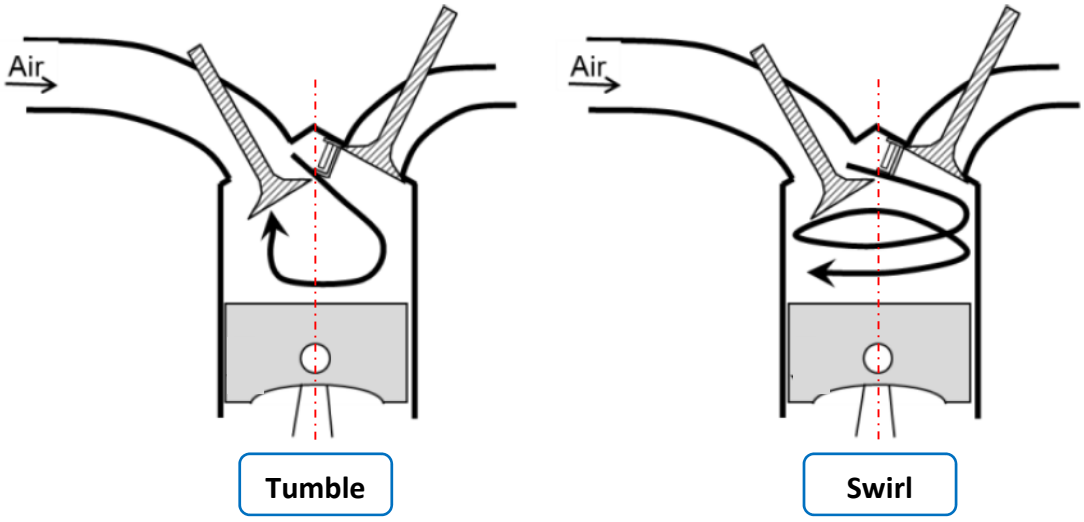


Figure 1.2: Illustration of in-cylinder tumble and swirl flows

These kinds of large-scale motion mainly rely on the intake port geometry [7-9], piston shape [9, 10] and valve lift [11, 12]. Tumble is mostly denoted for modern spark ignition (SI) engines. Tumble motion is more decisive than swirl motion for enhancing the mixing process and flame propagation rate [13-19]. Therefore, tumble ports are now standard means of controlling the combustion process in modern gasoline direct injection (GDI) engines. The large-scale tumbling motion is created during the intake stroke by restricting the flow rate on the outer side of the intake valve using straight ports oriented in such a way that most of the annular air jet exiting the intake valves is directed towards the exhaust side.

Two different methods are used to assess the in-cylinder tumble motion: macroscopic and microscopic approaches. The macroscopic methods evaluate the in-cylinder motion using some integral parameters such as flow coefficient, discharge coefficient, swirl ratio and tumble ratio. Steady-state flow rigs are considered as one of these methods. A cylinder head is mounted on the flow rig and the air is blown through the intake ports at certain valve lifts and pressure differences across the air intake valves. The swirl or tumble motion can be measured either from the rotation of a paddle wheel placed in the cylinder or using an impulse swirl meter to measure the torque exerted by the flow. For each value of intake valve lift (at certain pressure difference),

the values of torque/paddle wheel rotation and volume flow rate provide a measure of the swirling/tumbling intensity and the breathing demand of the engine. On the other hand, the microscopic methods can be used to provide comprehensive velocity field information about the in-cylinder flow and hence the understanding of the evolution of the swirl/tumble motion and its influencing factors. These methods include optical engines along with laser diagnostics such as Laser Doppler anemometry (LDA), hotwire anemometry (HWA) and particle image velocimetry (PIV). Whilst, the other type of microscopic methods is the Computational Fluid Dynamics (CFD) simulation.

The flow behavior inside the cylinder of modern engines is more complicated in which the flow moves with various scales both in time and space. The existing techniques (e.g. LDV and HWA) have large limitations leading to un-accurate capturing of flow information. This is due to their low spatial and temporal resolution as well as the low ranges of frequency associated with these techniques. One of the key tools that offer valuable understanding of the instantaneous aerodynamic in spark ignition engines is particle image velocimetry (PIV). More recently, a new extension was denoted as high-speed time-resolved stereoscopic particle image velocimetry (TR-SPIV) which enables the possibility to obtain sequences of temporally and spatially correlated image pairs. Particle image velocimetry (PIV) is a well-established and popular non-intrusive optical measurement technique that is capable of providing whole field and instantaneous velocity measurements simultaneously. The main concept of PIV is to seed the flow with micro sized tracer particles (seeding particles) with density similar to that of the fluid of interest. These particles are illuminated by a high-power laser sheet and the scattered light from these particles is captured by means of a charged coupled device (CCD) camera. A correlation technique is then applied on the particle images in order to extract the velocity vector fields.

Once the turbulent flow inside the cylinder is captured well, then another problem is how to extract useful information from the flow structures and to distinguish between coherent structures, turbulence and cycle-to-cycle variability. Coherent structures are characterized as distinguishable large-scale flow patterns that contain the maximum energy and maintain their shape for relatively long time against dissipation compared to small scale flow patterns. The interpretations and characterization of coherent

structures solely depend on the method used to identify these structures [20]. Therefore, there is a pressing need for accurate choosing of statistical methods for extracting the coherent patterns from multidimensional data sets. Several identification techniques have been proposed. Reynolds decomposition, Galilean decomposition and low-pass filtering are among the traditional approaches. In addition, there are some other new promising techniques such as conditional sampling [21], linear stochastic estimation [22], two-point correlation [23], critical-point analysis of local velocity gradient tensor [24] and wavelets. Recently, the proper orthogonal decomposition (POD) analytical technique introduced firstly by Lumley [25] to the turbulence research community is considered as a powerful method to extract the most energetic structures in turbulent flows. The POD decomposes a set of velocity distributions (snapshots) into a linear combination of spatial basis functions or space-dependent POD modes, (denoted $\varphi_m$) and their corresponding time-dependent coefficients, (denoted $C_m^{(k)}$).

The purpose of the current research is to combine the steady-state flow rig as a qualitative tool, the stereoscopic high-speed time-resolved particle image velocimetry (PIV) and the powerful statistical analysis technique proper orthogonal decomposition (POD) as quantitative tools so that a detailed flow structures can be acquired.

### 1.3 Problem Statement

Fundamentally, combustion is an exothermic chemical reaction. It is a complex process with a large number of sub-reactions which can be expressed through chemical kinetics models. The rate and nature of these reactions and hence the combustion phasing is controlled by the composition of the reactants, their temperature and the surrounding pressure. All combustion developments control these parameters with the aim of influencing the main reaction or the combustion phasing. Therefore, there is a need for accurate prediction of the temporal and spatial distribution of the charge composition in the cylinder and in depth understanding of the charge formation to inform the development of advanced combustion systems.

Numerical techniques coupled to chemical reaction models are effective tools for predicting the temporal and spatial composition of the charge. However, the charge

preparation processes are very complex and the accuracy of these tools need to be validated against detailed in-cylinder measurements. It is well accepted that charge preparation is largely influenced by the in-cylinder flow structure. Therefore, the understanding of in-cylinder flow characteristics became more than ever a challenge for the research community.

However, the in-cylinder flow measurements are extremely difficult to perform due to the compact and closed engine geometry and the high temperatures, pressures and velocities involved [26]. Research engines with optical access through the piston and the liner are the most elaborate way to perform in-cylinder flow measurements. These engines offer the advantage of simulating closely the real engine operating conditions and remain the most sophisticated tool for engine design. Although, several studies related to GDI in-cylinder flows and their interaction with direct fuel spray have been carried out recently using optical engines [27-35], they have suffered from several issues. These include the expensive cost, cycle-to-cycle variability, limited optical axis to the in-cylinder flow [28], limited engine speed range, dynamics effects and complexity of motored engines. It is worth recalling that, one of the main causes of cycle-to-cycle variability is the stochastic nature of the in-cylinder air motion [36-40]. Particularly, in GDI engines, cycle-to-cycle variability can lead to significant changes in air/fuel distribution and flame transport which in the worst cases lead to poor burning cycles and subsequently output power reduction and increase in the fuel consumption [32, 35, 41-44].

On the other hand, steady-state flow rigs have been used to evaluate the in-cylinder bulk flow motion. With the advent of new combustion systems to meet the recent pollution standards, the in-cylinder flows structures became of significant. Limited studies have been proposed by past researchers to gain a detailed information about the flow structures using flow rigs. However, these studies were all two-dimensional flow measurements while the flow in the cylinder of modern engines is three-dimensional. Moreover, another inherent problem was that, the laser reflection caused a significant signal degradation for the tumble measurements.

There is a need, therefore, for research methods that provide details of the characteristics of the in-cylinder flow and its interaction with the fuel spray which

avoids the complexity, expense and unsteady nature of the optical engines. The aim of this project is to develop one such method and to assess its availability and accuracy.

## 1.4 Research Objectives

The objectives of this study are:

1. To characterize the 3D full velocity vector fields of in-cylinder air flow using a steady-state flow rig and stereoscopic time-resolved particle image velocimetry (PIV).
2. To analyze the flow detailed structures using proper orthogonal decomposition (POD) techniques.
3. To investigate the spatial and temporal behaviors of intake air/direct fuel spray interaction.

## 1.5 Scope of the Research

The in-cylinder flow characteristics are proven to have a significant impact on the performance and emissions of internal combustion engines. Therefore, this work was developed as a joint project between the Universiti Technologi PETRONAS and one of the world's leading automotive consultants, Ricardo UK Ltd [45]. The main aim of the current study was to apply stereoscopic high-speed time-resolved particle image velocimetry (PIV) for studying the in-cylinder air flow and its interaction with the direct fuel spray in the cylinder of modern engines. The measurements were carried out on a steady-state flow rig. The flow rig was modified and chosen to avoid the cost and complexity of motored engines and to allow maximum optical access to the in-cylinder flow. The following points outline the scope of the present study.

- The bulk air motion was assessed at different valve lifts using two different techniques, namely paddle wheel and impulse torque meter. The flow motion was characterized in terms of measured air flow rate, flow coefficient, discharge coefficient and non-dimensional rig-tumble.

- RICARDO-VECTIS CFD simulation was validated with those of the experimental results from PIV measurements. VECTIS simulations of the same cylinder head were set up by using the same boundary conditions in an attempt to represent faithfully the experimental arrangement. The validation was limited to only three valve lifts and the in-cylinder flow was only compared based on flow pattern and velocity magnitude.

- The Forschungsgesellschaft für Energietechnik und Verbrennungsmotoren (FEV) flow rig was modified to measure full field velocity vector maps using a stereoscopic time-resolved particle image velocimetry technique (Stereo-PIV) in order to examine the effect of valve lift, measurement plane and pressure difference across the air intake valves. These three parameters were found to have the most effect on flow structures.

- The interaction between direct fuel spray and in-cylinder tumble motion was investigated using high-speed time-resolved PIV through the mid-injector plane. The measurements were limited to valve lift 10 mm where the tumble vortex was well established and dominated the whole cylinder volume. The effect of injection pressure on the interaction process was also investigated at two injection pressures 32.5 and 35 MPa.

- The proper orthogonal decomposition (POD) analytical technique was applied to the PIV velocity vector maps to characterize the details of flow structures at various valve lifts and different pressure differences. The analysis was carried out using two of the most analytical techniques, namely phase dependent and phase invariant POD. The POD was found the most efficient method to efficiently extract the most energetic structures and provide detailed information regarding the in-cylinder flow evolution and variation.

## 1.6 Thesis Outlines

The present thesis is organized into five chapters. The first chapter discusses the research motivation, research background, problem statement, research objectives and scope of the work. Chapter 2 presents the in-cylinder flow measurement techniques including intrusive and non-intrusive ones. In addition to the applications of POD for in-cylinder flow analysis. Chapter 3 presents the overall research methodology which can be divided into three main sections. The first part concerns the validation with Ricardo experimental and simulation work. This includes a detailed description of both flow rigs used in the current study, Ricardo and FEV steady-state flow rigs. In addition to a complete description for Ricardo VECTIS CFD simulation. The second part concerns the description of the particle image velocimetry (PIV) technique. The third part concerns the mathematical description of the statistical technique proper orthogonal decomposition (POD). Chapter 4 concerns the analysis of the results which can be divided into three main sections. The first section represents the in-cylinder air flow characterization under different experimental conditions obtained from the stereoscopic PIV measurements. This includes the effect of valve lift, the effect of measurement plane and the effect of pressure difference across the air intake valves. The second section presents the application of proper orthogonal decomposition on the in-cylinder flow. The third section presents the results obtained from 2D- high speed time-resolved PIV measurements for the interaction between the in-cylinder flow with the direct fuel spray. The conclusions drawn from this project and a list of recommendations for future work can be found in chapter 5. All appendices are situated at the very end of thesis.

CHAPTER 2

LITERATURE REVIEW

## 2.1 Chapter Overview

This chapter deals with the work conducted by previous researchers on different aspects of in-cylinder fluid flows using experimental and numerical techniques inside an engine cylinder particularly gasoline direct injection (GDI) engines. Therefore, this chapter is divided into five main sections as shown in Figure 2.1. The first and second sections show the development of spark ignition engines and how the detailed knowledge of in-cylinder flows is significant particularly for modern engines. Whereas, the third section highlights the in-cylinder flow measurement techniques including intrusive and non-intrusive methods. The fourth section introduces the particle image velocimetry (PIV) technique and highlights its application for in-cylinder flows measurements. While the last section puts a spot light on the decomposition technique, proper orthogonal decomposition and its applications in in-cylinder flows analysis.

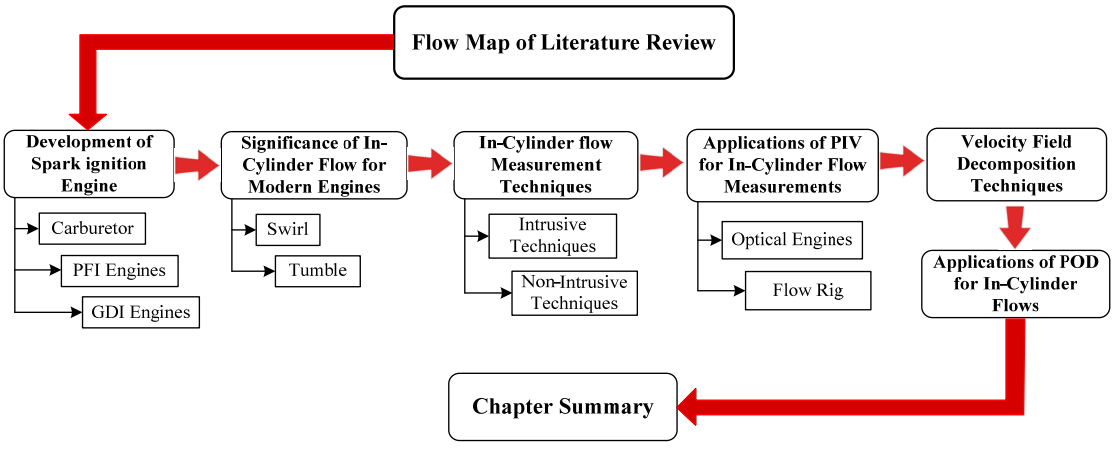


Figure 2.1: Map of the topics reviewed in this chapter

The key aim behind this chapter is to recognize the research areas which require further understanding and more experimental investigations. By identifying these research gaps in knowledge, new research investigations can be carried out to provide more useful findings and new information which may support other research groups and engine developers.

## 2.2 Development of Spark Ignition (SI) Engines

Previously, the problem with engines with carburetor was that they could not work at stoichiometric mixtures at various working conditions, therefore three-way catalytic converter could not be used in these engines. After that, port fuel injection (PFI) systems were used instead of carburetor since 1980's. In PFI systems, the amount of fuel can be metered precisely and injected in the intake port. Therefore, PFI systems offered some advantages over the carburetor system in terms of, higher volumetric efficiency and thus improved output torque and power, lower exhaust emissions, lower fuel consumptions, more rapid engine reaction to variations in throttle position and less noise due to less moving parts in the fuel injection system [46]. After that, gasoline direct injection (GDI) systems were introduced instead of PFI systems since the 1990's. The air-fuel mixing in GDI engines is an internal formation process in contrast to carburetor and PFI systems where the mixing is external, as shown in Figure 2.2. GDI engines offered a number of merits over PFI systems in terms of, preventing fuel wall film in the intake port, reducing the throttling losses (pumping losses), higher thermal efficiency, higher compression ratios, lower fuel consumption, $CO_2$ and HC emissions and higher volumetric efficiency [46-48].

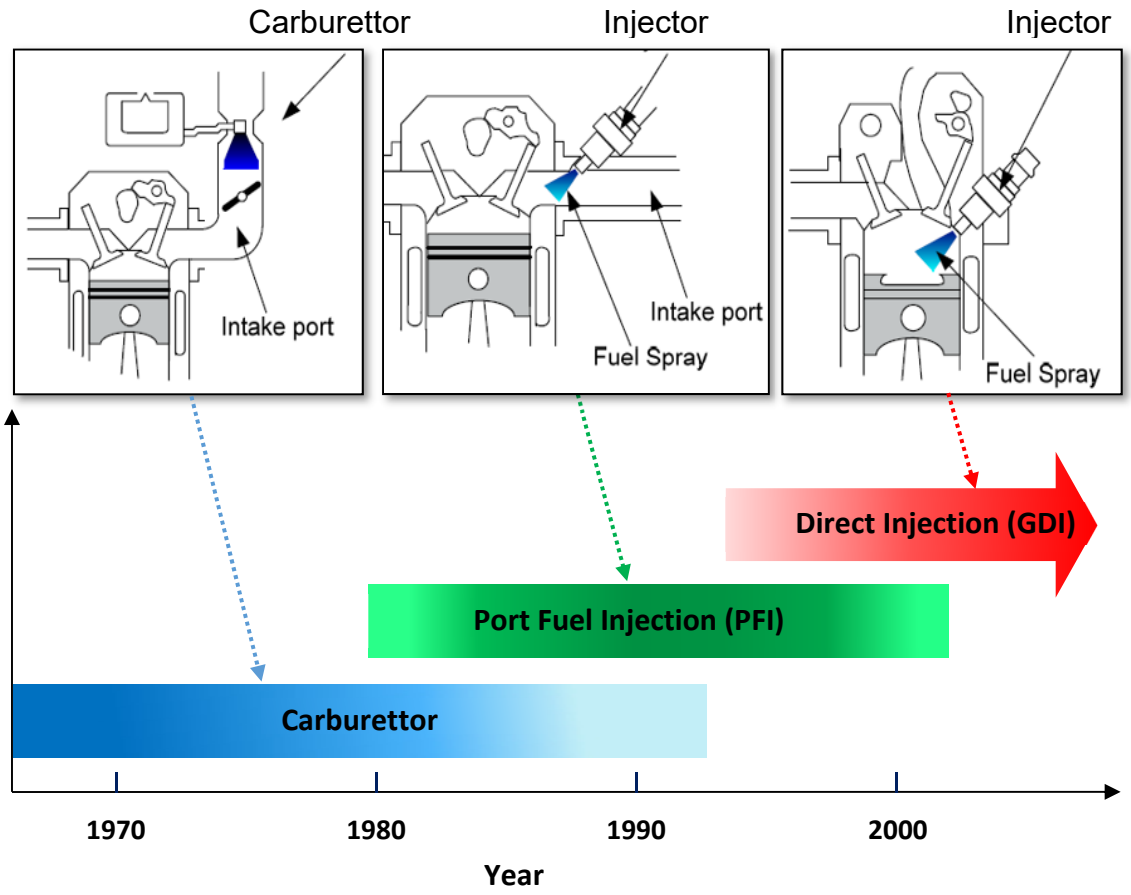


Figure 2.2: Mixture formation systems in the spark ignition engines [49]

GDI engines can be operated either in stratified charge mode or homogenous charge mode, as shown in Figure 2.3. A stratified charge mode (late injection) is utilized at lower engine speeds and loads as the fuel is injected late during the compression stroke. This mode enables engines to burn very lean mixtures with very high global air/fuel ratio which, in turn, cannot be achieved using either conventional carburetors or multi point port fuel injection [50]. However, more NOx emissions are generated due to lean burn. Therefore, exhaust gas recirculation (EGR) is used during this mode to reduce NOx emissions. A homogenous charge mode (early injection) is preferred for higher loads and higher engine speeds. The fuel is injected early during the intake stroke so more time is available for air-fuel mixture formation [50]. During this mode of operations, the engine operates with stoichiometric mixture which, in turn, decreases NOx emissions and thus the EGR is not required. The advantages of GDI engine technology compared to the PFI system are summarized in the following Table 2.1:

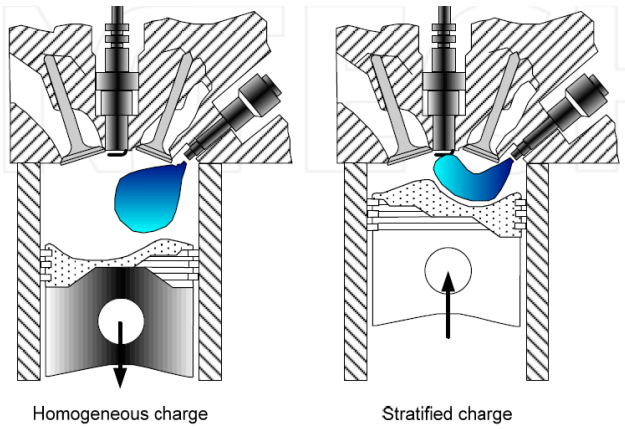


Figure 2.3: Stratified and homogeneous-charge mode [49]

Table 2.1: Improvements in GDI engines compared to PFI engines [51, 52]

| Source | Cause | Kume *et al.* (1996) | Alkidas and Tahry (2003) |
|---|---|---|---|
| Reduced Pumping Losses | Less throttling | 15% | 10% |
| Improved Charge Mixing | Lean combustion | 7% | 7.5% |
| Higher Compression Ratio | Charge air cooling | 4% | 3% |
| Reduced Heat Losses | Lower temperature combustion | 5% | 2% |
| Fuel Delivery Response | Better transient operation | - | 3.5% |
| **Total** | | 31% | 26% |

In stratified mode, three different combustion systems are used to prepare and maintain a combustible mixture at the instant of ignition near the spark plug. These are wall-guided, air-guided and spray-guided [53]. The specific differentiation between the different combustion systems depends on whether the fuel spray impingement on the piston head, the in-cylinder flow field or the fuel spray features and dynamics are used to realize the concept of stratification [54], as shown in Figure 2.4. The improvement of the first generation of GDI engines has been mainly focused on the wall-guided combustion system, while the second generation of GDI is oriented on the spray-guided system [46]. However, it is important to acknowledge that regardless of this classification, the stratification achievement of real system is accomplished by some combination of these three combustion systems [46].

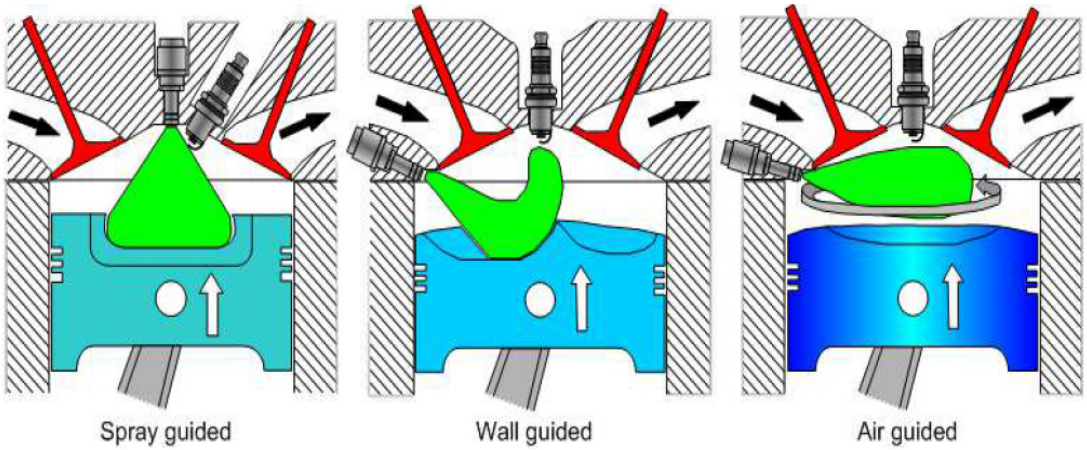


Figure 2.4: The wall-guided, air-guided and spray-guided GDI combustion systems [55]

### 2.2.1 Wall-Guided Combustion System

Wall-guided is categorized as a wide-spacing combustion mode. The injector is located away from the centrally situated spark plug in the combustion chamber. The fuel spray is redirected towards the spark plug depending on the interaction between the spray itself and the especially shaped surface on the piston head [56]. However, more unburned hydrocarbons HC and CO emissions are generated because the fuel is directly injected on the piston crown subsequently, it cannot totally evaporate [57]. For these reasons, there are two main critical challenges facing the development of this combustion system, the piston crown optimization and spray/crown matching [46]. Moreover, the mixture formation is slightly affected by the in-cylinder flow either swirl or tumble motion [58].

### 2.2.2 Air-Guided Combustion System

In the air-guided combustion system, the injector is still away from the spark plug (wide-spacing system). However, the mixture formation around the spark plug is based on a well-defined in-cylinder flow. Theoretically, the direct impact of the fuel spray on the piston surface head is prevented by the air motion, thus the expected unburned HC emission is less compared to wall-guided combustion system. However, any

fluctuations in turbulence and cycle-to-cycle variability (CCV) may affect the mixture formation process and lead to combustion instability [46]. Moreover, the combustion stability deteriorates at lower engine speeds because of the level of strength of air motion is reduced. Therefore, a special design for the intake ports and piston head is essential for inducing in-cylinder charge motion and supporting the mixture motion towards the spark plug at the instant of ignition over the engine speed range.

### 2.2.3 Spray-Guided Combustion System

The spray-guided combustion system is categorized as narrow-spacing system as the spark plug is located near the center of combustion chamber. The narrow-spacing concept has the fuel injector positioned with only moderate eccentricity (< 12%) from the center of the chamber. The stratification process is enhanced simply by the juxtaposition of the spark plug and the fuel injector. Therefore, the stratification capability for spray guided system is significantly higher than both wall-guided and air-guided systems [59]. The spray-guided concept combines the advantage of both centrally-located spark plug and fuel injector. For centrally-located spark plug, a symmetric flame propagation, higher specific power, higher burning rate, lower heat losses and auto ignition tendency can be acquired. For centrally-located direct fuel injector, more charge homogeneity than side-mounted injector, reduction in CO and smoke emissions and higher ignition stability over the engine operating map can be gained [59-61]. However, this combustion system has some shortcomings associated with spark plug fouling, sensitivity to fuel spray characteristics variations, and reduction of intake valves diameters.

## 2.3 In-Cylinder Fluid Motion

With the recent and prompt development of new technologies in spark ignition engines, there is, more than ever, a need for comprehensive knowledge of the air/fuel motion within the engine cylinder. It is well documented that the in-cylinder flows generated during the intake stroke and modified during the compression stroke have a significant effect on engine performance, combustion and emissions [62]. Therefore, it is important

to understand the whole process of air inducting into the cylinder which includes the flow through the intake valves followed by the large-scale flow structure generation inside the engine cylinder.

### 2.3.1 Intake Valve Jet Flow

The flow behind a valve has been widely studied and is now well understood. For a single valve with straight perpendicular port exiting into an infinite volume, the induced steady flow streamlines form a torus, as some of the fluid particles come back to the axis of symmetry of the valve (see Figure 2-5 (a)). Outside this vortex, the main conical jet exits the port at an angle determined by the geometry and the valve lift. The vorticity lines are perfect which axes coincide with the valve axis (see Figure 2-5 (b)). However, in real production engines, the vortex ring can be dramatically distorted by the boundaries of the confined space defined by the cylinder walls, the piston top and other obstacles such as spark plug or pent-roof surfaces. As the jet impinges onto these boundaries, the flow is directed and, in some cases, heavily restricted. For design consideration, the inlet valves are rarely centered in the cylinder, thus provoking an uneven angular distribution of the flow rate around the valve (see Figure 2.5 (c)). The in-cylinder configuration combined with the inlet port geometry determines the final shape of the vortex ring. Port design parameters such as the angle formed by the port and the valve axis or the curvature have a vast influence on the large-scale flow pattern. The shape of the combustion chamber is also determinant as the Coanda effect can be used to control the direction of the jet, particularly in pent-roof engines. Helical ports can be utilized to enhance the swirl pattern by adding a tangential component to the velocity vectors. Valve masking techniques can be applied to control the flow field by partially or completely blocking the flow on one side of the valve. The shape of the vortex can also be distorted by the incoming flow from other inlet valves or the back-flow from the exhaust side.

The flow through the intake valves is highly dependent on the valve lift [11, 13]. Three segments are shown in Figure 2.6 correspond to different valve lifts. At very low valve lifts, the flow is highly attached to the valve head and seat. At intermediate valve

lifts, the flow starts to separate from the valve head at the inner edge of the valve seat. At high valve lifts, the flow is detached from the inner edge of the valve seat as well [63].

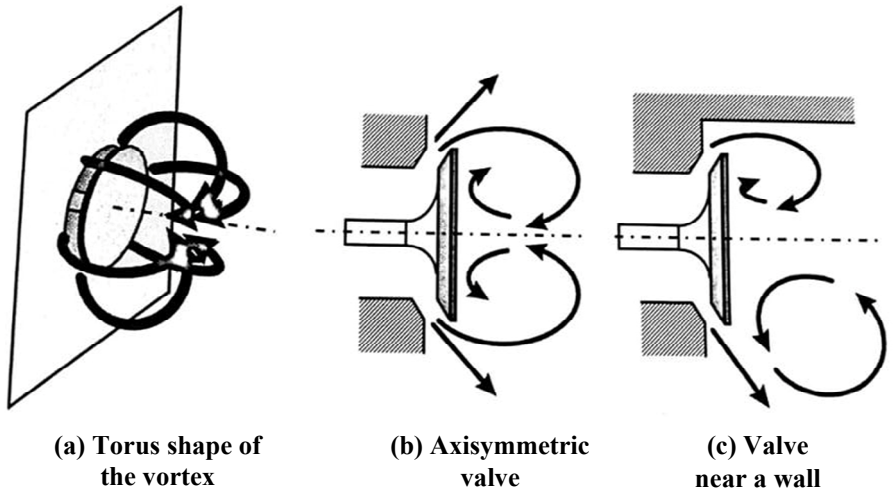


Figure 2.5: Flow behind a valve [64]

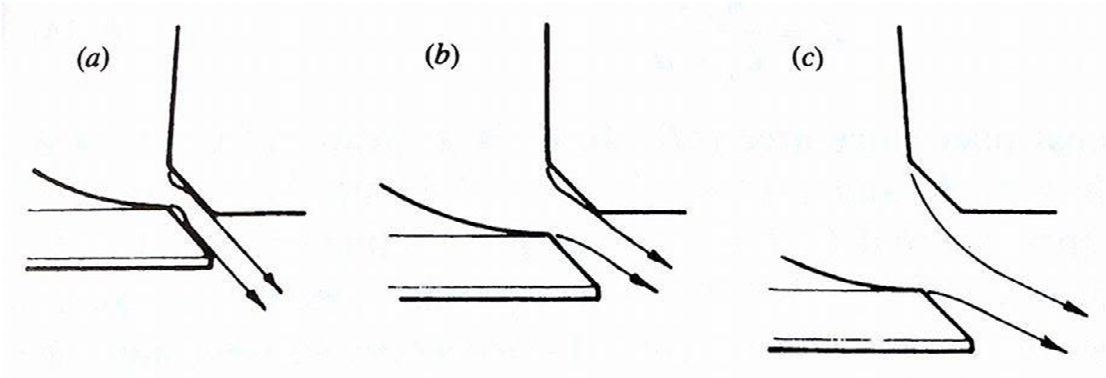


Figure 2.6: Air flow through the intake valve, (a) low valve lift, (b) intermediate valve lift and (c) high valve lift [63]

### 2.3.2 Large Scale In-Cylinder Flow Structures and their Significance

The previous section illustrated the formation of high velocity jet within the cylinder resulting from the pressure difference across the intake valves during induction. The main objective of the intake system is to convert these forms of jet-like structures coming through the intake valves into large-scale motions inside the engine cylinder. The in-cylinder flow structures can be divided into two main categories of large-scale

rotational motions; swirl and tumble. The distinction between swirl and tumble can be achieved through their rotational axis. If the axis of rotation of the large vortex is parallel to the cylinder axis, this is called swirl, whereas a rotational structure with a main axis perpendicular to the cylinder axis is denoted tumble [65, 66]. Key features of both swirl and tumble are presented in Table 2.2. In addition, one of the main concerns with GDI engines is the ability to produce a stable mixture during the stratification mode of operation. Consequently, tumble motion is notably important to modern GDI engines [13, 19, 67]. By the end of the compression stroke, the tumble motion generated during intake is expected to break up into small-scale structures leading to an increase in turbulence level by the time of ignition. This is in turn speculated to compensate for the low flame speed during the stratification mode, enhance the idle stability, improve the combustion stability and extend the EGR susceptibility [7, 18, 68]. An example showing the benefits of high tumble motion on the combustion process can be seen in Szengel *et al*., [69]. This example demonstrates the increase in turbulence level at the time of ignition for an increase in the tumble flow, and how this led to a reduction in the burn duration. Figure 2.7 and Figure 2.8 show the variation of turbulence kinetic energy and burn duration with different positions of tumble flap located in the intake port (tumble level variation), respectively. Therefore, it is significantly important to gain a comprehensive understanding of the in-cylinder tumble motion characteristics during intake and compression strokes.

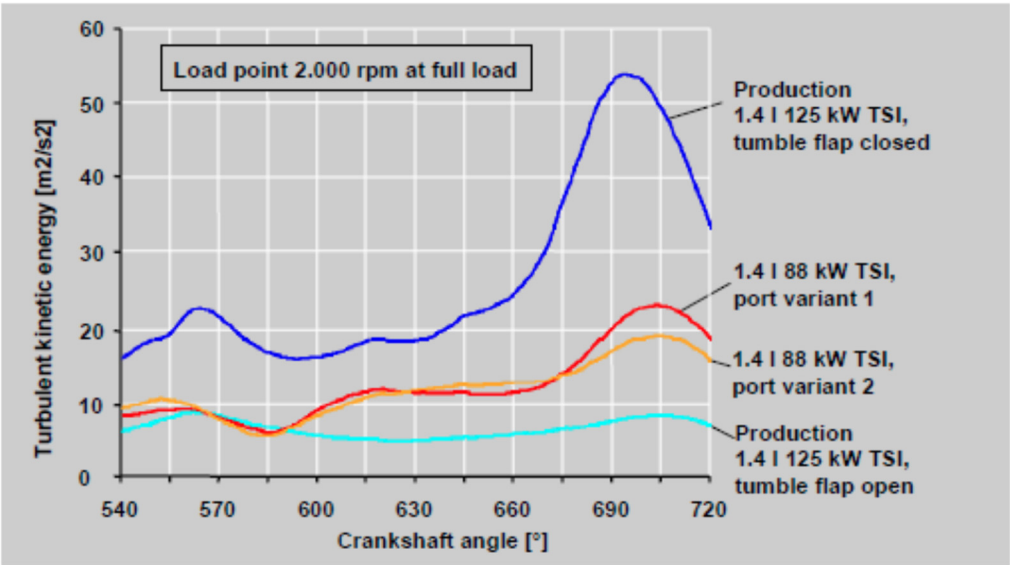


Figure 2.7: The influence of tumble on turbulence level [69]

Table 2.2: key features of swirl and tumble

| Parameters | Swirl | Tumble |
|---|---|---|
| **Definition** [13] | Swirl is the in-cylinder flow where the flow rotational axis is parallel to the cylinder axis | Tumble is the in-cylinder flow with an axis perpendicular to that of the cylinder |
| **Targeted Engines** | Two-valves and four-valves compression ignition engines and two valves spark ignition engines | Pent-roof four valves spark ignition engines |
| **Effective Geometric Parameters** [70] | - Intake port geometry,<br>- Bore/stroke ratio<br>- Combustion chamber shape<br>- Piston shape<br>- Valve lift | - Intake port geometry,<br>- Bore/stroke ratio<br>- Combustion chamber shape<br>- Piston shape<br>- Valve lift |
| **Effective Operating Conditions** [70] | -Engine speed<br>-Compression ratio | -Engine speed<br>-Compression ratio |
| **Generation and Enhancement Methods** [66] | - Helical ports or tangential ports.<br><br>- Swirl is generated inside the intake port prior to induction inside the cylinder in case of helical ports.<br><br>- While tangential ports are designed to add a tangential component to the velocity vectors. | - Using straight ports oriented in such a way that most of annular jet exiting the valve is directed towards the exhaust side.<br><br>- Tumble can be enhanced using valve masking techniques but to the detriment of the engine breathing demand at high speed or high load.<br><br>- Installation of a tumble flap into the intake port. |
| **Planes of Measurement** | Planes parallel to the piston top | Planes perpendicular to the piston top |
| **Quantification** | Swirl ratio | Tumble ratio |

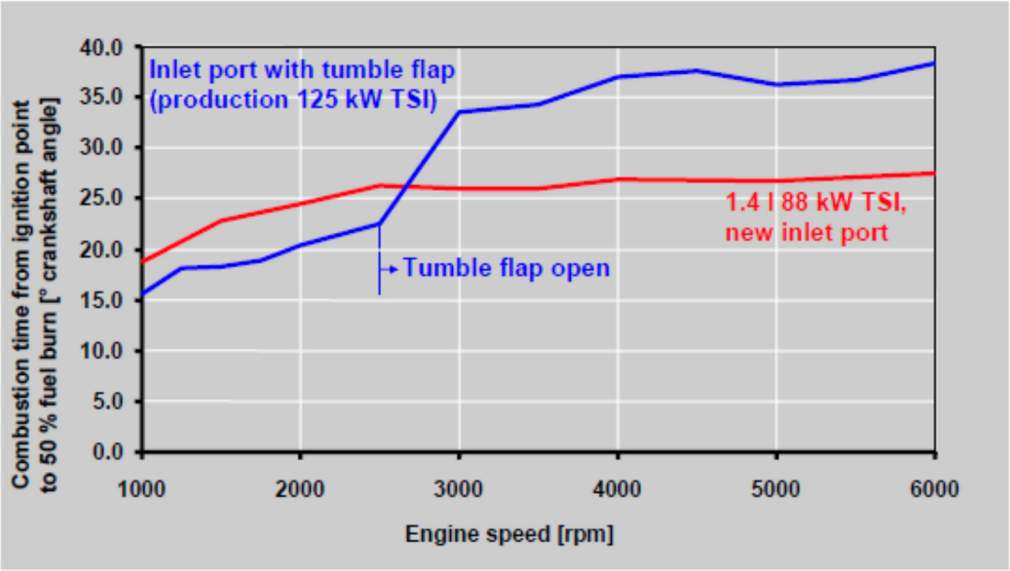


Figure 2.8: The influence of tumble on burn duration [69]

## 2.4 In-Cylinder Flow Analysis Techniques

In-cylinder flow measurements are extremely difficult to perform due to the compact and closed engine geometry and also to the high temperatures, pressures and velocities involved [36]. Several techniques have been used to measure either the bulk flow motion or the flow velocities and structures during the inlet and compression strokes. Figure 2.9 summarizes the methods used for in-cylinder flow measurements.

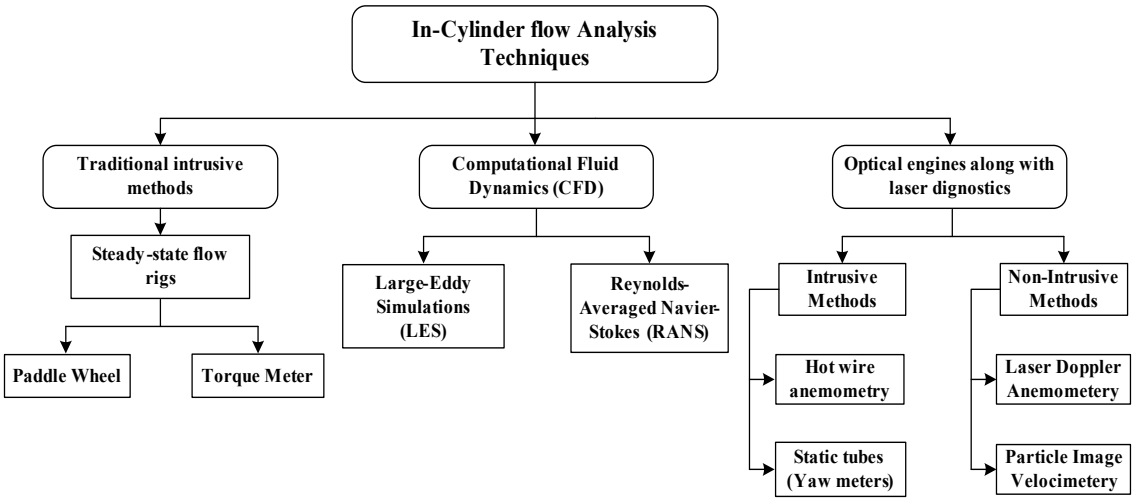


Figure 2.9: In-cylinder flow analysis techniques

### 2.4.1 Steady-State Flow Rigs

In the automotive industry, steady-state flow rigs are a standard and economical way of characterizing the bulk in-cylinder air motion during the early stages of engine development in terms of some integral parameters such as flow coefficient, discharge coefficient, tumble ratio and swirl ratio [19, 71]. These measurements are used to assess the design of the engine intake ports and the combustion chamber concerning the engine flow capacity and the in-cylinder flow pattern of the charge motion. This is accordingly of a great interest to the engine combustion, performance and emissions. The main principle is that, a dummy cylinder is fitted onto the cylinder head and air is blown through the intake ports at a certain valve lift and pressure difference across the intake valves [19]. The engine flow capacity is mainly assessed by using the ratio of the measured air flow rate to the theoretically calculated air flow rate through a certain reference area in the port/valve assembly. This flow rate ratio is normally called 'flow coefficient' or 'discharge coefficient' depending on which flow area is used as the reference. Figure 2.10 depicts the difference in reference area between the flow coefficient and the discharge coefficient.

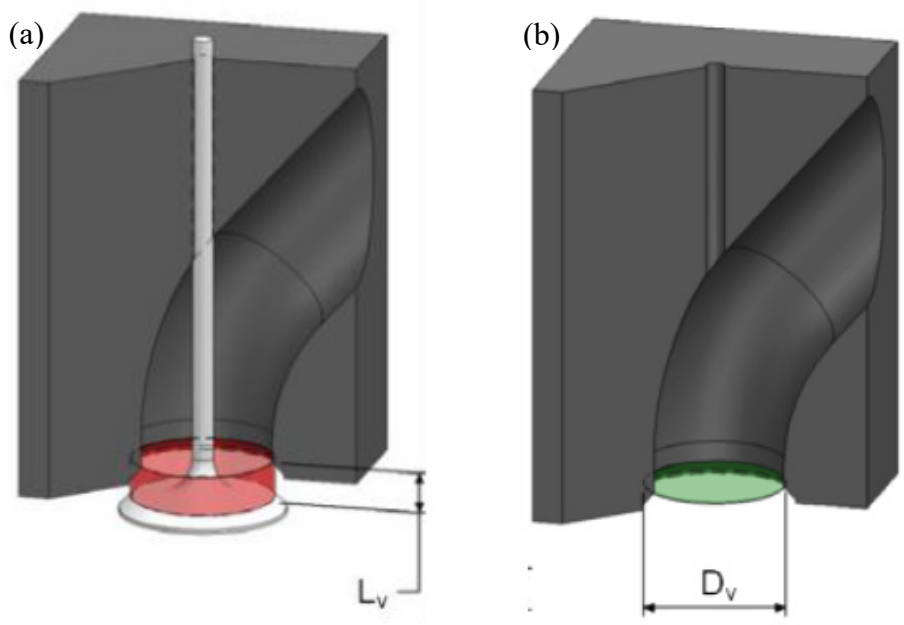


Figure 2.10: The reference area in the port/valve assembly, (a) reference area for discharge coefficient and (b) reference area for flow coefficient [72]

Whilst, two intrusive methods associated with the steady-state flow rigs can be used to measure either the swirl or tumble rotational motion as a function of valve lift for a given pressure difference across the air intake valves, namely paddle wheel anemometer and torque meter [71]. The first intrusive method is a paddle wheel anemometer placed in the cylinder. The tumble level is gained by assessing the rotational speed of a paddle wheel with an axis perpendicular to the cylinder axis. While the swirl level is gained by measuring the rotational speed of a paddle wheel with an axis parallel to the cylinder axis. The main concerns with this method are due to the disturbance of the flow, friction of the wheel bearing and slip between the vanes and the flow [71]. On the other hand, the second widely adopted method now employs the impulse swirl meter to measure the torque exerted by the flow. This meter consists of a honeycomb flow straightener mounted at a certain distance from the cylinder head (usually 1.2 bore diameter). This technique has been extended to tumbling motion by fitting a tumble adaptor, such as those used by Ricardo [73], which converts the tumble motion in the cylinder into a swirling flow in the extended perpendicular pipe. Two common configurations of the tumble adaptor are used, the “T-type” and the “L-type” [74]. For each value of the intake valve lift, the values of torque and volume flow rate provide a measure of swirling or tumbling intensity and the breathing demand of the engine. Figure 2.11 depicts the techniques used for tumble measurements on steady-state flow rigs. Unfortunately, no standardized testing methodology exists at present and great care has to be taken when comparing data coming from different sources [75]. Hongming Xu illustrated a comprehensive review of the most widely adopted techniques [71].

The main advantage of the steady-state flow rig remains its simplicity and cost effectiveness. Moreover, it is widely used in the automotive industry and has become a standard tool in engine port design. On the other hand, the disadvantage of the steady-state flow rig is that in its standard form it only supplies integral values of the flow, with no information regarding the flow structures. These flow structures are now becoming extremely important to modern engine designs.

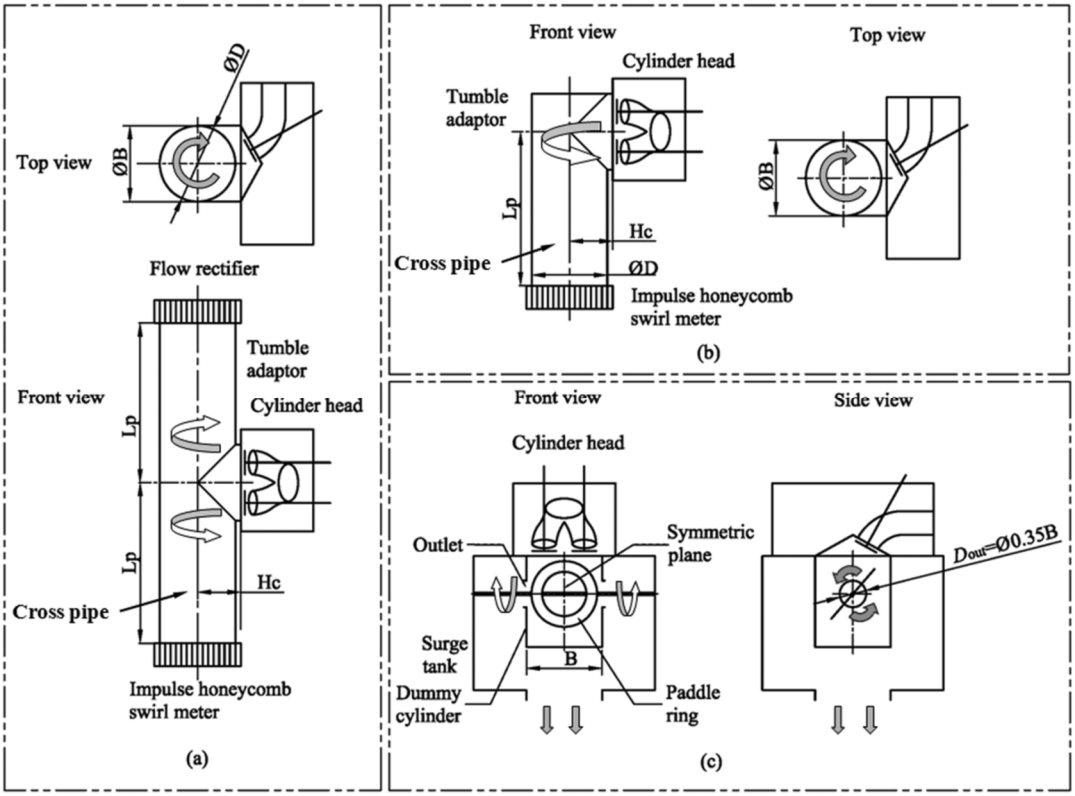


Figure 2.11: Configuration for tumble test methods, (a) the "T-type" tumble adaptor, (b) the "L-type" tumble adaptor and (c) paddle wheel [74]

### 2.4.2 Optical Engines Along with Laser Diagnostics

An internal combustion (IC) engine that permits for optical access to the combustion chamber is denoted as an optical engine, as shown in Figure 2.12. Optical engines are the most elaborate way to perform in-cylinder flow measurements. The engine is operated in the closest conditions to reality while optical access through the piston, the liner or the cylinder head makes measurements and sometimes visualization possible. These engines are usually coupled to a dynamometer to provide the torque to motor them or to apply the necessary load. They can be operated either in a motored mode to study the flow during the intake and compression stroke or in a fired mode to investigate the injection and combustion processes. Even though, these engines offer the advantage of simulating the real engine operating conditions they are very complex and therefore usually more expensive and time demanding than other simpler set-ups. An optical access of the complete engine cylinder needs to be available which is very

expensive, and in such a severe environment the measurements are difficult to perform. Moreover, the application of optical measurements in IC engines is also associated with several practical experimental difficulties. These include gaining optical access into the engine cylinder, providing a guiding path for the illuminating light sheet and choice of seeding particles [28, 76, 77]. It is worth recalling that, limitations related to optical access, physical space surrounding the engine, thick curved glass cylinder, and engine vibrations caused major issues in PIV measurements and affected the accuracy of experimental results [76]. Moreover, their operation is limited to engine speeds below 2000 rpm. The high-speed operation limit is a result of vibration issues, increased temperatures and unwanted oil films developing on the optical surfaces. Accordingly, In-cylinder flow measurements at high engine speed range has not been investigated except the trials of Stansfield *et al*. [77, 78]. Optical engines operate usually along with optical measurement techniques such as laser Doppler velocimetry (LDV) and particle image velocimetry (PIV) to the study of in-cylinder flow processes. The following sections provide an overview of different visualization techniques used to quantify the in-cylinder flows, including their advantages and disadvantages. These techniques can be divided into single point and whole field measuring techniques.

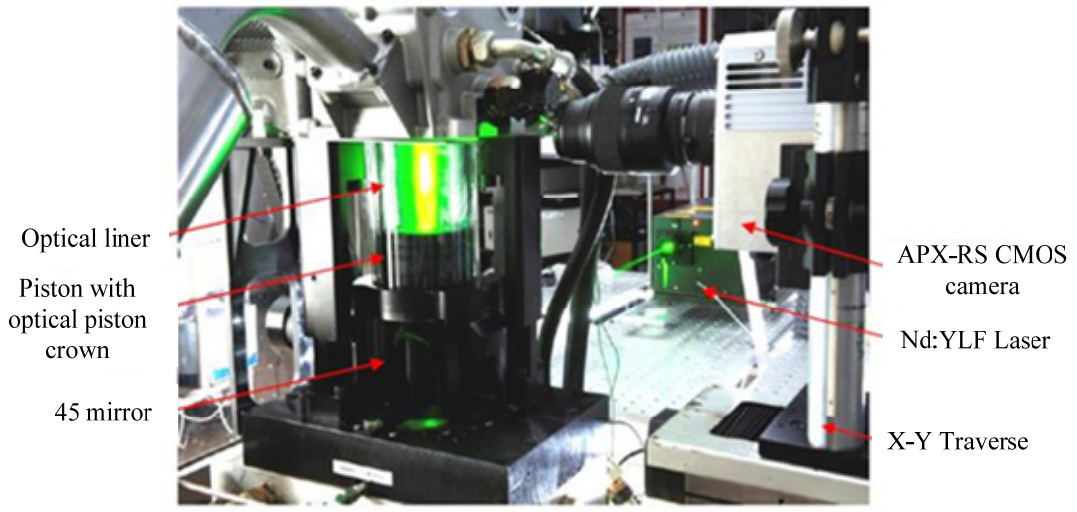


Figure 2.12: Optical engine for 2D PIV measurements [79]

*2.4.2.1 Single-Point Measurement Techniques*

The application of hot wire anemometry (HWA) and, Laser Doppler Velocimetry (LDA) to engine flow studies, allowed detailed qualitative study of in-cylinder flow through single point measurements of velocity. Hot wire anemometry (Figure 2.13), however, suffers from directional confusion, is intrusive and the weakness of the probes and calibration issues prohibit their use in many conditions within real engines.

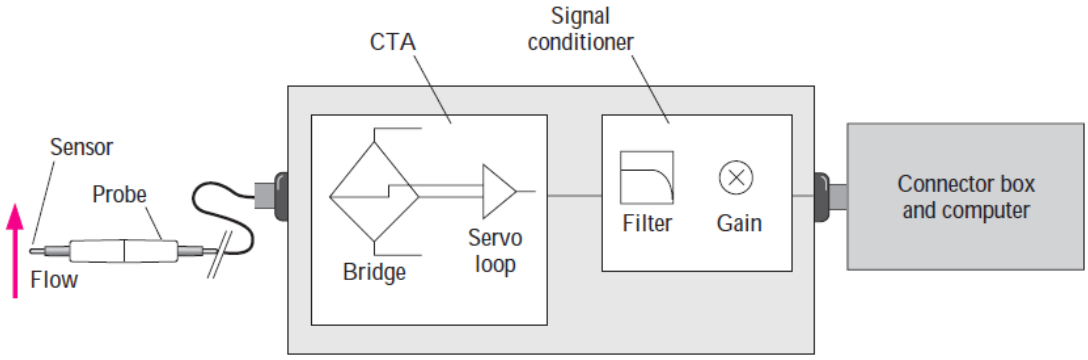


Figure 2.13: Schematic of hot wire anemometer system [80]

By contrast, Laser Doppler Velocimetry introduced first by Yeh and Cummins in 1964 [81], (Figure 2.14) is non-intrusive and limited engine modification is required in the form of optical windows. LDA utilize the Eulerian approach that measures the velocity of flow particles as they pass the point of measurement (it is known as measurement volume). The measurement volume is easily traversed through the flow for velocity profile measurement without interfering with the flow structure [82, 83]. LDV measurements in steady flow rigs have contributed much to the knowledge of the behavior of valve flows at different valve lifts [84]. Even though LDA techniques remain the most adapted methods for the measurement of velocity and turbulence in unsteady flows, the fact that they are point-wise techniques is a serious limitation for the study of large-scale flow structures. Attempts, have therefore been made to overcome the limitations of single point measurements while avoiding the practical considerations and data reduction problems associated with whole field techniques. Even though these developments have gone some way to overcoming the limitations of single point measurements the need for truly whole field flow visualization and

measurement has seen an increase in the application of particle tracking and particle image velocimetry.

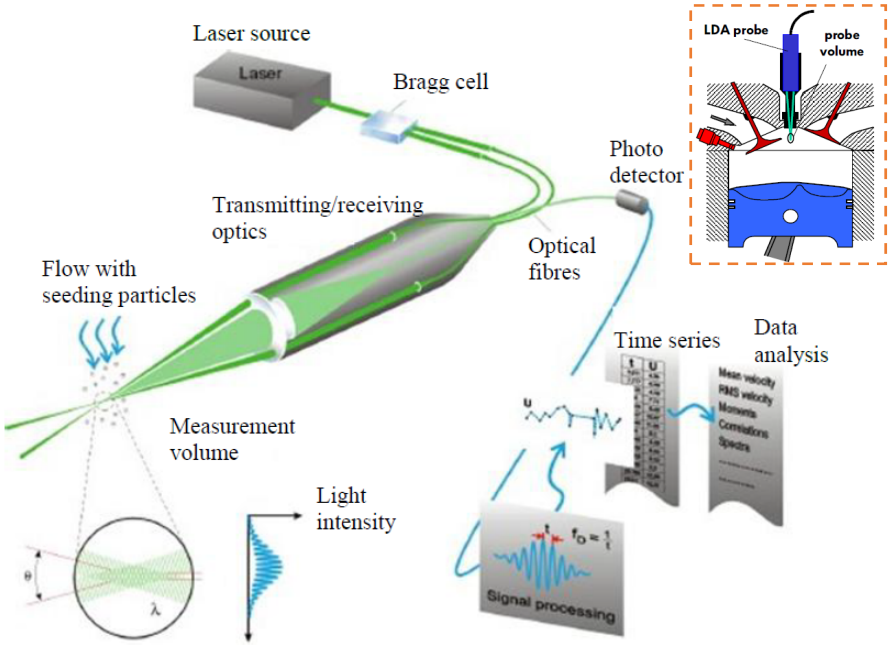


Figure 2.14: Schematic of LDV system (Dantec Dynamics)

## 2.5 Whole Field Measurement Technique

The full field metrology technique identified as particle image velocimetry (PIV) was first introduced by Pickering [85] and Adrian [86] in the mid-1980. The technique is derived from laser speckle velocimetry (LSV) which itself was an adaptation of laser speckle photography (LSP) to fluid flow measurements. The principle of laser speckle technique is to obtain optically Young's fringes from speckle images and to extract velocity components from the fringe patterns. PIV is a class of methods used in experimental fluid mechanics in order to determine instantaneous velocity vector fields by means of measuring the displacement of seeding particles (tracer particles) suspended within the flow over a known time separation [28]. Therefore, a careful selection of the geometric and physical properties of these particles is highly recommended to ensure that the particles faithfully follow the highest frequency structure within the flow [87, 88]. For 2D-PIV measurements, a high-power laser light sheet illuminates the area of interest (field of view-FOV) over which velocity

measurements are to be calculated. The light scattered by these seeding particles as they pass through the laser sheet is recorded by means of a Charged Coupled Device (CCD) camera, positioned perpendicular to the laser sheet. This camera works mainly on a double frame mode, as each image pair has two frames in which the time between these frames should be known. Capturing successive image pairs of the particles enables the velocity of the particles to be calculated. A spatial cross correlation is used to determine the particle displacements between image pairs, enabling two in-plane velocity components to be calculated over the field of view [32, 89]. The main principle of PIV technique is depicted in Figure 2.15. The recent development in both camera and laser specifications has led to the development of high-speed PIV systems allowing two-dimensional velocity vector fields to be captured at kHz rates. These systems provide the opportunity to quantify the temporal and spatial development of in-cylinder flow structures.

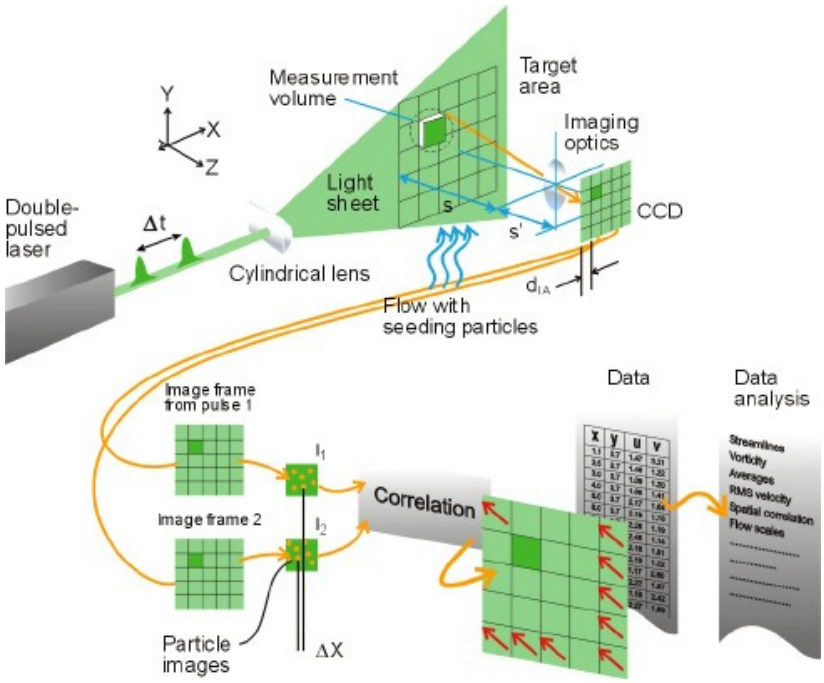


Figure 2.15: Schematic of experimental setup for 2D PIV measurement (Dantec Dynamics)

In spite of all its advantages, the classical PIV (2D-2C) technique underlies some disadvantages which includes the absence of the out-of-plane velocity component. This may lead to considerable measurement errors of the local velocity vector particularly in case of highly three-dimensional flow [90]. One of the approaches capable of

recovering the complete set of velocity components is the additional PIV recording from different viewing axis utilizing a second camera. Therefore, the most recent application of PIV is termed as stereoscopic high-speed PIV. The main principle of stereoscopic configuration is to record the flow with two synchronized cameras at different view angles. The three components of the velocity vectors can then directly be obtained from the two measured vector fields [76, 90]. A schematic of stereoscopic set up is presented in Figure 2.16. Further details of the PIV setup and analysis procedures for 2D and stereoscopic measurements is provided in Chapter 3.

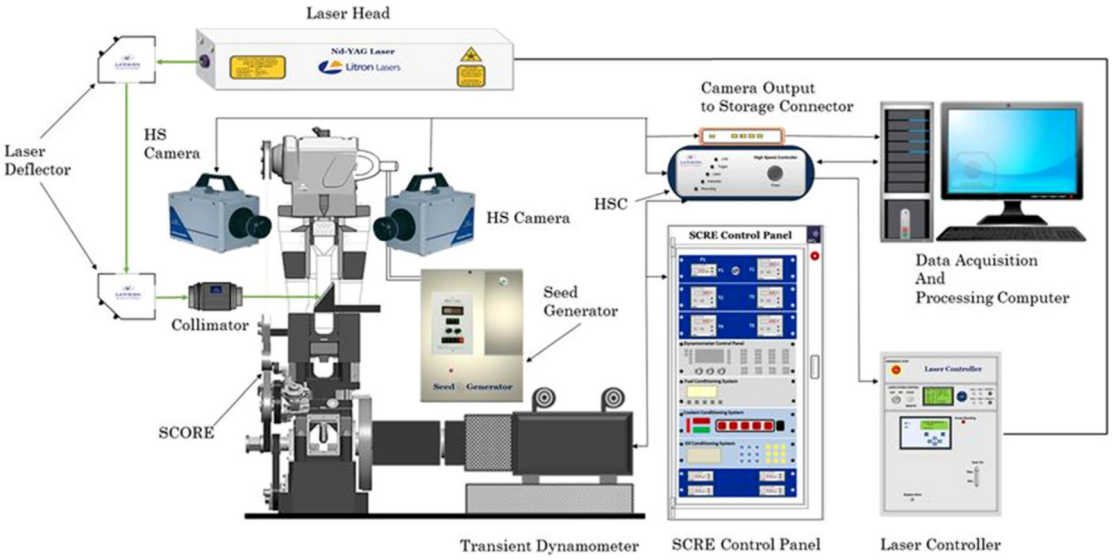


Figure 2.16: Experimental setup for Stereoscopic PIV in an optical research engine [76]

Basically, almost all quantitative measurements of fluid flow before the advent of PIV were carried out using single-point probes that measure different quantities in the flow for instance, velocity, and temperature and pressure measurements [91, 92]. These single-point measurements have a number of demerits because of measurements are carried out only at a single-point at a time and information about the underlying flow pattern is missing. Moreover, there is difficulty of taking spatial derivatives instantaneously which impedes getting information about a number of useful fluid mechanical properties such as rate of strain, vorticity and viscous dissipation.

Therefore, PIV technique offers a number of advantages which are summarized as follow:

- PIV is a measurement technique for measuring two or three components of velocity in a variety of flows.

- PIV is well-established non-intrusive optical measurement technique. This allows the application of PIV in places where the flow may be disturbed by the presence of probes as in high speed flow with shocks or in boundary layers near to the wall.

- PIV combines the quantitative nature of single-point measurements techniques such LDA and Phase Doppler Anemometry (PDA) and instantaneous measurements at multiple measurements (whole velocity field), which is more valuable for cases such as studying of coherent structures in turbulent flows.

- Due to the high data acquisition rate of PIV, testing time can be reduced especially in huge test sections such as, large wind tunnels.

- PIV is a powerful technique for computational fluid dynamics (CFD) codes validation.

### 2.5.1 The Applications of PIV for In-Cylinder Flows Measurements

As a consequence of the disadvantages of single-point measurements, researchers were attracted to use PIV to understand the complex in-cylinder flow evolution in internal combustion (IC) engines. The first applications of PIV to an IC engine was carried out by Reuss in 1989 [93]. More recently, a variety of experiments were carried out through the whole process of air and fuel mixing process using PIV in one engine cycle of a gasoline direct injection engine, as shown in Figure 2.17. These included the characterization of air flow through the intake and compression strokes [44, 70, 76], fuel spray, air/spray interaction process [16, 27, 33, 94], flame propagation and its interaction with the in-cylinder flows. In addition, by measuring multiple cycles, the study of cycle-to-cycle variability was achieved [28, 95]. The following sections provide a detailed information regarding the applications of PIV for in-cylinder flows measurements on both optical research engines and steady-state flow rigs.

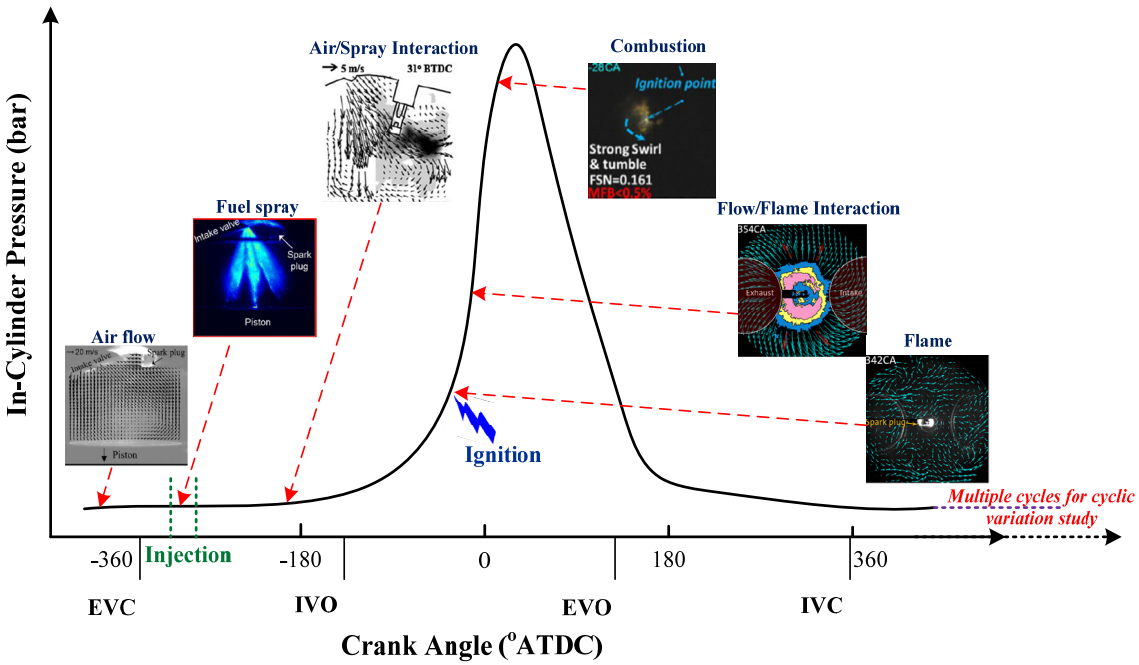


Figure 2.17: PIV measurements in gasoline direct injection optical research engines

### *2.5.1.1 Effect of Engine Parameters and CCV on Spatial Flow Structures Using PIV*

The engine parameters have a substantial influence on preparing a proper air fuel mixture in the cylinder in order to achieve faster combustion, improved fuel economy and reduced emissions [70]. The in-cylinder flow field structures strongly rely on the intake port profile and configuration [7, 8, 65, 96] as well as the shape of the combustion chamber [10, 97-100] and the piston crown shape [9, 10]. Moreover, cycle-to-cycle variations (CCV) understanding is considered one of the key challenges in modern engine design [10, 101]. Cyclic variations have significant effects on the air/fuel mixing process, and the combustion process because of the variations in the in-cylinder flow structures during the intake and compression strokes. There are many bad effects because of these instabilities which include, changes in the early flame kernel development and the combustible mixture might be transported away from the spark plug or it might arrive at an unfavorable crank angle which lead finally to incomplete combustion that increases emissions [32-34]. Therefore, the investigation of cycle-to-cycle variations through flow measurements are a key topic in the literature. Figure 2.18 presents an example for CCV in peak cylinder pressure generated inside the engine

cylinder. Considerable researches have been implemented using PIV to evaluate the effect of geometric and operating parameters and CCV on in-cylinder flow structures. Table 2.3 depicts a summary of PIV measurements in GDI engines for in-cylinder flow measurements.

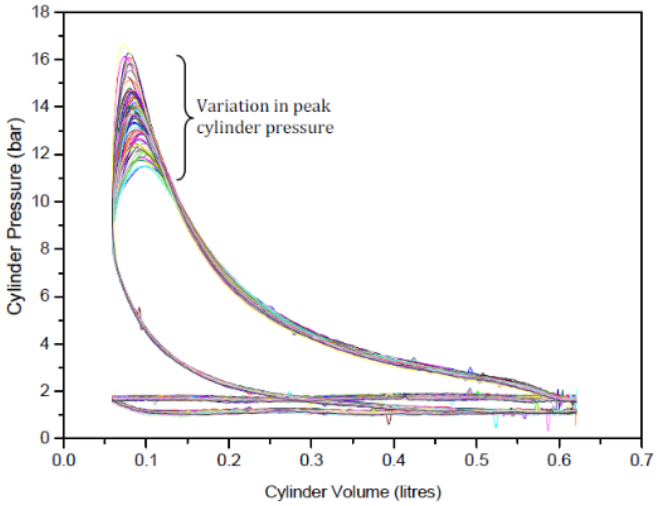


Figure 2.18: Pressure vs. volume for optical engine highlighting CCV in peak cylinder pressure [79]

Table 2.3: Summary of PIV applications for in-cylinder flows measurements in GDI optical research engines

| First Author | Year | Engine parameter | PIV-Configuration | Main Conclusions |
|---|---|---|---|---|
| Y Li [102] | 2004 | -Partially shrouding the lower periphery of the intake valves to produce a strong tumble motion | - 2D-2C PIV<br>-Central vertical tumble plane | - Large-scale tumble vortex was formed at the end of the intake stroke and remained towards the end of the compression stroke. |
| Phil Stansfield [77] | 2007 | -Effect of engine speed until 3500 rpm<br><br>-Add a discussion of the issues arising from applying the PIV at engine speeds higher than normally reported. | - 2D-2C PIV<br>-Central vertical tumble plane | At higher engine speeds:<br>- Optimization of the PIV system was difficult due to the greater dynamic velocity ranges in the cylinder and the pressure wave fluctuations from the inlet and exhaust system.<br>- Reducing the homogeneity of seeding particle density.<br>- Maximum frame rate of the camera was unable to capture an image pair every engine cycle. |
| B. Krishna. [14] | 2009 & | Effect of engine speed | - 2D-2C PIV | -The overall in-cylinder tumble flows and TR were mainly reliant |

| | | | | |
|---|---|---|---|---|
| & Carlos Alberto [103] & Roberto Berlini [104] | 2015 & 2017 | | -Central vertical tumble plane | on crank angle position irrespective of the engine speed. -Both average and max TKEs were higher at full intake valve opening position and higher engine speeds. -Large CCV of the flow field were observed, which were quantified by variations in the TKE, and the location of the tumble vortex center. |
| B. Murali Krishna [105] | 2009 | -Effect of different piston crown shapes at engine speed 1000 rpm | - 2D-2C PIV -Central vertical tumble plane | The pentroof-offset-bowl piston showed improvements of about 41% and 103 % in the TR and TKE compared to flat piston. |
| Jawali Maharudrp pa [106] | 2010 | -Effect of intake manifold orientation on in-cylinder tumble flows - 0, 30, 60 and 90° intake manifold orientation angles were used. | - 2D-2C PIV -Central vertical tumble plane | -90° intake manifold orientation showed an improvement in TR and TKE compared to other orientations considered. - The in-cylinder tumble flow structures were greatly affected by fluid entry angle into the engine. |
| J. Danemann [107] | 2011 | -Effect of measurement plane. | - 2D-2C PIV | -The vector fields confirmed the flow within the cylinder to possess a highly three-dimensional character. |
| Tianyou Wang [11] | 2015 | - Effect of valve lift (6.8 mm, 4.0 mm and 1.7 mm) | - 2D-2C PIV - two vertical tumble plane | -The ensemble averaged flow fields showed that higher valve lifts produced stronger vertical flows which turned more toward to the piston top and finally formed large scale tumble flow structure with higher values of TR. |
| AddepalliK rishna [70] | 2016 | -Effect of crank angle -Effect of compression ratio -Engine speed | - 2D-2C PIV - Central vertical tumble plane | -The in-cylinder flow was highly dependent on crank angle position - The level of TKE is higher at higher engine speeds. -Increasing the compression ration decreased the TKE and TR. |
| J. Bode [28] | 2016 | -Three dimensional features of the in-cylinder flow. | 2D-2C dual-plane, time-resolved PIV at central tumble plane and mid valve plane simultaneously | -Tumble motion evolution in dual planes were presented. -The highest velocities were found within the mid-valve plane. |
| Avinash Kumar [76] | 2017 | -The in-cylinder flow evolution during intake and compression strokes at 1200 rpm. | 2D-3C Stereoscopic-PIV -Central vertical tumble plane | -The randomness of air-flow fields during the intake stroke was very high, which became more homogeneous during the compression stroke. -By the end of compression stroke, there was a breakage of |

| | | | | |
|---|---|---|---|---|
| | | | | large-scale flow structures because of lower cylinder volume, which increased the turbulence level. |
| Wei Zeng [101] | 2018 | Effect of large-scale flow features on CCV of flame-initiation | - 2D-2C high-speed PIV<br>-Central vertical tumble plane | -In-cylinder large-scale flow features caused a significant CCV of flame development from the initial flame growth to fully turbulent combustion. |
| J. Bode [95] | 2018 | Effect of large-scale flow features on combustion CCV | 2D-2C high-speed PIV in three vertical planes simultaneously | -The analysis showed the high relevance of a detailed analysis of the large scale in-cylinder flow structures like the tumble vortex and their mutual interaction to understand combustion CCV. |

*2.5.1.2 In-Cylinder Flow/Fuel Spray Interaction*

In the development of GDI engines, the injection process is considered to play a vital role in the effort to achieve a proper control of the mixing and combustion processes [94]. The crucial task is to gain the required fuel spray atomization and distribution inside the combustion chamber, in a wide range of engine operating conditions. Moreover, the correct matching between fuel spray characteristics and in-cylinder air flow is essential to achieve the required mixture specification under each operating condition [94]. Laser diagnostics enable detailed investigation through high spatial and temporal resolutions particularly, the application of high-speed time-resolved PIV. The summary of the high-speed PIV application to air and spray interaction in GDI engines is given in Table 2.4.

Table 2.4: Summary of PIV applications to air /spray interaction

| First Author | Year | PIV-Configuration | Main Conclusions |
|---|---|---|---|
| B. Peterson [16] | 2009 | -Simultaneous application of 2D high-speed PIV and planar laser induced fluorescence (PLIF) of biacetyl (fuel concentration). | -The measurements showed a substantial increase in equivalence ratio, velocity magnitude, shear strain rate, and vorticity values with large CCV during the spray event. |
| Ming Zhang [108] | 2014 | -2D-2C a novel high-speed two-phase PIV<br><br>-In constant volume chamber | -The high-speed two-phase PIV technique provided an efficient diagnostic tool for simultaneous two-phase flow measurements.<br>-During the spray injection, the kinetic energy of the ambient gas |

| | | | |
|---|---|---|---|
| | | | increased rapidly due to the spray injection momentum input and the momentum transfer process was enhanced. |
| Wei Zeng [33] | 2014 | -Simultaneous 2D-2C high-speed PIV and spray images. | -The CCV of the in-cylinder flow speed prior to injection was measured to be higher at 2000 rpm compared to 1000 rpm.<br>- The injected liquid spray reduced the flow-speed cyclic variability after injection.<br>-The flow, fuel/air mixing and heat-release rate were dominated by the spray, but the intake-generated gas flow contained sufficient momentum to affect the mixing rates and turbulence level and thereby caused CCV of the stratified combustion, especially at higher speeds. |
| Xianhui Zhang [30] | 2015 | -2D-2C high speed PIV<br>-Mid injector vertical plane<br>- Introducing a tumble flap in the intake manifold to control the tumble intensity | Under high tumble ratio condition:<br>-The maximum shear strain rate of the spray increased<br>-The contact area between the spray droplets and air became larger<br>-The momentum exchange between them was intensified |
| Wei Zeng [35] | 2015 | -2D-2C high speed PIV<br>-Vertical tumble plane between the injector tip and the spark plug.<br>-Single injection strategy | - Differences in radial penetration between spray plumes and spray angles were observed as a result of in-cylinder flow variability. |
| Roman Stiehl [43] | 2016 | -Time-resolved PIV in plane of symmetry and Mie-scattering of fuel droplets<br>- Temporal evolution of the in-cylinder flow field and spray formation<br>- Trible injection strategy | -During the first injection, substantial momentum was added to the gaseous flow.<br>-Shear forces between the spray and surrounding air generate local vortices that contributed significantly to the local turbulent flow field. Turbulence levels were increased and length scales were locally modified<br>-CCV of the large-scale tumble vortex had a big impact on the spray shape of the second injection, in contrast, the first injection was unaffected. |
| B. Peterson [27] | 2016 | -3D-3C high speed tomographic PIV<br>-Single injection strategy | - PIV measurements spatially quantified the increase of turbulent kinetic energy, shear and vorticity from injection and distributions were compared against non-injection operation. |
| Hao Chen [94] | 2018 | -2D-2C high speed PIV & Mie-scattering of the fuel spray<br>-Mid injector tumble plane | -Spray changed the air flow structure shortly after the fuel injection, and increased the kinetic energy of the air flow. |

*2.5.1.3 PIV Applications on Steady-State Flow Rig*

As discussed before, steady-state flow rigs have been used by many researchers to quantify the in-cylinder bulk flow inside an engine cylinder during the early stages of engine design. However, with the development of internal combustion engines particularly, in GDI engines, the detailed flow structures became very significant. To obtain these detailed information, optical techniques such as LDA and PIV have been used. There is no much literature on the application of particle image velocimetry on a flow rig. One of the first attempts to apply PIV for such measurements on steady-state flow rigs was carried out by Graham Pitcher *et al*. [109]. The authors illustrated that the major advantage observed from the PIV work was the ability to image full plane data in two components. However, the reflections from the glass liner were found to cause significant signal degradation for the tumble measurements and indicated that more work needs to be done for this particular issue. Figure 2.19 shows the experimental set up and the carried-out steps of pre-processing to solve the problem associated with laser reflection for tumble plane measurements. Saud Binjuwair *et al*. [110] conducted an experimental study to investigate the in-cylinder flow structures under steady-state conditions of model cylinder head using 2D-PIV measurements in the swirl and tumble planes. The experiments were conducted at two pressure drops of 250 and 635 $mmH_2O$ that correlated to engine speeds of 2500 and 4000 rpm respectively. However, the authors stated also that the measurements in the vertical tumble planes were not reliable as a result of the flare noise that was caused by cylinder liner reflections or by higher levels of seeding within the cylinder. B.M. Krishna *et al.* [111] investigated the in-cylinder flow pattern around the intake valve using 2D-PIV on a flow rig at different air flow rates considering the mid valve vertical tumble plane and fixed values of valve lifts. The results illustrated that the tumble ratio was higher at higher intake valve opening and was not much affected by the air flow rates. More recently, Jean Rabault *et al*. [19] used planar 2D-PIV considering the swirl plane to investigate the flow structures generated by parallel valves diesel-engine cylinder head (High Swirl Configuration (HSC) prototype) through test-bench measurements at constant pressure drop of 100 $mmH_2O$. In the swirl plane, complex jet-dominated vertical structures were detected close to the cylinder top. Moving away from the cylinder top, a counter-rotating vortex-pair structure was observed from which a single coherent swirling

structure develops further down the cylinder. By introducing a strong swirling motion, the flow was stabilized which was seen by tracking the instantaneous position of the swirl center.

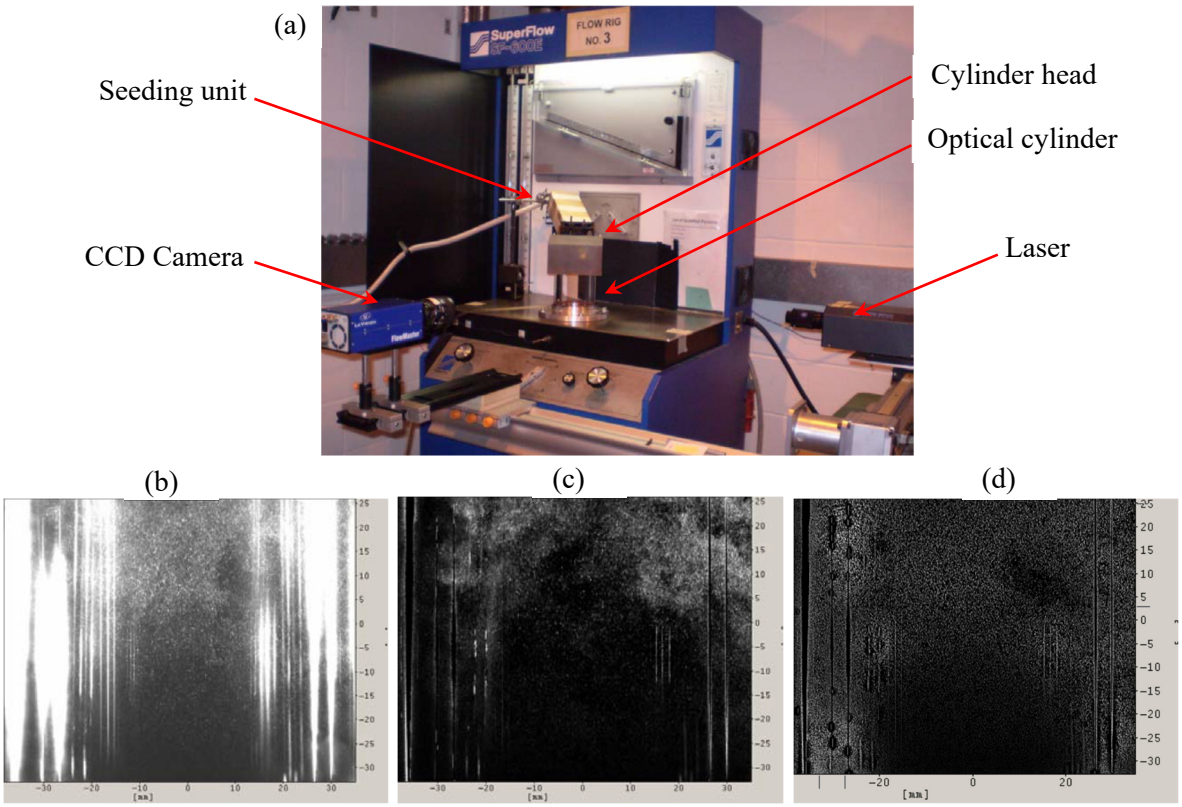


Figure 2.19: (a) PIV set up for measurements in the vertical plane, (b) raw image, (c) background subtraction and (d) intensity normalized [109]

## 2.6 Relation between Steady-State Measurements and those in Optical Engines

One of the most significant factors is the relationship between the in-cylinder flow measurements under steady-state and those measurements in motored optical research engine. Through the literature, only one study was carried out for that specific purpose [112]. The in-cylinder flow measurements were carried out using laser doppler anemometry (LDA) on both steady-state flow rig and optical research engine considering almost similar conditions for comparison. The author illustrated that cycle-to-cycle variability (CCV) is one of the main problems associated with real engine operation. Figure 2.20 Shows the in-cylinder flow velocity measured by LDA for four

cycles along with the ensemble average for all cycles considered. Moreover, the main difference between both measurements is that the pressure difference across the intake valves is variable during the intake stroke because of the motion of the piston and intake valves. Therefore, for matching the conditions between the two systems, the velocity measured on the flow rig was normalized by the mean velocity calculated based on the air flow rate (the mean velocity is equivalent to the mean piston speed in real engine). While mean velocity measured on real engine was normalized by the instantaneous piston speed to reflect the transient nature of the flow. The comparison was performed for the normalized velocities and tumble ratio calculated on both systems. The results revealed that, the tumble ratios and flow structures measured on the flow rig using LDA gave a closer approximation to those measured on motored engine considering same experimental conditions. The transient nature of the flow in the engine appeared to have a little effect on the flow field. The authors finally revealed that the steady-state flow measurements can be used to provide good expectation of the tumble pattern in real engine. Figures 2.21 shows a comparison between the normalized velocities measured on flow rig and motored engine using LDA at valve lift 8.5 mm considering the mid cylinder tumble plane.

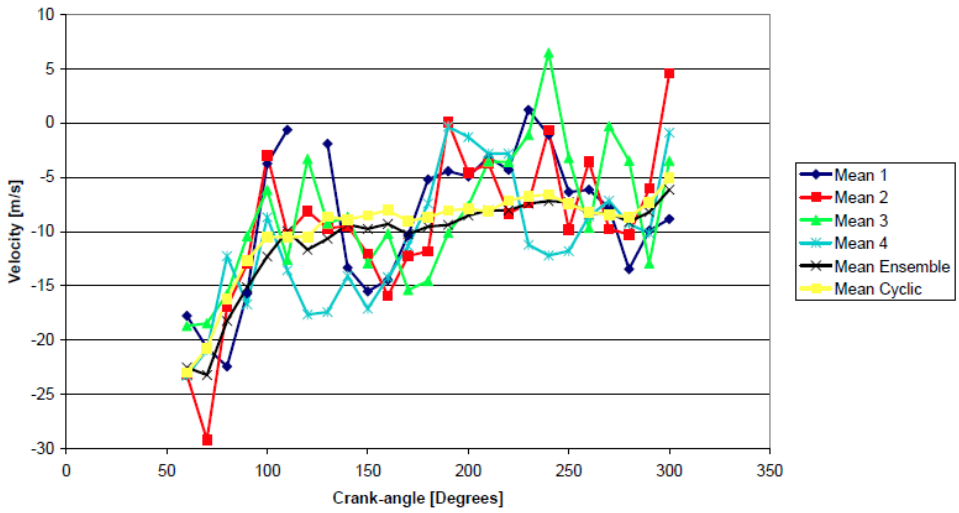


Figure 2.20: The flow velocity for four engine cycles along with their ensemble average to show the cyclic variability [112]

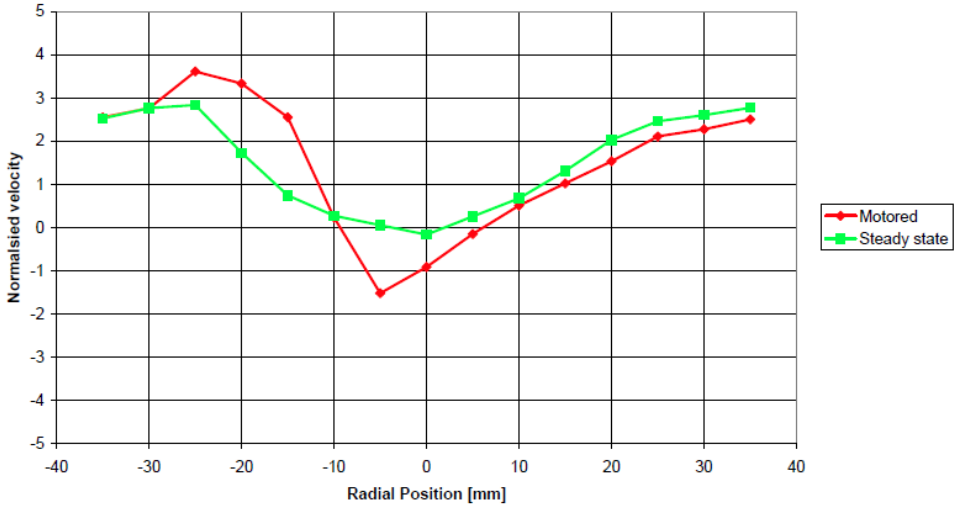


Figure 2.21: Comparison between the normalized velocities measured by LDA on both flow rig and motored engine at valve lift 8.5 mm [112]

## 2.7 Computational Fluid Dynamics (CFD)

Computational Fluid Dynamics (CFD) simulation of the in-cylinder flow is another alternative method which can be used to understand and predict a wide range of phenomena which occur during the full four-stroke cycle of an IC engine. The term encompasses both numerical modelling and finite element computational fluid dynamics. With the continuously decreasing cost of computer power, it can be foreseen that CFD will become a fast and accurate means of predicting engine behaviour. However, the simulation of a full cycle internal engine can still be considered as one of the most difficult problems to be modelled by CFD since it involves moving boundaries, complex heat transfer, turbulent flows, combustion, etc. Furthermore, experimental research has shown that small variations in the inlet port shape could lead to dramatic changes in the combustion characteristics, which indicated that the problem is likely to be extremely sensitive to parameters such as the mesh geometry and the initial conditions. The development and validation of CFD codes for internal combustion simulation was firstly discussed by Khalighi *et al.* in 1995 [113, 114] for SI engines. It was clear from these publications that CFD as a diagnostic tool in engine research remains immature and that the time and cost for the analysis is still high. However, the published results already show that CFD can provide detailed insight into

in-cylinder processes which cannot at present be obtained by another technique. As Khalighi *et al.* [114] concluded in their article," it is not anticipated that CFD will ever replace experiments, but rather that there will be an evolving blend of CFD and measurements". In parallel to experimental investigations, simulations have been used to generate additional knowledge. Reynolds-averaged Navier-Stokes (RANS) and large-eddy simulations (LES) are powerful computational tools to predict engine flows and are widely used for the design and optimization of engine development [19]. Starting with Reynolds Averaged Navier-Stokes (RANS) simulations, considerable researches have been conducted, simulating the effect of engine geometric parameters on in-cylinder flow structures studies [12, 50, 62, 115-117], predicting the in-cylinder tumble motion [13, 104]. The increase in computer power has allowed more accurate Large Eddy Simulations (LES) [118-121]. More recently, Direct Numerical Simulations (DNS) have been performed for idealized engine configurations to investigate the origin of cycle-to-cycle variations [122, 123]. Despite progress accomplished in engine flow simulations [124], simulating configurations reproducing in detail a true engine remains challenging. As a consequence, experiments cannot be by-passed and are required to build knowledge about specific engine configurations and generate data that can be used to validate simulations [19, 104].

## 2.8 Velocity Field Decomposition Techniques

It is of significant importance to analyse spatially and temporally the structures embedded in the instantaneous velocity data sets in order to understand the nature of turbulence. Despite being random in nature, turbulent flow has large-scale regular flow structures which can be described as coherent structures. It is commonly acknowledged that since its inception, coherent structures studies became significant for acquiring new visions related to dynamics, kinematics and scales of turbulent flows. Coherent structures are characterized as distinguishable large-scale flow patterns that contain the maximum energy and maintain their shape for relatively long time against dissipation compared to small-scale flow patterns [125]. Basically, the interpretations and characterization of coherent structures solely depend on the method used to identify these structures [20]. Therefore, there is a pressing need for accurate choosing of

statistical methods for extracting the coherent patterns from multidimensional data sets. Several identification techniques have been proposed. Reynolds decomposition, Galilean decomposition and low-pass filtering are traditional approaches [126]. In addition, there are some other new promising techniques such as, two-point correlation [23], critical-point analysis of local velocity gradient tensor [24], wavelets [127] and proper orthogonal decomposition (POD) [39]. The selection from these identification techniques rely on the nature of coherent structures to be investigated for particular purposes. Some of these techniques are suitable for extracting small scale eddies while the other is suitable for extracting large scale eddies. Thus, the investigation of coherent structures requires an accurate, unbiased and statistical method which can exploit the quantitative nature of the data to extract coherent patterns from multidimensional data sets. POD is one such efficient method that takes advantage of the spatial information of the multipoint instantaneous velocity fields acquired either from experimental PIV measurement or numerical simulations [20].

### 2.8.1 Proper Orthogonal Decomposition (POD)

POD is a statistical and powerful mathematical tool that decomposes a set of velocity distributions into a linear combination of spatial basis functions (or empirical eigenfunctions) (or empirical orthogonal functions) (or space-dependent POD modes, (denoted $\varphi_m$) and their corresponding time-dependent coefficients, (denoted $C_m^{(k)}$) [39, 128]. The source data for this technique can be either experimental PIV data, or numerical simulation data.

POD is truly efficient for extracting the dominant energetic structures of a multi-dimensional process while employing only a few modes. The classical POD technique was firstly presented to the turbulence research by Lumley [25] however, it was restricted because of high computational power. While the snapshot POD technique was introduced by Sirovich [129] which proved to be an efficient method and has many potentials in fluid mechanics, as illustrated by Berkooz *et al.* [130] and Bakewell *et al.* [131]. A detailed description of the mathematical procedure of POD is given in chapter 3.

*2.8.1.1 POD Applications in Internal Combustion (IC) Engines Flows*

Recently, POD has been adopted for the analysis of the in-cylinder flows inside internal combustion engines [39]. POD was conventionally used to extract an optimal set of dominant (in terms of kinetic energy) spatial modes (coherent structures identifications), so that only a small number of modes was needed to represent a particular engine flow condition. However, the application was daunting, and physical interpretation of proper orthogonal decomposition was ambiguous. Therefore Hao Chen et al. [39, 128] proposed practical procedures for the application of POD to IC engine flows. The POD analysis was performed on synthetic velocity vector fields with known characteristics in order to extract some fundamental properties of the POD technique. These data were used to reveal how the physical properties of coherent structures were captured and distributed among the POD modes, in addition to illustrate the difference between subtracting and non-subtracting the ensemble average prior to conducting POD on datasets. With the recent development in optical diagnostic techniques, high-frame rate imaging for hundreds of engine cycles have been enabled [132, 133]. Thus, a powerful and sophisticated analysis tool for extracting useful information from the complicated data set and revealing the cyclic variability was highly required. POD technique was proposed to fulfil this need. The POD analysis technique was implemented for the first time to reveal the cycle-to-cycle variation of pulsing spray characteristics of GDI engine by Hao Chen *et al*. [134-136]. The physical interpretations of different modes and their corresponding coefficients on cycle-to-cycle variations of spray characteristics were identified. Specifically, the first mode pattern mostly captured the ensemble-averaged spray pattern, and the coefficients of mode 1 were used to identify the intensity variation among the different cycles of spray. The second mode pattern and its coefficients provided the quantification of the spatial variation of the spray plume distribution. Mode 3 and higher modes further identified the cycle variations of the small-scale spray structures. Hanyang Zhuang *et al.* [137] combined high-speed time-resolved PIV and POD to determine the ensemble average and variations of the flow field structure among 200 cycles in diesel engine considering the swirl plane. The first POD mode showed the most dominant flow fields which were similar to the ensemble average PIV data while the higher modes captured the smaller structural variations of the flow field. Moreover, Hanyang Zhuang *et al.* [138] extended

their work to study the effect of intake air swirl ratio (SR) on the flow structure by applying the POD technique. The intake air swirl motion was achieved by adjusting the opening of a swirl ratio (SR) control valve which was installed in one of the two intake ports. The results illustrated that combining the PIV and POD analysis provided more physical insights into the engine in-cylinder flow process. The first modes captured the dominant flow structure containing more than 50% of the total energy. While the first POD mode coefficients were highly correlated with the measured SR. A strong linear regression with the coefficient of determination ($R^2$) of 0.9692 was found, as shown in Figure 2.22. This result confirmed that the SR, which represented the strength of swirl motion, was linearly proportional to the increase in mode 1 coefficients.

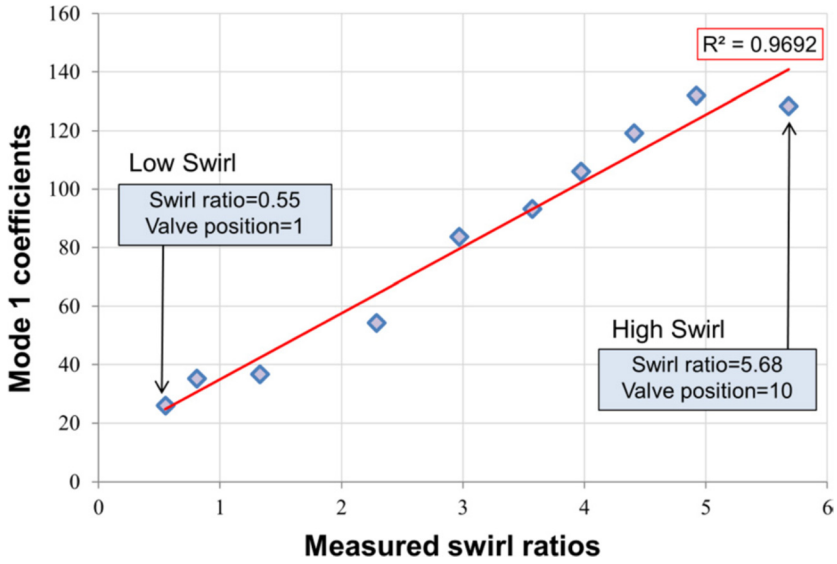


Figure 2.22: The correlation of POD mode 1 coefficients and the measured SR at different swirl control valve positions [138]

Two main POD approaches can be used to process the in-cylinder turbulent flow datasets, which are “phase-dependent POD” and more recently “phase-invariant POD”. The phase-dependent POD approach is to implement the POD at each phase of the flow separately. Whilst, on the other hand, the phase-invariant POD approach is to perform the POD over all available phases of the flow at the same time [67]. With the phase-invariant POD method proposed firstly by Fogleman [139], the velocity fields from different phases are decomposed into a single set of POD modes. In this manner, the POD modes can be used to represent any phase of the flow. In addition, the changes of the POD coefficients over different phases demonstrate how the flow evolves within

engine cycles [138]. Phase-invariant POD not only focused on resolving the cycle-to-cycle variations but also revealing the temporal properties of the flow. Very recently, Liu *et al.* [140], and Abraham *et al.* [141] performed phase-invariant POD on both the experimental dataset (high-speed PIV) and simulation (large eddy simulation, LES) with the attempt to (1) investigate the flow evolution and variations; and (2) validate the cyclic varied LES flow fields by the cycle-to-cycle varying PIV data. Hao Chen *et al.* [142] carried out an experimental study using PIV phase-invariant POD technique to provide the insight into the flow evolution and variations during intake and compression strokes. The high-speed PIV measurement was conducted in a single-cylinder optical SIDI engine and provided the velocity fields from different CADs of 200 consecutive cycles. Then the velocity vector fields were analysed using phase invariant POD. The energy captured by the first three modes together was more than 80% of the total energy (total kinetic energy from all 8200 input velocity fields), as shown in Figure 2.23. Therefore, only the physical meanings of the first three POD modes were investigated in this paper, as shown in Figure 2.24. The authors illustrated that the phase-invariant POD provides an effective and promising way to simultaneously illustrate the flow evolution and quantify the cycle-to-cycle variations of the in-cylinder engine flow characteristics.

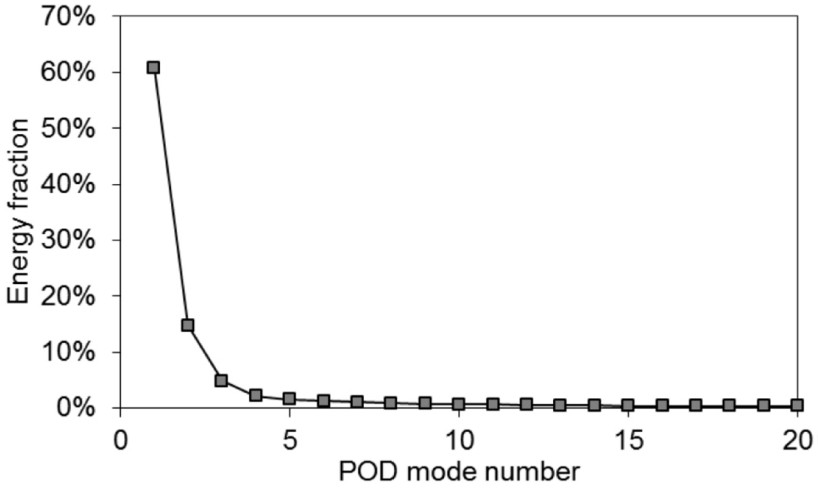


Figure 2.23: Kinetic energy fraction captured by the first 20 phase-invariant POD modes [142]

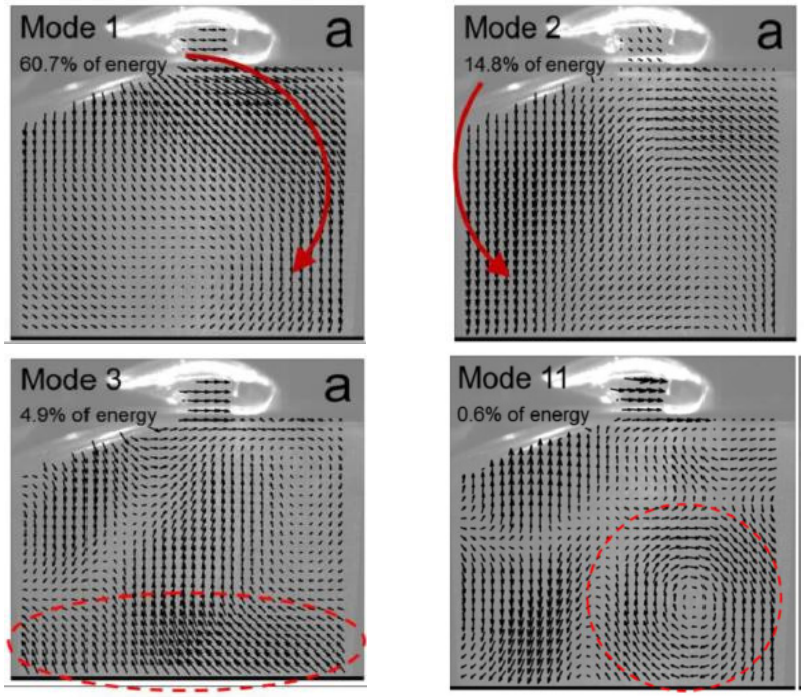


Figure 2.24: Phase-invariant POD of 1st, 2nd, 3rd and 11th modes [142]

## 2.9 Chapter Summary

Based on the comprehensive review in this chapter, it was clear that the flow field in an engine is rather complex, inherently unsteady, turbulent and three dimensional. At each point in the cylinder the velocity is made up of 'steady time-dependent' component based on the valve lift and crank angle, and unsteady or 'random' components which are caused by cycle-to-cycle variations, large and small vortex structures and turbulence. The interaction of these complex flow structures and fuel spray leads to unmanageable analysis of detailed experimental data from engine measurements. Traditionally, engine combustion system designs were based on 'integral' bulk air characterisation parameters (swirl and tumble). Increasingly there is strong belief in the industry that these methods are not adequate for the sophisticated and detailed designs required to meet the ever-increasing stringent emission regulations. Detailed temporal and spatial behaviour of the flow is required to inform the design process of the new combustion systems of these engines.

Furthermore, the need for fast combustion system design optimisation, the fast developments in the level of sophistication of numerical modelling, and huge increase in affordable computer power, has led to the industry relying more and more on 'virtual' design tools such as RANS, LES and DNS. These tools require detailed and reliable temporal and spatial experimental validation acquired from HWA, LDA, PDA, PIV. When looking through the literature, it quickly becomes apparent that, various research related to GDI in-cylinder flows and their interaction with direct fuel spray have been carried out using PIV on optical research engines. However, most of reviewed studies showed that the measurements were done within one tumble plane using 2D-PIV measurements which suffer from errors due to the large out-of-plane velocity components. In addition, there are problems associated with these engines which included the high cost, cycle-to-cycle variability, limited optical access and limited speed range. Therefore, the combination of steady-state flow rig measurements and stereoscopic high-speed time resolved PIV and POD analytical technique eliminates these problems and allows more realistic and useful analysis of the data. This, in turn, provides more in-depth understanding of the characteristic of the flow and their interactions with fuel spray and hence provide a more appropriate validation data for numerical techniques. Therefore, the research gaps are identified as follows:

- The evaluation of integral flow parameters is not enough for modern engines as more detailed temporal and spatial information regarding the flow structures are highly required.

- Steady-state flow measurements are needed to validate the CFD results to avoid the random cycle-to-cycle flow variations associated with the real engine.

- Two-dimensional PIV measurements in optical engines suffer from errors as a result of the out-of-plane velocity components in modern engines where the flow is largely three dimensional.

- Measurements at several tumble planes using stereoscopic PIV are highly required to fully characterize the tumble motion.

# CHAPTER 3

# RESEARCH METHODOLOGY

## 3.1 Chapter Overview

This chapter presents the overall research methodology which comprises three main sections. The first section concerns a detailed description for the validation with Ricardo experimental and simulation work. Therefore, a complete description of both the Ricardo and the FEV steady-state flow rigs, together with details of the equipment and calculations used to process the results are presented. The second part concerns a detailed description of the non-intrusive experimental technique, particle image velocimetry (PIV). This description includes PIV fundamentals, the seeding arrangement and the method of setting up and analysis. The third and final part comprises a complete description of the identification technique used in this thesis, proper orthogonal decomposition (POD). The flow chart of the experimental methodology employed in this study is depicted in Figure 3.1.

## 3.2 Verification and Validation of Ricardo Experimental and Simulation Work

The validation work was divided into two sections: validation with Ricardo steady-state flow rig and validation with Ricardo VECTIS CFD simulation. A spray-guided gasoline direct injection (GDI) cylinder head was mounted on both flow rigs; Ricardo and FEV. The experiments were carried out using the same pressure difference across the air intake valves for fixed values of valve lifts from 1 mm to 9 mm in 1 mm increments in order to compare the results. The following sections provide a detailed description of cylinder head and both flow rigs as well as the calculations used to process the final outcomes.

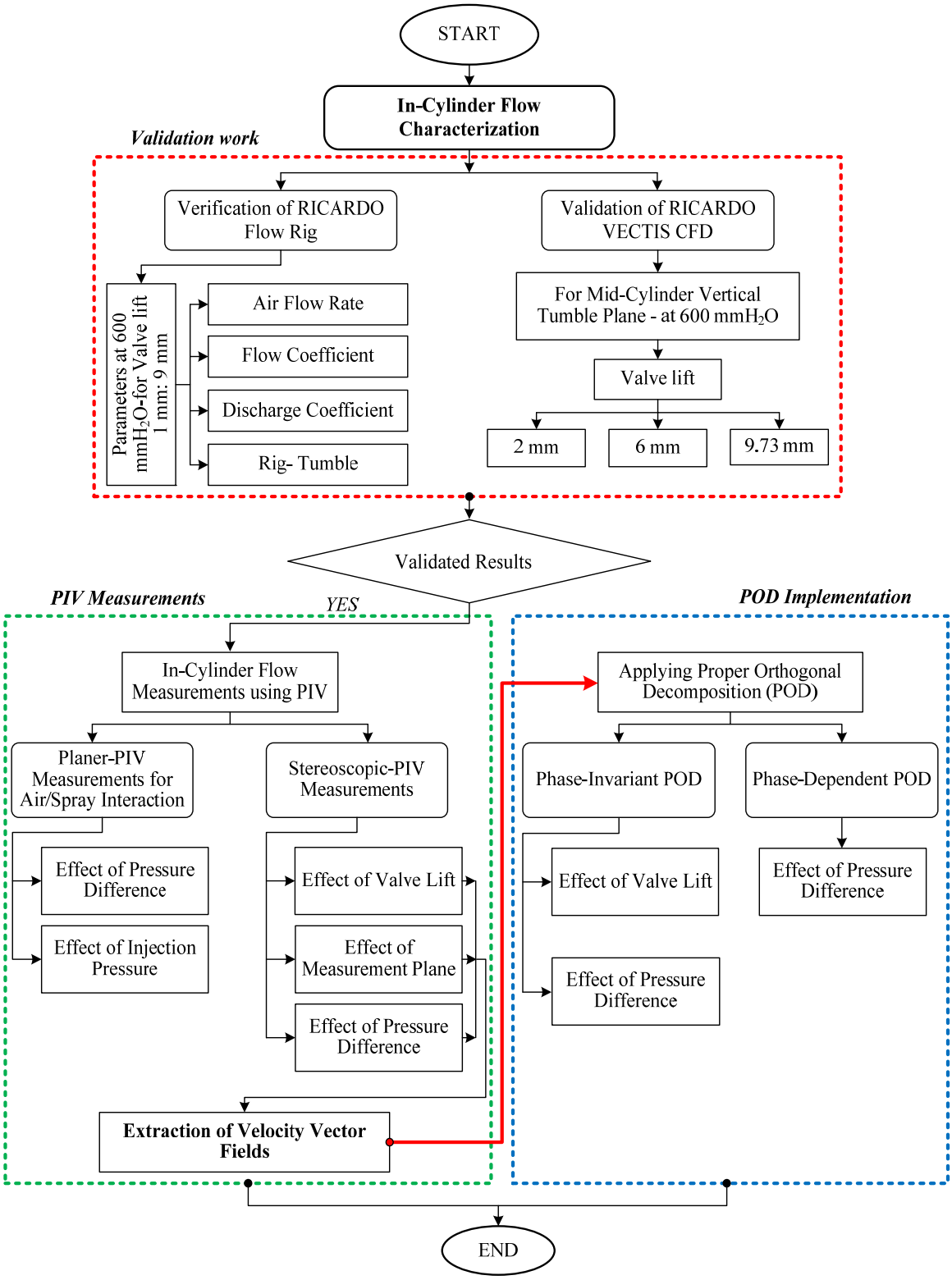


Figure 3.1: Flow chart of the research methodology

### 3.2.1 Cylinder Head and Cylinder Liner Specifications

A four valves pent-roof gasoline direct injection head (shown in Figure 3.2) was used on both flow rigs. The cylinder head specifications are shown in Table 3.1. The two intake valves were manually adjusted using a micrometre and positioned at a constant valve lift of 1 mm to 9 mm. The cylinder head was fixed on top of the cylinder. The cylinder liner was made of Plexiglas, having an internal bore diameter of 92.5 mm, stroke of 116 mm, and wall thickness of 3 mm, as shown in Figure 3.3. It was used to provide optical access through the full stroke length for PIV measurements. Two outlet ports with a recommended diameter of 35% of the bore diameter and a distance of 67 mm from the gas face were cut at both sides of the cylinder liner. A flat piston was placed at the bottom of the liner at the same distance of the engine stroke.

Figure 3.2: Gasoline direct injection cylinder head

Table 3.1: Cylinder head specifications

| Parameters | Values |
|---|---|
| Bore [mm] | 92.5 |
| Number of inlet valves per cylinder | 2 |
| Number of exhaust valves per cylinder | 2 |
| Intake valve inner seat diameter, D [mm] | 33.7 |
| Seat angle [degree] | 45° |
| Valve head diameter [mm] | 36 |
| Valve stem diameter [mm] | 5.5 |
| Max valve lift, $L_{max}$ [mm] | 10 |

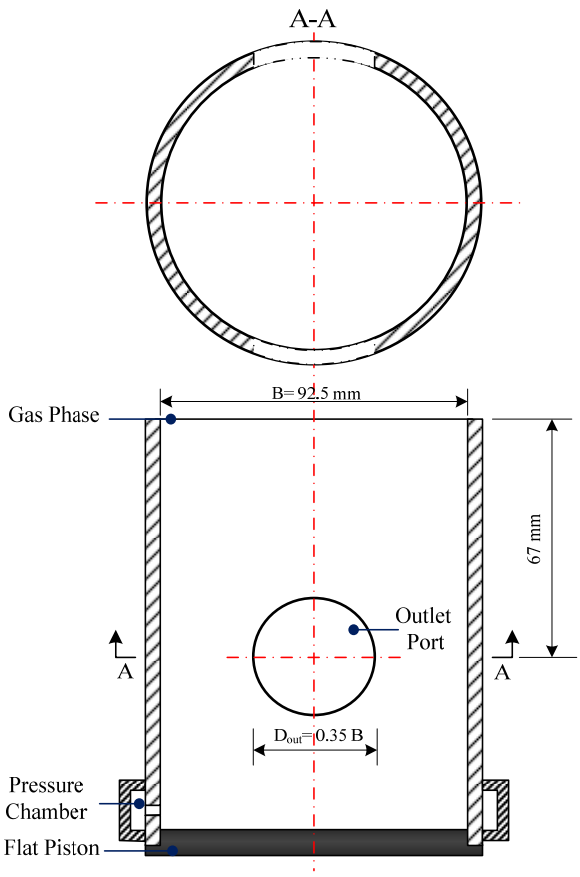


Figure 3.3: Cylinder liner specifications

### 3.2.2 Inner Seat Diameter and Test Pressure Selection

All port flow calculations need to be based on one characteristic dimension which can be applied to all ports tested. Ricardo use “inner seat diameter” (ISD) which was defined as the minimum contact diameter between the seat on the valve head and the seat on the insert. The pressure difference of 600 mm$H_2O$ was selected based on Reynolds number criteria for validation results depending on intake valve inner seat diameter of 33.7 mm to insure fully turbulent flow.

### 3.2.3 Ricardo Steady-State Flow Rig

Several assumptions were considered with the use of Ricardo induction model which are summarized as:

- Flow into the engine occurs between inlet valve opening and closing and hence flow is dependent on valve lift.
- The pressure drop across the port is constant during induction.
- Volumetric efficiency is assumed to be unity.

Figure 3.4 shows a schematic layout of Ricardo flow rig used for tumble measurements. The test equipment consisted of a centrifugal fan driven by a continuously variable speed direct current (DC) motor. The air volume flow rate was measured using a viscous flow air meter (VFAM). This was due to the pressure drop across the element in such flow-meter was directly proportional to the magnitude of flow rate, moreover, it had an excellent turn-down ratio. A pressure box was attached to the cylinder head manifold face. It was designed to act as a reservoir of air under conditions approaching stagnation and contains flow straighteners to eliminate any directional flow influence from the flexible pipe.

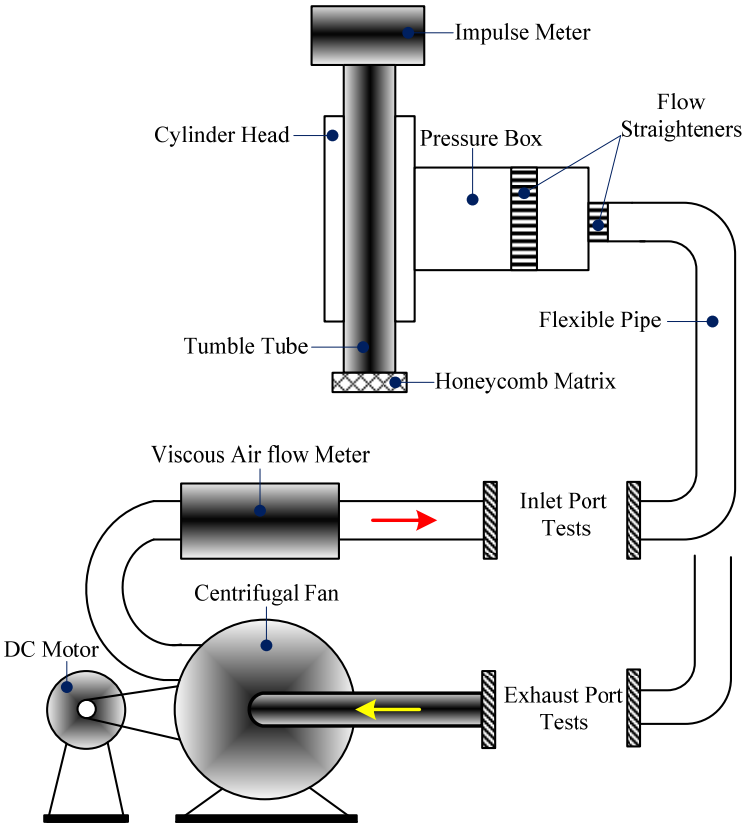


Figure 3.4: Schematic diagram of Ricardo flow bench used for tumble measurement [73]

Pressure and temperature were measured in the entry box and were used as the reference conditions for the calculations of results. Bulk air motion was quantified by an impulse swirl meter (ISM). The ISM operated on the principal of flow rectification. By converting any rotational flow into purely axial flow, the measured torque is directly related to the angular momentum of the rectified flow.

#### *3.2.3.1 Tumble Test*

A tumble rig was used to conduct a tumble test as shown in Figure 3.5. The cylinder head was mounted with the gas face vertical, and a tumble rig was attached via an adaptor plate mounted on the gas face of the cylinder head. The ISM was mounted on top of the tumble tube. At the lower end of the tube a second piece of honeycomb element was mounted to produce an equal flow resistance to the swirl meter element on the top of the tumble tube. The tumble rig adaptor plate was designed to allow the cylinder head to be rotated (with the gas face in the vertical plane) with the tumble rig remaining vertical. Hence tumble measurements were taken in any direction around the cylinder axis. The test procedures for tumble tests were summarized as follows:

- The cylinder head is mounted on the tumble rig.
- The fixed pressure drop across the valve used to conduct the test is selected depending upon inner seat diameter of the valve to ensure fully turbulent flow based upon a Reynolds number.
- The intake valves are opened incrementally over the valve lift range. Compressor output rate is increased to maintain a constant pressure drop across the port. Flow and impulse meter torque are measured at each position.
- The air flow is measured using a viscous flow air meter. Comparison of measured and ideal flow rates define port flow efficiency.
- The angular momentum of the air generated by the port and chamber features is arrested by the impulse swirl meter and measured as torque. The ratio of

calculated tangential to theoretical axial velocity provides an indication of the charge air motion at each discrete valve lift.

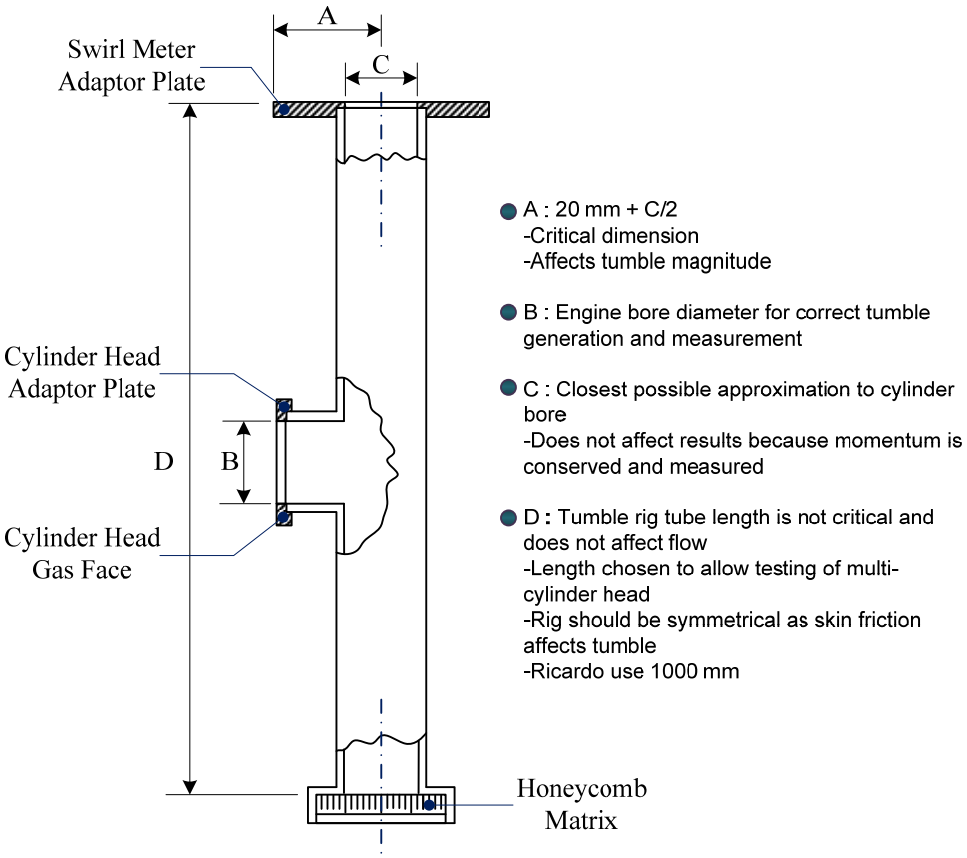


Figure 3.5: Tumble Rig Design Features [73]

### *3.2.3.2 Terminologies Used in Ricardo Port Performance Analysis [71]*

A number of terms can be deduced from the port flow and air motion measurements which are used to define the port performance characteristics. Port flow characteristics are defined by a flow coefficient ($C_f$) and discharge coefficient ($C_d$). These coefficients are measures of port efficiency and compare actual port performance with that of a theoretically unrestrictive port. The flow coefficient is based on inner seat area ($A_{seat}$) and the discharge coefficient is based on the area of a frustum formed perpendicular to the valve and seat insert faces ($A_V$), as shown in Figure 3.6. Port performance is therefore assessed at low valve lifts by the discharge coefficient where valve to seat outlet area is the primary restriction. Performance at high valve lift is described by the

flow coefficient where the port itself is normally the major restriction to flow. Non-dimensional rig swirl or non-dimensional rig tumble characterises any rotational flow produced by the port at a given valve lift. This is defined as the ratio of the tangential swirl velocity compared to the ideal velocity. The tangential swirl velocity is the velocity at the bore surface of a forced vortex, assuming solid body rotation, that produces an equal angular momentum to that recorded during test work with the impulse swirl meter.

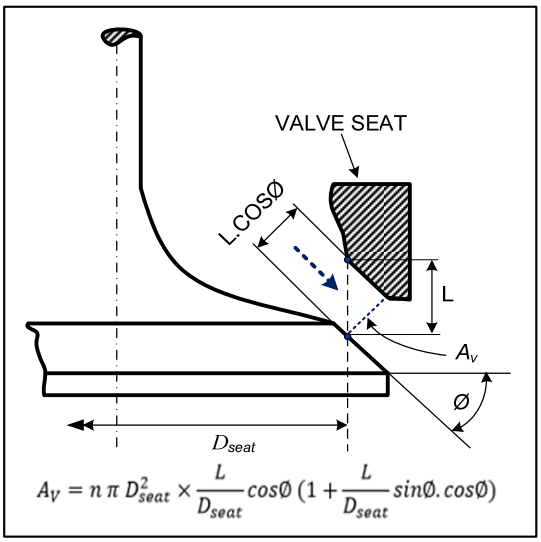


Figure 3.6: Area used for calculation of discharge coefficient [73]

- Flow Coefficient ($C_f$)

$$C_f = \frac{Measured\ volume\ flow\ rate}{Ideal\ volume\ flow\ rate} \tag{3.1}$$

$$C_f = \frac{Measured\ volume\ flow\ rate}{Refernce\ area \times ideal\ velocity} = \frac{Q}{A_{seat} \times V_o} \tag{3.2}$$

Where: $Q$ ≡ Measured air volume flow rate, ($m^3$/sec)

$A_{seat}$ ≡ Inner seat area=$\pi/4 \times D_{seat}$, ($m^2$)

$D_{seat}$ ≡ Inner seat diameter of the intake valve, (m)

$V_o$ ≡ Velocity head=$\sqrt{((2 \times \Delta P)/\rho)}$, (m/sec)

$\Delta P$ ≡ Total pressure drop over port, (N/m$^2$)

$\rho$ ≡ Air density, (kg/m$^3$)

- Coefficient of Discharge ($C_d$)

$$C_d = \frac{Measured\ volume\ flow\ rate}{Refernce\ area \times ideal\ velocity} = \frac{Q}{A \times V_o} \quad (3.3)$$

Where: $Q$ ≡ Measured air volume flow rate, (m$^3$/sec)

$A_V$ ≡ Orifice area between valve head and seat at low valve lifts (m$^2$)

$$= n \times \pi \times D_{seat}^2 \times \frac{L}{D_{seat}} \times cos\emptyset\ (1 + \frac{L}{D_{seat}} \times sin\emptyset.cos\emptyset) \quad (3.4)$$

$n$ ≡ Number of intake valves

$L$ ≡ Valve lift, (m)

$\emptyset$ ≡ Valve seat angle, deg.

- Non- dimensional rig-tumble ($N_{T-R}$)

$$N_{T-R} = \frac{2 \times Charge\ tangential\ velocity\ at\ bore\ edge}{Ideal\ velocity} = \frac{8 \times G}{\dot{m} \times V_o \times B} \quad (3.5)$$

Where: $G$ ≡ Torque measured by impulse meter (N.m)

$\dot{m}$ ≡ Measured mass flow rate (kg/sec)

$B$ ≡ Cylinder bore diameter (m)

The second flow rig used in this study to conduct the experimental work was the FEV. The next section describes the FEV flow rig layout and its performance analysis procedures.

### 3.2.4 FEV Flow Rig

FEV developed an evaluation methodology and test bench, in order to quantify tumble and swirl of the in-cylinder charge motion. Figure 3.7 depicts the layout of the test rig for FEV steady swirl and tumble. For the measurement, the cylinder head was mounted onto the rig and the air was inducted by a centrifugal compressor through the intake port, the cylindrical tube, the compensation tank and through the rotary piston gas meter. During the experiments, all measurements were conducted at constant pressure difference between the cylindrical tube and atmosphere. The pressure adjustment, which was required for different valve lift settings was achieved by using a by-pass valve which was controlled by a stepper motor. The air flow rate was measured using a rotary-piston gas meter.

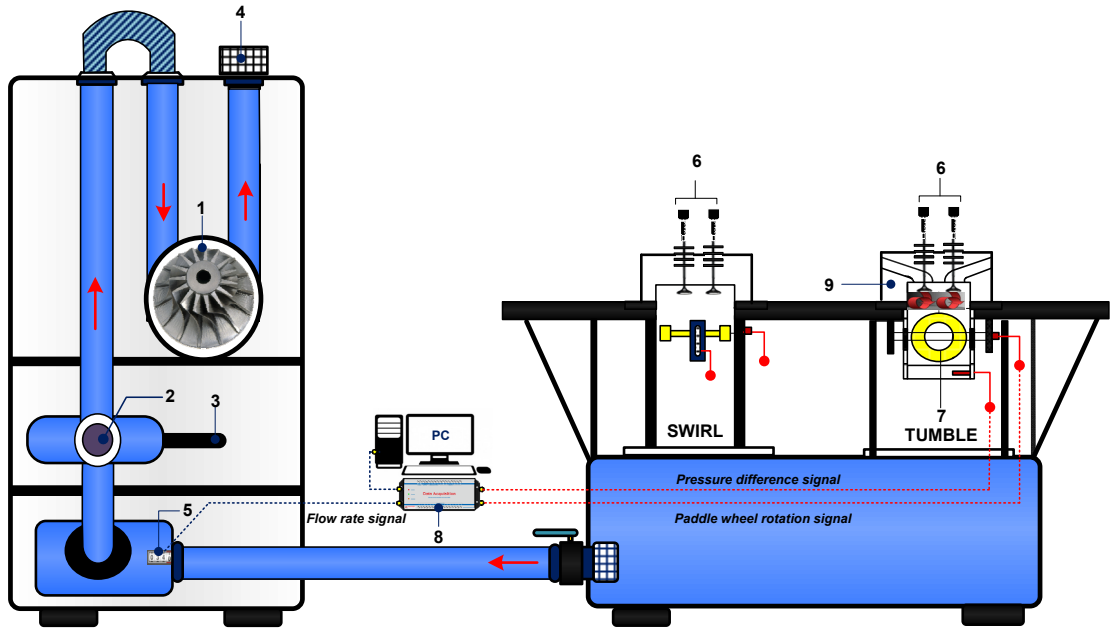


Figure 3.7: Layout of FEV steady-state flow bench

The tumble level was obtained by evaluating the rotational speed of a paddle wheel anemometer with horizontal axes of rotation in order to determine the rotation of a vortex perpendicular to the cylinder axis (Tumble). The geometrical data of the paddle wheel was defined relative to the cylinder bore diameter (see Figure 3.8). The piston

crown plays an important role for the development of the tumble vortex; therefore, the piston was included in the test rig. An acquisition system linked to a computer for capture and storage of measurements, including air volume flow rate, paddle wheel rotation speed, temperatures, and pressures.

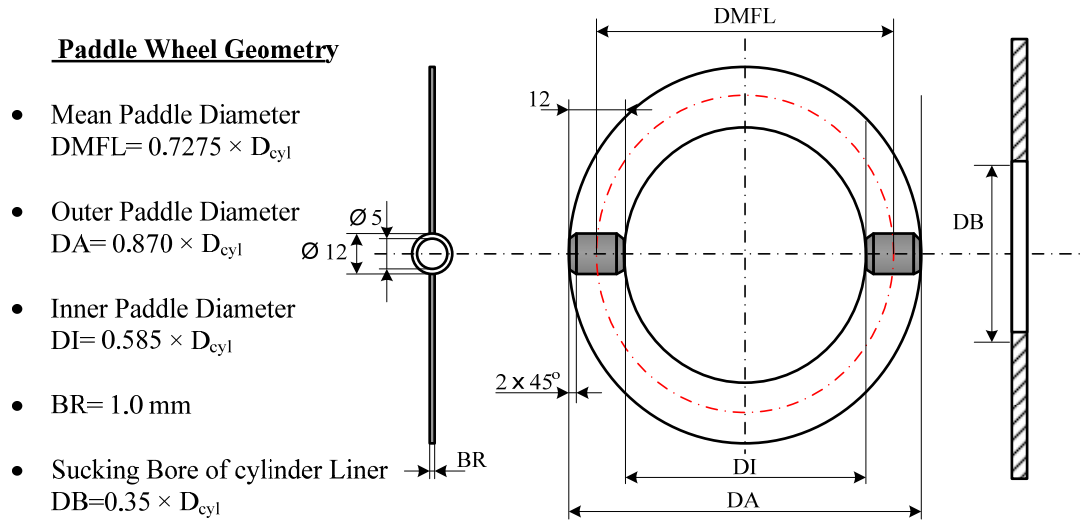


Figure 3.8: Tumble paddle wheel geometry

### *3.2.4.1 Terminologies Used in FEV Port Performance Analysis*

- Flow Coefficient ($C_f$)

The flow coefficient is defined as the ratio of the empirically obtained mass flow rate and the theoretical mass flow rate:

$$C_f = \frac{\dot{m_{real}}}{\dot{m}_{theor}} \tag{3.6}$$

The actual air mass flow rate was measured on the test bench:

$$\dot{m}_{real} = \dot{V} \times \frac{P}{R \times T} \tag{3.7}$$

Where: $\dot{V}$ ≡ Volume flow rate ($m^3$/sec) ; $T$ ≡ Temperature (K);

$P$ ≡ Pressure ($N/m^2$) ; $R$ ≡ Gas constant (J/kg. k)

The theoretical mass flow rate ($\dot{m}_{theor}$) for a defined cross-sectional area ($A_{seat}$) was obtained as:

$$\dot{m}_{theor} = A_{Seat} \times \rho s \times Cs \tag{3.8}$$

Where: $A_{Seat}$ ≡ Inner seat area= $\frac{\pi}{4} \times D_{seat}^2$, (m$^2$)

$D_{Seat}$ ≡ Inner seat diameter of the intake valve, (m)

$\rho s$ ≡ Air density under isentropic conditions, (kg/m$^3$)

$Cs$ ≡ Flow velocity under isentropic conditions (m/sec)

The flow velocity ($Cs$) is calculated with the formula for isentropic flow:

$$C_s = \sqrt{\frac{2 \times k}{k-1} \times R \times T_1 \times \left[1 - \left(\frac{P_2}{P_1}\right)^{\frac{k-1}{k}}\right]} \tag{3.9}$$

Where: $P_1$ ≡ air pressure upstream of the valve (N/m$^2$)

$T_1$ ≡ Air temperature upstream of the valve (K)

$P_2$ ≡ Air pressure downstream of the valve (N/m$^2$)

$k$ ≡ Isentropic exponent for air (1.4)

Likewise, the density under isentropic conditions was computed as:

$$\rho_s = \frac{P_1}{R \times T_1} \times \left(\frac{P_2}{P_1}\right)^{\frac{1}{k}} \tag{3.10}$$

Definition of pressures $P_1$and $P_2$ for suction condition (Intake stroke)

$P_1 = P_{ambient}$

$P_2 = P_{ambient} - |\Delta P|$

Where: $\Delta P$ ≡ Pressure difference between environment and cylinder liner

- Discharge Coefficient ($C_d$)

The discharge coefficient ($C_d$) is defined as the ratio of the experimentally obtained mass flow rate and the theoretical mass flow rate:

$$C_d = \frac{\dot{m}_{real}}{\dot{m}_{theor}} \tag{3.11}$$

The theoretical mass flow rate ($\dot{m}_{theor}$) for a defined orifice area between valve head and seat at low valve lifts ($A_V$) was obtained as:

$$\dot{m}_{theor} = A_V \times \rho s \times Cs \tag{3.12}$$

Where: $A_V$ ≡ Orifice area between valve head and seat at low valve lifts, ($m^2$)

$$= n \times \pi \times D_{seat}^2 \times \frac{L}{D_{seat}} \times cos\emptyset \left(1 + \frac{L}{D_{seat}} \times sin\emptyset . cos\emptyset\right)$$

- Non- dimensional rig tumble ($N_{T-FEV}$)

In order to describe the measured tumble intensities independently from the mass flow, the non-dimensional rig tumble is indicated as a non-dimensional quantity $C_T/C_A$, $C_T$: circumferential velocity of the tumble motion at the mean paddle radius, $C_A$: mean axial velocity in the cylinder).

The linear circumferential speed of the tumble motion was computed as follows:

$$C_T = 2 \times \pi \times N \times R_{MFL} \tag{3.13}$$

Where: $N$ ≡ Paddle wheel speed (RPS)

$R_{MFL}$ ≡ Mean paddle wheel radius (m)

$$= 0.36375 \times D_{cyl}$$

$D_{cyl}$ ≡ Cylinder bore diameter, (m)

Likewise, the axial velocity of the air flow in the cylinder was calculated as follows:

$$C_A = \frac{\dot{m}real}{\rho_{cyl} \times A_V} \tag{3.14}$$

Where: $\rho_{cyl}$ ≡ Air density inside the cylinder = $\frac{P_2}{R \times T_2}$, (kg/m$^3$)

Appendix A shows an example of processed data and results for both FEV and Ricardo flow rigs.

### 3.2.5 Ricardo VECTIS CFD Simulation of the In-Cylinder Flow

In this part of research, the experimental results from PIV measurements were compared with those a RICARDO-VECTIS CFD simulation of the same cylinder head and the same experimental conditions. Several steps were carried out in order to perform the simulations, these steps are depicted in Figure 3.9.

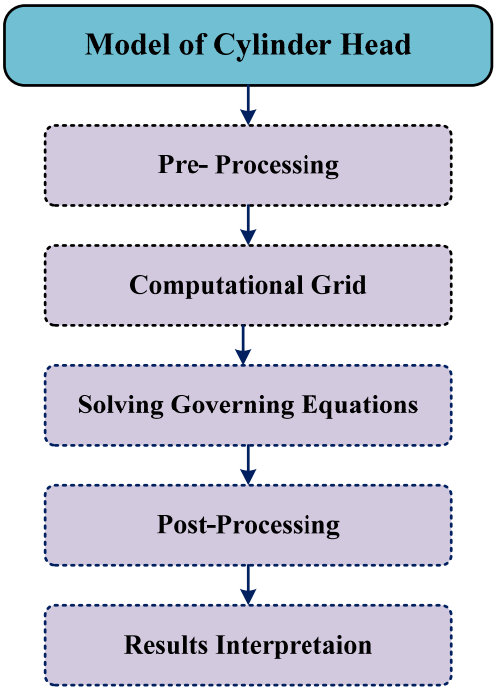


Figure 3.9: Simulation steps in VECTIS

A complete surface model of the intake plenum, intake ports, intake valves, combustion chamber and the cylinder liner were passed directly to VECTIS from a Computer Aided Design (CAD) system. Figure 3.10 depicts the geometrical model of the intake plenum and the cylinder head used in the current work. All dimensions of the cylinder head were provided by FORD motor company as the manufacturer of this cylinder head to ensure geometrical consistency between the simulation and

experimental work. One of the key steps in CFD is the generation of the computational grid, which consists of computational cells. The governing equations were solved in computational cells. The individual computational meshes were generated automatically by using a third-party mesh generation tool to create a polyhedral mesh with prism cells to provide local mesh refinement near the boundaries in order to accurately capture the surface definition. Figure 3.11 shows the 3D meshed geometrical model and the surface geometry sectioned at the mid intake valve plane at different valve lifts to show the computational mesh. In addition to local boundary mesh refinement, block refinement (where cells were forced to be refined irrespective of their proximity to boundaries) was applied in the region of the valve gaps to ensure the accuracy of the solution. Table 3.2 summarizes the mesh sizes for different valve lifts.

VECTIS is a finite volume, pressure-based solver, solving Reynolds Averaged Navier-Stokes (RANS) equations, in this work using the SIMPLE algorithm. The working fluid was air, and it was considered as an ideal compressible gas for the density predictions, while its laminar viscosity, thermal conductivity as well as specific heat capacity were taken to be constant, corresponding to experimental reference temperature. The Turbulence was modelled using VECTIS realizable (time–scale bounded) $k-\varepsilon$ model in conjunction with the standard wall functions. The bounded MINMOD convective scheme (90% MINMOD, 10% upwind) was employed. Boundary conditions were those used during experiments, shown in Table 3.3. Thus, stagnation conditions were specified at the plenum inlet boundary using a total pressure boundary condition whilst a constant static pressure was prescribed at the outlet pressure boundary.

Table 3.2: Number of nodes, faces and elements mesh sizes for different valve lifts

| **Valve Lift** | **2 mm** | **6 mm** | **9.73 mm** |
|---|---|---|---|
| **Nodes** | 4804146 | 5011031 | 5695268 |
| **Faces** | 5901891 | 6146944 | 6938083 |
| **Elements** | 904511 | 939165 | 1047110 |

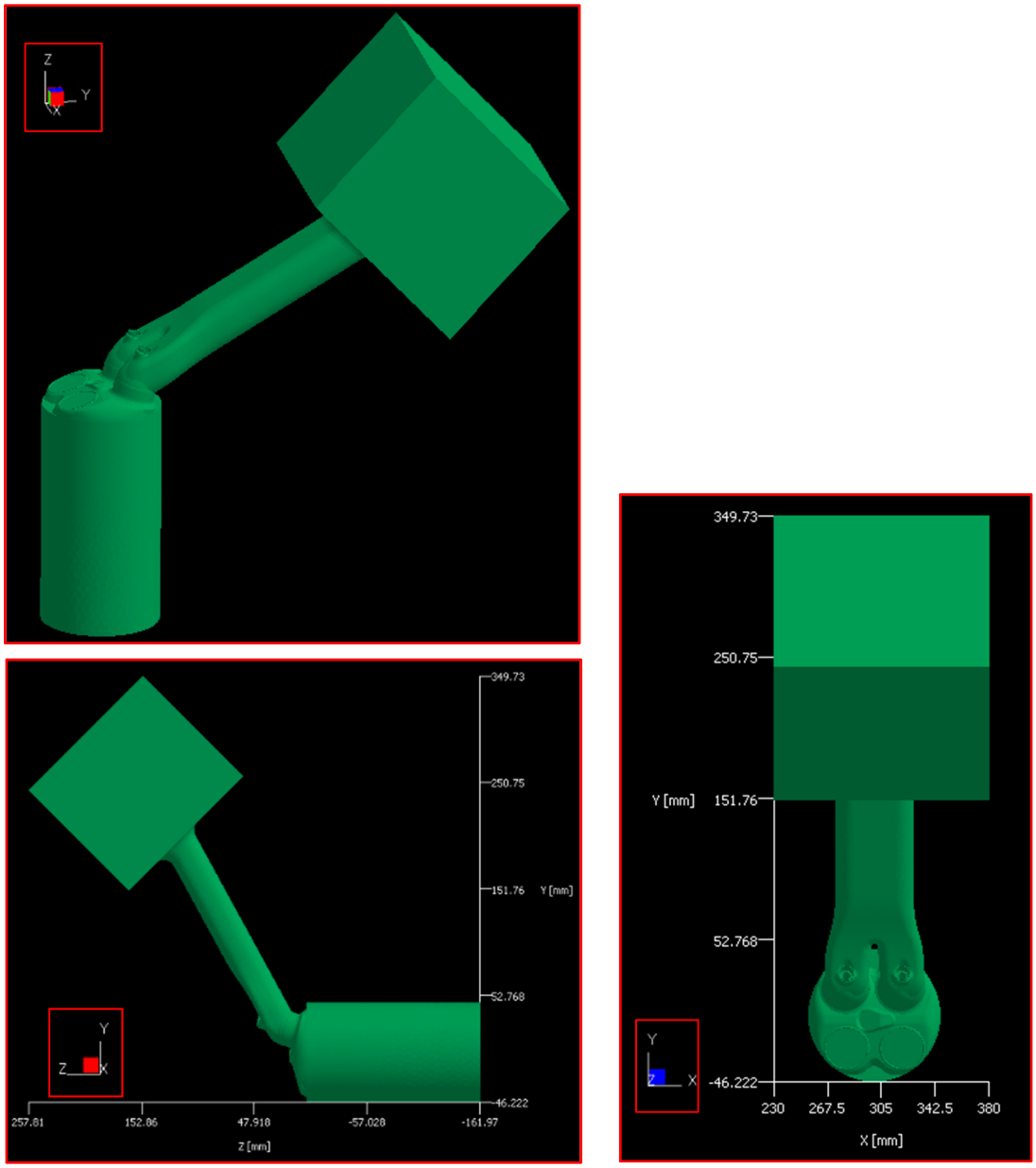


Figure 3.10: Geometrical model of the cylinder head and intake plenum

Table 3.3: Experimental conditions used for validation

| Case | Valve Lift [mm] | Pressure Difference [mm$H_2O$] | Conditions |
|---|---|---|---|
| **1** | 2 | 600 | Steady-state conditions |
| **2** | 6 | 600 | Steady-state conditions |
| **3** | 9.73 | 600 | Steady-state conditions |

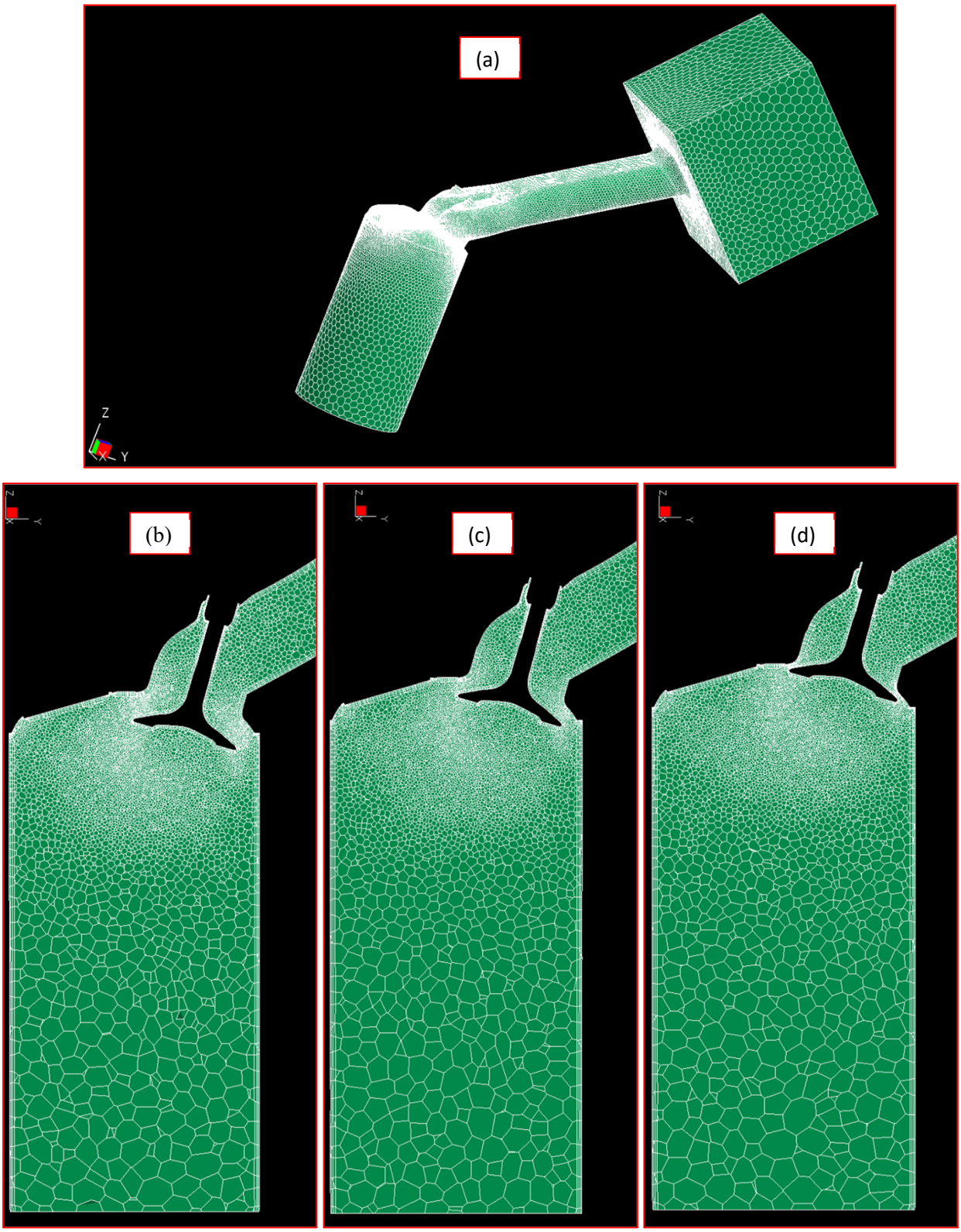


Figure 3.11: Geometrical mesh (a) 3D meshed geometrical model, (b) valve lift 9.73 mm (at mid valve plane), (c) valve lift 6 mm, (d) valve lift 2 mm

## 3.3 Characterization of In-Cylinder Flow Structures

Two steps are required in order to characterize the turbulent flow inside the cylinder, velocity field estimation and coherent structures extraction and analysing. The velocity fields were estimated using particle image velocimetry (PIV) in different tumble planes. The tumble plane was chosen because modern GDI engines are considered as tumble-dominated engines. Whilst, the flow structures were extracted and analysed using proper orthogonal decomposition (POD).

### 3.3.1 Velocity Field Estimation Using PIV

Typically, the experimental set-up of a PIV system involves several subsystems, seeding particles, illumination source, imaging system and processing unit (PIV processor). Mainly, the flow has to be seeded with a suitable type of tracer particles having a similar density to that of the fluid. Within a short time-interval, these tracer particles have to be illuminated twice using high power double-pulsed laser. The scattered light from the particles has to be captured either on double frames or on single frame using Charged Coupled Device (CCD) camera. The image frames are then sub-divided into smaller areas called “interrogation area-IA” and the displacement of the tracer particles between the light pulses has to be determined through means of statistical methods (auto- or cross-correlation). The velocity associated with each interrogation area is the displacement over the time between the two exposures. An advanced post-processing is essential with a view to make use of the great amount of data which can be acquired using the PIV technique. Figure 3.12 shows a typical experimental set-up required for 2D-PIV recording. Figure 3.13 shows the significant steps required to perform PIV measurements.

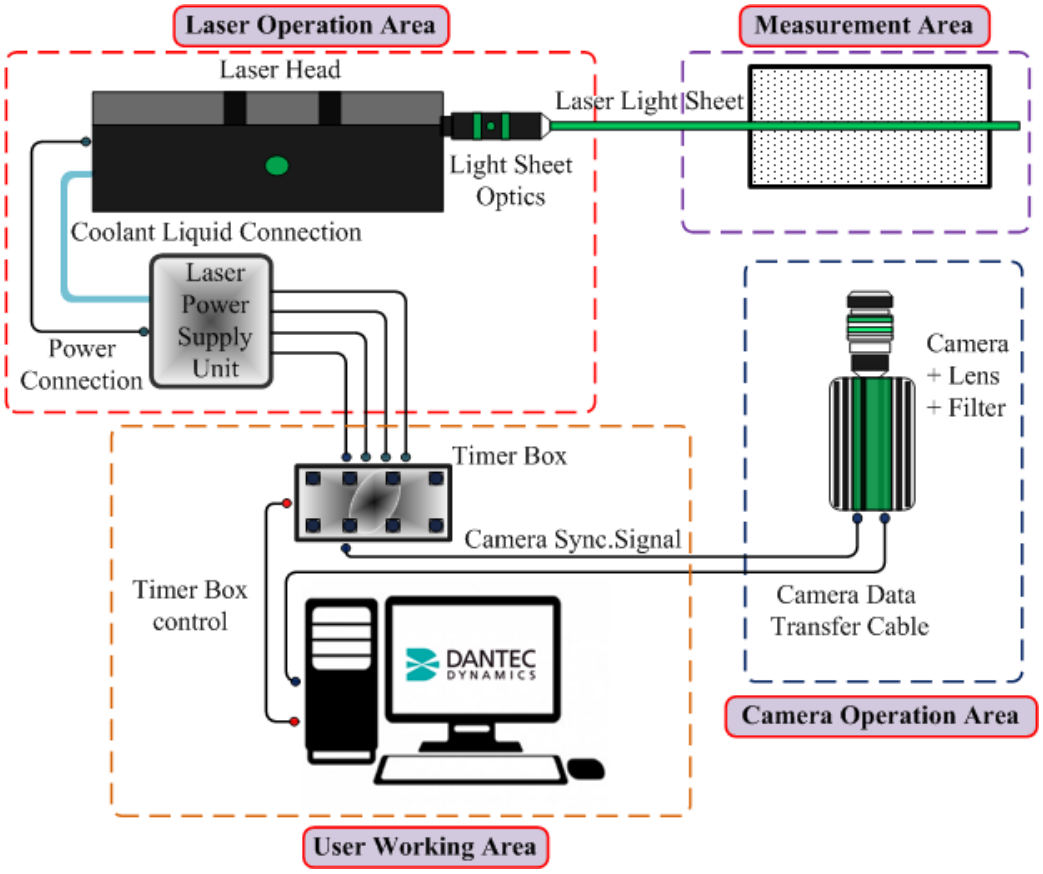


Figure 3.12: Basic components of 2D-PIV measurement

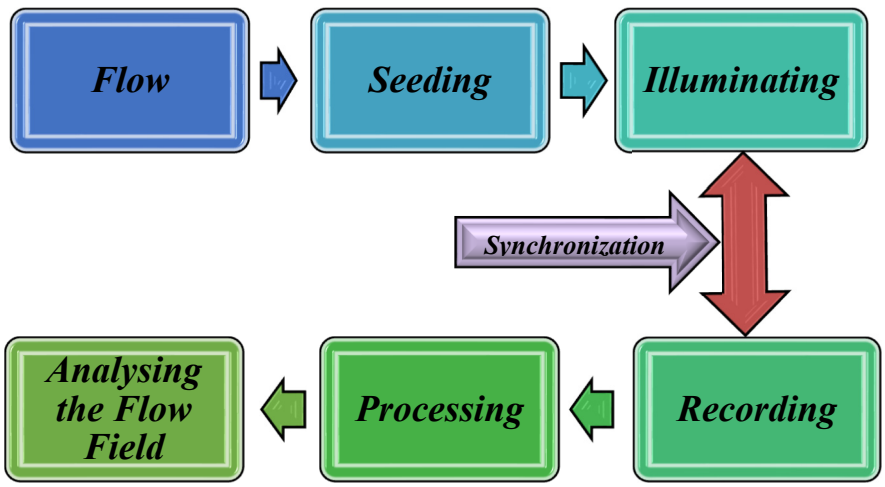


Figure 3.13: Steps required to perform PIV measurement

### 3.3.2 Seeding Particles (Flow Tracer Particles)

With PIV, the velocity of particles suspended in the flow of interest is measured-i.e. seeding particles are used as "velocity probes". Therefore, the precise choice of seeding particles is critical to the successful implementation of PIV experiments. A proper compromise between two fundamental aspects is essential during the selection of particle diameters. Seeding particles not only must be small enough to follow the flow fluctuations faithfully (tracking characteristics of particles), but also must be large enough to generate a strong scattering light (scattering characteristics of particles). Detailed information about both tracking characteristics and scattering characteristics of particles can be found in [87, 88]. Subsequently, some important properties must be considered during the selection of seeded particles, which can be summarized as follows:

- Particles should be neutrally buoyant in the fluid.
- Able to follow the flow with low temporal error (typically less than 1 %)
- Good light scatters.
- Conveniently generated (and cheap).
- Non-toxic, chemically inactive (and clean), non-corrosive and non-volatile.
- The size of the particles must be appropriate, not too small that they cannot be visualized by the camera or too large that they alter the fluid properties.
- Spherical shaped particles have higher Mie-scattering as compared to irregular shaped particles.
- Particles with higher refractive property are suitable as they scatter more light at lower intensity of light.
- Uniform seeding is important to get optimal results. No tracer particles, no velocity. Too low seeding will result in loss of information while heavily seeded flow will result in speckle scattering that will lead to spurious results.

*3.3.2.1 Particle Generation and Supply*

It is commonly acknowledged that not only the proper choice of seeding particles is crucial but also the proper choice of a suitable method for seeding the flow is crucial in order to acquire optimized and reliable results. During this study, Titanium Dioxide ($TiO_2$) was used as seeding particles and generated by means of solid particle seeder and mixed with air through the inlet port. $TiO_2$ was selected because of its better scattering characteristics. This provides the advantages of aerodynamic response and has therefore, become a promising choice for seeding particles in PIV measurements of high-speed flows [143-145]. A summary of seeding particles properties used in the current experiments is given in Table 3.4.

Table 3.4: General specifications of seeding particles used for air [145]

| Seeding particles material | Titanium Dioxide powder ($TiO_2$) |
|---|---|
| Mean particle size [μm] | 0.3 |
| Particle shape | spherical |
| Density [g/cm$^3$] | 4.2 |
| Refractive index | 2.6 |

One of the significant factors associated with seeding particle selection is their ability to follow the flow faithfully. Since the size of seeding particles is in order of magnitude of micrometre, their motion is controlled by viscous forces and difference in density compared to the surrounding flow [146]. Consequently, in conjunction with the equations of motions for particle, Stokes'Drag Law can be applied to calculate the viscous drag force being exerted and the associated frequency response of the particles. Drain (1980) illustrated that the radius of the recommended seeding particles ($r_p$) by assuming that the particle velocity may differ 1 % from the local mean velocity of the fluid is given by [147]:

$$r_p^2 < o.1 \frac{\mu_{fluid}}{f_u \rho_p} \tag{3.15}$$

Where, $r_p$ is particle radius (m), $\mu_{fluid}$ is fluid viscosity (air) ($kg.m^{-1}s^{-1}$), $f_u$ is the maximum frequency the particles can follow (Hz) and $\rho_p$ is the density of seeding particles ($kg/m^3$).

By rearranging the previous equation and substituting the air viscosity at $28^{\circ}C$ and $r_p$ of 0.15 $\mu m$ then the maximum frequency of the particles can follow is given by:

$$f_u = o.1\frac{\mu_{fluid}}{r_p^2\,\rho_p} = o.1\left(\frac{1.84\times10^{-5}}{(0.15\times10^{-6})^2\ \times 4200}\right) \tag{3.16}$$

$$f_u \approx 19.47kHz$$

Tennekes and Lumley (1972) developed an approximation of the maximum frequency of flow oscillations in an engine to an order of magnitude using the Kolmogorov scale, $\eta_k$ defined as [148]:

$$\eta_k \cong L \times R_e^{-\frac{3}{4}} \tag{3.17}$$

Where $L$ is approximated as the size of the largest eddies of the flow [148] and given as the engine bore by Heywood (1988) [63]. $R_e$ is calculated as:

$$R_e = \frac{S_P\,L}{\upsilon} = \frac{5.8\times0.094}{1.539\times10^{-5}} = 35425$$

Where $S_P$ is the mean piston speed (calculated at equivalent engine speed 1500 rpm) and $\upsilon$ is the kinematic viscosity of air at 23°C.

Then an approximate maximum frequency of flow oscillations, $f_{max}$ , is given by:

$$f_{max} = \frac{S_P}{2\pi\eta_k} = \frac{5.8}{2\pi\times4.5\times10^{-5}} = 20.5\ KHz$$

This demonstrates that the maximum flow oscillations expected in our cylinder are of the same order that the Titanium Dioxide solid particles are capable of following.

Figure 3.14 shows the arrangement of experimental set up used as powder seeder. The setup included three main components namely, seeder pressure vessel, air pressure regulator and variable voltage power supply. Figure 3.15 depicts the schematic of powder seeder generator. The main principle of operation depended on the rotation of a drum (powder container) about horizontal axis inside a pressure vessel. At each

revolution a small amount of seeding powder was dispensed through a small hole into the fluidized powder compartment. The rotation rate of the drum was adjustable by means of variable speed electric motor. Thus, the dispensed rate of the seeding powder was fully adjustable. Once the seeding powder was dispensed into the pressure chamber, a series of six sonic air-jets were used to break it up into the smallest particles. Some heavy agglomerates that remained below inside the pressure vessel as they were too heavy to be carried out by the air flow, were agitated with the help of the baffles that were attached to the outer side of the powder drum (see Figure 3.16). Also, the drum had a grommet which allowed it to be filled with seeding particles.

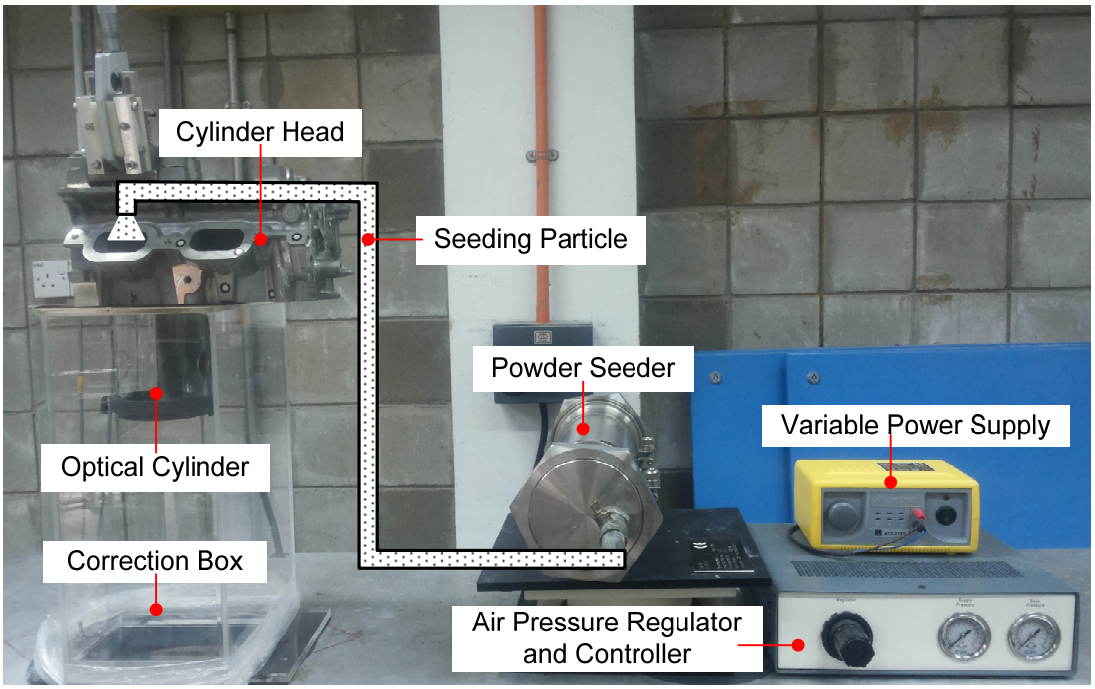


Figure 3.14: Powder seeder arrangement

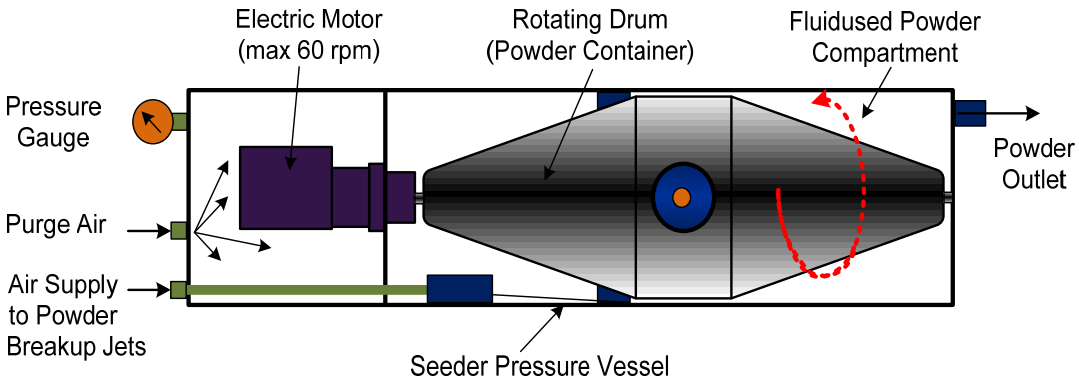


Figure 3.15: Components of powder seeding generator

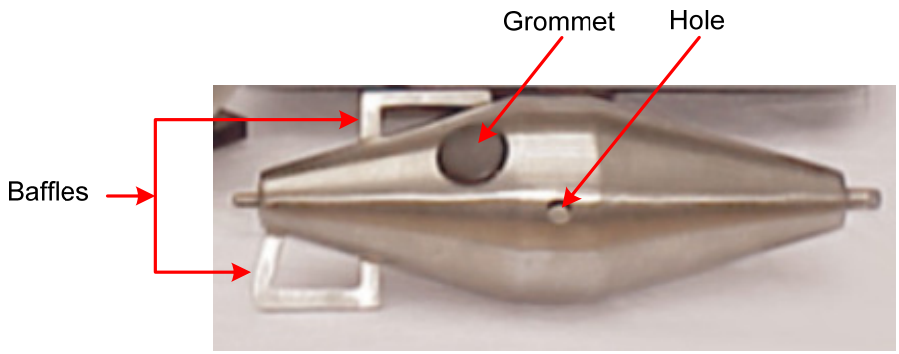


Figure 3.16: Powder container drum with baffles

### 3.3.3 Laser Illumination

A high-power pulsed laser is the common illumination source in PIV measurements. This is because of their capability to emit monochromatic light with high energy density, which can simply be bundled into thin light sheets for illuminating the seeding particles without chromatic deviations. Moreover, as PIV measurements rely on micro-sized tracer particles suspended in the flow, subsequently, it is necessary to use a high-power light source in order to ensure sufficient scattering light from these particles which can be captured by the CCD camera.

For the PIV experiments, a variety of laser light sources such as Helium-neon laser (He-Ne lasers λ=633 nm), Copper-vapor lasers (Cu lasers λ=510nm, 578nm), Argon-ion lasers (Ar+ lasers λ=514nm, 488 nm), Semiconductor lasers, Ruby lasers (Cr3+ lasers λ=694 nm), Neodym-YAG laser (Nd: YAG lasers λ=532 nm) and Dual Nd: YLF (neoddymium: yttrium lithium Fluoride) lasers can be used. This is depending on the requirements for pulse power, duration, and time between pulses. Nd: YAG (neodymium doped yttrium aluminium garnet) lasers are commonly used in PIV systems over a wide range of applications. Nd: YAG lasers have a high amplification and good mechanical and thermal properties. Excitation is achieved by optical pumping in broad energy bands and nonradiative transitions into the upper laser level. Dual Nd: YLF lasers are quite similar to Nd: YAG lasers but emit light at a wave length of λ=527 nm. Dual Nd: YLF lasers offer some advantages over Nd: YAG lasers in terms of higher repetition rates up to 1 kHz with a laser pulse energy of 10-20 mJ per pulse, good beam stability and better beam profile [149].

The light source used in the current study was two of CW Q-switched Nd: YLF DPSS laser resonators producing infrared laser light at 1053 nm which was converted to visible 527 nm laser light by an intra-cavity Harmonic Generation Assembly (HGA). The harmonic generator produced a laser output at 527 nm (green). Nd: YLF double pulsed laser capable of 20 mJ at 1 kHz at 527nm per laser head per pulse. An optical laser arm (Dantec Dynamics) was used to guide the laser light to the measurement area. The laser intensity was adjusted through the PIV software. Figure 3.17 depicts the main components of laser system. The summarized properties and specifications of Nd: YLF PIV-laser systems are given in Table 3.5.

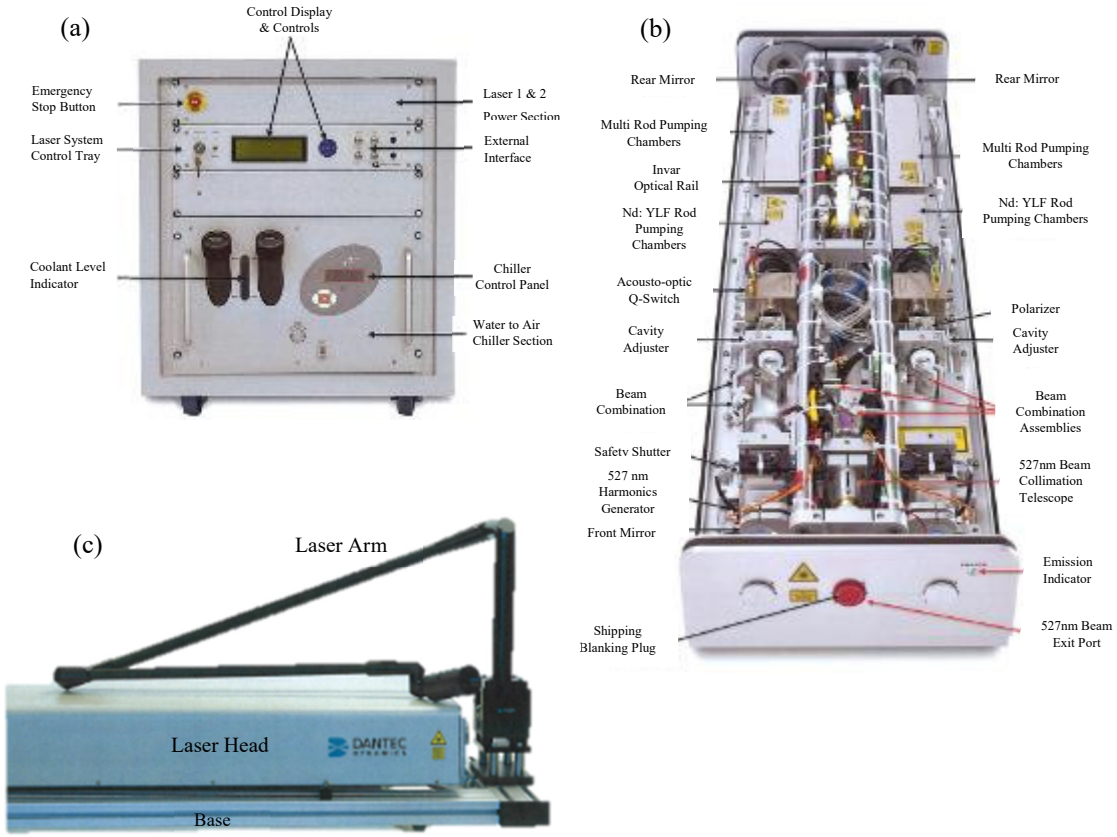


Figure 3.17: LDY 303 PIV (Dantec Dynamics), Nd: YLF (a) LDY-LPU Power supply, (b) LDY-PIV Laser Head and (c) laser head, base, mirror arm and light sheet optics [150]

Table 3.5: Nd: YLF laser basic specifications

| Model | LDY 303 PIV (Dantec Dynamics) |
|---|---|
| Laser medium | Nd: YLF |
| Output Energy at 1kHz at 527nm per laser head per pulse [mJ] | 20 |
| Wave length [nm] | 1053, 527 |
| Pulse duration [ns/CW] | 100 |
| Max output [W] | 150 |
| Repetition rate (each cavity) [kHz] | 1-20 |
| Pulse-to-pulse stability [± %] | 1 |
| Beam diameter [mm] | 5 |
| Pulse width @ 1kHz [ns] | -150 |

### 3.3.4 Imaging System

Once the seeding particles are illuminated by high-power laser sheet they scatter light. A charged-couple device (CCD) camera with an optical axis perpendicular to the plane of the laser sheet for 2D experiments was used to capture the scattering light (which corresponds to the positions of the seeding particles in the flow field illuminated by the laser light sheet). For the purposes of PIV analysis, two consecutive images with a small-time interval (which corresponds to the time between two laser pulses) were recorded and stored directly in a computer memory in areal time frame.

In the present study, a Speed Sense M310 Dantec Dynamics camera running in double-frame mode was used. A point of particular importance was the choice of the aperture used to capture the images. The aperture controls the amount of light striking the camera sensor. As a consequence, it affects both the luminosity of image and the depth of focus. The larger the aperture, the smaller the depth of focus, the higher the luminosity of the picture, as shown in Figure 3.18. The aperture here was adjusted at 8 (*f*8) in order to allow enough amount of light to pass through and achieve appropriate depth of focus. The final PIV images (1280 pixels by 800 pixels, 12-bit grey scale) were

saved directly to the hard drive of the computer for analysis. The summarized properties and specifications of Speed Sense M310 camera are given in Table 3.6.

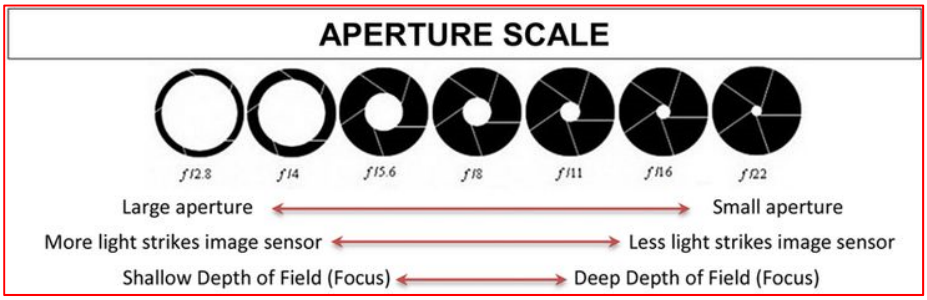


Figure 3.18: The effect of aperture on the luminosity of the picture and the depth of focus [146]

Table 3.6: Specifications of imaging system

| Model | Speed Sense M310 (Dantec Dynamics) |
|---|---|
| Maximum spatial resolution [pixels] | 1280 × 800 |
| Pixel depth [bit] | 12 |
| Minimum exposure time [µs] | 1 |
| Minimum Interframe time [ns] | 500 |
| FPS at full resolution | 3260 |
| Pixel size [µm] | 20 |
| Camera aperture opening | 8 |
| Double frame trigger mode | Yes |

### 3.3.5 Time between Pulses ($\Delta t$)

The time between laser pulses ($\Delta t$) rely on the flow velocity in the measurement plane. The precise choice of this time is crucial for successful implementation of PIV experiments and subsequently accurate determination of particles displacement through the measurement plane and thus, accurate velocity field can be determined. In case of this time was too small, compared to the flow velocity, the displacement of some particles during this small time will be too small (less than one pixel). In these cases, the determination of the exact value of displacement and subsequently the velocity of these particles is associated with high uncertainties. On the other hand, if the time

between pulses was too long, the displacement of many particles will be too high and might go out of the laser sheet during this time. Due to the out-of-plane velocity, too much information will be lost and the maximum velocity in this direction will be determined to be inferior to the exact one. Even some particles remain inside the laser plane, the algorithm will need a large interrogation area to do the correlation.

Therefore, to avoid any problems due to the out-of-plane velocity, the displacement perpendicular to the laser sheet during the time between pulses should be less than one quarter (1/4) of the laser sheet thickness [36]. Moreover, in the case of the in-cylinder flows of internal combustion engine, the characteristic velocity is given by equation (3.18) [63]:

$$v_o = \sqrt{\frac{2\Delta P}{\rho_{air}}} \tag{3.18}$$

where; $v_o$ is the characteristic velocity, $\Delta P$ is the pressure difference across the intake valves (N/m$^2$) and $\rho_{air}$ is the air density (kg/m$^3$).

Therefore, the characteristic velocity for a pressure difference 1470 Pa (150 mm$H_2O$) can be calculated as follow:

$$v_o = \sqrt{\frac{2 \times 1470}{1.2}} = 49.5\ m/sec$$

Recall that the laser sheet thickness was about 5 mm, then the time between pulses can be calculated as follow:

$$\Delta t = \frac{distance}{velocity} = \frac{\frac{1}{4} \times 0.005}{49.5} = 25.25\ \mu s$$

This characteristic velocity gives an indication to the maximum velocity that the flow might reach somewhere inside the cylinder; usually very close to the intake valves. As the measurement area was away from the intake valves, then the maximum velocity in different cases of measurement planes during this study was much smaller so the time between laser pulses was increased.

### 3.3.6 Laser–Camera Synchronization

PIV systems consist of complex components such as laser and digital cameras, frame grabbers that typically need to be synchronized well. Therefore, synchronization between laser and camera is important. Figure 3.19 shows a schematic diagram for a typical PIV timing system which is called 'frame straddling'. The timing was such that the first laser pulse was set to occur during the camera exposure time for the first frame (frame A). Whereas the second laser pulse was set to occur during the camera exposure time for the second frame (frame B). The synchronizer used for the current research to link the computer, frame grabber, camera, laser and external trigger. Moreover, cameras and laser were not only synchronized in time but also, they were synchronized in movement. The cameras and laser head were horizontally positioned on the same traverse system (shown in Figure 3.20) at the same height as the measurement area and moved as one unit.

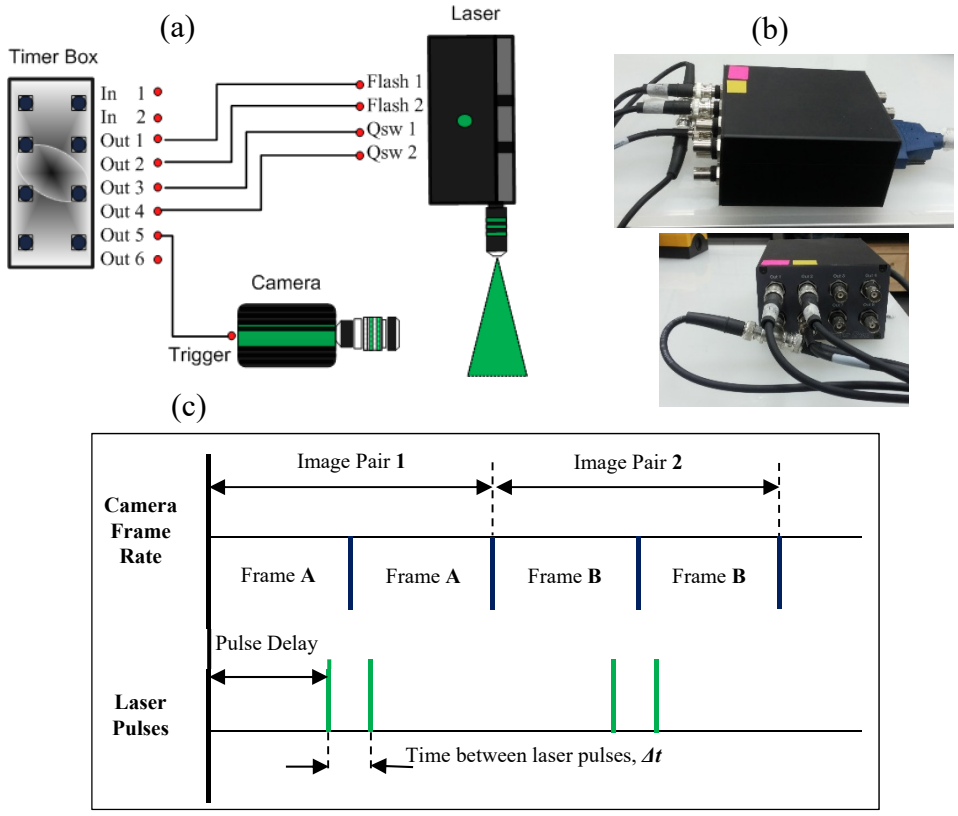


Figure 3.19: A typical PIV timing system (frame straddling technique) (a) schematic diagram, (b) Dantec Dynamics Timer box and (c) synchronisation of laser pulses to camera frame rate

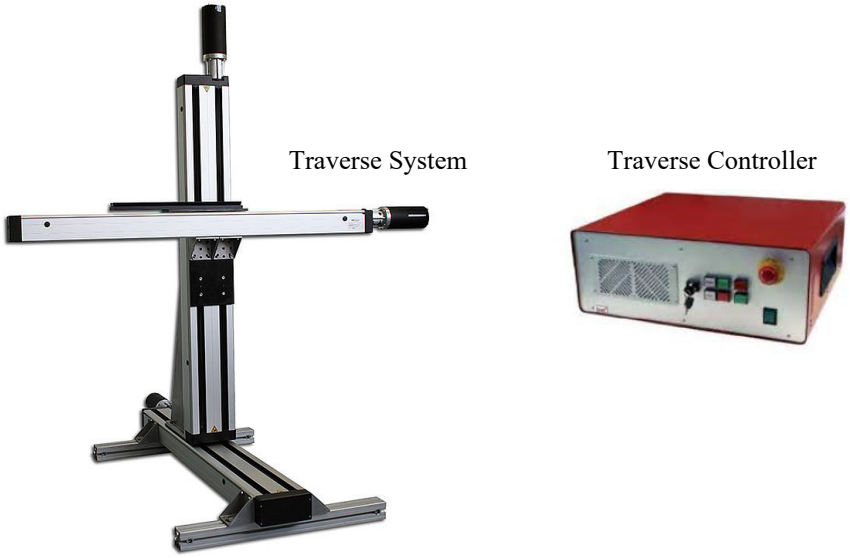


Figure 3.20: Dantec Dynamics traverse system and controller [150]

Once the image sequence of in-cylinder flow was captured by setting of above imaging system, several pre-processing and post-processing steps were applied to the raw image sequences. This was in order to enhance the quality of images for cross correlation. The next sections present the processing steps for PIV raw images in detail.

### 3.3.7 Processing of PIV for In-Cylinder Flow Measurements

Three stages were applied on the raw images captured by the CCD camera in order to acquire the instantaneous velocity vector fields. A set of 1000 double frame images were captured and stored in the computer memory for PIV processing. The PIV processing was carried out using DANTEC Dynamics Studio V5 software which included four stages: pre-processing, vector calculation, post-processing and output results. The database structure of PIV processing steps is shown in Figure 3.21.

#### *3.3.7.1 Pre-processing*

The pre-processing stage denoted also as "raw-image processing stage "is an important stage to enhance the quality of the raw images and increases the signal to noise ratio (SNR) of data. This was because the raw images were affected by several noise sources

such as, multiple reflections of particles, background light and extra laser reflections due to the effect of curved surfaces. Therefore, background subtraction and masking out of the unwanted regions were employed as pre-processing techniques to eliminate these issues. Figure 3.22. shows a sample of raw images before and after pre-processing steps. By averaging the pixel intensity of the 1000 sample images, a common image (mean image) was identified and subtracted from all sample images. Again, the unwanted regions with strong laser reflections were masked out to prevent any spurious results.

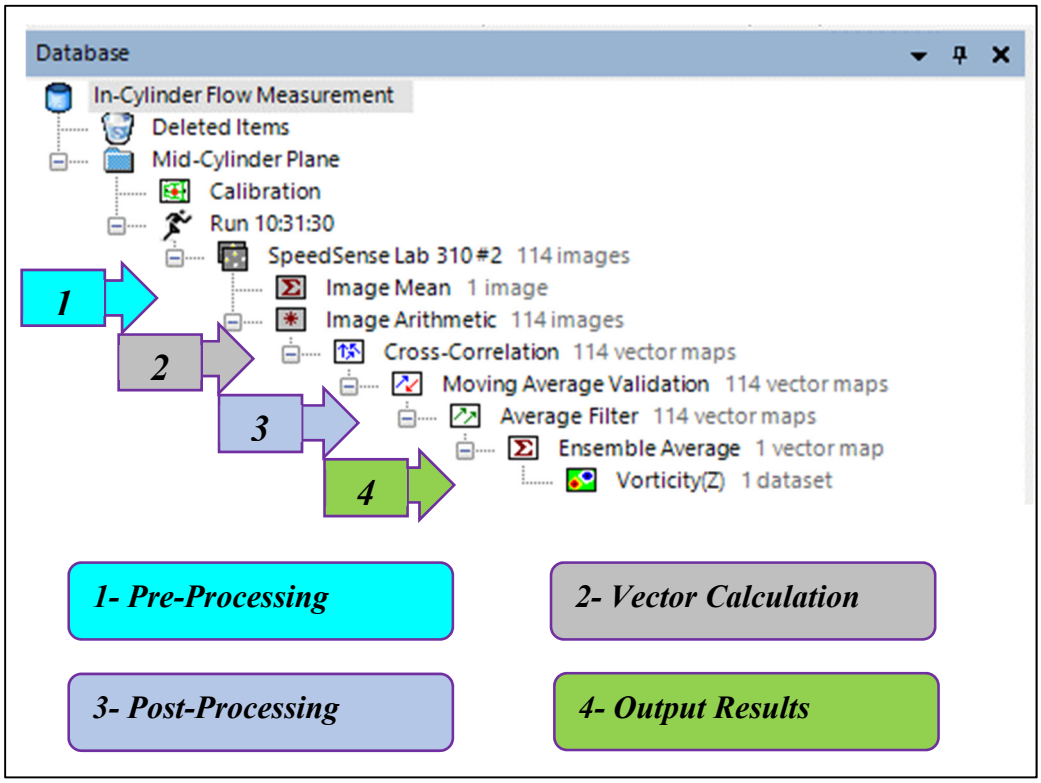


Figure 3.21: DynamicStudio database structure

*3.3.7.2 Vector Calculation*

PIV is an indirect velocity measurement technique which depends on the illumination and recording of seeding particles suspended within the flow to quantify the flow being studied over a defined region of interest (measurement area). The velocity of the tracer particles can be calculated by capturing the relative displacements of these particles within a known time interval ($\Delta t$). Extensive research has been carried out in order to

improve the correlation techniques (algorithms) used for particle displacements determination. Two different correlation techniques can be used for vector calculation, namely auto-correlation and cross-correlation techniques.

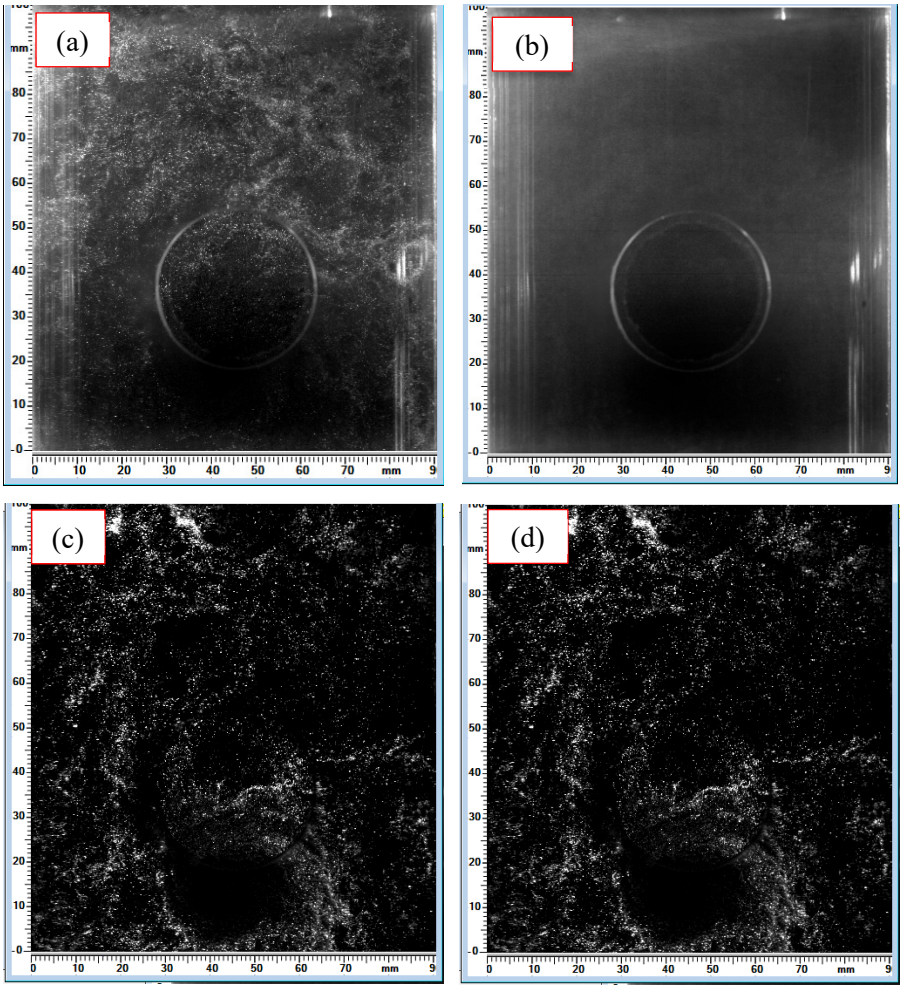


Figure 3.22: Pre-processing stages applied to enhance raw images quality (a) raw input image, (b) average image intensity (constant background- 'mean image'), (c) subtracted raw image; (d) final raw image after masking

- **Auto-Correlation Technique**

It is also denoted as single frame/double exposure as the scattering light from the first and the second exposure of the particles is recorded in one frame. The full image frame is firstly divided into "sub-regions" small resolution areas denoted as interrogation areas (IA) and each interrogation area corresponds to an element of fluid and should therefore be sufficiently small so that a single velocity vector is enough to describe its

behaviour. Each interrogation area is evaluated by auto-correlation function which is characterized by two identical correlation peaks around the highest central peak indicating zero displacement. This technique was used in the past because the camera speed was not fast enough to capture two frames within small time interval. In addition, the main issue of this technique was that it was difficult to know which particles on the frame came from the first exposure and which ones came from the second exposure, thus the displacement direction was not available. Figure 3.23 displays the schematic of the auto-correlation technique of evaluating PIV images.

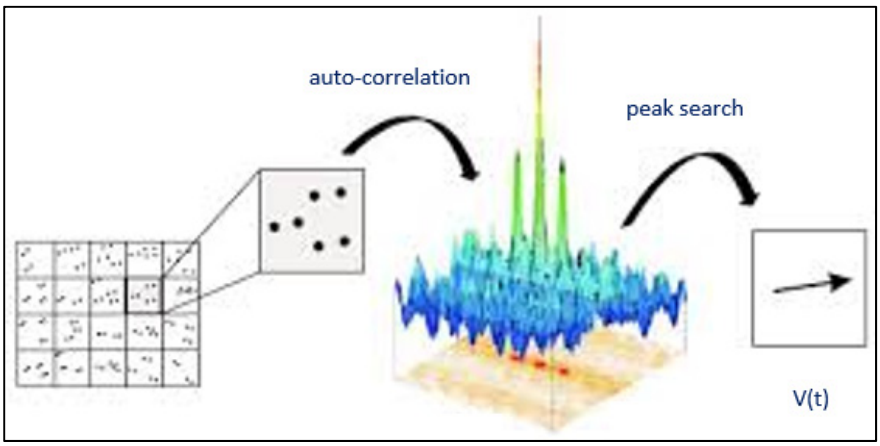


Figure 3.23: Evaluation of PIV recordings using auto-correlation [151]

- **Cross-Correlation Technique**

The second technique, cross-correlation is the method used the most nowadays. It is also denoted as double frame/double exposure as the scattering light from the first and the second exposure of the particles is recorded in two frames (frame A and frame B). Once captured, each image frame is divided into small interrogation areas that are at the same location on the two pictures. As in the case of auto-correlation, the interrogation areas are linearly spaced, can overlap and usually are of uniform size, typically 16 × 16, 32 × 32, 64 × 64 or 128 × 128 pixels in size. The size of the interrogation areas has an influence on the number of vectors in the final map and, of course, the accuracy of the results. Ideally, the interrogation area should be infinitesimally small to correspond to a parcel of fluid in the sense of fluid mechanics. However, it should also comprise enough pixels to ensure a good accuracy when determining the velocity vector and to satisfy seeding requirements and to be four times

greater than the average in-plane displacement of the particles. Overlapping of the interrogation areas is often used to cover the complete area of interest and to obtain a smaller grid spacing and a larger number of vectors. The main concept of cross correlation technique is illustrated in Figure 3.24. In the current study, the evaluation was carried out using cross-correlation technique with a size of 32×32 pixels interrogation area and 50% overlapping, as shown in Figure 3.25.

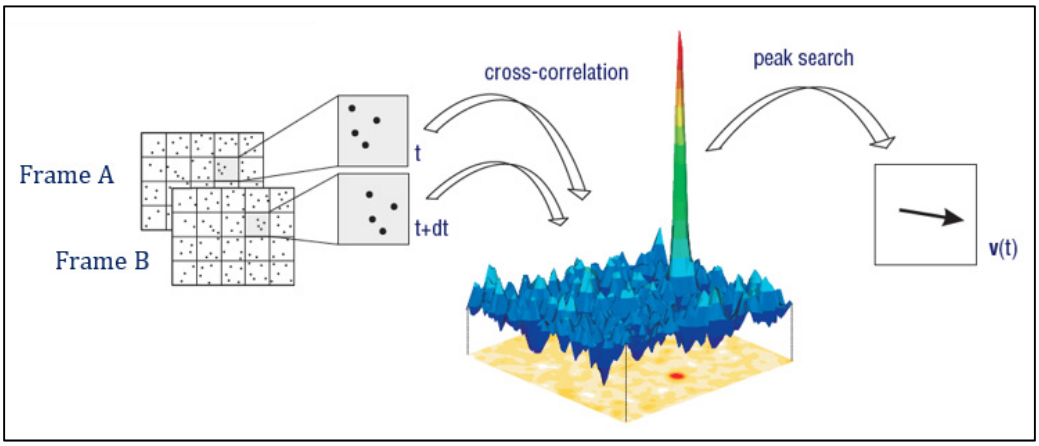


Figure 3.24: Principle of cross-correlation [151]

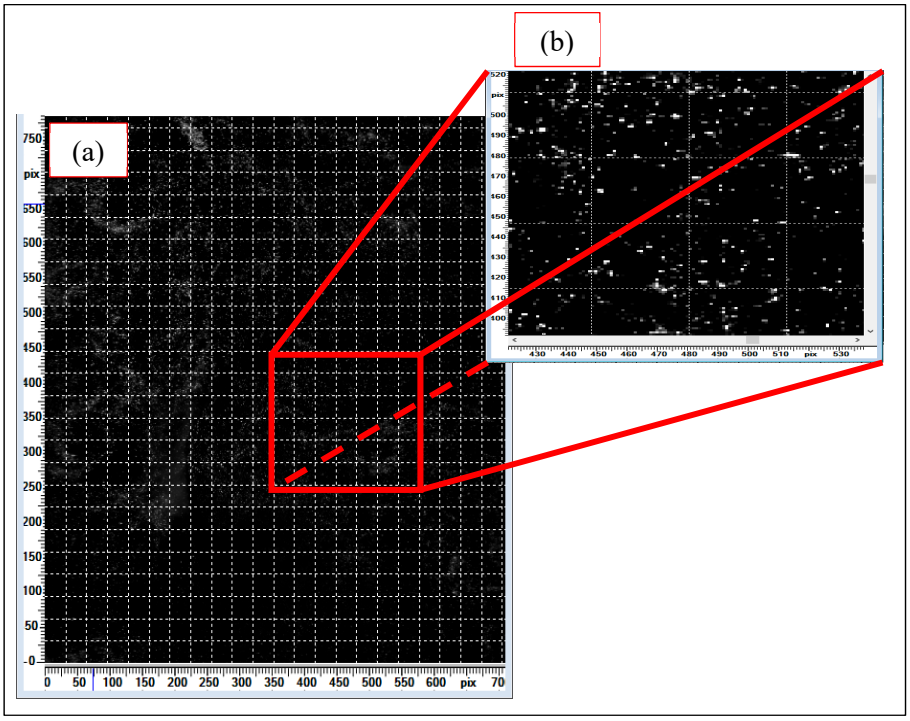


Figure 3.25: Raw image divided into small interrogation areas of 32 × 32 (b) Zoomed in view of an interrogation area

*3.3.7.3 Post-Processing*

Post-processing is an important step to remove the spurious vectors resulting from noisy input data or poor cross-correlation coefficients. After generating the velocity vector fields using the cross-correlation technique, the spurious vectors can be easily distinguished. These vectors can potentially appear with different size and direction when compared with their neighbours. In the current study, post-processing of the resulting velocity vector maps was carried out using two validation techniques to fix and repair the spurious (outliers) vectors. These were the moving average validation and the average filter.

- **Moving Average Validation**

This method is used to validate the velocity vector maps by comparing each vector with the average of other vectors in a defined neighbourhood. Considering the assumption of the continuity in the flow field behaviour, vectors that deviate too much from their neighbours within an averaging area of size ($m \times n$), can be replaced by the average of the neighbours as a reasonable estimate of true velocities. The averaging formula is given by:

$$\overline{U}(x,y) = \frac{1}{mn} \sum_{i=x-\frac{n-1}{2}}^{x+\frac{n-1}{2}} U(i,j) \sum_{j=x-\frac{n-1}{2}}^{x+\frac{n-1}{2}} U(i,j) \tag{3.19}$$

where; $\overline{U}$ is the average velocity within the averaging neighbourhood area of size ($m \times n$) and $U$ is the vector velocity.

Then each vector velocity is compared with the above average velocity and is rejected if:

$$\left|U(i,j) - \overline{U}(x,y)\right| > H \tag{3.20}$$

where; $H$ is a number defined by:

$$H = \varepsilon \, max_{x,y} \left|U(i,j) - \overline{U}(x,y)\right| \tag{3.21}$$

where; ε is the acceptance factor, and $0 < \varepsilon < 1$

The moving average validation technique was applied with averaging area size of 5 × 5 vectors to all 1000 velocity vector fields and the spurious vectors were validated and replaced as displayed in Figure 3.26 (a).

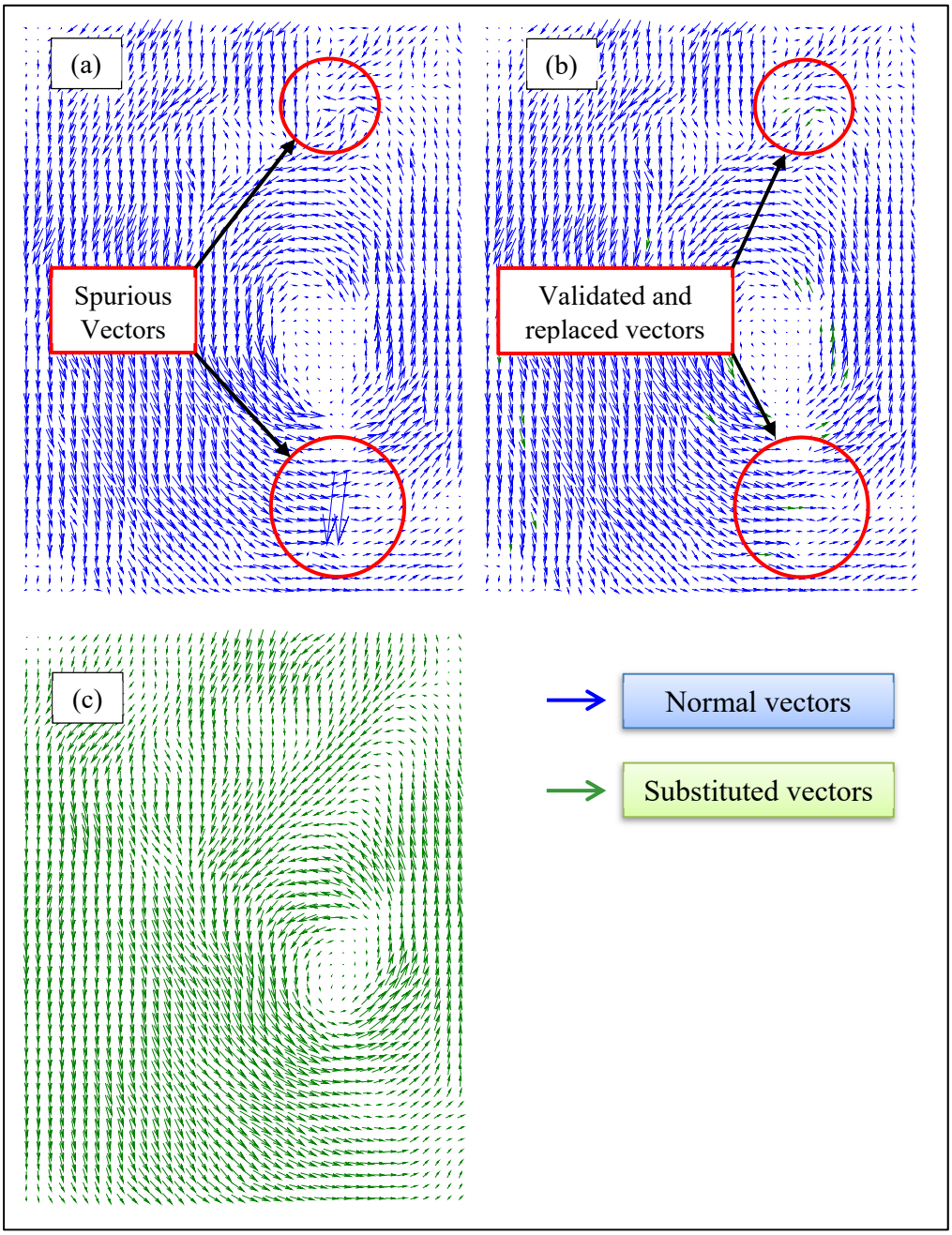


Figure 3.26: Post-processing steps, (a) raw vector map containing spurious vectors, (b) applying moving average validation and (c) further applying average filter to remove noise

- **Average Filter**

By enabling the filter functions, the validated velocity vector fields were post-processed in order to reduce the noise. This was done by the average filter. This method was used to filter out vector maps by arithmetic averaging over vector neighbours. The size of 5 x 5 vector was selected in the current study, inside which individual vectors were smoothed out by the average vector. Figure 3.26 (b) depicts the filtered velocity vector field after applying the average filter.

### *3.3.7.4 Planes of Illumination*

The PIV analysis can be carried out in three different planes depending on the nature of the in-cylinder flow to be studied. Planes parallel to the cylinder axis and parallel to a line joining the inlet and exhaust valves are named tumble planes (Figure 3.27 (a). The planes which are perpendicular to the cylinder axis are called swirl planes and are viewed through the piston (Figure 3.27 (b). Finally, the planes parallel to the cylinder axis and perpendicular to the tumble planes are identified as cross-tumble planes (Figure 3.27 (c). The plane positions are measured from the cylinder head gas face for the swirl and from the mid-cylinder plane for tumble and cross tumble.

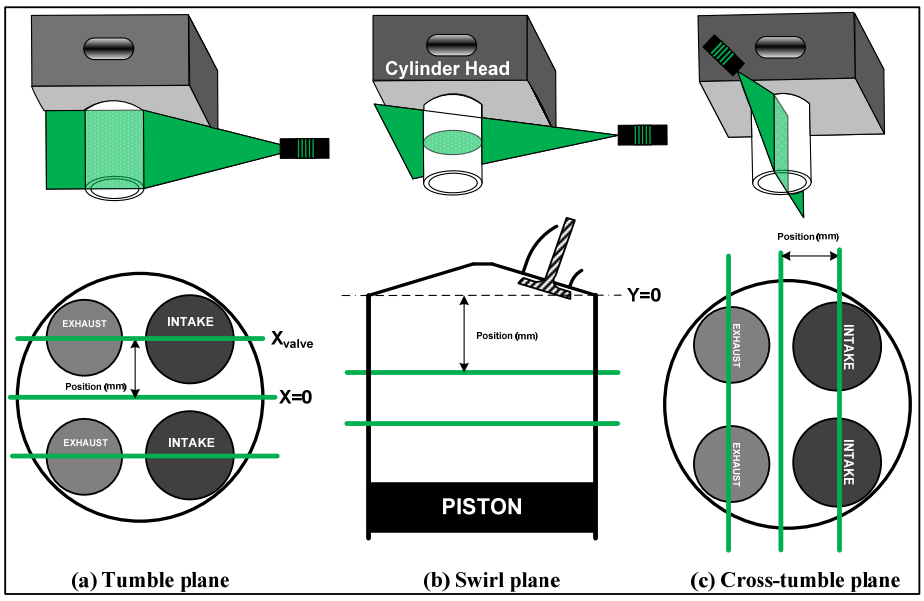


Figure 3.27: PIV plane positions, (a) tumble planes, (b) swirl planes and (c) cross-tumble planes

### 3.3.8 Rig Modification for 2D-2C PIV Measurements

Necessary modifications were carried out on the FEV steady-state tumble-rig for 2D-PIV measurements to provide an optical access to the cylinder. These included firstly the removal of the paddle wheel in order not to disturb the flow. Secondly, an acrylic box was designed to connect between the cylinder head and the rig and to allow enough extended area for the whole stroke measurements. This box also worked as a correction box to minimize the optical distortion caused by the curvature of the pipe, as shown in Figures 3.28, 3.29 and 3.30.

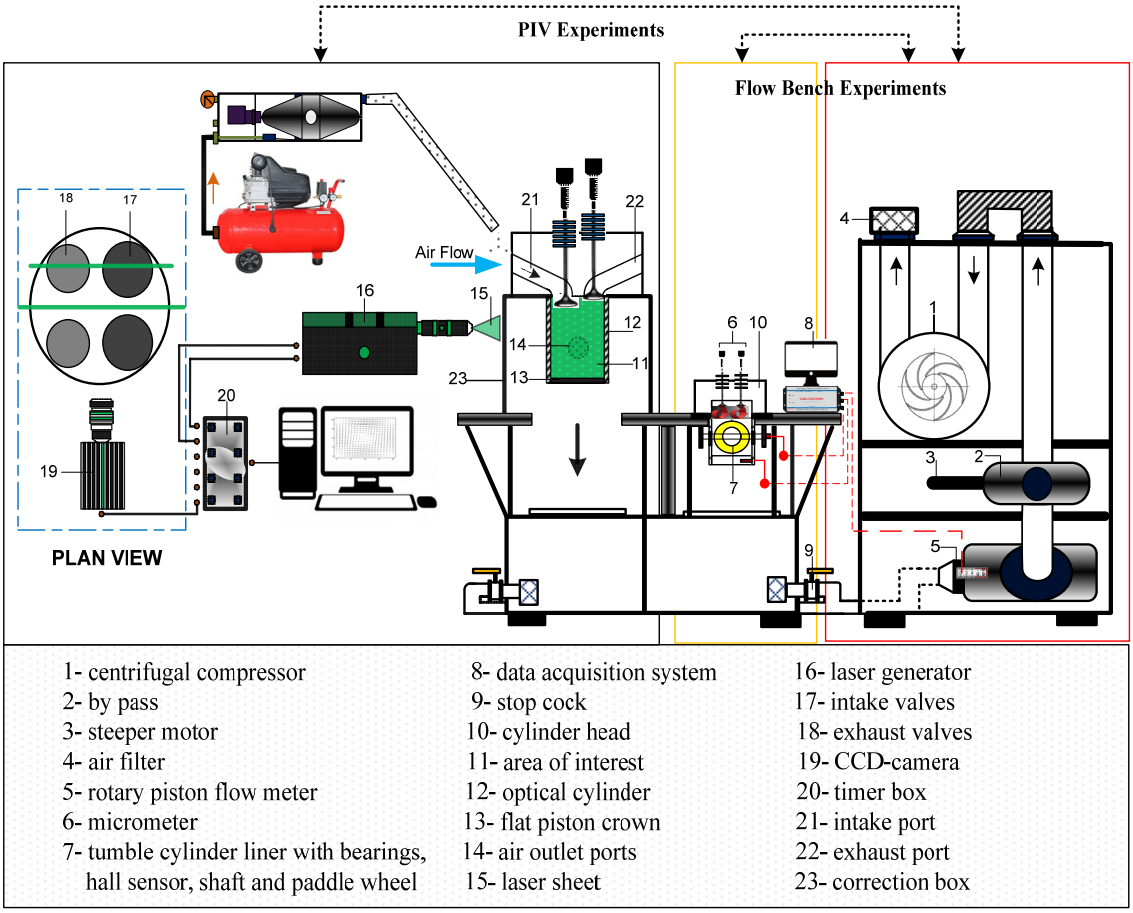


Figure 3.28: Schematic diagram for both flow bench and PIV experiments

Figure 3.29: Correction box for 2D-PIV measurements

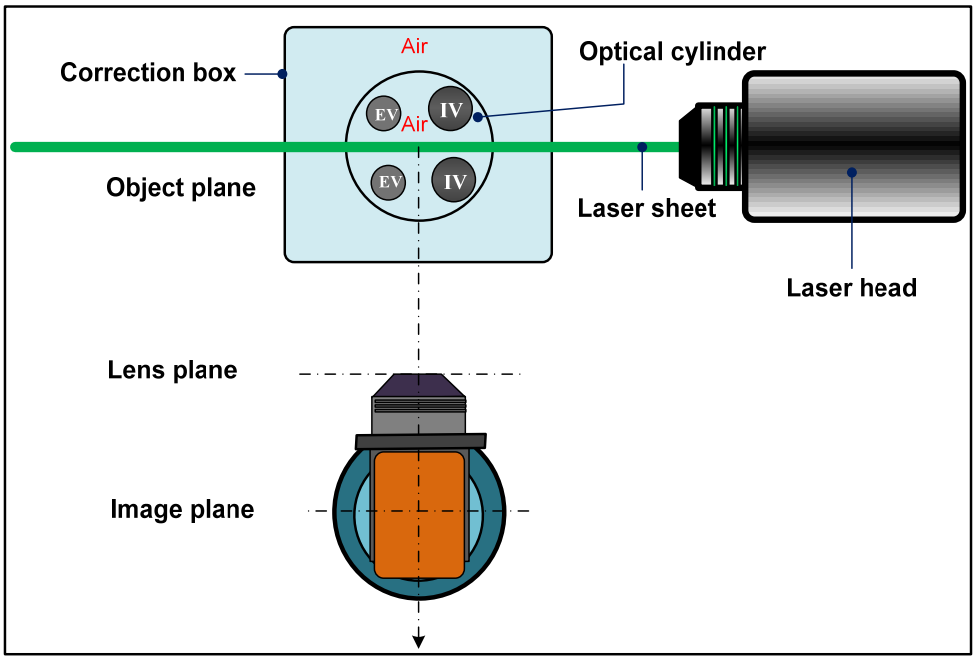


Figure 3.30: Top view of 2D-2C PIV camera configuration showing the correction box

In spite of all its advantages, the classical PIV technique underlies some disadvantages which includes the absence of the out-of-plane velocity component. This may lead to considerable measurement errors of the local velocity vector particularly in case of highly three-dimensional flow. One of the approaches capable of recovering the complete set of velocity components is the additional PIV recording from different

viewing axis utilizing a second camera, which can be commonly denoted as Stereoscopic PIV. The next section presents a detailed description of stereoscopic PIV used to capture the in-cylinder flow.

### 3.3.9 2D-3C Stereoscopic-PIV Measurements

Stereoscopic particle image velocimetry (Stereo-PIV) measurement are based on the same fundamental principles as human eyesight and it is also known as stereovision. When we look at a given object, our left and right eyes see two similar but not identical images. The brain compares the two images and interpret the slight variation to re-build the three-dimensional information of the object observed. Similarly, stereo-PIV system measures particles displacements using two CCD cameras. Each camera plays the role of the human eye, looking at the flow field from different angles while a specific analysis software (Dynamics Studio in this study) plays the role of the brain, relating the observed (2×2D) displacements to 3D displacements. Figure 3.31 depicts the main principle of stereoscopic PIV. Mathematically, the most accurate determination of particles displacements (and thereby the measurements precision of the out-of-plane component) is obtained when the angle between the two cameras is set to 90°.

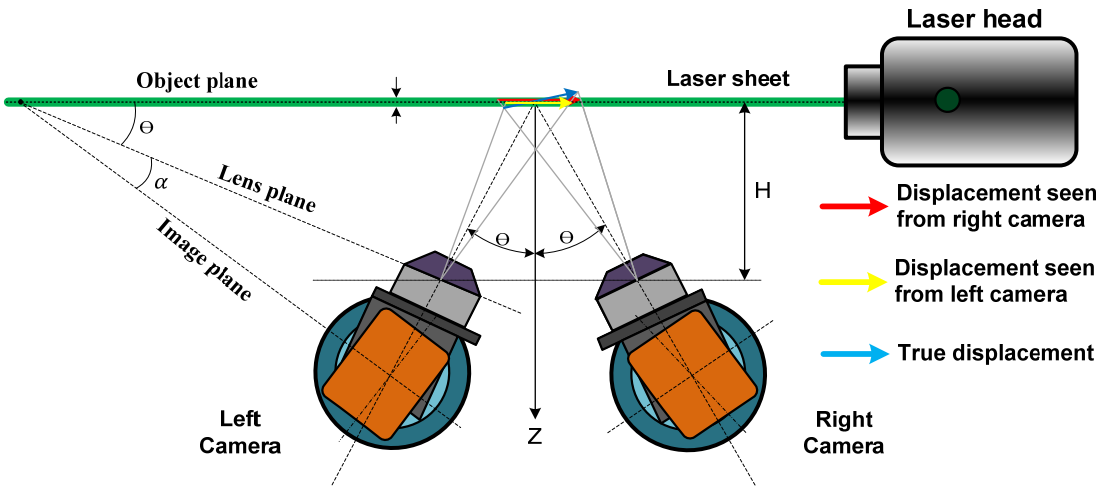


Figure 3.31: Scheimpflug stereoscopic camera configuration

In case of a restricted optical access, stereoscopic imaging at smaller angles has been demonstrated at the cost of a somewhat reduced accuracy. Further, experience

indicates that excellent 3D stereo PIV measurements can also be performed with camera viewing angles of ± 30°.

### *3.3.9.1 Stereoscopic-PIV Main Components*

In the following section, the technical basis, the experimental set-up and components of a stereoscopic PIV arrangement are described. Mainly the experimental set-up of stereo PIV consists of the following elements, pulsed laser system, two CCD-cameras, two stereo (Scheimpflug) camera mounts, a calibration target and analysis software. The laser system and CCD camera specifications were the same as used before for 2D-PIV measurements (see sections 3.3.3 and 3.3.4 for more details) except that a pair of cameras located on both sides of the cylinder were used for stereoscopic measurements. Moreover, the cameras and laser head were horizontally positioned on the same traverse system at the same height as the measurement area and moved as one unit, as shown in Figure 3.32. The new components added for 3D measurements are described in the following sections.

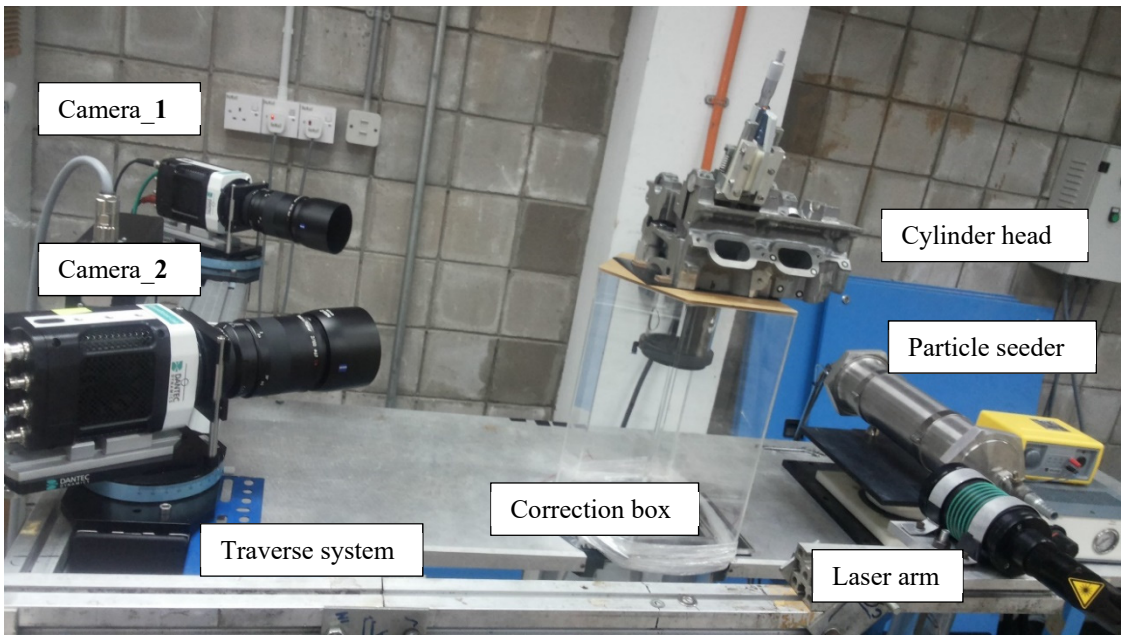


Figure 3.32: Picture of stereoscopic PIV set up

*3.3.9.2 Scheimpflug Camera Mount*

The Scheimpflug principle is a geometric rule that describes the orientation of the plane of focus of camera when the lens plane is not parallel to the image plane (When looking at the light sheet at an angle instead of head on, the camera has to be tilted with respect to the lens) as illustrated in Figure 3.33. To fulfil the Scheimpflug condition and ensures proper focusing (which requires that the object plane, the lens plane and the image plane are collinear) a special camera mount is required. This mount shown in Figure 3.34 made it possible to tilt the image-plane (CCD-plane) relative to the lens-plane around CCD axis. The gap between the camera and the lens holder was enclosed by a flexible bellow to prevent surrounding light from reaching the CCD chip.

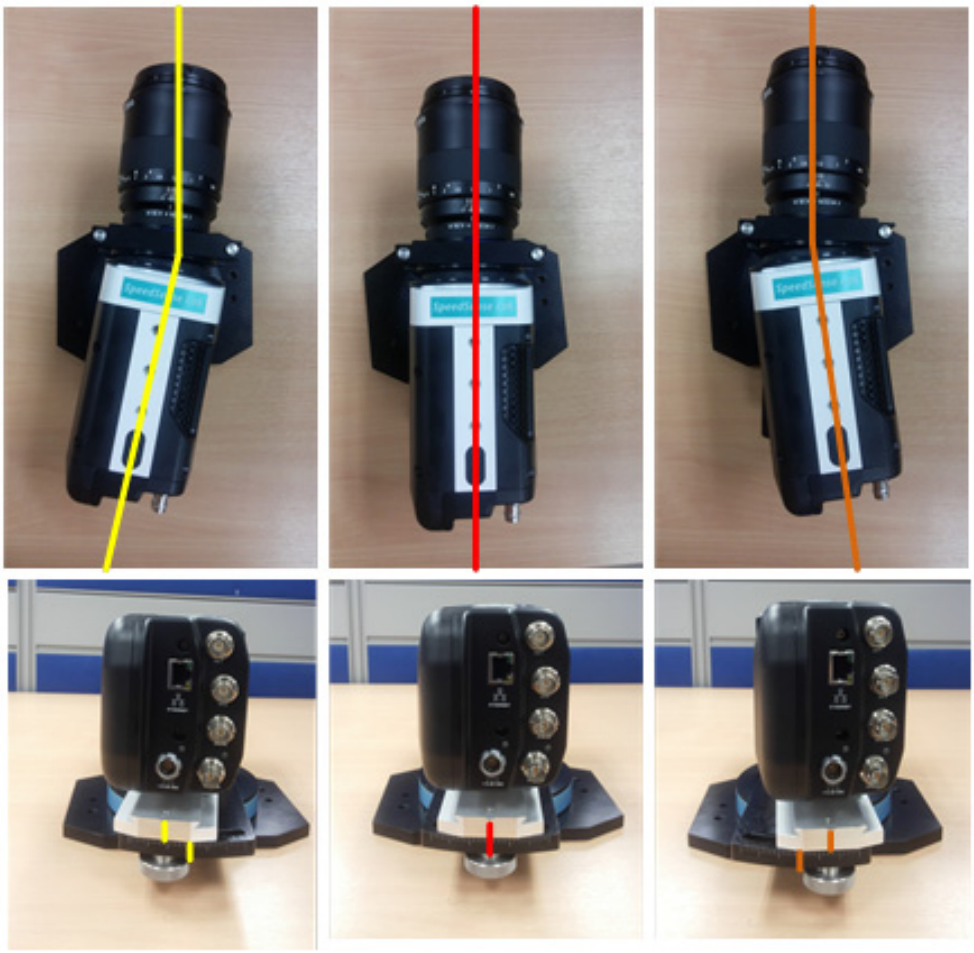

Figure 3.33: Different cases for the orientation between the camera planes (image plane) with the lens plane

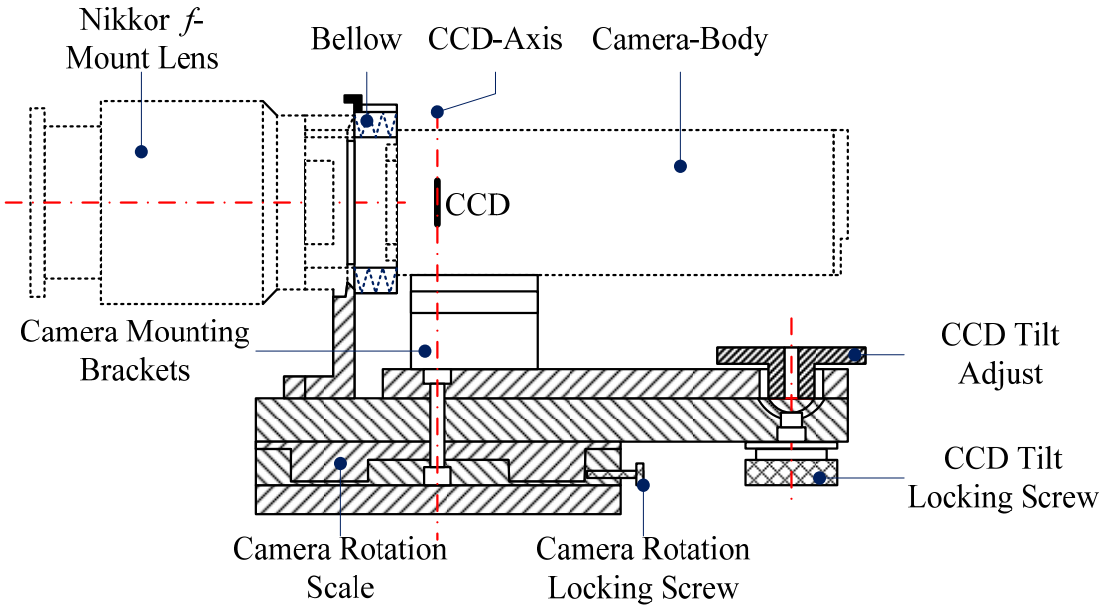


Figure 3.34: Camera mount with CCD-camera and lens mounted

*3.3.9.3 Calibration Target*

Reconstruction of displacements from the image plane to the object plane can be numerically performed, provided it was known how 'points' in the object plane were imaged onto the image plane: this was achieved by calibration. The calibration was done by means of a standard calibration target which had a well-defined grid of dots, as shown in Figure 3.35. The standard calibration target 100 mm by 100 mm was one-sided plate containing black dots on a white background with spacing of 5 mm. In the centre of the calibration target was a larger dot "Zero marker" surround by four smaller dots (axis marker). By definition the larger dot was the origin of the coordinate system (0, 0, Z) and the common fix point for the two cameras. The four smaller points identified the X- and the Y-axis. Therefore, both cameras must be able to see the large dot surrounded by the four smaller ones.

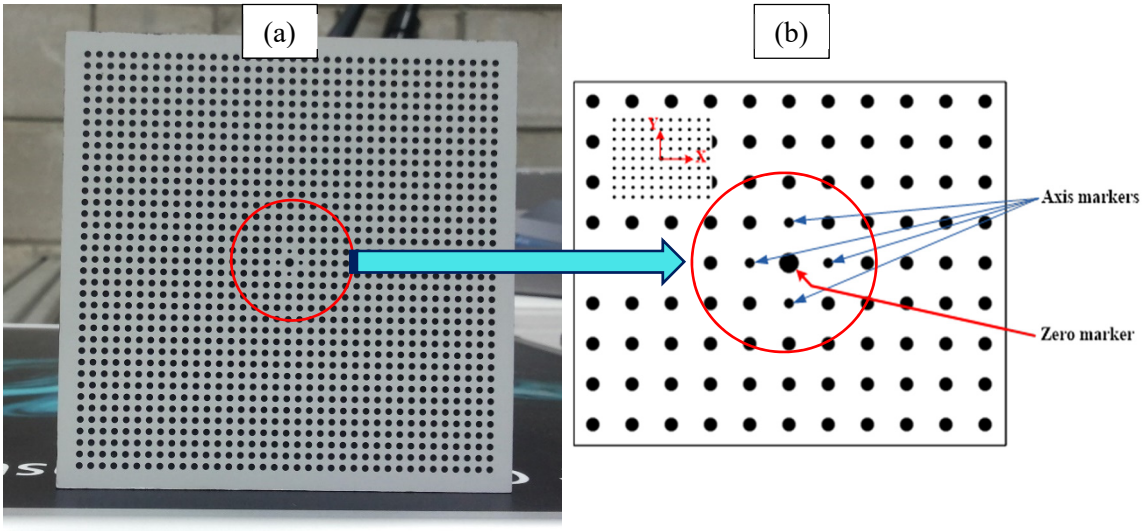


Figure 3.35: Calibration target (a) photo of physical calibration target (b) schematic showing zero and axis markers

*3.3.9.4 Stereoscopic-PIV Calibration Procedure*

For the classical 2D-PIV the angle between camera and laser sheet was perpendicular, however in the case of Stereo-PIV it was not the case anymore (the view of the cameras was not at 90 degrees), as shown in Figure 3.36. For 2D-PIV, only a scaling step through taking a direct image of the area of interest was necessary to achieve pixels' dimensions and calculate the scale factor between pixels and millimetre. However, the stereoscopic PIV calibration step was more complex than the scaling for classical PIV.

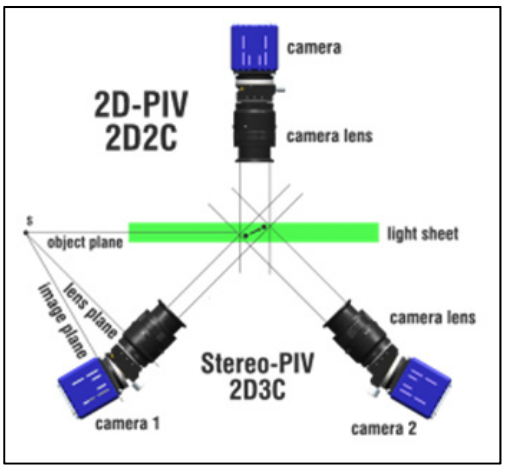


Figure 3.36: Schematic showing differences between 2D-2C PIV and Stereoscopic-2D-3C PIV [151]

*The calibration procedures of stereoscopic PIV are summarized as follows:*

1. The calibration target was installed in the centre of the flow field and aligned with the centre of the laser sheet (this position was corresponding to Z=0). For this a half-cut cylinder of the same dimensions as the cylinder used for the current study, was used for this purpose, as shown in Figure 3.37. The X-axis was assumed positive to the right, the Y-axis positive upwards and the Z-axis positive towards the cameras.

2. The position at which the calibration-plane was centred in the laser sheet equals (Z=0), while positions closer to the cameras were considered positive (Z>0) and positions further away from the cameras were considered negative (Z<0). The idea behind traversing the calibration target through the laser sheet thickness was to cover all possible out-of-plane particle displacements

3. The calibration target illumination was uniform and bright giving an excellent contrast. Moreover, it was made sure that, the two cameras captured the large dot surrounded by the four smaller dots (shown in Figure 3.35) because this was the only common fix-point for each of the two cameras.

4. The overlap area between the two camera images was maximized, as shown in Figure 3.38. This was done by keeping the same calibration target-camera distance for both cameras, tilting the cameras until the same number of dots left and right of the large dot was seen in both camera images and achieving best possible focus over the entire images.

5. The two cameras were run at single-frame mode and captured the first pair of images (at Z=0) then saved for calibration.

6. The calibration target was moved 1mm forward towards the two cameras in order to acquire the second pair of images (this position was corresponding to Z= +1 mm).

7. The calibration target was then moved 1 mm more forward in order to acquire the third pair of images (this position was corresponding to Z= + 2 mm).

8. The calibration target was moved 1mm backward away from the two cameras (behind the zero position) in order to acquire the fourth pair of images (this position was corresponding to Z= -1 mm).

9. The calibration target was moved 1mm more backward in order to acquire the fifth pair of images (this position was corresponding to Z= - 2 mm).

10. Once all positions were completed, all the calibration images recorded with the first camera were selected and Image Model Fit (IMF) method was adopted in order to calculate IMF calibration file for the first camera.

11. The same procedure for the second camera was run to create an IMF file corresponding the second camera view.

12. The verification of successful calibration images was done by superimposing the calibration model fit plots to the corresponding calibration images. It was made sure that, the IMF grid intersected at all the other marker positions and provide the average reprojection error of less than 1%, as shown in Figure 3.39.

13. The calibrated cameras were traversed back to the target plane.

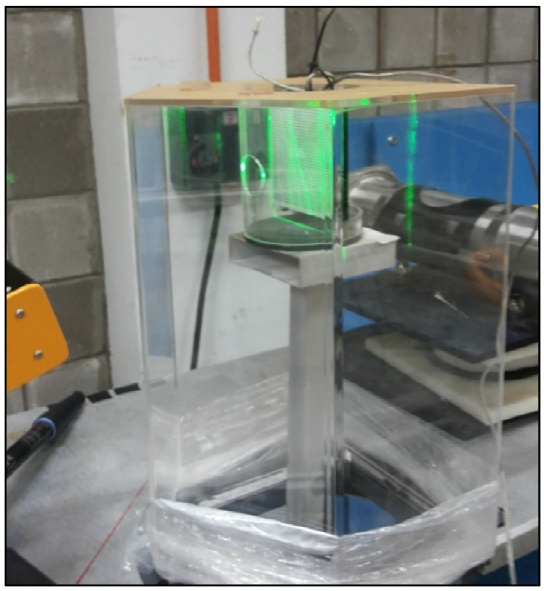

Figure 3.37: Calibration target alignment in the centre of the flow field with the centre of the laser sheet

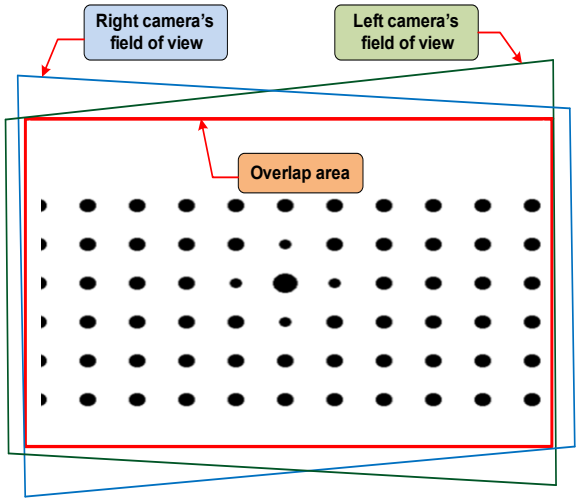


Figure 3.38: Common overlap area between two cameras

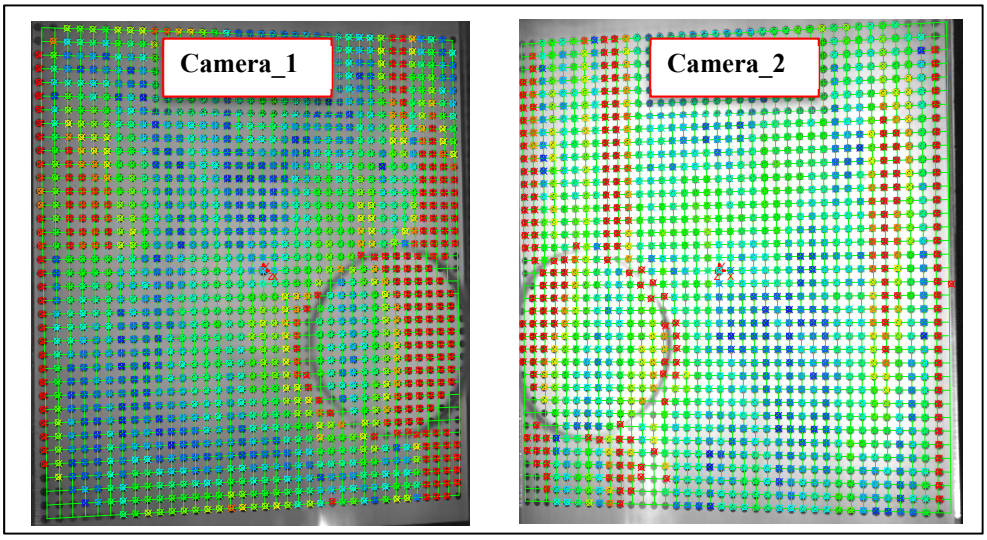


Figure 3.39: Superimposing the calibration model fit plots to the corresponding calibration images as verification for successful calibration

### *3.3.9.5 2D-3C Stereoscopic PIV Data Processing*

Figure 3.40 shows a complete description of the processing required for computing 2D-3C stereoscopic PIV velocity vector maps. Appendix B shows an example for stereoscopic PIV processing. The data processing steps are summarized as follows:

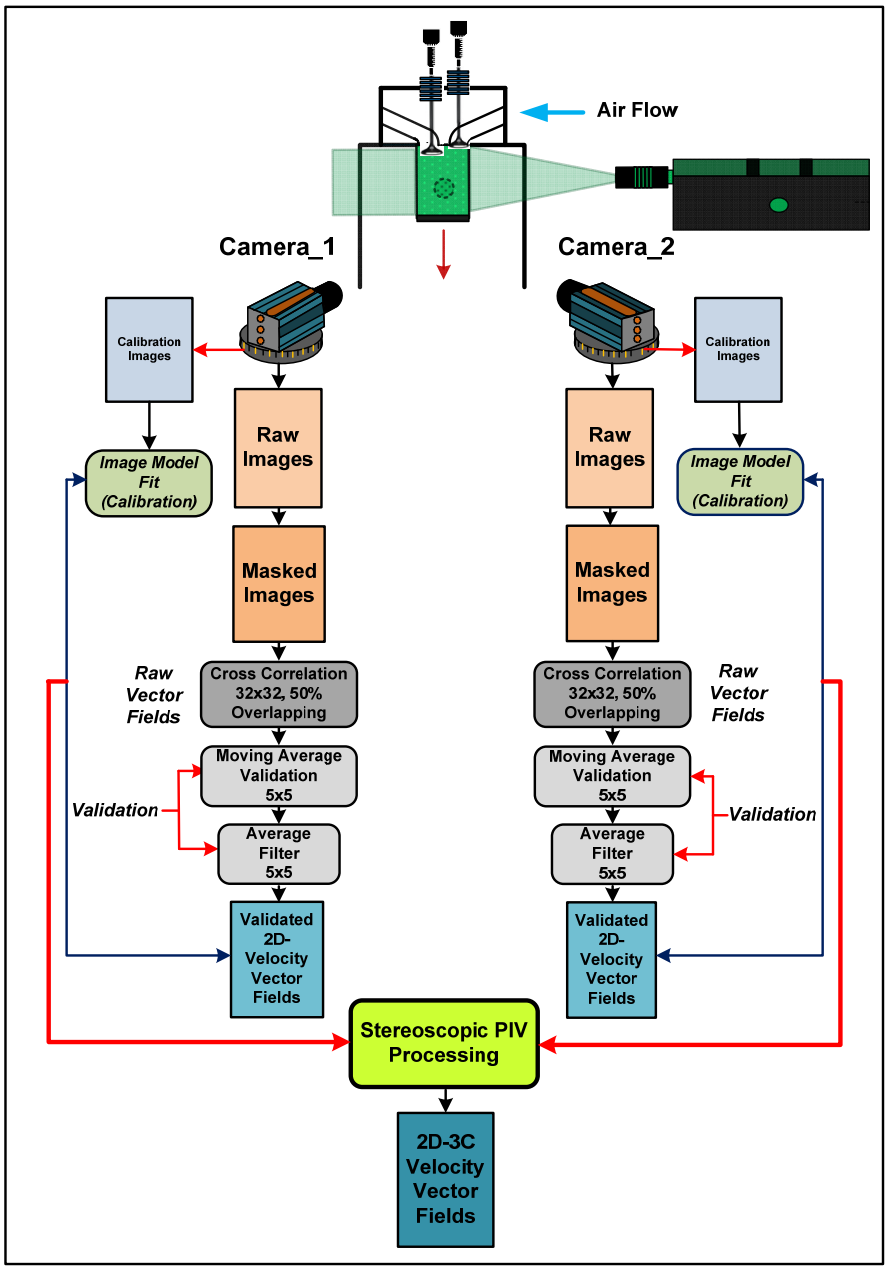


Figure 3.40: Flow chart representing vectors calculation process for stereoscopic PIV

1. The two camera views were calibrated by recording images of a standard calibration target.

2. Image Model Fit (IMF) calibration files for camera 1 and camera 2 were calculated using Dantec DynamicStudio software.

3. Stereoscopic–measurements started with conventional 2D-PIV processing of PIV images recorded simultaneous flow field as seen from the cameras (i.e. not correlated by the angular view).

4. Using the camera view calibrations calculated earlier (IMF) and these two 2D vector maps from both cameras were then combined into one single 2D-3C vector map using stereoscopic PIV processing method.

### 3.3.10 Rig Modification for 3D-PIV Measurements

The FEV steady-state flow bench was modified to provide an optical access into the cylinder region for stereoscopic PIV measurements in the tumble planes, as shown in Figure 3.41. The same modifications used before for 2D PIV measurements were applied again. However, the design of the correction box was different to match with both cameras, as shown in Figure 3.42 and Figure 3.43. Figure 3.44 shows a schematic for the field of view for different vertical tumble planes.

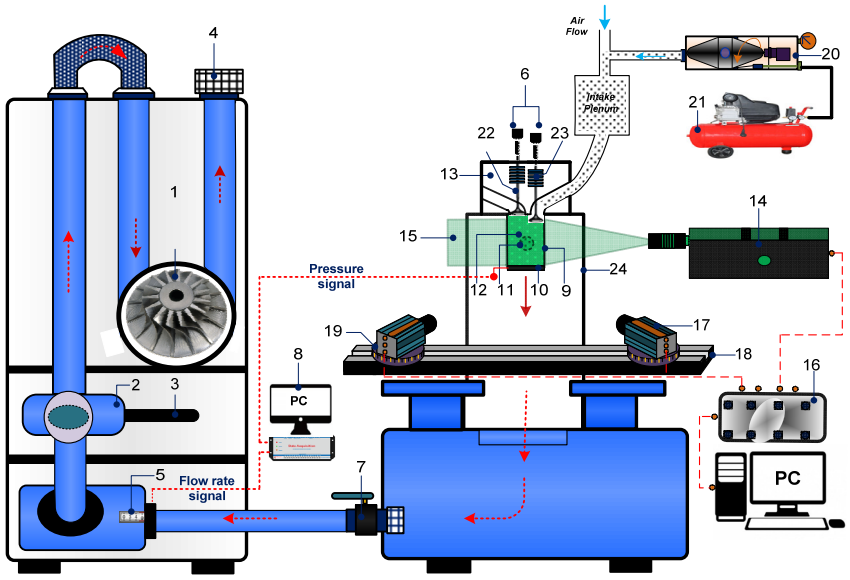


| | | |
|---|---|---|
| 1- Centrifugal compressor | 9- Optical cylinder | 17- CCD-camera |
| 2- By pass | 10- Flat piston crown | 18- Traverse system |
| 3- Steeper motor | 11- Air outlet ports | 19- Scheimpflug camera mount |
| 4- Air filter | 12- Area of interest | 20-Powder seeding generator |
| 5- Rotary piston flow meter | 13- Cylinder head | 21-Air compressor |
| 6- Micrometer | 14- Laser generator | 22- Exhaust valves |
| 7- Stop cock | 15- Laser sheet | 23- Intake valves |
| 8- Data acquisition system | 16- Timer box | 24- Correction box |

Figure 3.41: Schematic for Stereo-PIV set up on FEV steady-state flow bench

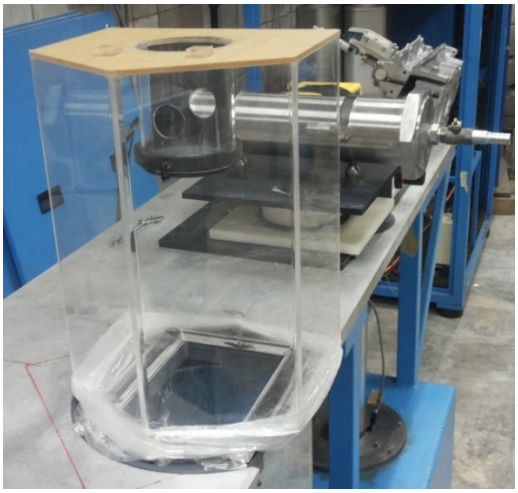

Figure 3.42: Correction box for 3D-PIV measurements

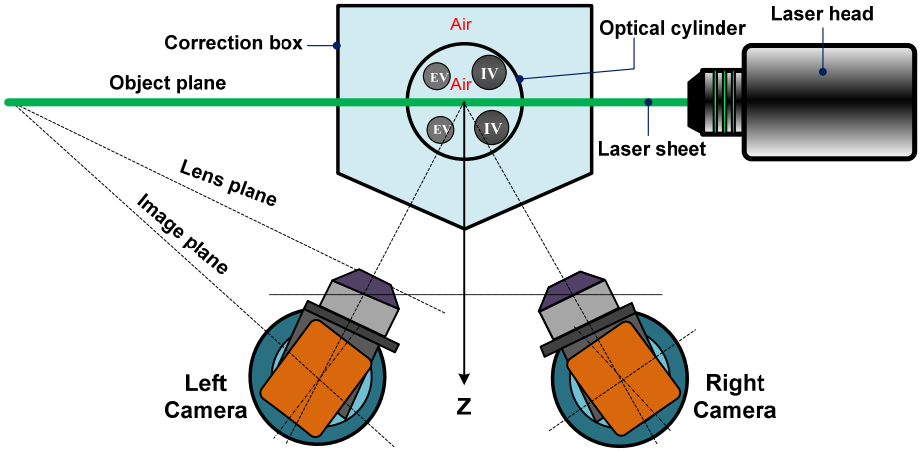


Figure 3.43: Top view of Scheimpflug stereoscopic camera configuration showing the correction box

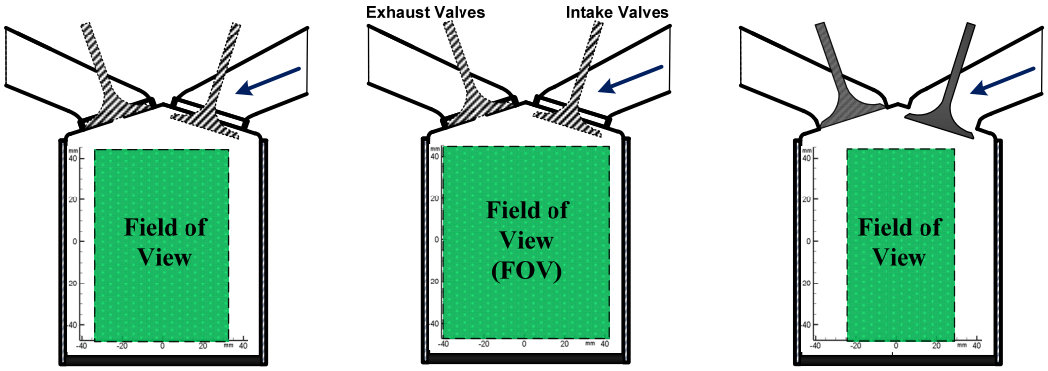


Figure 3.44: Schematic for the field of view, (a) mid-injector plane, (b) mid-cylinder plane and (c) mid-intake valve plane

### 3.3.11 In-Cylinder Air Flow Measurement Configurations

Three measurement configurations were used on the flow tumble rig in order to study the in-cylinder air flow. This included the effect of measurement plane, valve lift and the pressure difference across the air intake valves. The next sections present details of the three configurations.

#### *3.3.11.1 Effect of Measurement Plane*

Since modern GDI engines are characterized by tumble-dominated flow fields, pure tumble patterns in the four-valves pent-roofs GDI engine head were investigated by illuminating the flow in three different vertical planes. These included the mid-cylinder plane (plane of symmetry at Z=0), the mid-injector plane situated on one side of the mid-cylinder plane position (Z=-8mm) and the mid-intake valve plane (plane including the centre of the intake valve at Z=20 mm), as shown in Figure 3.45. These experiments were carried out at fixed values of valve lifts of 7, 8, 9 and 10 mm for 150 mm$H_2O$ pressure difference.

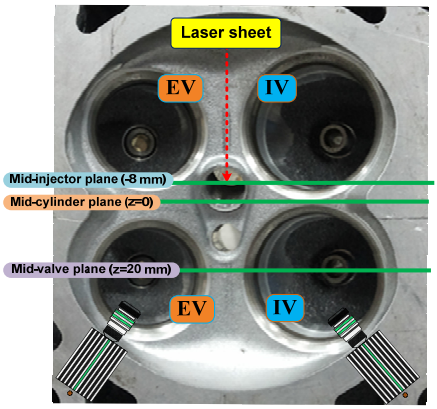


Figure 3.45: Top view for the location of the measurement vertical tumble-planes

#### *3.3.11.2 Effect of Valve Lift*

Stereoscopic PIV measurements were carried out in the mid-cylinder vertical tumble plane (plane of symmetry) at different valve lifts. The valve lift was changed from 1 mm to 10 mm for fixed pressure difference across the air intake valves of 150 mm$H_2O$.

*3.3.11.3 Effect of Pressure Difference*

Stereoscopic PIV measurements were carried out in the mid-cylinder tumble plane at different pressure differences at fixed values of valve lifts of 2 mm, 5 mm and 10 mm. Three pressure differences were used 300, 450 and 600 mm$H_2O$.

The aim of the next part of this research was to investigate the influence of high-pressure direct fuel injection (single-injection strategy) on the in-cylinder flow structures. Moreover, the interaction under different experimental parameters was investigated. These parameters included the pressure difference and the fuel injection pressure. This aim was achieved through, the application of high-speed time-resolved PIV which was capable of capturing many pairs of images in a short time period to reveal the temporal development of the flow and to quantify the air/spray interaction.

## 3.4 Spray/Air Interaction Measurements Using Time-Resolved PIV

As illustrated before, the main target of this part was to understand the influence of single fuel injection pulse on the in-cylinder tumble motion generated at high valve lift. The region of interest was slightly lower than that used for air flow measurements in order to increase the camera frame rate. The region of interest for air/spray interaction experiments was 600 mm by 800 mm. For this area of interest, the camera pixel resolution was 640 by 800 pixel, with frame rate of 3066 KHz and consequently a PIV frequency of 1 KHz. The measurement area was located at the mid injector vertical tumble plane, as shown in Figure 3.46. Particle image pairs were captured before, during and after the fuel injection event.

PIV measurements for air/spray interaction were divided into three parts. The first part was the characterization of fuel spray only without air motion. The laser sheet illuminated the fuel spray only at different injection pressures, 32.5 and 35.0 MPa for fixed injection duration of 4 ms. In the second part, PIV measurement was focused on the tumble plane passing through the middle of injector with both air and fuel spray but the air was not seeded with particles. Therefore, the laser illuminated the spray deformation under the effect of air motion at valve lift 10 mm and different pressure

differences, 150, 300, and 450 mm$H_2O$ and different injection pressures of 32.5 and 35.0 MPa. For the third part, PIV measurements were focused in the same vertical tumble plane. The laser sheet in this case illuminated both seeded air and fuel spray before, during and after the injection event, so air and fuel spray structures were imaged simultaneously. A relatively thick laser sheet (5 mm) was used to reduces out-of-plane seeding particle loss between PIV frames.

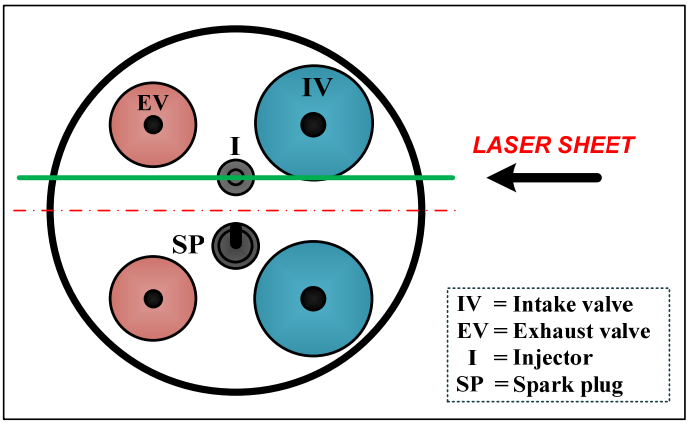


Figure 3.46: Schematic showing the measurement location for air/spray interaction

### 3.4.1 Fuel Injection System Set up

Figure 3.47 shows the experimental set up for the fuel injection system. The fuel injection system consisted of a fuel tank, fuel filter, high pressure pump, high pressure lines, common rail, pressure regulator and fuel injector. The fuel pump was driven by an electric motor running at constant speed. The common rail pressure was regulated by a pressure regulator and measured by a pressure gauge and was considered as the injection pressure. The injector was a symmetric, multi holes (8 holes) with nozzle diameter of 0.2 mm and electromagnetically operated needle. For single injection strategy, one hole was kept while the other holes were blocked using laser welding. The injector was tilted such that the fuel was injected vertically slightly off the cylinder axis (8 mm away from the vertical axis of the cylinder towards the exhaust side). The fuel used for the current research was diesel fuel. This choice was based onto two main aspects. Firstly, due to safety issues, the diesel fuel was selected instead of gasoline fuel because of its high flash point. The fuel droplets were speculated to move with air flow

because of the suction effect of the centrifugal compressor and mainly an increase in temperature was expected to happen through the compressor. Secondly, since the aim of this work was to quantify spatially and temporally the in-cylinder air flow and its interaction with direct injection fuel spray, diesel fuel was selected as a non-vaporized fuel instead of gasoline fuel which has higher volatility. The gasoline fuel was expected to evaporate faster and hence the flow velocity could not be measured using PIV leading to an absence of data during the injection event. The injection duration utilized here (4 msec) was chosen based on the camera frame rate to capture enough images for the interaction process.

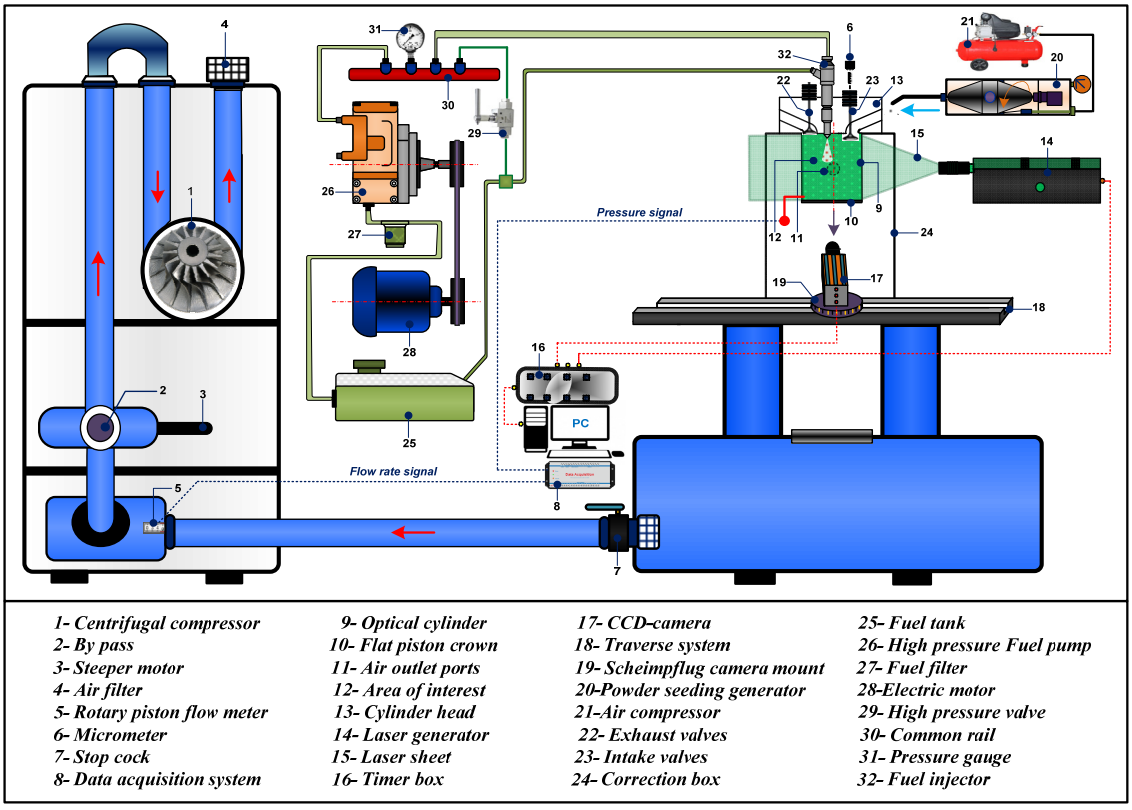


Figure 3.47: Schematic of experimental set up for air/spray interaction

### 3.5 Uncertainty in PIV Measurements

PIV measurements depend on detecting seeding particles motion to calculate the flow velocity. Random error and bias (systematic) error are the main sources of uncertainty in digital PIV measurements [152]. Gaining velocity vector field with minimal uncertainty relies on a number of parameters such as, seeding particles, optical medium,

camera configuration (setting), PIV algorithm (interrogation area, post processing... etc.). In this section, a brief description of these parameters is presented. Optimum parameters found from previous studies and used in the current study are presented together with their respective uncertainties.

Titanium Dioxide with 0.3 μm average diameter was selected as seeding particles. As presented before in section (3.3.2.1), these particles were able to have a 95% response to turbulent frequencies of what could happen inside the engine cylinder. The seeding density 8-10 particles for a 32×32-pixel interrogation areas were suggested by Megerle et la. [153] and was verified to give a 2% uncertainty of the local average pixel displacement. Moreover, it was reported that the maximum particle displacement was no more ¼ of the interrogation area size to eliminate loss of in-plane particles [154]. A bias error could be introduced as well if the particle displacement was too small (< 1 pixel) but was reported to be less than 1% in a 32×32 interrogation area [155]. Camera setting is considered as a significant parameter to obtain accurate PIV data. For high quality particle images, it was important to have as much light as possible with the greatest depth of field. Megerle et al. [153] illustrated that RMS error increases with increasing aperture of the camera. For the current work, the aperture of PIV camera was adjusted at 8 to provide good depth of view. Regarding the pre and post-processing of the captured PIV images, the particle images were pre-processed with subtracting the background to eliminate the noise. For PIV processing, the images were cross-correlated with 32×32-pixel interrogation area size and 50% overlapping. For post processing, two validation techniques were used to fix and repair the spurious vectors; the moving average validation and the average filter. The uncertainty of PIV measurements for the current study was estimated using the particle disparity approach [156] by Dynamic Studio software. The particle disparity technique identifies individual particles on frames 1 & 2 and tries to match pairs based on the measured displacement vectors. If particle pairs in the vicinity of a vector all show comparable displacements the uncertainty is considered small, if particle displacements in the vicinity of the vector fluctuate the uncertainty is higher. The particle disparity technique outputs uncertainties for both U, V velocity components plus the number of matching particle pairs found within the interrogation area corresponding to the vector. Sciacchitano et al. stated that 6-7 matched particle pairs were preferred for reliable

statistics, but it was mathematically possible to perform the analysis with just 2 [156]. The uncertainty in the magnitude of the velocity is equal to the root of the square of the U plus the square of the V and their uncertainty. The uncertainty in the velocity calculation for these measurements was 5%. Uncertainty in velocity calculation could be higher with out-of-plane motion.

### 3.6 Flow Characterization Parameters

Even though the visual inspection of the velocity vector fields was very important to develop good understanding of the in-cylinder flow behaviour, a number of parameters are still essential to quantify the overall in-cylinder flow characteristics. These included, turbulent kinetic energy (TKE), vorticity and tumble ratio (TR). These quantities were calculated from the ensemble average velocity vector fields of 1000 instantaneous velocity vector field data set.

#### 3.6.1 Vorticity

Vorticity is an important quantity for characterizing turbulence and its rotational structures. PIV provides the instantaneous velocity vector fields from which the vorticity fields can be calculated from the velocity gradients as given by equation (3.22):

$$\omega_z = \frac{\partial v}{\partial x} - \frac{\partial u}{\partial y} \tag{3.22}$$

PIV is the best suitable technique for the measurements of vorticity using the instantaneous or mean velocities which otherwise is quite hard to measure [157]. The above equation gives the z-component of the vorticity using the velocity gradients in the x and y directions.

### 3.6.2 Turbulent Kinetic Energy (TKE)

Turbulence plays a significant contribution in the mixing mechanisms, as the velocity fluctuation enhances mixing and turbulent dispersion. The kinetic energy provides quantitative information for the better understanding of turbulence mechanisms since it is affiliated with both fluctuating and mean velocities. The turbulent kinetic energy is that part of the kinetic energy of the fluid that exists in the fluctuation velocities. The turbulent kinetic energy is given by equation (3.23):

$$TKE = \frac{1}{2}\,\rho\, V_{rms}^2 = \frac{1}{2}\rho(u_{rms}^2 + v_{rms}^2 + w_{rms}^2) \tag{3.23}$$

Where '$u_{rms}$', ' $v_{rms}$' and '$w_{rms}$'are the RMS velocity components in the X, Y and Z directions respectively and '$\rho$ ' is the air density [158].

In turbulent flows, the turbulent kinetic energy is produced by friction or buoyancy, or fluid shear. The turbulent kinetic energy is mostly contained in the large-scale structures and is then transferred down to the small-scale structures through the turbulence energy cascading process and is eventually dissipated by viscous forces.

### 3.6.3 Tumble Ratio Based on Angular Momentum ($TR_1$)

The tumble ratio is defined by the ratio of the actual angular momentum of the fluid to the total fluid mass M assuming solid body motion at crank angle speed ω, and it is given by equation (3.24) [77]:

$$TR_1 = \frac{\sum_{i=1}^{m}\sum_{j=1}^{n}(r_{ij} \times V_{ij}).\,\Delta M}{solid\ dody\ angular\ momentum} \tag{3.24}$$

Where; the total solid body angular momentum for a cylinder of diameter B and unity depth can be calculated using equation (3.25):

$$\text{solid body angular momentum } = \int_0^{B/2} (\omega r).r.(\rho.2\pi r.dr)$$

$$= \rho.2\pi.\omega \int_0^{B/2} r^3 dr = \rho.2\pi.\omega.\frac{(B/2)^4}{4} = \frac{M.\omega}{2}.(B/2)^2 \tag{3.25}$$

Then equation (3.24) can be arranged as follow:

$$TR_1(x_c, y_c) = \frac{\Delta M \sum_{i=1}^{m} \sum_{j=1}^{n} (v_{ij} \,.(x_c - x_{i,j}) - (u_{ij} \,.(y_c - y_{i,j}))}{\frac{M.\omega}{2}.\left(\frac{B}{2}\right)^2} \tag{3.26}$$

As for a uniform grid $\frac{\Delta M}{M} = \frac{1}{m.n}$, equation (3.26) then becomes:

$$TR_1(x_c, y_c) = 8.\frac{\sum_{i=1}^{m} \sum_{j=1}^{n} (v_{ij} \,.(x_c - x_{i,j}) - (u_{ij} \,.(y_c - y_{i,j}))}{(m.n).\omega.B^2} \tag{3.27}$$

$\omega$ is the angular speed of the crank shaft (rad/sec) which was estimated based on constant axial velocity across the bore in the steady port flow bench condition was defined as [159]:

$$\omega = \frac{4\dot{m}}{B^2.S.\rho_{cyl}} \tag{3.28}$$

The tumble ratio $TR_1$ is derived from the angular momentum equation and when calculated from equation (about the centre of the cylinder) should give values close to those measured on a traditional steady-state flow rig. The disadvantage of using $TR_1$ is that it is dependent on the position of a centre-point in the flow (either mid cylinder or eddy centre) and its value is sensitive to velocity vectors far from the centre-point.

### 3.6.4 Tumble Ratio Based on Vorticity ($TR_2$)

Tumble ratio is defined as the mean value of vorticity normalised by twice the crank angle speed ω [160].

$$TR_2 = \frac{\bar{\xi}}{2\omega} = \frac{\sum_{i=1}^{m} \sum_{j=1}^{n} \xi_{i,j}}{2.(m.n).\omega} = \frac{\sum_{i=1}^{m} \sum_{j=1}^{n} \left(\frac{\partial v}{\partial x} - \frac{\partial u}{\partial y}\right)}{2.(m.n).\omega} \tag{3.29}$$

This ratio represents the relative amounts of large and small-scale rotation in the flow. For a rotating solid body, the mean vorticity has a constant value of twice the angular velocity.

### 3.6.5 Basic Equations of Turbulence

A huge amount of research and literature is available on turbulence, some basic governing equation and terminologies important in the study of turbulence is provided in this section for completeness.

#### *3.6.5.1 Continuity and Navier-Stokes Equation*

The Navier-Stokes equations, when combined with the continuity equation (conservation of mass), provide a complete mathematical description of the flow of an incompressible Newtonian fluid. The Navier-Stokes equations and continuity equation for an incompressible Newtonian fluid with constant density and viscosity can be written as,

$$\frac{\partial u_i}{\partial t} + u_j \frac{\partial u_i}{\partial x_j} = -\frac{1}{\rho}\frac{\partial p}{\partial x_i} + v\frac{\partial^2 u_i}{\partial x_j \partial x_j} \tag{3.30}$$

and

$$\frac{\partial u_i}{\partial x_i} = 0 \tag{3.31}$$

Respectively, where $v = \mu/\rho$ is the kinematic viscosity, $\rho$ is the density of the fluid, and $p$ is the pressure, $u_i$ represents the $i$th velocity components and $x_j$ represents the $j$th coordinate direction.

#### *3.6.5.2 Reynolds Averaged Navier-Stokes (RANS) Equation*

The random-looking behaviour of a turbulent flow suggests that it is useful to consider each of the flow variables to consist of mean and fluctuating components. The fluctuating part contains the turbulent aspects of the flow. This decomposition is known as Reynolds decomposition which is, an idea first introduced by Reynolds. The velocity and pressure fields are decomposed as follows:

$$u_i = \bar{u}_i + u_i' \tag{3.32}$$

$$p_i = \bar{p}_i + p_i' \tag{3.33}$$

Where the overbar ( $\bar{.}$ ) denotes the time average and the prime $(.)'$ represents the fluctuation. The process of deriving the Reynolds averaged equations for a turbulent flow consists of writing each flow variable $u_i$ , $p$ as the sum of a mean and fluctuating components, inserting the sums into each governing Equation (3.30) and (3.31), then averaging each equation and employing the averaging rules to evaluate each term. The continuity equation and the Navier-Stokes equation take the form,

$$\frac{\partial \bar{u}_i}{\partial x_i} = 0 \tag{3.34}$$

$$\frac{\partial \bar{u}_i}{\partial t} + \bar{u}_j \frac{\partial \bar{u}_i}{\partial x_j} = -\frac{1}{\rho}\frac{\partial \bar{p}}{\partial x_i} + v\frac{\partial^2 \bar{u}_i}{\partial x_j \partial x_j} - \frac{\partial \overline{u_i' u_j'}}{\partial x_j} \tag{3.35}$$

In appearance, the Reynolds averaged Equations (3.35) and the Navier-Stokes Equations (3.30) are the same except for an additional unknown term on the right-hand side of Equation (3.35), which appears in the results of Reynolds decomposition. This term, $\overline{u_i' u_j'}$ , is generally known as Reynolds stresses and it involves the time averaging of the product of the fluctuating components of the velocity. This Reynolds stress tensor introduces an added stress on the fluid caused by the turbulence. The difficulties in analytically predicting the Reynolds stresses even for the one-dimensional case have proved insurmountable without the aid of experimental or direct numerical simulation data.

### 3.7 Proper Orthogonal Decomposition (POD)

POD is an unbiased, statistical and powerful mathematical tool that decomposes a set of velocity distributions $V^{(k)}$ into a linear combination of spatial basis functions (or empirical eigenfunctions) (or empirical orthogonal functions) (or space-dependent POD modes, (denoted $\varphi_m$) and their corresponding time-dependent coefficients, (denoted $\mathrm{C}_m^{(k)}$). The source data for this technique can be either experimental PIV dataset, or numerical simulation dataset. Figure 3.48 summarized the main principle of POD. The linear decomposition is formulated as follows:

$$V^{(k)} = \sum_{m=1}^{M} \mathrm{C}_m^{(k)} \times \varphi_m \tag{3.36}$$

### 3.7.1 Theory and Mathematics of POD

In this section, the mathematical description and basic equations of the POD theory is outlined. Consider $V^{(k)} = (u, v)_{i,j}^{(k)}$ is a set of two-dimensional velocity fields (snapshots) with total number of $(K)$ to be analysed (three-dimensional velocity fields can be analysed by the same principle). Here, $i, j$ are the indices of the grid points in the PIV measurement plane and $K$ ($k$ =1, 2, … $K$) is the total number of velocity fields (total number of snapshots). This dataset may be collected at a certain valve lift, measurement plane or at a certain pressure difference. Due to the expected cyclical changes in the process of in-cylinder flow motion (snapshot-to-snapshot variation) and turbulent flow characteristics, hundreds or even thousands of velocity fields are usually to be processed. The POD decomposes the set of velocity distributions $V^{(k)}$ $(k = 1,2,3, \dots \dots, K)$ into a linear combination of $(M)$ POD modes, ( $\varphi_m, m = 1, 2, \dots, M$) and their corresponding time-dependent coefficients, ($\mathrm{C}_m^{(k)}$). The total number of modes is equal to the total number of snapshots, $M = K$. The main target of POD is to get a set of orthogonal POD modes, which denotes the most dominant energetic structures from the given velocity fields. From a mathematical perspective, that is to be achieved by minimization of the following function:

$$J\,(\varphi_1, \varphi_2, \dots, \varphi_M) = \sum_{k=1}^{k} \left\| (V)^{(k)} - \sum_{m=1}^{M} \mathrm{C}_m^{(k)} \times \varphi_m \right\|^2 \rightarrow \min \tag{3.37}$$

Subject to:

$$\left(\varphi_i, \varphi_j\right) = \delta_{ij} = \begin{cases} 1 & if\ i = j \\ 0 & if\ i \neq j \end{cases} \tag{3.38}$$

where; $\| . \|$ denotes the $L^2$-norm and $\delta_{ij}$ is the Kronecker delta and $\left(\varphi_i, \varphi_j\right)$ indicates standard inner product. The POD modes contain the 'flow patterns', normalized in $L^2$ space so that the sum of the squares of all the vectors in an individual POD mode $\varphi_m$ is unity [161].

$$\sum_{i=1}^{I} \sum_{j=1}^{J} \left(\mu_{i,j}^2 + v_{i,j}^2\right) = 1 \tag{3.39}$$

where; $\mu$ and $v$ are the x and y components of $\varphi$, respectively. In addition, each POD mode is orthogonal to all others. This corresponds to the following mathematical relation as:

$$\int \varphi_m(x)\ \varphi_p(x)\, dx = \delta_{m,p} \tag{3.40}$$

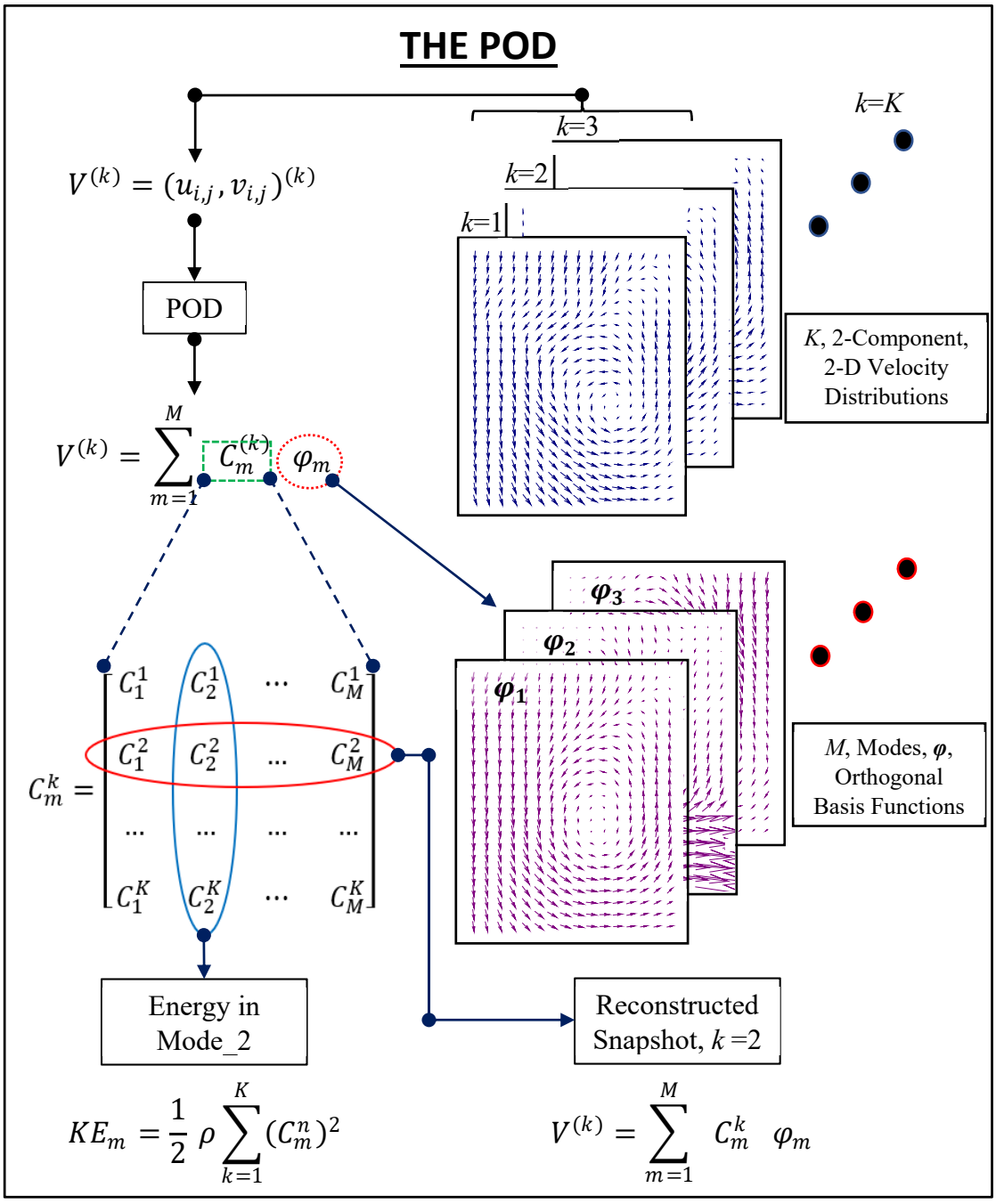


Figure 3.48: Schematic showing the main principle of POD

The orthogonality condition implies that the individual basis functions are independent of each other. Therefore, if the basis function satisfies Equation (3.38), the scalar product between the different basis functions is zero, and the scalar product of the same basis function is unity, that is, the unit functions are orthogonal to each other. In this way, the calculation of the coefficient $C_m^{(k)}$ is only related to $\varphi_m$, and has nothing to do with other basis functions, which greatly optimizes the computational efficiency. In summary, the calculation goal is: under the constraint condition of Equation (3.38), the minimization of Equation (3.37) is achieved.

*3.7.1.1 Solving the problem*

The solution of the problem requires the Lagrange method [161]. First, define Lagrangian functions based on the problems that need to be solved:

$$L\left(\varphi_1, \varphi_2, \dots, \varphi_M, \lambda_{1,1}, \lambda_{2,2}, \dots, \lambda_{M,M}\right) = J\left(\varphi_1, \varphi_2, \dots, \varphi_M\right) + \sum_{i,j=1}^{M} \lambda_{i,j}\left(\varphi_i^T \varphi_j - \delta_{i,j}\right) \tag{3.41}$$

Solving (3.41), you need to achieve the following conditions:

$$\frac{\partial L}{\partial \varphi_i}\left(\varphi_1, \varphi_2, \dots, \varphi_M, \lambda_{1,1}, \lambda_{2,2}, \dots, \lambda_{M,M}\right) = 0 \quad \text{for } i = 1,2, \dots M$$
$$\frac{L}{\partial \lambda_{i,j}}\left(\varphi_1, \varphi_2, \dots, \varphi_M, \lambda_{1,1}, \lambda_{2,2}, \dots, \lambda_{M,M}\right) = 0 \quad \text{for } i,j = 1,2, \dots M \tag{3.42}$$

Solving formula (3.42), the following results are obtained:

$$\frac{\partial L}{\partial \varphi_i} = 0 \;\Leftrightarrow\; \sum_{j=1}^{n} V(j)\, V(j)^T \varphi_i = \lambda_{i,i}\, \varphi_i \;\&\; \lambda_{i,j} = 0 \;\; for \; i \neq j$$
$$\frac{\partial L}{\partial \lambda_{i,j}} = 0 \;\Leftrightarrow\; \varphi_i^T \varphi_i = \delta_{i,j} \tag{3.43}$$

Let $\lambda_i = \lambda_{i,i}$, we can deduce that we need to solve the eigenvalue problem shown below:

$$V\, V^T \varphi_i = \lambda_i \varphi_i \tag{3.44}$$

In this case, the eigenvalue problem of the correlation matrix ($V\, V^T$) of the set of original flow fields is solved, and the problems raised previously can be solved. In order

to satisfy expression (3.38), the minimization of the following formula (3.37) in any M is realized, and the eigenvalue problem shown in formula (3.44) needs to be solved.

### 3.7.2 Calculation Process in Detail

The set of velocity fields to be processed is: $V^{(k)} = (u, v)_{i,j}^{(k)}, (k = 1,2,3, \dots \dots, K)$. Here, $i, j$ are the spatial position coordinates of the velocity vector in the velocity field, $k$ the velocity field index and $u, v$ are the velocity components in x and y directions respectively. Organize a total of I×J velocity vectors in all $K$ velocity fields and each velocity field is collated as follows:

$$U = \begin{bmatrix} U^{(1)} \\ U^{(2)} \\ \vdots \\ U^{(K)} \end{bmatrix} = \begin{bmatrix} u_{i=1,j=1}^{(1)} & u_{i=1,j=2}^{(1)} & \dots & u_{i=1,j=J}^{(1)} & u_{i=2,j=1}^{(1)} & \dots & u_{i=I,j=J}^{(1)} \\ u_{i=1,j=1}^{(2)} & u_{i=1,j=2}^{(2)} & \dots & u_{i=1,j=J}^{(2)} & u_{i=2,j=1}^{(2)} & \dots & u_{i=I,j=J}^{(2)} \\ \dots & \dots & \dots & \cdots & \cdots & \dots & \cdots \\ u_{i=1,j=1}^{(K)} & u_{i=1,j=2}^{(K)} & \dots & u_{i=1,j=J}^{(K)} & u_{i=2,j=1}^{(K)} & \dots & u_{i=I,j=J}^{(K)} \end{bmatrix} \quad (3.45)$$

The y-direction velocity is made to be the same as the formula (3.45), and the matrix V is obtained. Then, define the spatial correlation matrix as follows:

$$C = \frac{1}{K}(U\,U^T + V\,V^T) \quad (3.46)$$

As mentioned in the previous section, in order to solve the minimization problem, the eigenvalue problem of the spatial correlation matrix needs to be solved, namely:

$$C\,\beta_m = \lambda_m\,\beta_m \quad (3.47)$$

Where; $\lambda_m$ is the eigenvalue of the spatial correlation matrix of the input flow field set, and $\beta_m$ is its eigenvector.

Each eigenvalue corresponds to a characteristic vector. The larger the eigenvalue, the longer the corresponding coordinate axis, and the stronger its dominance. POD modes are arranged in descending order according to the magnitude of eigenvalues as:

$$\lambda^1 > \lambda^2 > \lambda^3 \dots \dots > \lambda^K = 0 \quad (3.48)$$

By selecting several eigenvectors with the highest eigenvalues to represent the set of flow fields being processed, a few dominance features are used to perform dimensionality reduction on complex data sets in the engine cylinder.

The POD coefficients ($C_m^{(k)}$) are obtained by projecting the input velocity field $V^{(k)}$ onto the basis function $\varphi_m$. Finally get a K×M POD coefficient matrix:

$$C_m^{(k)} = \begin{bmatrix} C_1^{(1)} & C_2^{(1)} & \dots & C_M^{(1)} \\ C_1^{(2)} & C_2^{(2)} & \dots & C_M^{(2)} \\ \vdots & \vdots & \vdots & \vdots \\ C_1^{(K)} & C_2^{(K)} & \dots & C_M^{(K)} \end{bmatrix} \tag{3.49}$$

The coefficient $C_m^{(k)}$ in Equation (3.49) represents the strength of the input flow field $V^{(k)}$ in the flow field structure of the basis function $\varphi_m$. For the flow field, $\frac{1}{2}\left(C_m^{(k)}\right)^2$ is equal to the kinetic energy in the flow field $V^{(k)}$ extracted by the basis function $\varphi_m$. For any input flow field $V^{(k)}$, the coefficients in Equation (3.49) can be used to perform the recombination by multiplying and superimposing according to Equation (3.36). The kinetic energy extracted by a certain basis function in all input flow field sets can be calculated by:

$$ke_m = KE_m / \sum_{m=1}^{M} KE_m \tag{3.50}$$

As mentioned earlier, the basis functions are sorted in descending order of energy, that is, the first basis function contains the highest share of energy, and the second basis function contains the second highest share of energy. For most of the engine's in-cylinder analysis, five or more basis functions can obtain more than 90% of energy. By analysing these basis functions, i.e., the ordered flow field structure, a large number of complex in-cylinder flow fields can be objectively and quantitatively analysed.

### 3.7.3 POD In-Cylinder Flow Analysis

POD was firstly applied to a sample of synthetic velocity vector fields with known characteristics to gain more physical understanding about the fundamental properties and the important features of POD. The aim was to reveal:

1. What physical properties of the large scale (coherent) structures were captured by the POD?

2. How these physical properties were captured and distributed among the POD modes?

Furthermore, POD analysis was extended to evaluate the effect of valve lift and pressure difference across the air intake valves on the in-cylinder air flow variation and evolution.

#### *3.7.3.1 Evaluation of the Effect of Valve Lift using Phase-Invariant POD*

A large dataset of 5000 velocity vector fields (snapshots) with the same grid size (same number of vectors) from different valve lifts from 1 mm to 10 mm (500 snapshots per valve lift) were arranged to be in one input file and analysed by using phase-invariant POD to extract the most energetic and organized coherent structures. In this manner, the POD modes could be used to describe the flow structures at any valve lift. While their corresponding coefficients could be used to demonstrate the flow evolution.

#### *3.7.3.2 Evaluation of the Effect of Pressure Difference using Phase-Invariant POD*

In order to characterize the influence of pressure difference on flow structures, three data sets at valve lift 10 mm for three pressure differences 300, 450 and 600 mm$H_2O$ (1000 velocity vector fields from each pressure difference) were combined into a single file to implement phase-invariant POD. Consequently, under this scenario, for these 3000 input snapshots, 3000 phase-invariant POD modes and their corresponding coefficients were constructed accordingly.

### 3.7.4 Convergence Criterions of POD Modes

The convergence criterion of POD modes means the determination of how many input snapshots (velocity vector fields) are required for reconstruction. Here, each instantaneous PIV measurement was considered to be a snapshot of the flow. The following is an illustrative example to show how the number of input snapshots was determined before employing POD. Different datasets at valve lift 10 mm with different number of velocity vector fields of 50, 100, 200, 300 and 400 respectively, were arranged to implement the POD. Figure 3.49 shows energy fraction distributions for the first 10 modes with variations in the number of input snapshots. It was clear that well-converged POD results were obtained with 400 snapshots of data. The energy convergence related to 300 and 400 snapshots was quite identical showing that the use of more input snapshots did not modify the energy distribution. Moreover, the number of input snapshots affects the accuracy of the computed eigenvalues (λ). Cazemier *et al*. [162] mentioned that the higher the number of snapshots the more accurate measure of the Eigen functions. The Eigen value reflects the relative kinetic energy associated with a corresponding mode and their sum indicates the total energy. Therefore, the convergence of the computed eigenvalues with the number of snapshots was investigated [20]. Figure 3.50 shows the variation of eigenvalues with the number of snapshots for the first POD mode. It was noticed that no significant changes were noticed in the consecutive magnitude of eigenvalues for the first POD mode once the sample size exceeds 300. Therefore, based on the above comparison, more than 300 snapshots were considered quite accurate for POD analysis in this study. Two different ways were used to implement the POD; DynamicStudio software and MATLAB code. Appendix C shows the MATLAB code used for POD implementation.

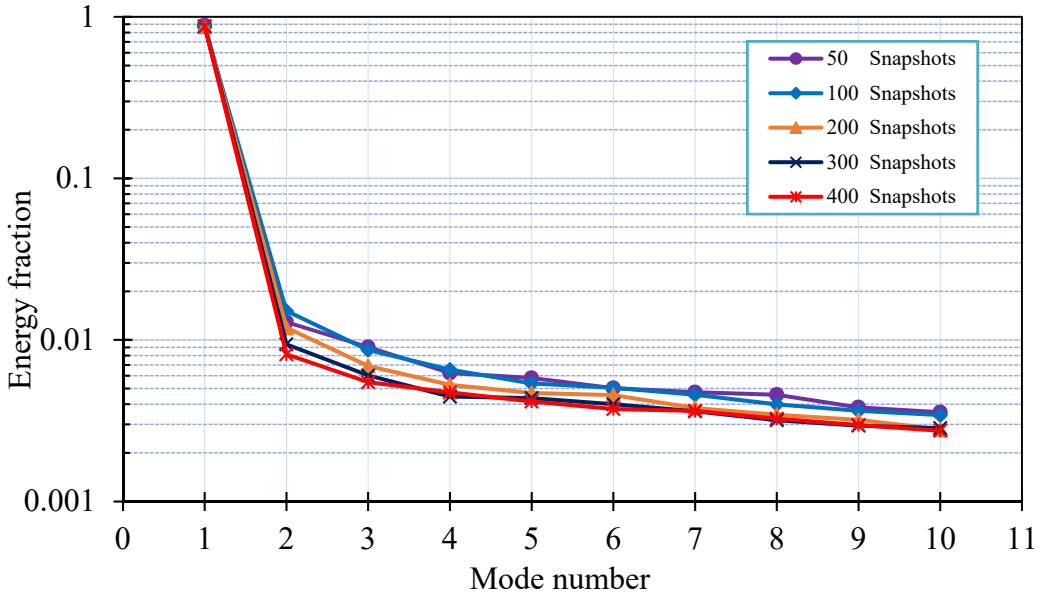


Figure 3.49: Energy fraction distributions for the first 10 modes with variations in the number of input snapshots

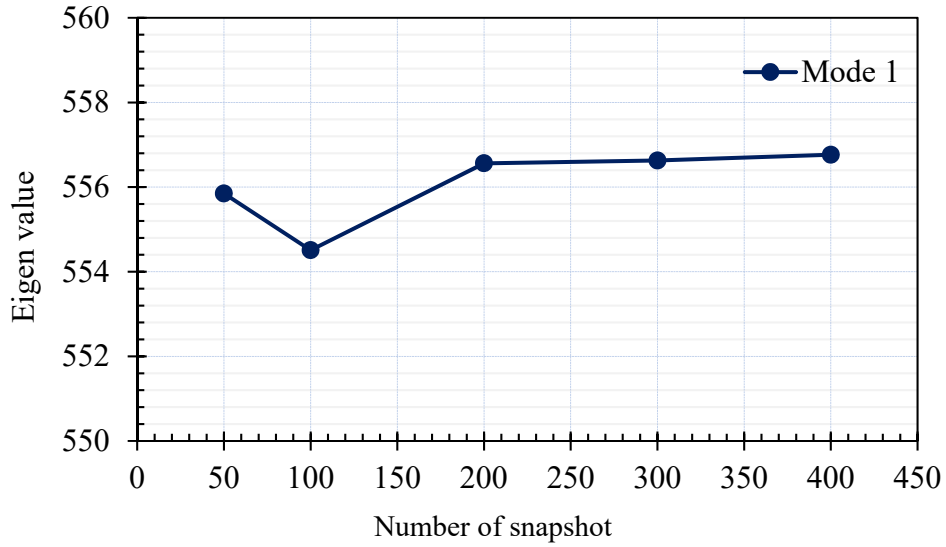


Figure 3.50: Effect of number of snapshots on the magnitude of eigenvalue of the first mode

# CHAPTER 4

# EXPERIMENTAL RESULTS AND DISCUSSION

## 4.1 Chapter Overview

In this chapter, first of all, the FEV flow rig was validated against Ricardo flow rig to test its suitability for particle image velocimetry measurements. Next, the results of stereoscopic particle image velocimetry (PIV) measurements in different vertical tumble planes are presented and discussed for different valve lifts and different pressure differences across the air intake valves. Then, the proper orthogonal decomposition (POD) analytical technique was applied to PIV measured velocity vector maps to characterise the flow structures. Finally, the results for air/spray interaction are presented and discussed.

## 4.2 Validation with Experimental and Simulation Work of Ricardo

The significant role of the port and valve assembly is to enable the engine to work under higher volumetric efficiency for realising more output torque and power. Therefore, there are some important parameters which can be studied using a steady-state flow rig to assess the effect of the valve and port assembly on the engine capacity at different ranges of valve lifts and pressure differences. One of these parameters is the discharge coefficient which has a significant effect on engine capacity particularly at lower valve lifts. Moreover, there are some other important parameters which reflect the intensity and direction of the in-cylinder flow motion: tumble ratio and swirl ratio.

For the current work, the cylinder head was mounted on both flow rigs and tests were carried at the same pressure difference of 600 mm$H_2O$ across the air intake valves. The valve lift was varied from 1 to 9 mm in 1 mm steps and the experimental

results were presented in terms of measured air flow rate, flow coefficient, discharge coefficient and non-dimensional rig tumble.

### 4.2.1 Measured Air Flow Rate

The variation of air volume flow rate as a function of valve lift for both Ricardo and FEV steady-state flow rigs at 600 mm$H_2O$ pressure difference is shown in Figure 4.1. As can be seen from the figure, as the valve lift increased the supplied air volume flow rate increased to maintain the constant pressure difference. There was an acceptable agreement between the two curves till 6 mm valve lift but the difference increased as the valve lift increased. This was mainly due to chocking of the flow due to the small discharge area in the case of the FEV flow rig. This was thought to be due to the recommended value of the air discharge port being 35% of the bore diameter.

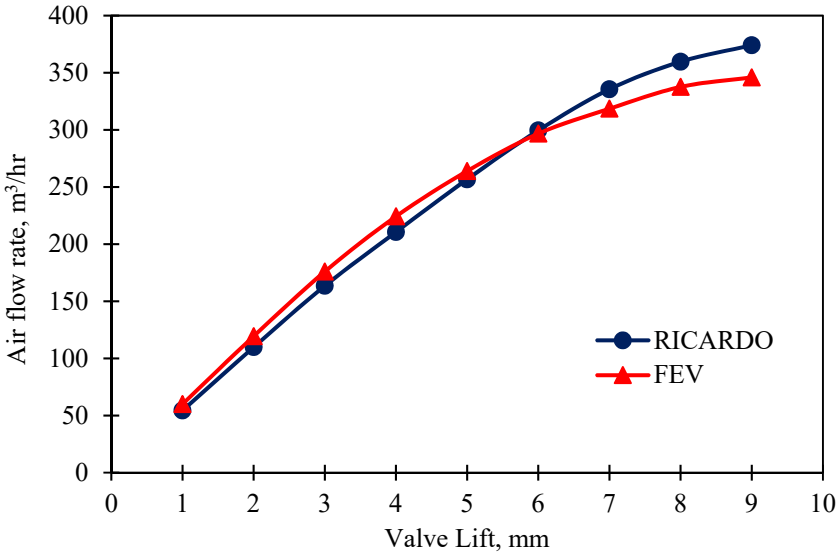


Figure 4.1: Measured air flow rate variation with valve lift for both Ricardo and FEV steady-state flow benches

### 4.2.2 Flow Coefficient

The flow coefficient seems to be equivalent in definition to the discharge coefficient, however the main difference is that the reference area used here is the inner seat

diameter of intake valves ($A_{seat}$) instead of the area of a frustum formed perpendicular to the valve and seat insert faces ($A_V$) in the case of the discharge coefficient. The flow coefficient reflected the flow restriction made by the intake port geometry. This flow restriction became more significant when the area formed between the valves and their seat lips became equivalent to or exceeded the minimum port area (throat area). The flow coefficient was measured using both steady-state flow rigs at different valve lifts as plotted in Figure 4.2. The flow coefficient increased monotonically from zero with valve lift since the effective flow area through the valve increased with lift. Moreover, the figure shows that the flow coefficient affected the engine breathing capacity significantly. In fact, the higher valve lift caused more air flow into the engine and thus higher engine breathing capacity. It is clear also from the figure that there was a good agreement between both curves especially till 6mm valve lift.

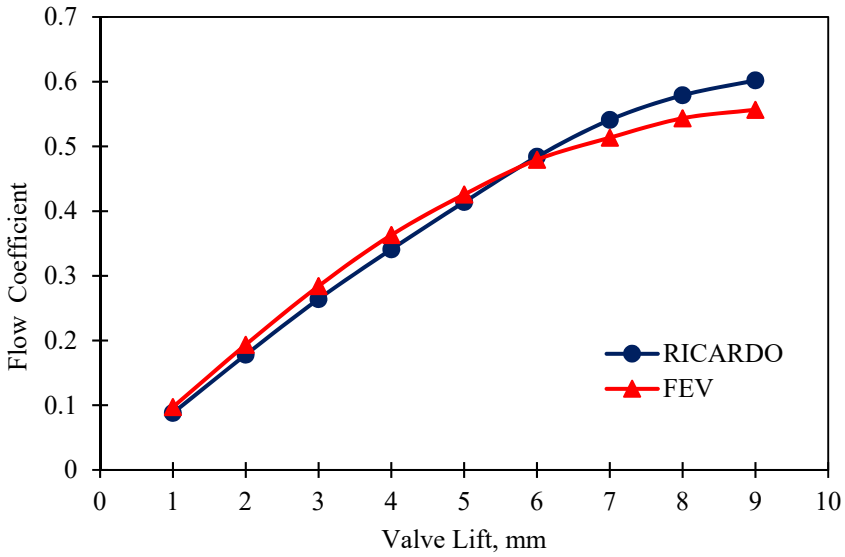


Figure 4.2: Flow Coefficient variation with valve lifts for both Ricardo and FEV steady-state flow benches

### 4.2.3 Discharge Coefficient

The discharge coefficient reflected the flow restriction caused by intake valves and seat lips particularly at low valve lifts. This flow restriction was used to determine the orifice area of the incoming air flow. Basically, the profile geometry of intake valves and their seat lips were key factors which affect the flow significantly particularly at low valve

lifts [63, 163]. The dependence of the discharge coefficient on valve lift can be understood from Figure 4.3. Theoretically, the incoming air flow filled the whole area available between intake valves and their seat lips, but in reality, it is more dependent on valve lift [164]. At low valve lifts, the inlet air jet was attached to both the seat and the valve, and thus was affected by viscous shear. If the jet was attached, then the discharge coefficient decreased slightly with increasing the Reynolds number since the viscous effects in the jet decreased. At high valve lifts, the fluid inertia prevented the flow from turning along the valve seat, so the flow broke away, forming a free jet. There was also good agreement between both curves.

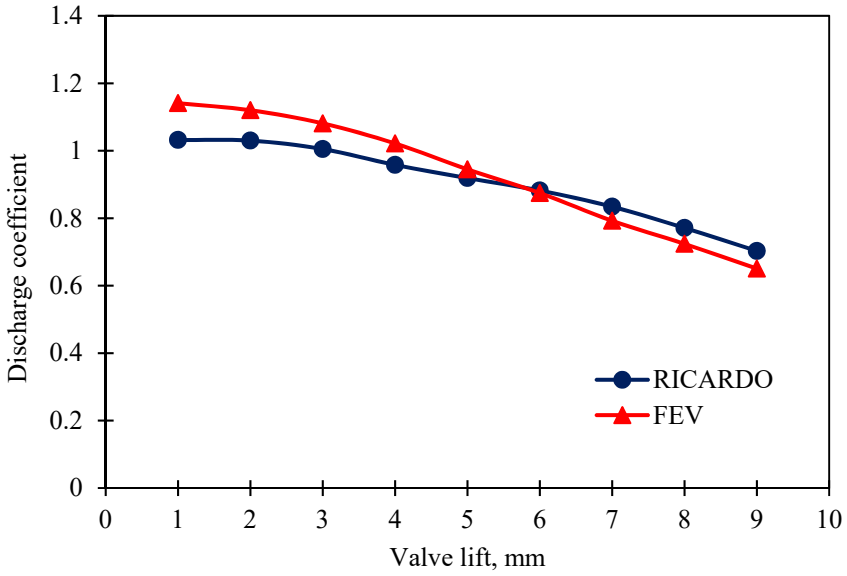


Figure 4.3: Discharge coefficient variation with valve lifts for both Ricardo and FEV steady-state flow benches

### 4.2.4 Non-Dimensional Rig-Tumble

The variation of non-dimensional rig tumble versus the valve lift is shown in Figure 4.4. The large-scale tumbling motion is usually created during the intake stroke by restricting the air flow rate on the outer side of the intake valves. At low valve lift, the flow was highly restricted on the right side of the cylinder therefore, the higher velocities generated in this side produced negative values of non-dimensional rig-tumble which can be called also as reverse tumble (clock-wise direction). After that, a symmetric flow distribution occurred at the valve seat area which resulted in no tumble

at about 5 mm valve lift for paddle wheel flow rig (FEV) and at about 4 mm for impulse torque meter flow rig (Ricardo). At higher valve lifts, an asymmetric flow distribution occurred again with the flow directed more towards the exhaust valves. Intensified by the deflection at the piston crown this jet flow led to the generation of a strong tumbling motion within the cylinder with positive values which can be called as normal tumble (counter clock-wise direction).

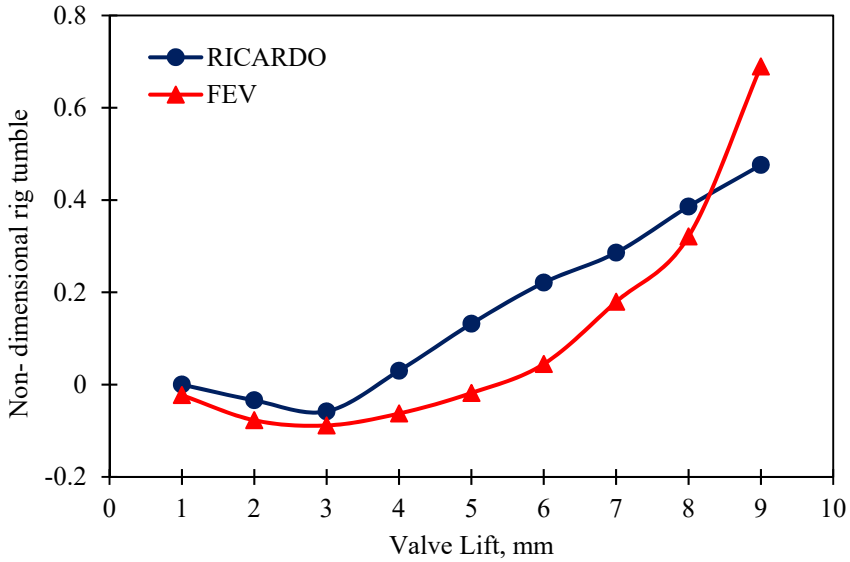


Figure 4.4: Non-dimensional tumble rig variation with valve lifts for both Ricardo and FEV steady-state flow benches

The difference between both curves was related to the fact that different techniques were used for tumble measurements, paddle wheel for FEV flow rig while an impulse-torque meter for Ricardo flow rig. Moreover, in the case of the torque meter method (Ricardo method) there was no piston but in the case of the paddle wheel the piston was there. The rate of increase of non-dimensional rig tumble for FEV flow rig became very high starting at 6 mm valve lift. This was mainly because of the arrival of chocking condition therefore more air trapped inside the cylinder which, in turn, increased the rotation rate of the paddle wheel.

### 4.2.5 Validation of VECTICS CFD Simulation Work

This section presents the validation between the experimental results obtained from the PIV measurements with those of RICARDO-VECTIS CFD simulations at identical operating conditions. PIV measurements were carried out at the mid-cylinder vertical tumble plane (plane of symmetry) at three fixed valve lifts, 2, 6 and 9.73 mm for 600 mm$H_2O$ pressure difference across the air intake valves. VECTIS CFD simulations of the same cylinder head were set up by using the same boundary conditions in an attempt to represent faithfully the experimental arrangement. Figure 4.5 depicts a comparison of the ensemble average velocity vector fields obtained by PIV measurements in the vertical central plane with those obtained by VECTIS CFD simulations at different valve lifts. From the presented data it can be observed that, the air flow coming through the intake valves into the cylinder formed two air jets, intake side jet and the exhaust side jet. The intake air jet was almost parallel to the intake side cylinder wall while the exhaust side jet interacted with the combustion chamber walls then the exhaust side cylinder wall forming a counter-clock wise tumble vortex behind the exhaust valves. At valve lift 2 mm, the flow was highly restricted on the right-hand side of the intake valves, therefore the flow velocity was maximum behind the intake valves. At valve lift 6 mm, the problem associated with the flow restriction was less and the air velocity was distributed almost equally between both jets. At valve lift 9.73 mm, a significant amount of air was highly directed by the intake ports towards the exhaust side, therefore the maximum velocities were transferred to the exhaust side. Considering the limitations in optical access, the VECTIS CFD simulation results provided further insights into the in-cylinder flow structure through the whole cylinder area. The agreement with PIV measurements were broadly good in terms of in-cylinder flow motion and structure, however the maximum predicted velocity magnitudes were to some extent higher than those measured by PIV. This in turn means that VECTIS CFD simulation can be used confidently to predict more useful information regarding the in-cylinder flow behaviour at different operating conditions. However, further ‘tuning’ of the code may be necessary particularly the turbulence model used in order to achieve more accurate quantitative predictions.

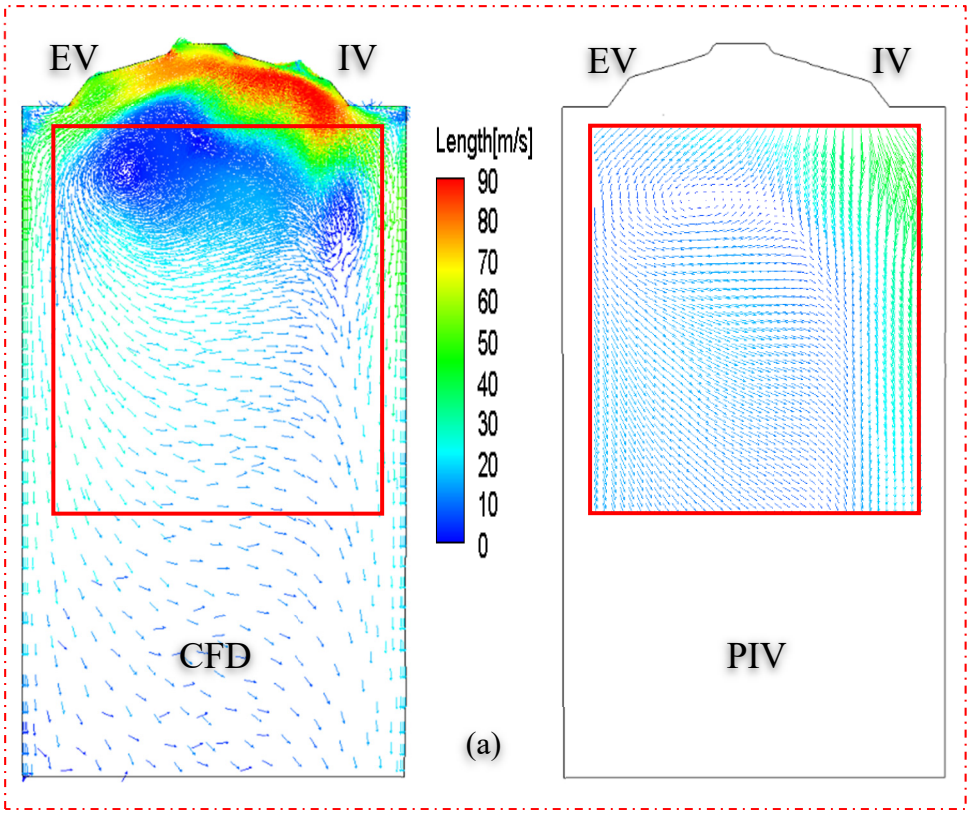
EV
IV
Length[m/s]
90
80
70
60
50
40
30
20
10
0
CFD
EV
IV
PIV
(a)

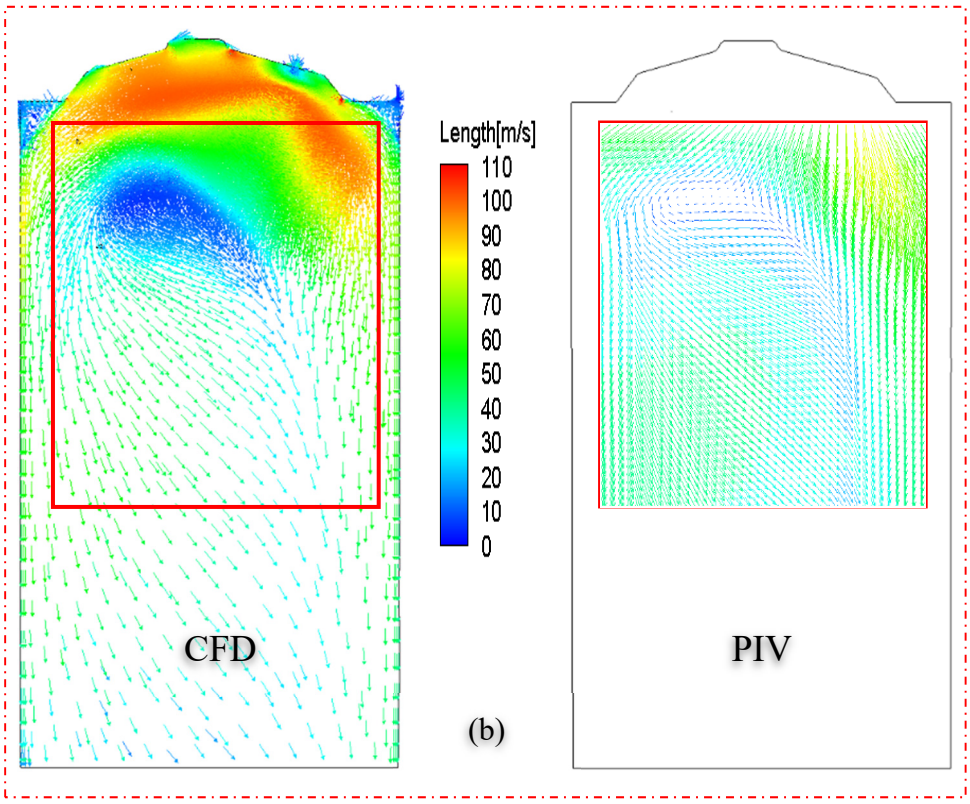
Length[m/s]
110
100
90
80
70
60
50
40
30
20
10
0
CFD
PIV
(b)

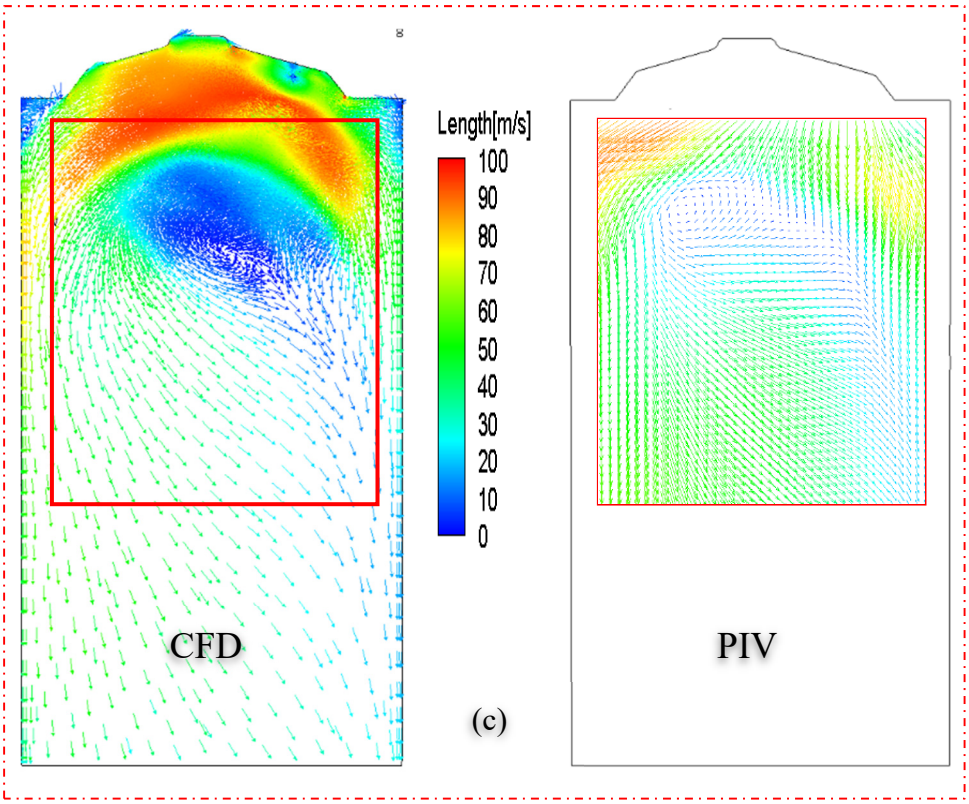


Figure 4.5: Comparison of ensemble average velocity vector fields obtained by PIV with those obtained by VECTIS CFD simulations, (a) valve lift 2mm, (b) valve lift 6 and (c) valve lift 9.73 mm

### 4.3 Stereoscopic Particle Image Velocimetry Results for Air-Flow

In this section, the PIV results for the vertical tumble-plane are presented. Three sub-sections are presented which include the effect of valve lift, the effect of measuring plane and finally the effect of changing the pressure difference across the air intake valves on the in-cylinder flow structures.

#### 4.3.1 The Effect of Valve Lift

Stereoscopic 2D-3C PIV measurements were carried out in the plane of symmetry at different valve lifts. The valve lift was changed from 2 mm to 10 mm for fixed pressure difference of 150 mm$H_2O$. The effect of valve lift on in-cylinder flows, which was

characterized by the ensemble average, vorticity, turbulent kinetic energy (TKE) and tumble ratio (TR), obtained from PIV experiments is presented in the next sections.

#### *4.3.1.1 The Effect of Valve Lift on Flow Structures*

Figure 4.6 shows the ensemble average velocity vector fields in the vertical tumble plane passing through the centre of the cylinder at various valve lifts. Velocity directions are represented by vectors and magnitudes by colour-scale. Figure 4.6 (a)-(c) shows the in-cylinder velocity vector fields at valve lifts 2, 3 and 4 mm, respectively where the intake valves were partially open. It can be seen that, generally the air velocity increased with increasing the valve lift as expected. In addition, the incoming air into the cylinder through the intake valves formed two separate jets. The right-side jet was mostly parallel to the cylinder wall with higher velocities compared to the left side because of the narrow passage between the intake valves and the right side of the cylinder wall. The air coming from the left side was deflected firstly by the combustion chamber walls towards the exhaust side then by the cylinder wall forming the left side jet with a recirculation zone behind the exhaust valves.

Figure 4.6 (d)-(f) shows the in-cylinder velocity vector fields at valve lifts 5, 6 and 7 mm, respectively where the intake valves were opened more. At valve lift 5mm, there was a symmetrical velocity distribution between the left and right-side jets. With increasing the valve lift more to 6 and 7 mm, more air was directed by the intake port towards the exhaust side then deflected by the cylinder wall towards the right bottom side of the cylinder thus transferring the dominant flow features to the left side of the cylinder.

Figure 4.6 (g)-(i) shows the in-cylinder velocity vector fields at valve lifts 8, 9 and 10 mm, respectively where the intake valves were fully opened. At these valve lifts, tumble vortices in the clock-wise and counter clock wise directions were generated in the upper half of the cylinder. A strong tumble vortex was formed in the lower half of the cylinder in the counter clock-wise direction with its centre almost coinciding with the vertical centre of the field of view and growing in the radial direction with increasing the valve lift. At valve lift 10 mm, the flow was dominated by a strong tumble

vortex with diameter almost equal to the bore of the cylinder. These strong tumble vortices at the higher valve lifts were the result of the orientation of the intake ports and the bent roof shape of the combustion chamber, the flow was directed toward the exhaust side then deflected by the cylinder walls and the piston at the bottom.

#### *4.3.1.2 The Effect of Valve Lift on Vorticity Contours*

Vorticity is the rotation rate of the fluid and is also known as pseudo vector field that represents the fluid's local spinning motion around a point and is used to describe the total vortex strength of the flow fields. Figure 4.7 shows the vorticity magnitudes in the central vertical plane at various valve lifts. It can be observed that the vorticity magnitudes changed with blue representing the flow rotation in the clock-wise direction (negative) while green and red represent the flow rotation in the counter clock-wise direction (positive). Significant differences can be seen between the low and high valve lifts. Generally, the vorticity strength increased with increasing the valve lift. At low valve lifts, the flow inside the cylinder was divided into two regions. The region behind the intake valves was characterized by clock-wise vortices while the area behind the exhaust valves was characterized by counter clock-wise vortices. However, at high valve lifts, the cylinder was dominated by a strong tumble vortex in the counter clock wise direction except in the small area behind the intake valves. In addition, one method of studying the increase in vortex strength was to observe the turbulent kinetic energy of the flow field at different valve lifts.

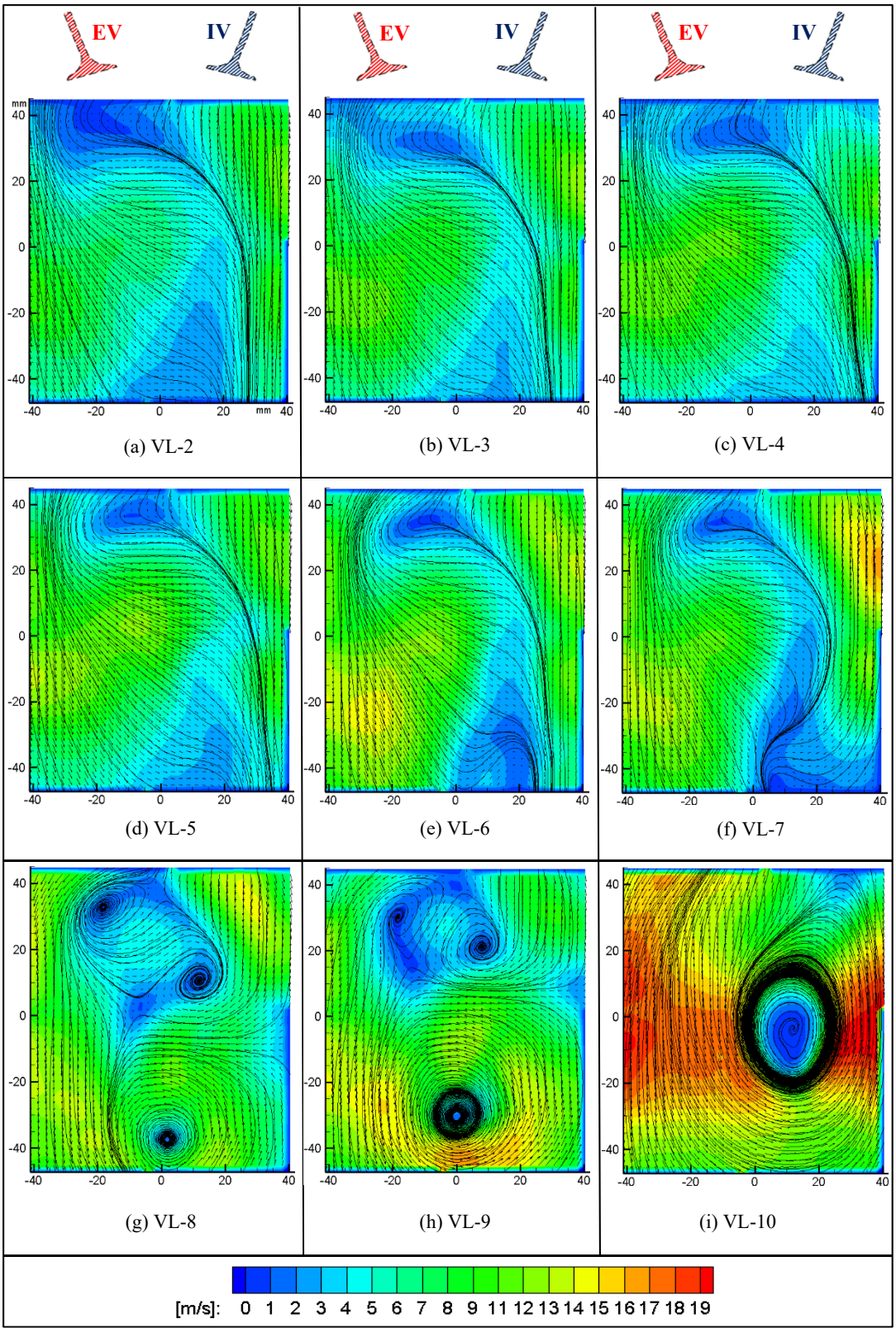


Figure 4.6: The ensemble average velocity vector fields at different valve lifts

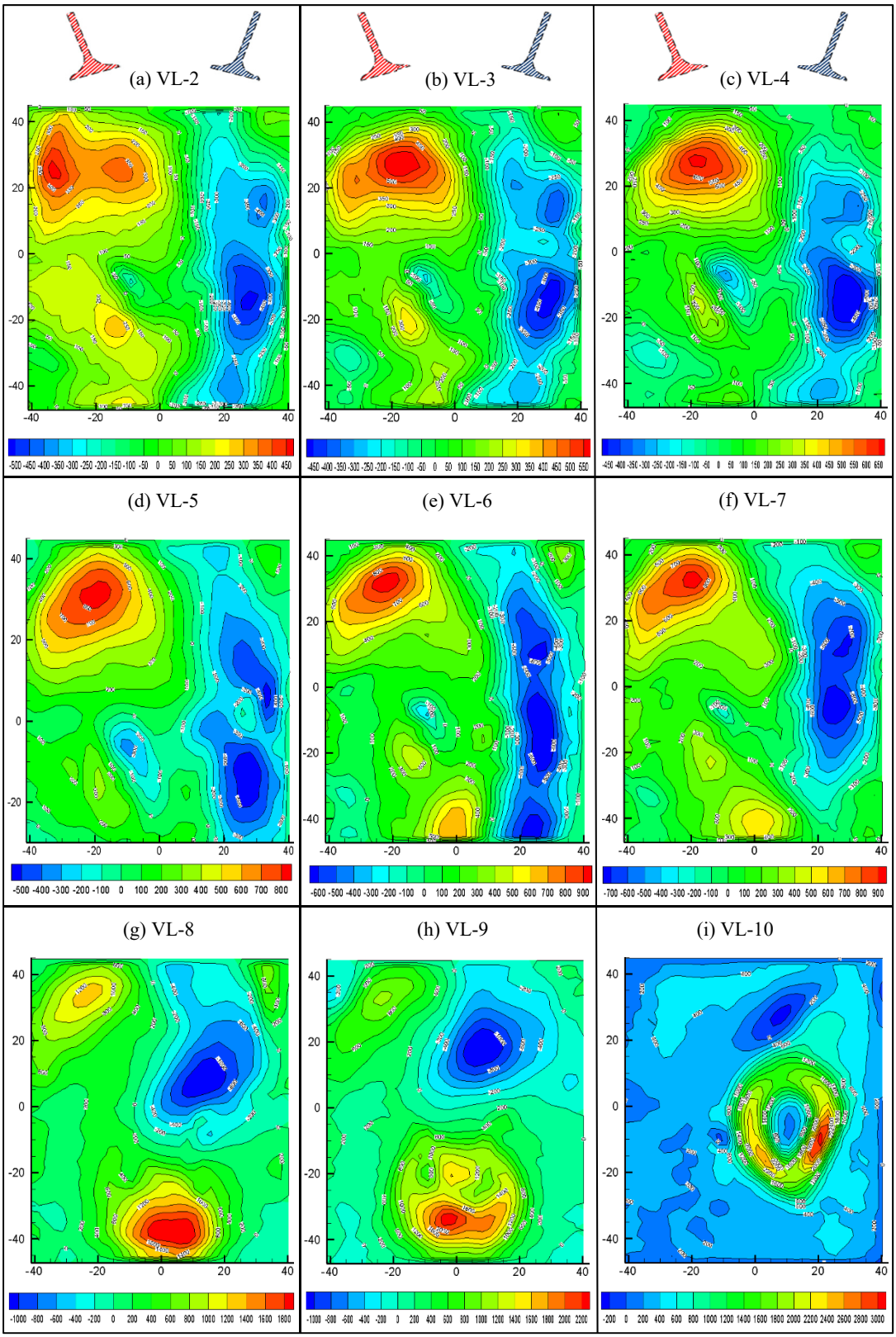


Figure 4.7: Vorticity magnitudes (rad /sec) at different valve lifts

*4.3.1.3 Effect of Valve Lift on the Turbulent Kinetic Energy*

Generally, the intensity of the in-cylinder air flow can be expressed by the turbulent kinetic energy (TKE). In the current study, the TKE of the in-cylinder flow was calculated from the root mean square (RMS) velocity vector fields, which were obtained from the ensemble average velocity fields by DynamicStudio V5 software, using 1000 instantaneous velocity vector fields. Higher TKE is a measure of strength of the air flow. Figure 4.8 shows the variation of the turbulent kinetic energy with valve lift. It can be observed that, the TKE increased gradually from 2 to 7 mm valve lift. Then it started to increase rapidly with increasing the valve lift further reaching a maximum value at 10 mm valve lift. The slow rise in TKE at the lower valve lifts was because of, (i) the lower air flow rates into the cylinder, and hence (ii) the lower velocity of air jet entering the cylinder. However, at higher valve lifts the rate of increase became more obvious because of high velocity of the air jet entering the cylinder, which had high mean and fluctuating velocity components. It was found that the TKE increased by about 41.3% and 82% when the valve lift increased from 4 to 7 mm and from 7 to 10 mm valve lift respectively. This high level of turbulent kinetic energy was expected to transfer down into small scale turbulence by the effect of compression.

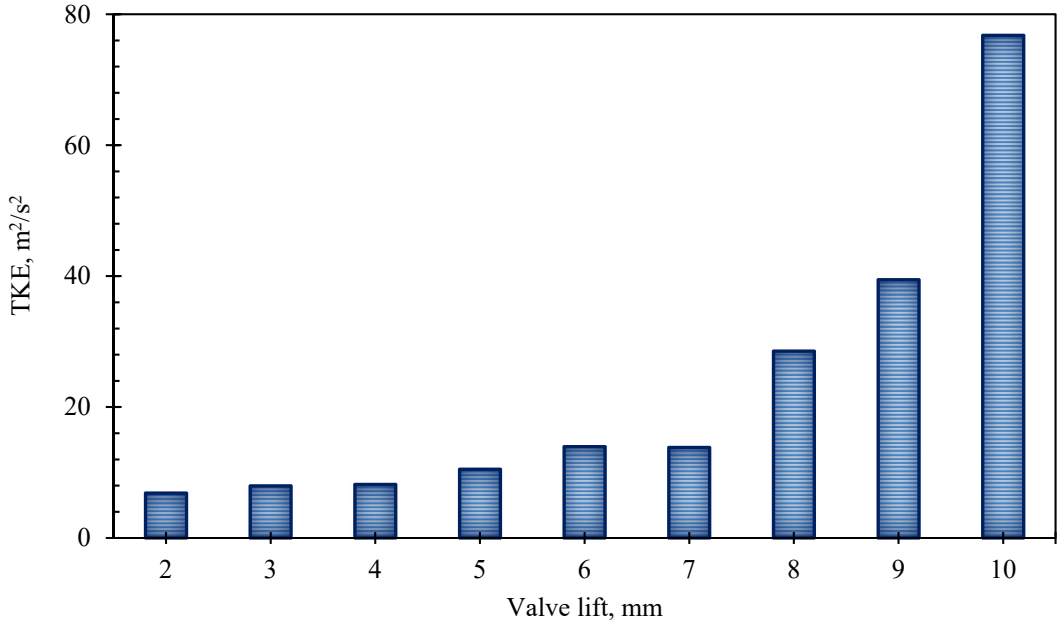


Figure 4.8: Variation of TKE at various valve lifts

*4.3.1.4 Effect of Valve Lift on Tumble Ratio*

Two different ways were used to calculate the tumble ratio at different valve lifts. The first method was the tumble ratio based on angular momentum ($TR_1$) while the second method was based on vorticity ($TR_2$). $TR_1$ was defined by the ratio of the actual angular momentum of the fluid to the total fluid mass M assuming solid body motion at crank angle speed ω while the center of rotation was taken to be the center of the field of view. While, $TR_2$ was defined as the mean value of vorticity normalised by twice the crank angle speed ω. The mean vorticity was calculated by considering the rotation of horizontal and vertical velocity components about the center of field of view. This ratio represents the relative amounts of large- and small-scale rotation in the flow. For a rotating solid body, the mean vorticity has a constant value of twice the angular velocity. Figure 4.9 shows the tumble ratio calculated from both the angular momentum and from the curl of the vector fields at different valve lifts. It can be seen that; no significant differences were observed in tumble ratio between the two ways. The high valve lifts generated more powerful tumble pattern, for instance 2.67 and 2.04 at valve lift 10 mm for $TR_1$ and $TR_2$, respectively.

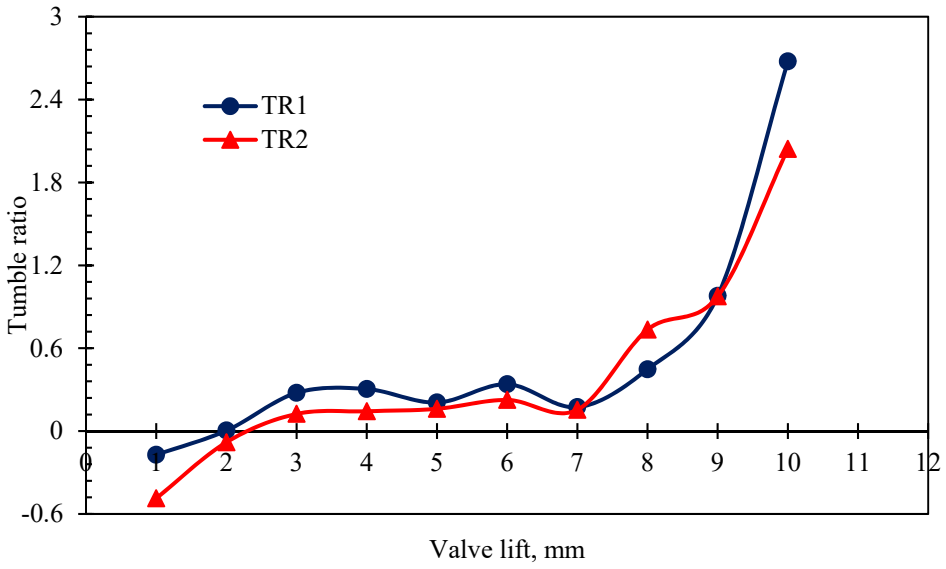


Figure 4.9: Tumble ratio at different valve lifts

These very high value of tumble ratio was due to both the high velocity generated by the ports and good flow distribution within the vortex, particularly at valve lift 10

mm. Table 4.1 gives a summary of the tumble ratios calculated form both the curl of the vector field and the angular velocity at different valve lifts.

Table 4.1: Tumble ratios calculated from both the curl of the vector field and the angular momentum at different valve lifts

| Valve Lift, mm | $TR_1$ | $TR_2$ | Non-Dimensional Rig Tumble |
|---|---|---|---|
| **1** | -0.17167 | -0.48704 | -0.0228 |
| **2** | 0.00358 | -0.08119 | -0.0772 |
| **3** | 0.27657 | 0.12414 | -0.0885 |
| **4** | 0.30414 | 0.14354 | -0.0627 |
| **5** | 0.20665 | 0.16107 | -0.018 |
| **6** | 0.33908 | 0.22547 | 0.0446 |
| **7** | 0.17311 | 0.15416 | 0.179 |
| **8** | 0.44730 | 0.73408 | 0.321 |
| **9** | 0.97859 | 0.97511 | 0.6892 |
| **10** | 2.67617 | 2.04259 | - |

### 4.3.2 The Effect of Measurement Plane

Stereoscopic 2D-3C PIV measurements were carried out in three different vertical tumble planes; the mid cylinder plane, the mid injector plane and the mid intake valve plane. Averages of 1000 PIV instantaneous vector maps were produced at fixed values of valve lifts of 7, 8, 9 and 10 mm for 150 mm$H_2O$ pressure difference. The effect of measurement plane variation on in-cylinder flows, which was characterized by the ensemble average, vorticity, TKE and TR, obtained from PIV experiments is presented in the next sections.

*4.3.2.1 Flow Structures at Different Measurement Planes (Spatial distribution)*

The three-dimensionality of the flow necessitates the measurement of all three velocity components via stereoscopic particle-image velocimetry in multiple planes. Figure 4.10 depicts the ensemble average velocity vector fields of the in-cylinder tumble motion in three measurement planes for fixed values of valve lift. Number of observations can be extracted from this figure. Firstly, although the differences between the three planes were clearly visible in the vector maps, some similarities could be found in the flow patterns. In all measurement positions the PIV maps for all valve lifts, because of the design of the intake port, a significant amount of the incoming air flow was directed towards the exhaust side in the form of jet-like structure. Because of the interaction between this jet flow and the left cylinder wall and the flat piston in the bottom of the cylinder, a strong tumble vortex was generated in the counter clock wise direction. The intensity of this vortex increased with increasing the valve lift. In addition, this vortex was more significant especially at valve lift 10 mm as it dominated the full cylinder with no significant change in the flow pattern could really be noticed between the different positions and represented an ideal solid body rotation model. Secondly, one of the more significant observations from these contour plots was the difference in flow structures between the mid injector and the mid cylinder planes from one side and the mid valve plane from the other side, where the presence of the intake valve caused a separate vortex to form behind the intake valve. Thirdly, the average flow velocity was higher in the mid valve plane for all cases. The average velocity increased from 7.5 m/s to 7.96 m/s and from 12.1 m/s to 12.7 for valve lifts 8 mm and 10 mm respectively when comparing between mid-cylinder and mid valve plane. Fourthly, the fact that the position of the vortex centre in the tumble planes did not change significantly across the cylinder volume for all valve lifts, a potentiality of the tumble pattern to remain during the compression stroke was highly likely. Moreover, the measurements indicated that while the dominant tumble vortex was mostly two-dimensional, other flow structures confirmed that there were other significant three-dimensional features of the flow which must be considered when evaluating air/fuel mixing in the cylinder.

*4.3.2.2 Distribution of Vorticity Contours in the Different Measurement Planes*

Vorticity is a very important quantity for characterizing turbulence and its rotational structures. PIV provides the instantaneous velocity fields from which the curl of the vector field which is equivalent to the vorticity can be measured from the velocity gradients. Figure 4.11 illustrated the vorticity maps at different measurement planes for different valve lifts. It can be noticed that the vorticity magnitudes were positive and negative indicating the different directions of vortex spins seen in the velocity vector maps. The figure clearly shows the strength of vorticity increased in both directions of rotation with increasing the valve lift except for valve lift 10 mm which was dominated by a strong counter clock wise tumble vortex with a center coinciding with the center of the cylinder. Moreover, when comparing for the same valve lift at different planes, it was found that there were not significant changes in the vortex strength and shape except for the mid valve plane which was distinguished with reverse tumble vortex behind the intake. This might be attributed to the fact that, for a single valve with straight perpendicular port exiting into a finite volume, the inducted steady-state flow streamlines form a torus, as some of the fluid particles come back to the axis of symmetry of the valve. However, in real engines, the vortex can be dramatically distorted by the boundaries of the confined space defined by the cylinder walls and pent roof surfaces. As the air jet impinges onto these boundaries, the flow is directed and, in some cases, heavily restricted. For design consideration, the inlet valve is rarely cantered in the cylinder, thus uneven angular distribution of the flow rate around the valve is inevitable. Therefore, for the current study, the flow was highly restricted on the right side of the intake valves (the restriction decreases with increasing the valve lift), thus a reverse tumble vortex was formed behind the intake valves because of the interaction between the right air jet with internal boundaries of the cylinder head and the cylinder.

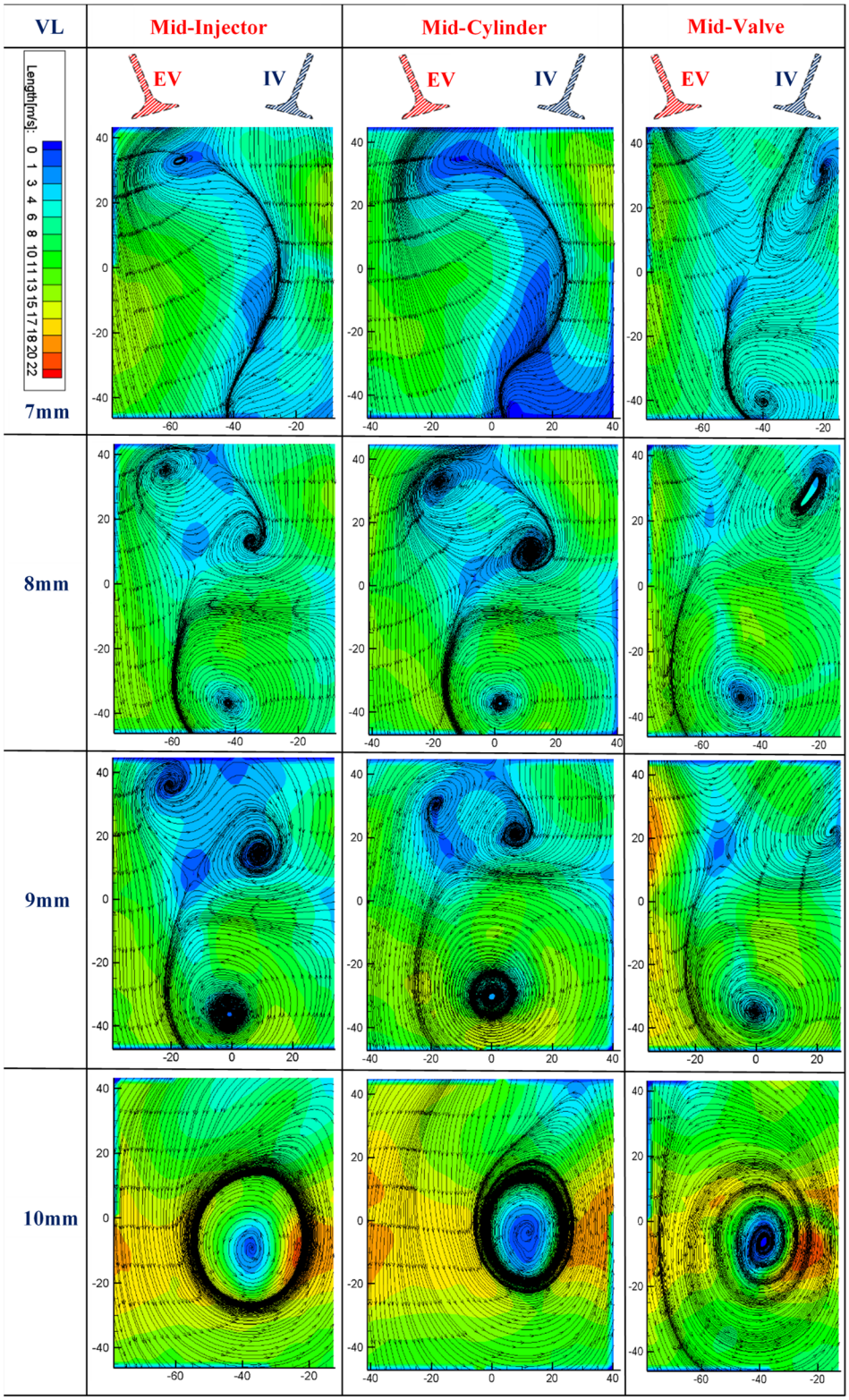


Figure 4.10: Ensemble average velocity vector fields at different measurement tumble planes

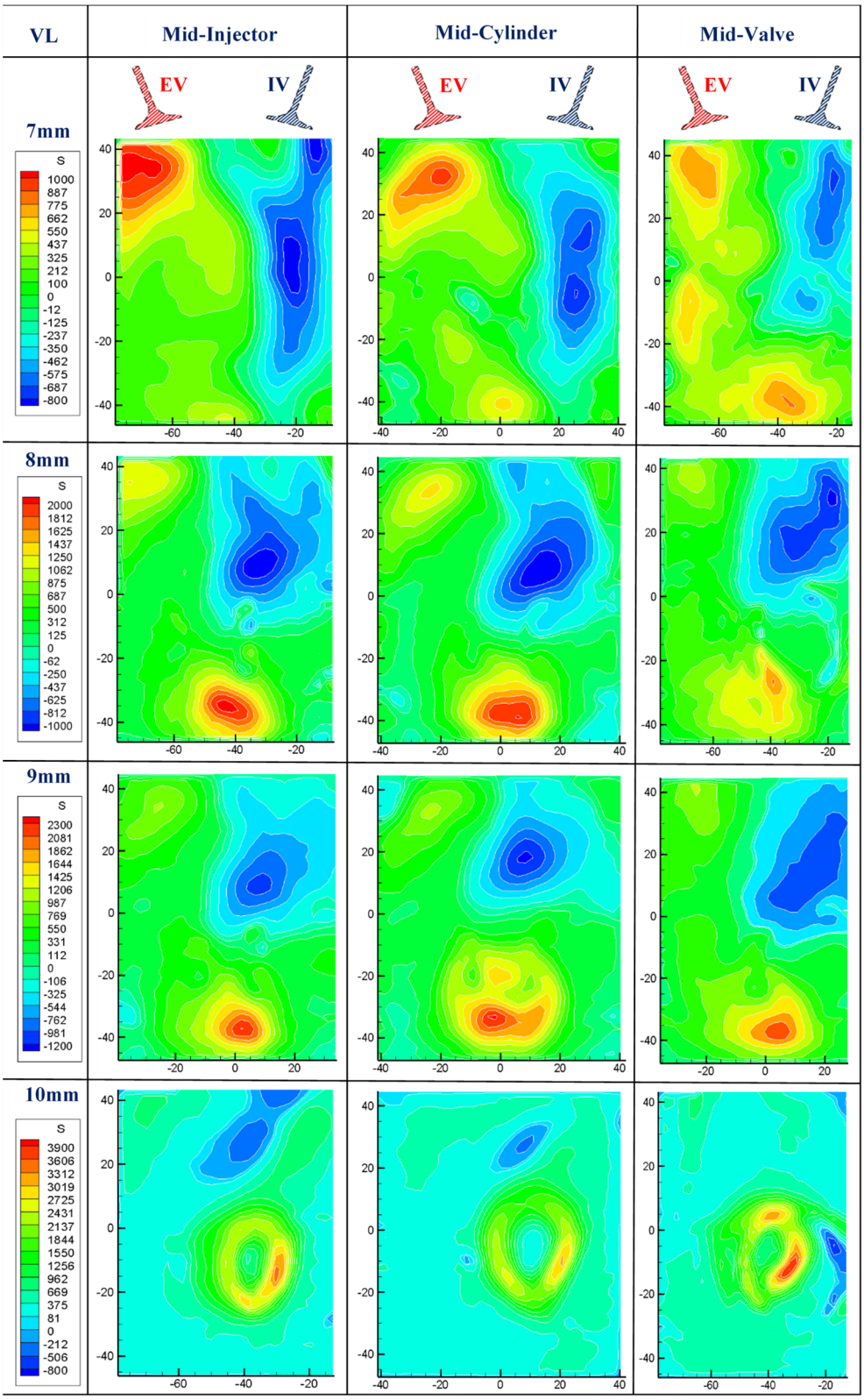


Figure 4.11: Vorticity maps at different measurement tumble planes

*4.3.2.3 TKE Distribution in the Different Measurement Planes*

In the world of fluid dynamics, turbulence plays a significant contribution in the mixing mechanisms, and in addition to that velocity fluctuations enhance the mixing and turbulent dispersion. The kinetic energy provides quantitative information for the better understanding of turbulence mechanisms since it is affiliated with both fluctuating and mean velocities. The intensity of in-cylinder air motion at different measurement planes for different valve lifts can be expressed by TKE as shown in Figure 4.12. It can be noticed that the turbulent kinetic energy followed the same trend as vorticity. Increasing the valve lift led to higher flow rates inside the cylinder with higher velocities which had high mean and fluctuating velocity components which in-turn enhanced the TKE and increased the strength of air motion. Agarwal *et al.* [165] also reported similar behaviour of TKE in the intake stroke using an optical engine. In addition, the lower intensity of TKE at valve lift 7 mm could be attributed to the collision between the intake jet-side with the exhaust jet-side. Moreover, the TKE was higher for the mid valve plane for all valve lifts which agreed well with the higher velocities acquired in this plane. This practically means that the intake generated vortices in all planes at high valve lifts could persist through the compression stroke.

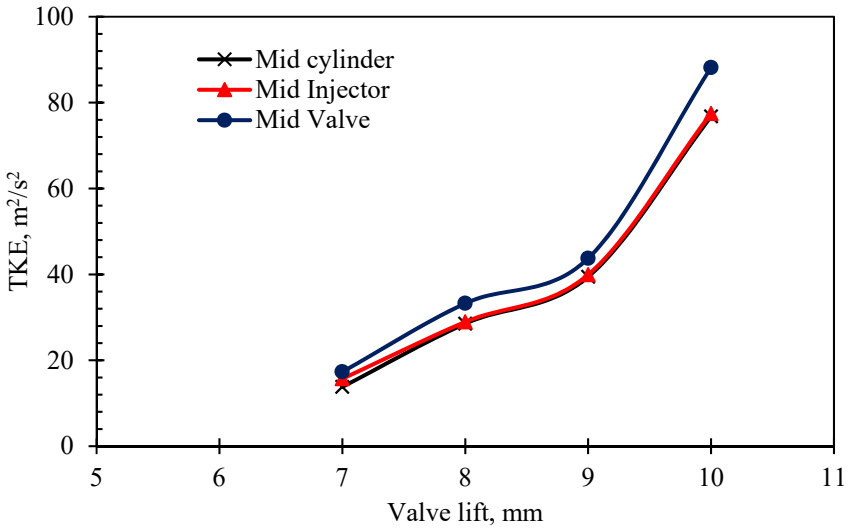


Figure 4.12: TKE at different measurement tumble planes

*4.3.2.4 Tumble Ratio Distribution in the Different Measurement Planes*

Figure 4.13 shows the tumble ratio calculated from both the angular momentum and the curl of the vector fields in different measurement tumble planes. It is clear from the figure that both methods followed the same trend of tumble ratio. The tumble ratio magnitude increased with increasing the valve lift indicating an improvement in the overall in-cylinder air motion. It can be noticed that the high fixed values of tumble ratio for all planes especially at the highest valve lift (10 mm) generated an outstandingly good tumble pattern as the vortex occupied the entire cylinder volume and high velocities were generated. Nevertheless, the lower values of tumble ratio generated for valve lift 7mm could be attributed to the fact that at this valve lift the tumble vortex started to form especially at the mid-valve plane which had higher values of tumble ratio compared to the other planes. While the lower values of tumble ratio for valve lifts 8 and 9 mm could be attributed to the two counter rotating vortices generated because of the interaction between the jets coming from both sides of the intake valve. A counter rotating vortex had an impact on the flow pattern as it prevented the main vortex from filling the complete cylinder volume and affected the stability of the tumble pattern. In addition, the tumble level was gained by assessing the rotational speed of the paddle wheel anemometer to calculate the non-dimensional rig-tumble. It can be seen also that; the trend of non-dimensional rig-tumble values were the same as the average values of tumble ratio calculated from different measurement planes. The difference between both curves might be related to the fact that for PIV, the values were calculated for a certain number of vertical planes in two dimensions. However, the paddle wheel result was an ‘integral’ of the three-dimensional flow structures. Furthermore, the calculation was carried out on the ensemble average values of all the velocity vector fields at each valve lift and measurement plane. Table 4.2 gives a summary of the tumble ratios calculated form both the curl of the vector field and the angular velocity at different measurement tumble planes side by side with the non-dimensional tumble rig measured on the steady-state tumble rig (the paddle wheel rotation).

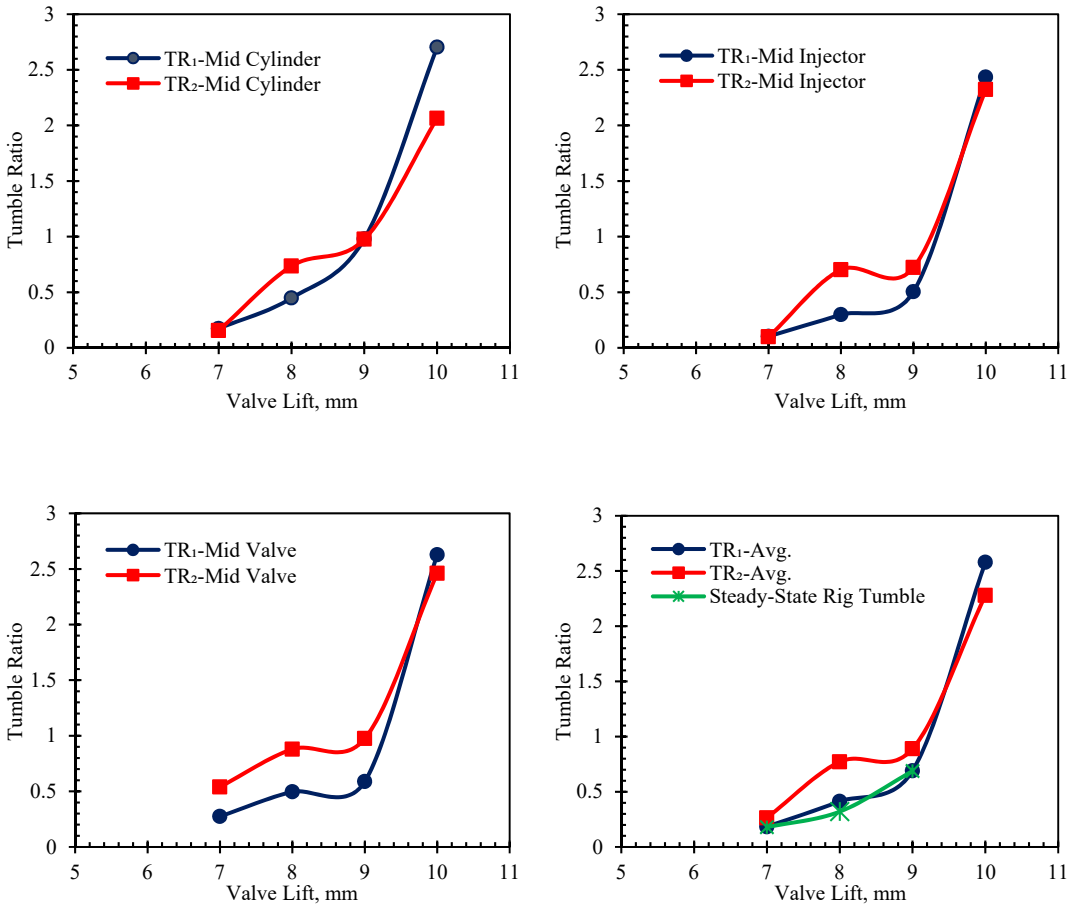


Figure 4.13: Tumble ratios calculated from both the curl of the vector field and the angular velocity at half bore below the cylinder head

Table 4.2: Tumble ratios calculated from both the curl of the vector field and the angular velocity at half bore below the cylinder head

| Pressure Difference [mmH₂O] | Measurement Plane | Valve Lift [mm] | PIV Tumble Ratio | |
|---|---|---|---|---|
| | | | TR1 | TR2 |
| 150 mmH₂O | Mid Cylinder | 7 | 0.173 | 0.154 |
| | Mid Injector | | 0.103 | 0.098 |
| | Mid Valve | | 0.274 | 0.540 |
| | Average for Planes | | 0.183 | 0.264 |
| | Steady-State Rig Tumble | | 0.179 | |
| | Mid Cylinder | 8 | 0.447 | 0.735 |
| | Mid Injector | | 0.298 | 0.702 |
| | Mid Valve | | 0.496 | 0.878 |
| | Average for Planes | | 0.413 | 0.771 |

| | | | | |
|---|---|---|---|---|
| | **Steady-State Rig Tumble** | | **0.320** | |
| | **Mid Cylinder** | **9** | 0.979 | 0.976 |
| | **Mid Injector** | | 0.503 | 0.721 |
| | **Mid Valve** | | 0.588 | 0.975 |
| | **Average for Planes** | | **0.69** | **0.890** |
| | **Steady-State Rig Tumble** | | **0.688** | |
| | **Mid Cylinder** | **10** | 2.70 | 2.06 |
| | **Mid Injector** | | 2.43 | 2.32 |
| | **Mid Valve** | | 2.62 | 2.46 |
| | **Average for Planes** | | **2.58** | **2.28** |
| | **Steady-State Rig Tumble** | | — | |

### 4.3.3 The effect of Pressure difference

Stereoscopic PIV measurements for the mid cylinder vertical plane (plane of symmetry) at different valve lifts 2mm, 5mm and 10 mm were carried out at different pressure differences across the intake valves 300, 450, and 600 mm$H_2O$. The effect of pressure difference on in-cylinder flows, which was characterized by the ensemble average, vorticity, TKE and TR, obtained from PIV experiments is presented in the next sections.

#### *4.3.3.1 Effect of Pressure Difference on Flow Structures*

Figure 4.14 shows the ensemble average velocity vector fields at different pressure differences across the intake valves for different valve lifts. The first observation which can be made is that increasing the pressure difference across the intake valves led to an increase in air flow rate into the cylinder, and subsequently an increase in air velocities. The maximum velocity approximately correlated well with the Bernoulli calculations for the maximum inlet velocities; for 300 mm$H_2O$ case was (72 m/sec), for 450 mm$H_2O$ case was (90 m/sec), and for 600 mm$H_2O$ case was (102 m/sec). At low valve lift (2 mm), the flow was highly restricted at the area between the valve and valve seat. The restriction was more pronounced on the right side of the intake valves because of the orientation of the intake port which resulted in high pressure drop across the intake valves. Therefore, a significant amount of the incoming flow was directed towards the exhaust side because of its inertia and the highly restricted area. Then because of the

low-pressure area under the intake valves the flow moved from the exhaust side to the intake side and then was deflected by the right cylinder wall and the flat piston surface forming a clock-wise vortex (reverse-tumble). At mid valve lift (5 mm), the problems associated with the restriction became less and it was clear that there was a symmetrical velocity distribution between both jets coming from both sides of the intake valves. These symmetrical distributions led to no-tumble motion at this valve lift. At high valve lift (10 mm), the left-hand side air jet was more dominant. Because of the interaction of this jet with the combustion chamber walls and the left cylinder wall then with flat piston, the in-cylinder flow was dominated by a well-defined strong counter-clock-wise vortex (tumble). It was reported that a well-defined tumbling single vortex is more stable than any other large scale in-cylinder flow structures which may break up by the end of compression stroke into small scale structures increasing the level of turbulence during the combustion [166]. Furthermore, in case of comparing the data for the same valve lift but for different values of pressure difference, the effect of the pressure difference on the flow behaviour was negligible compared to the effect of valve lift. This meant that the mean motion was much more dependent on the valve lift than the pressure difference across the intake valves. This is consistent with the work of experimental and numerical studies of Soder *et al.* [167] and Vernet *et al.* [168] which proved that the value of the pressure drop does not influence the flow structures in the cylinder. This was highly required since it ensured the same flow structures for all engine speeds.

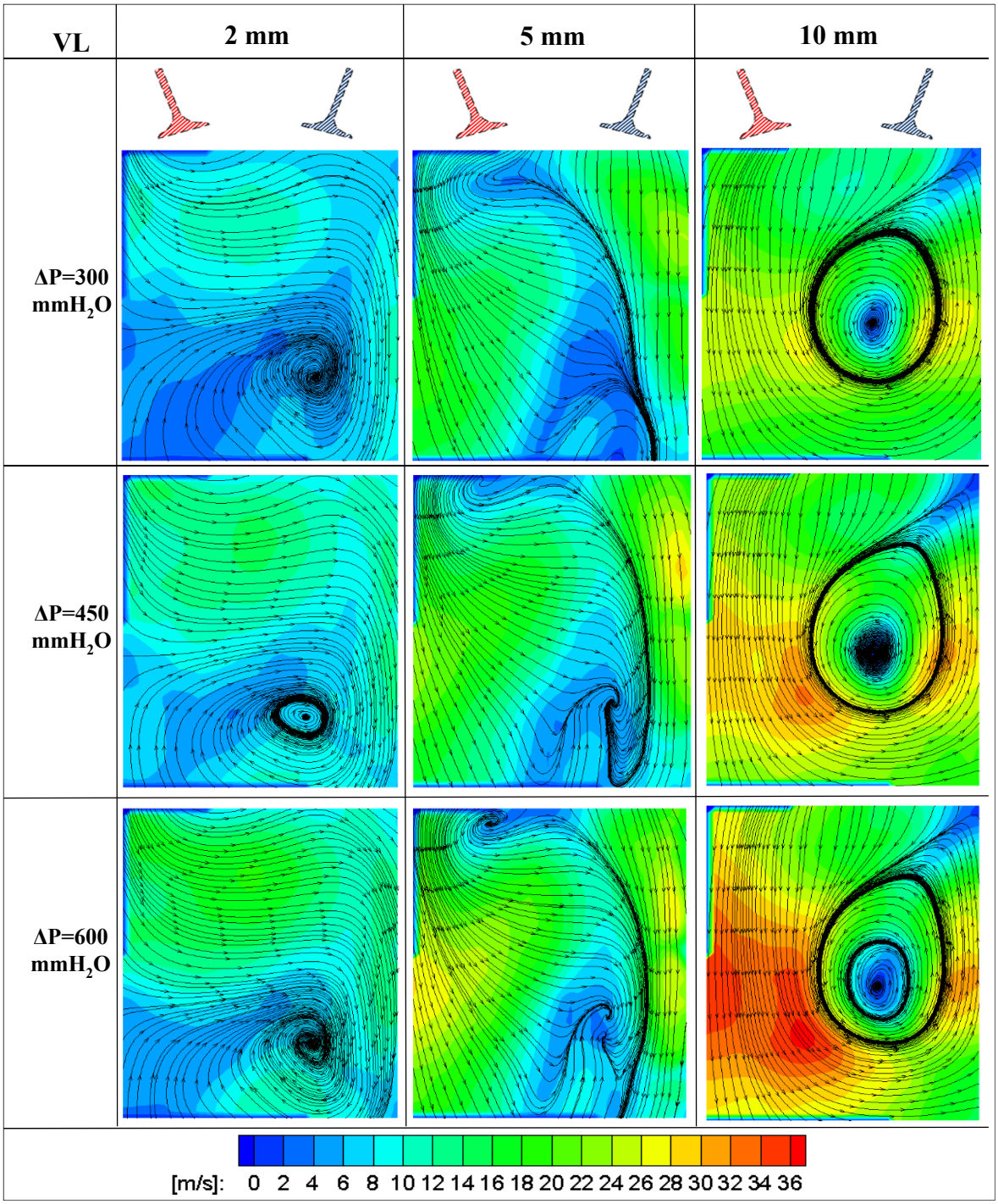


Figure 4.14: Ensemble average flow fields at different valve lifts and different pressure differences

#### *4.3.3.2 Effect of Pressure Difference on Vorticity Contours*

Figure 4.15 shows the variation in the vorticity contours caused by increasing pressure difference for various valve lifts. The blue area represents the flow rotation in clock-wise direction while the green area represents the flow rotation in counter clock-wise direction. As can be seen, the formed vortices preserved their shape for the same valve lift for different pressure differences. The only difference in all cases was that the vortex strength increased with increasing the pressure difference. It was also noticed that at 2 mm valve lift, the dominant feature was the reverse tumble motion in the clock wise direction. At 5 mm valve lift, there was a balance between tumble and reverse tumble motions. However, at 10 mm valve lift, a strong tumble vortex dominated the in-cylinder flow.

#### *4.3.3.3 Effect of Pressure Difference on Turbulent Kinetic Energy*

Figure 4.16 shows the variation of the turbulent kinetic energy (TKE) with valve lift for different pressure differences. Generally, the TKE increased with increasing the valve lift and pressure difference as more mass of air entered to the cylinder. However, it was noticed that, the rate of increase was higher from 5 mm to 10 mm valve lifts compared to the rate of increase from 2 mm to 5 mm valve lifts for all pressure differences. This might be attributed to the fact that, the increase in intake valve opening led to higher velocity of the air jet entering the cylinder, which had high mean and fluctuating velocity components. It was found also that the TKE increased by about 36.7 % and 10.7 % for valve lift 9 mm when the pressure difference increased from 300 to 450 mm$H_2O$, and from 450 to 600 mm$H_2O$ respectively.

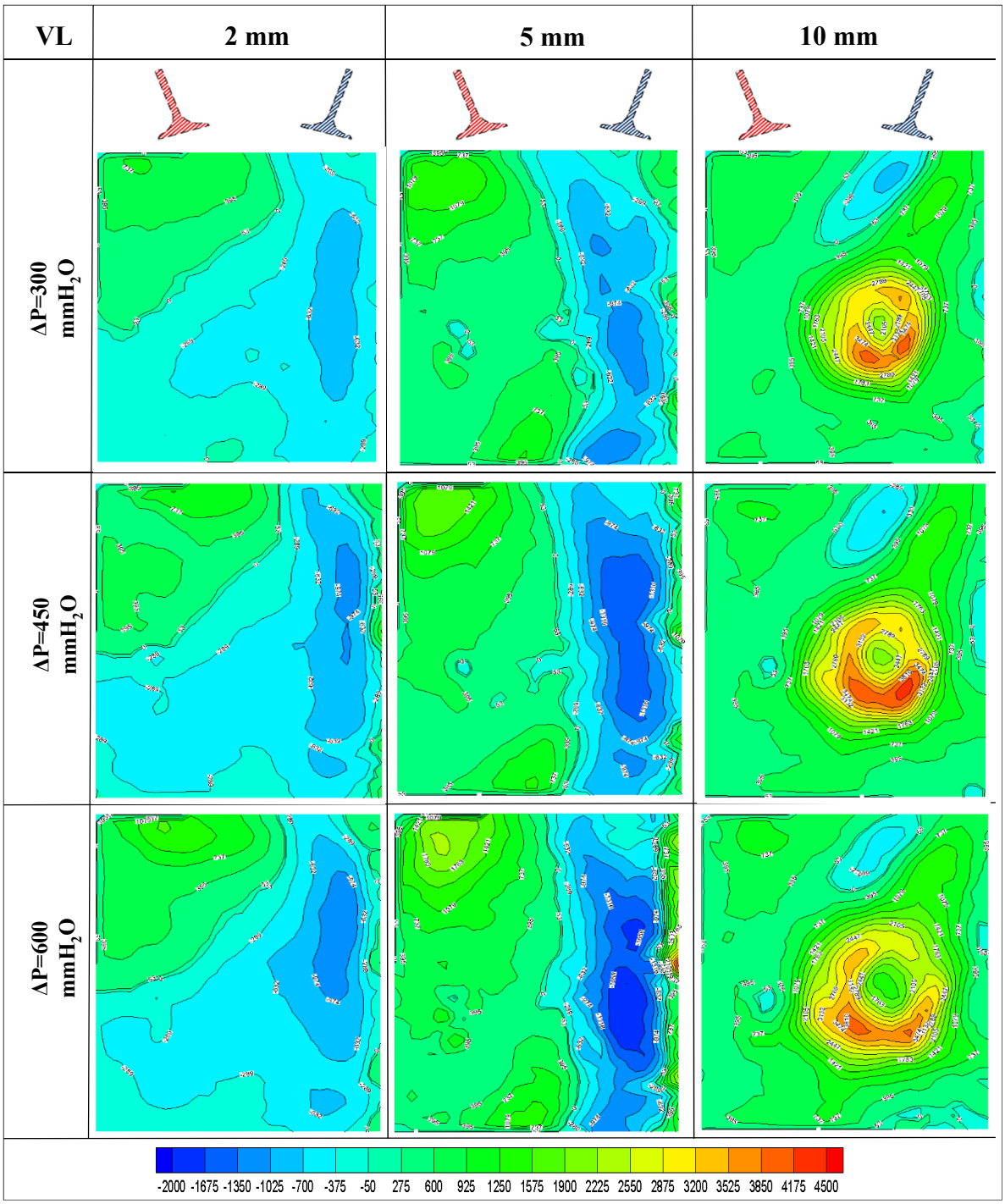


Figure 4.15: Vorticity magnitudes at different valve lifts and different pressure differences

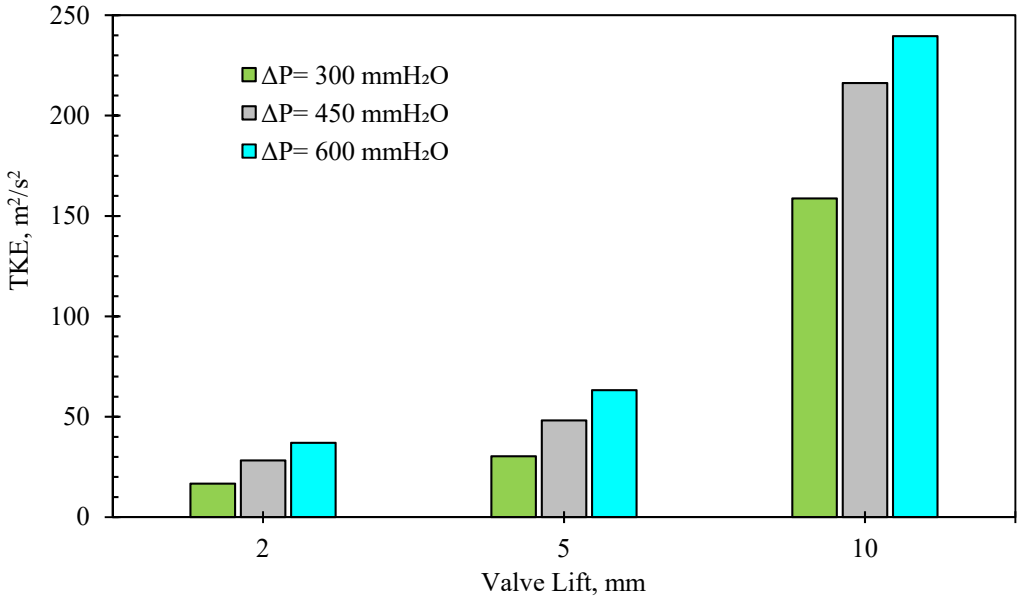


Figure 4.16: TKE at different valve lifts and pressure differences

*4.3.3.4 Effect of Pressure Difference on Tumble Ratio*

The tumble ratio (TR) was calculated at different valve lifts for different pressure differences using two methods. The $TR_1$ was calculated from the angular momentum. Whilst, the $TR_2$ was calculated from the plane averaged vorticity considering the rotation of the vertical and horizontal velocity components of a particle about the center of the field of view. Figure 4.17 shows the evolution of the tumble ratio at various valve lifts and different pressure differences. Generally, the tumble ratio calculated from both methods followed the same trend. It can be seen that the tumble ratio and therefore the mean motion was much more dependent on the valve lift than on the pressure difference. This is highly desirable since it guarantees the same flow structures for all pressure differences and subsequently for all engine speeds. This is consistent with the work of both Krishna [14] and Zhang [30]. It can be also noticed that at valve lift 2 mm, the negative values of tumble ratio were an indication of the reverse tumble motion in the clock-wise direction. However, at 5 mm valve lift, the symmetrical velocity distribution led to almost no tumble motion inside the cylinder therefore, the tumble ratio value was around zero. The positive values of tumble ratio at 10 mm valve lift,

were an indication of the strong normal tumble motion in the counter clock-wise direction.

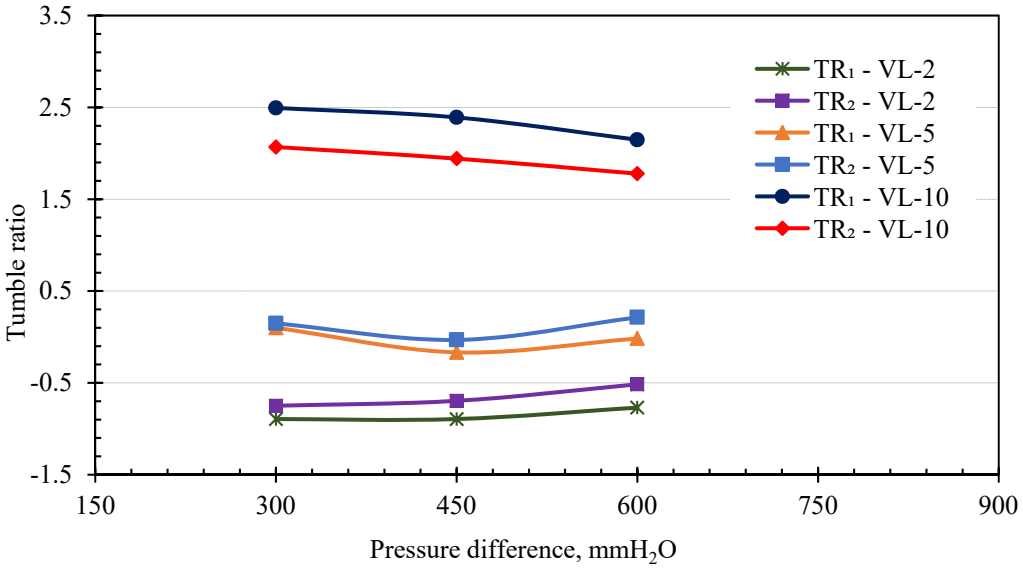


Figure 4.17: Evolution of the tumble ratio as a function of the pressure difference and the valve lift

## 4.4 Proper Orthogonal Decomposition (POD) Results

As illustrated in the previous chapter, the POD decomposes a set of velocity distributions (snapshots) with total number of (K) into a linear combination of (M) spatial basis functions or space-dependent POD modes, (denoted $\varphi_m$) and their corresponding time-dependent coefficients, (denoted $C_m^{(k)}$). First of all, proper orthogonal decomposition was applied to a sample of synthetic velocity vector fields with known characteristics to gain more physical understanding about the fundamental properties and the important features of POD. These synthetic velocity vector fields were extracted from the stereoscopic PIV measurements however; they were arranged in a particular manner in order to extract some important features regarding POD implementation. After that, POD was conducted on the datasets acquired at different valve lifts and different pressure differences. The aim was to extract the most energetic structures and study the evolution and variation of the in-cylinder air flow under theses experimental conditions.

### 4.4.1 Interpretation of POD of Synthetic Flow Fields

#### *4.4.1.1 POD of Repeated Identical Flow Structures*

Figure 4.18 shows how the energy of identically repeated flow structures was captured and distributed among the POD modes or (basis functions). One velocity vector field, showing the counter clock-wise tumble motion at valve lift 10 mm, was repeated in 100 snapshots. Consequently, 100 modes resulted without subtracting the ensemble average prior to performing the POD on the data set. This example demonstrated two main properties of POD. Firstly, it is well known that each POD mode comprises elements of all flow structures from all input snapshots therefore for this example mode 1 ($\varphi_1$) was enough to capture the same structures as the original snapshots having 99.99 % of total energy, as shown in Figure 4.19 and the other modes contained just noise. It could be concluded also that only the first mode was sufficient to reconstruct the physical flow structures. Secondly, as the same structure was repeated in all snapshots, the magnitude of coefficients for a specific POD mode which illustrated to what extent this mode was dominant for a particular snapshot was distributed equally between all snapshots, as shown in Figure 4.20.

For mode 1 coefficients, the values were identical and all positive, meaning that mode 1 was dominant in all snapshots and the positive values indicated that structures captured by mode 1 were in the same direction as the original snapshots. For mode 2 coefficients, they were all also similar but with negative values meaning that structures captured by mode 2 were in the opposite direction compared to the original snapshots.

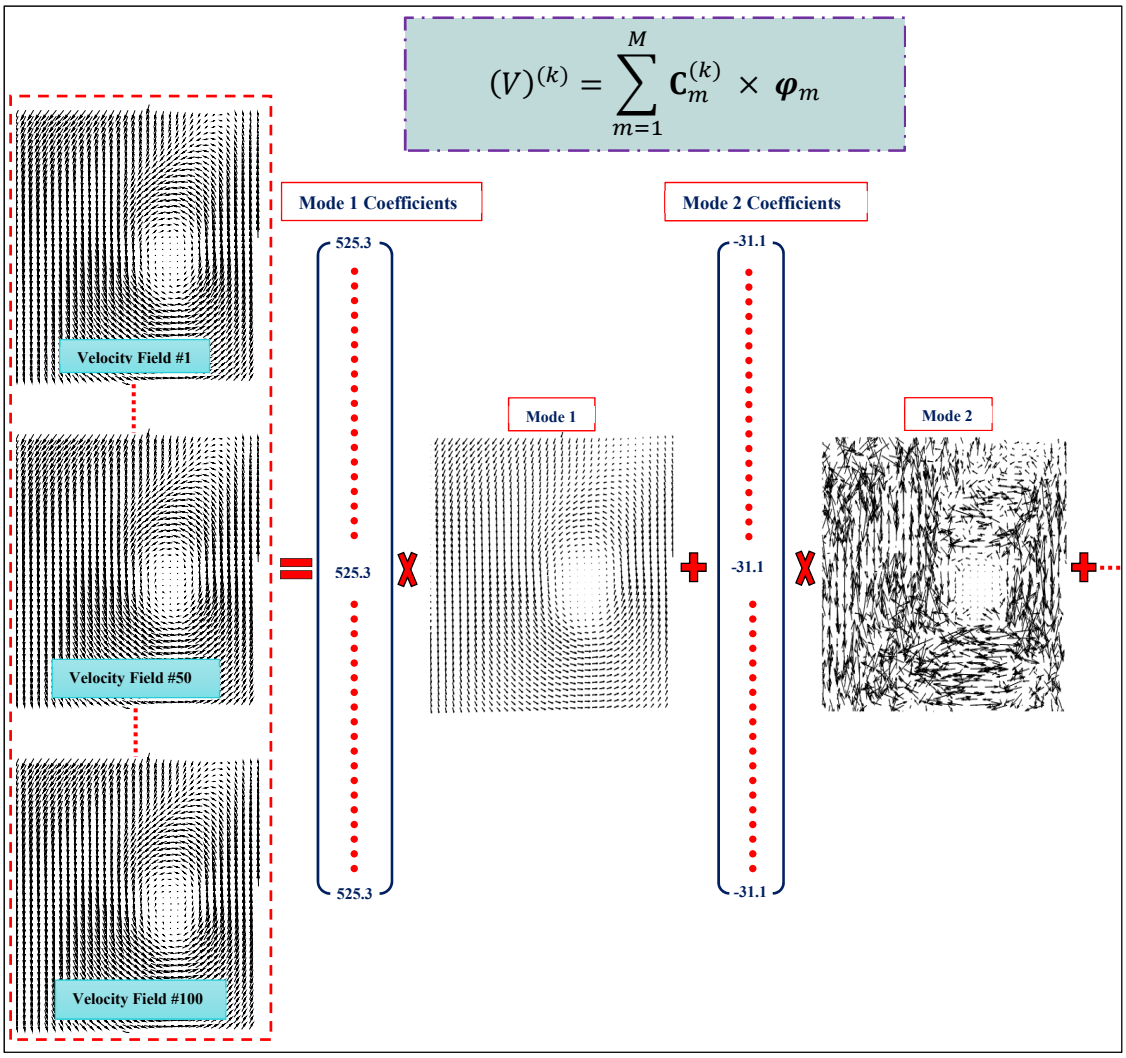


Figure 4.18: Illustration of POD for repeated identical flow structures

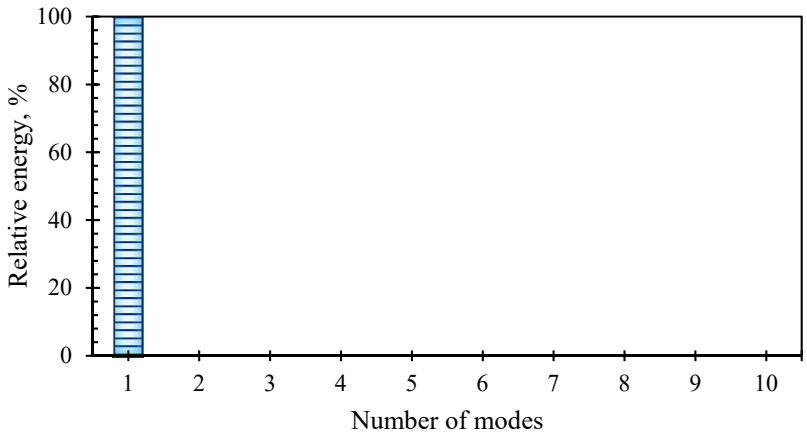


Figure 4.19: Kinetic energy fraction captured by the first 10 POD modes

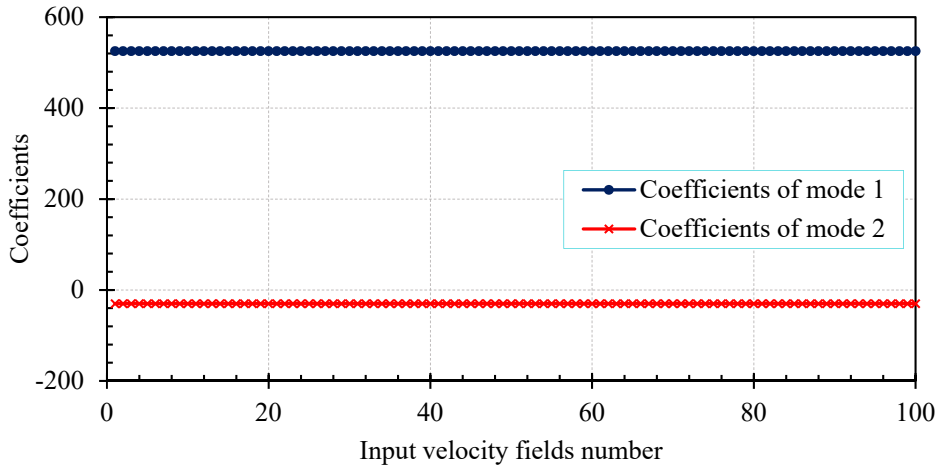


Figure 4.20: Coefficients of first two POD modes for all 100 input velocity fields

*4.4.1.2 POD Mode Capture of Coherent Structures*

Figure 4.21 reveals how coherent structures were captured and distributed throughout the POD modes. One velocity vector field contained the weakest structures, showing the reverse tumble motion in the clock-wise direction, was repeated at the same location and with the same orientation in 50 snapshots which had a total kinetic energy of 2,003,133 $m^2/s^2$ (40062.67 $m^2/s^2$ per one velocity field). Another velocity vector field contained the most energetic structures, showing a strong tumble motion in the counter clock-wise direction, was repeated at the same location and with the same orientation in 50 snapshots which had a total kinetic energy of 23,368,755 $m^2/s^2$ (467375.1 $m^2/s^2$ per velocity field). Consequently, 100 snapshots were created as the input velocity vector fields and resulted in 100 modes without subtracting the ensemble average prior to performing the POD on the data set. As can be seen from the figure, mode 1 ($\varphi_1$) captured only the structures which had the maximum kinetic energy found in the last 50 velocity fields $V^{(51-100)}$ comprising 92.5 % of total energy, as shown in Figure 4.22. Then mode 2 ($\varphi_2$) captured the structures found in the first 50 snapshots $V^{(1-50)}$ which had the lowest kinetic energy comprising 7.3 % of the total energy. The coefficients of the first two POD modes for all snapshots are listed in Figure 4.23, which reveals the magnitude and sign by which each mode was scaled. The coefficients of the first mode

$C_1^{(k=51-100)}$ were similar, positive and large for all k's since $V^{(51-100)}$ contained the strongest structures and almost all their energies were captured by mode 1 ($\varphi_1$).

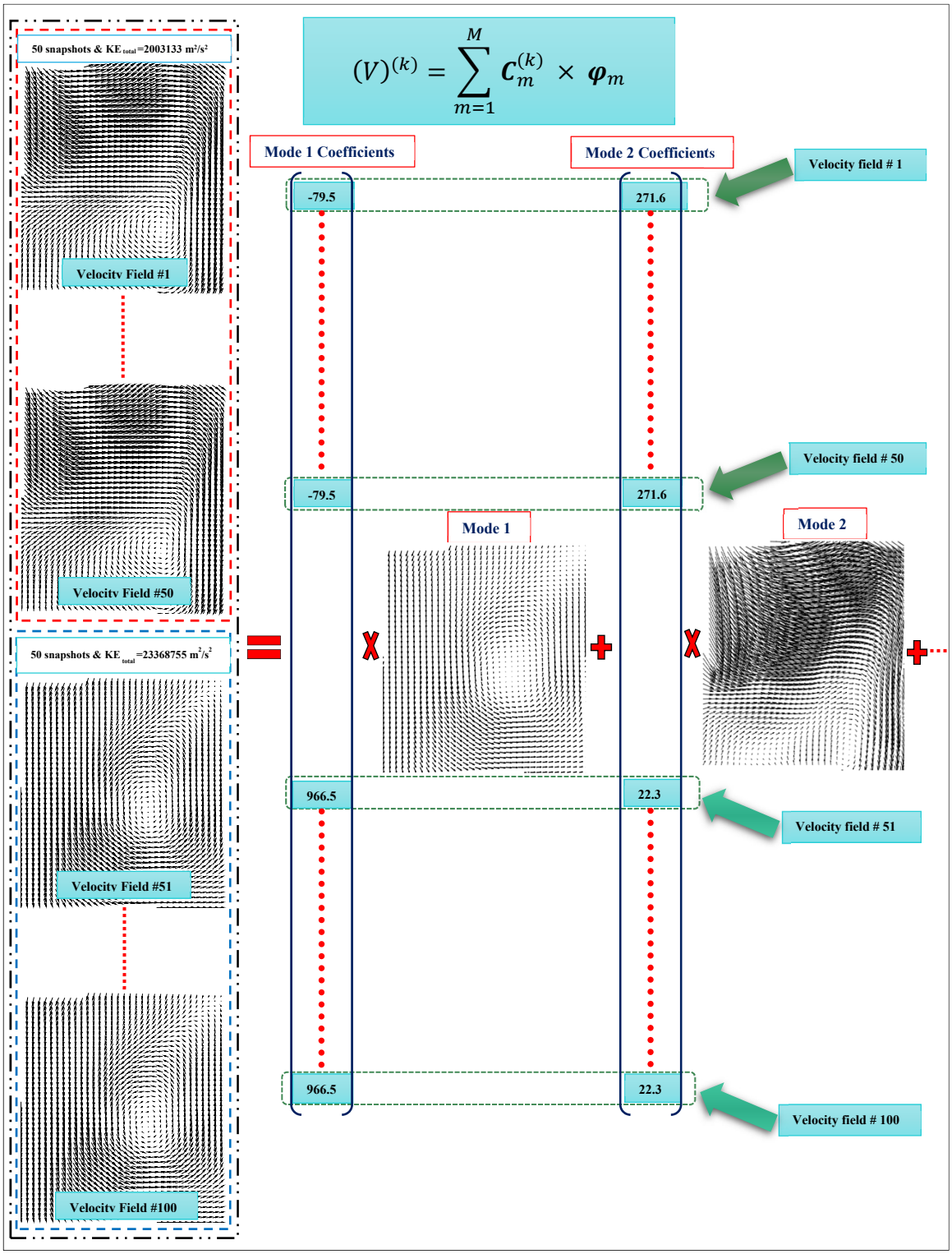


Figure 4.21: Illustration of POD for capturing of coherent structures

While on the other hand, the coefficients of the second mode $C_2^{(k=51-100)}$ were almost zero since they did not exist in $V^{(51-100)}$. Similar insight could be gained by analysing the behaviour of the coefficients of the second mode $C_2^{(k=1-50)}$. This example also demonstrated an important feature of POD about the snapshot-to-snapshot difference which could be captured by the corresponding coefficients. This principle was considered as a key factor for the quantitative study of cycle-to-cycle variation in real engine flow.

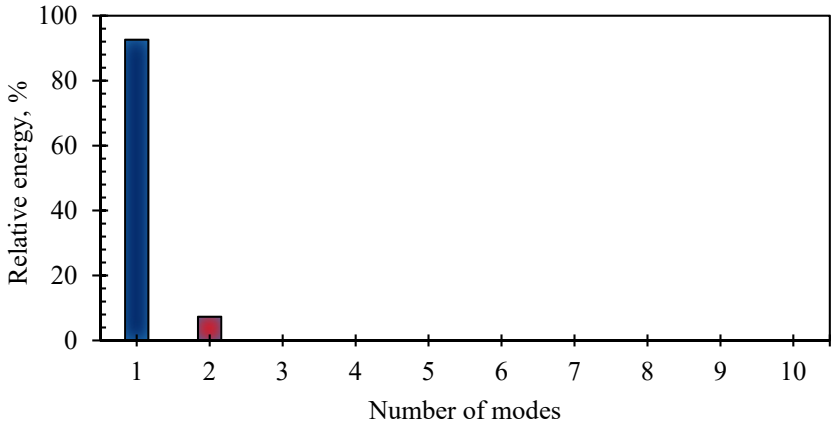


Figure 4.22: Kinetic energy fraction captured by the first 10 POD modes

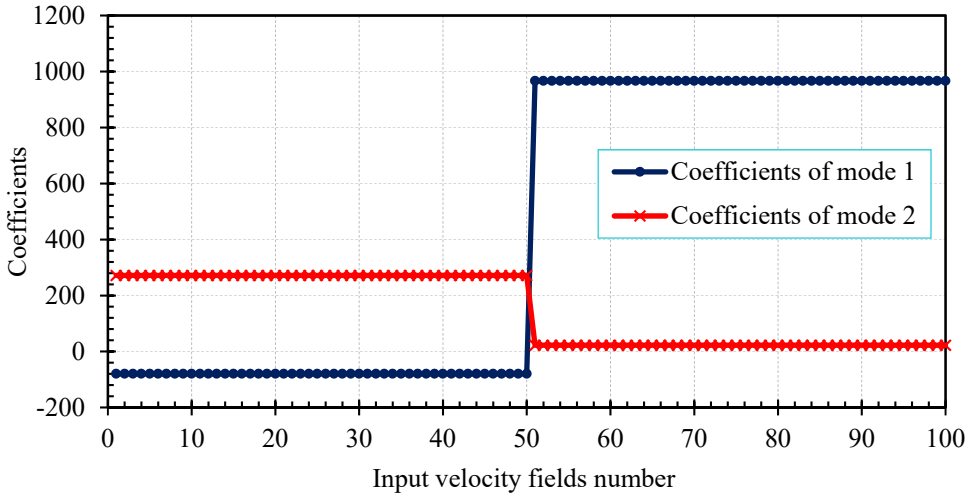


Figure 4.23: Coefficients of first two POD modes for all 100 input velocity fields

*4.4.1.3 POD and the RANS Turbulence*

The aim of this example was to reveal to what extent subtracting or not subtracting the ensemble average prior to performing the POD analysis on a data set was effective. This included a complete comparison between flow patterns of the POD modes derived with and without subtracting the ensemble average. In this example, a 200 instantaneous velocity vector fields ($K$=200) at valve lift 9 mm and 150 mm$H_2O$ pressure difference were used to reveal properties of the POD modes in this case.

**a) The ensemble Average and the First POD Mode Relationship**

Figure 4.24 compares the spatial structures of both mode1 ($\varphi_1$) created from the original velocity vector fields, $V$, and the ensemble average, $\langle V \rangle$. It can be noticed that the flow pattern of the first mode was an excellent estimate of the flow pattern of the ensemble average and had the same direction. This gave an expectation that the coefficients would be positive. The kinetic energy content of both the ensemble average and POD mode 1 are compared in Table 4.3.

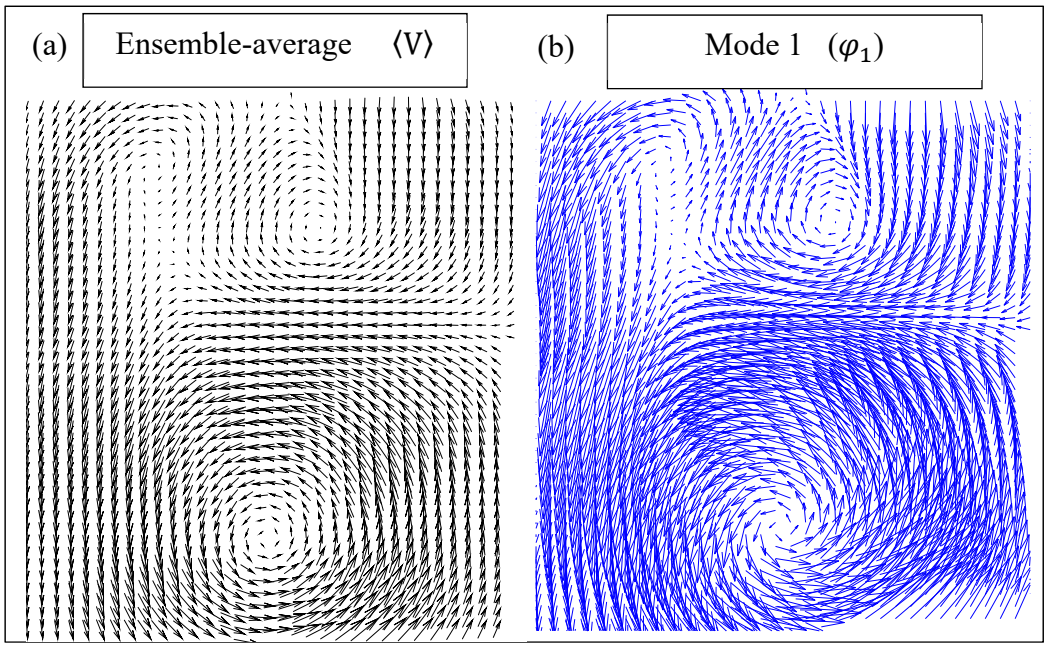


Figure 4.24: Ensemble average $\langle V \rangle$ and mode1 ($\varphi_1$) spatial structures without subtracting the mean prior performing POD

Mode 1 kinetic energy ($KE_1$) was calculated from the coefficients ($\frac{1}{2}(\mathbf{C}_1^{(k)})^2$) and divided by $K$=200 to provide the ensemble average value. It can be seen that the energy content of the first mode was almost equal to, but slightly larger than, that of the ensemble average value. Consequently, the combination of (a) the flow-pattern equivalency of ⟨V⟩ and $\varphi_1^V$ and (b) the approximate equivalency of the energy content led to the conclusion that the first POD mode $\varphi_1^V$ was an excellent estimate of, but not identical to, the ensemble average ⟨V⟩.

Table 4.3: Energy comparison of Reynolds decomposition and POD with and without subtracting the ensemble average

| | | KE | % ⟨*V*⟩ | % rms |
|---|---|---|---|---|
| **Reynold decomposition** | **⟨KE⟩** | 60442.3 | 100 | |
| | **$KE_{rms}$** | 27944.62 | | 100 |
| **POD on original velocity** | **$KE_{total}$ / *K*** | 88376.4 | | |
| | **$KE_1$/ *K*** | 60692.75 | 100.3 | |
| | **$KE_2$ / *K*** | 2818.4 | | |
| | **$KE_{2\text{-}200}$ / *K*** | 27683.65 | | 49 |
| | **$ke_1$** | 0.69 | | |
| **POD after subtracting the ensemble average** | **$KE_{total}$ / *K*** | 27944.62 | | 100 |
| | **$KE_1$/ *K*** | 2821.961 | | |
| | **$ke_1$** | 0.1 | | |

### b) POD and RANS Turbulence

Taking the conclusion of the previous section, it was reasonable to deduce that the modes from 2 to K ($K$=200) contained an estimate of the kinetic energy of the RANS turbulence, $K_{rms}$. Accordingly, subtracting the ensemble average from the instantaneous velocity vector fields (snapshots) prior to performing the POD, would, by definition, contain only the RANS turbulence. Thus, one can expect that, the flow pattern of $\varphi_m^{V-\langle V\rangle}$ and $\varphi_{m+1}^V$ will be identical in case of the flow patterns of the ensemble average and

mode 1 were identical. Figure 4.25 shows the spatial structures of POD modes with and without subtracting the mean. The visual comparison of the patterns of the modes showed that they were not identically equivalent because of the flow structures of mode 1 was not identical to the flow structures of the ensemble average. Moreover, as expected from energy conservation, Table 4.3 illustrated that $KE_{total}$ / K of $V - \langle V \rangle$ was almost equal to the RANS turbulence, Krms. Also, the $KE_1$/ $K$ of $V - \langle V \rangle$ was nearly 10 % of $KE_{total}$ / $K$ signifying that a large number of POD modes would be essential in order to reconstruct the most energetic structures of the Reynolds turbulence.

Figure 4.26 (a) & (b) shows the relative energy spectra and absolute energy spectra computed using equations ($KE_m = \frac{1}{2}\sum_{k=1}^{K}(C_m^k)^2$) and ($Ke_m = KE_m/KE_{total}$ ). It can be observed that, the shape of the energy curves for both energy fraction and absolute energy were quite insensitive to subtracting or not subtracting the ensemble average prior to implementing the POD on the dataset. The biggest change was that the Kinetic energy of mode 1, $KE_1$ for (V) was dominant and contained the main part of the total energy (70% in the current example). As a result, there was just an offset in the energy fraction and absolute energy at mode 1 (m =1) for V and $V - \langle V \rangle$ whereas for higher modes (m >1), the shapes of the energy curves were identical as shown in the Figures. Moreover, the cumulative energy curve shown in Figure 4.26 (c) reveals that prior to subtracting the mean, mode 1, ($\varphi_1^V$), contained 70 % of the energy whereas after subtracting the mean over 30 modes was required to capture 70 % of the total kinetic energy ($KE_{total}$) in case of $V - \langle V \rangle$.

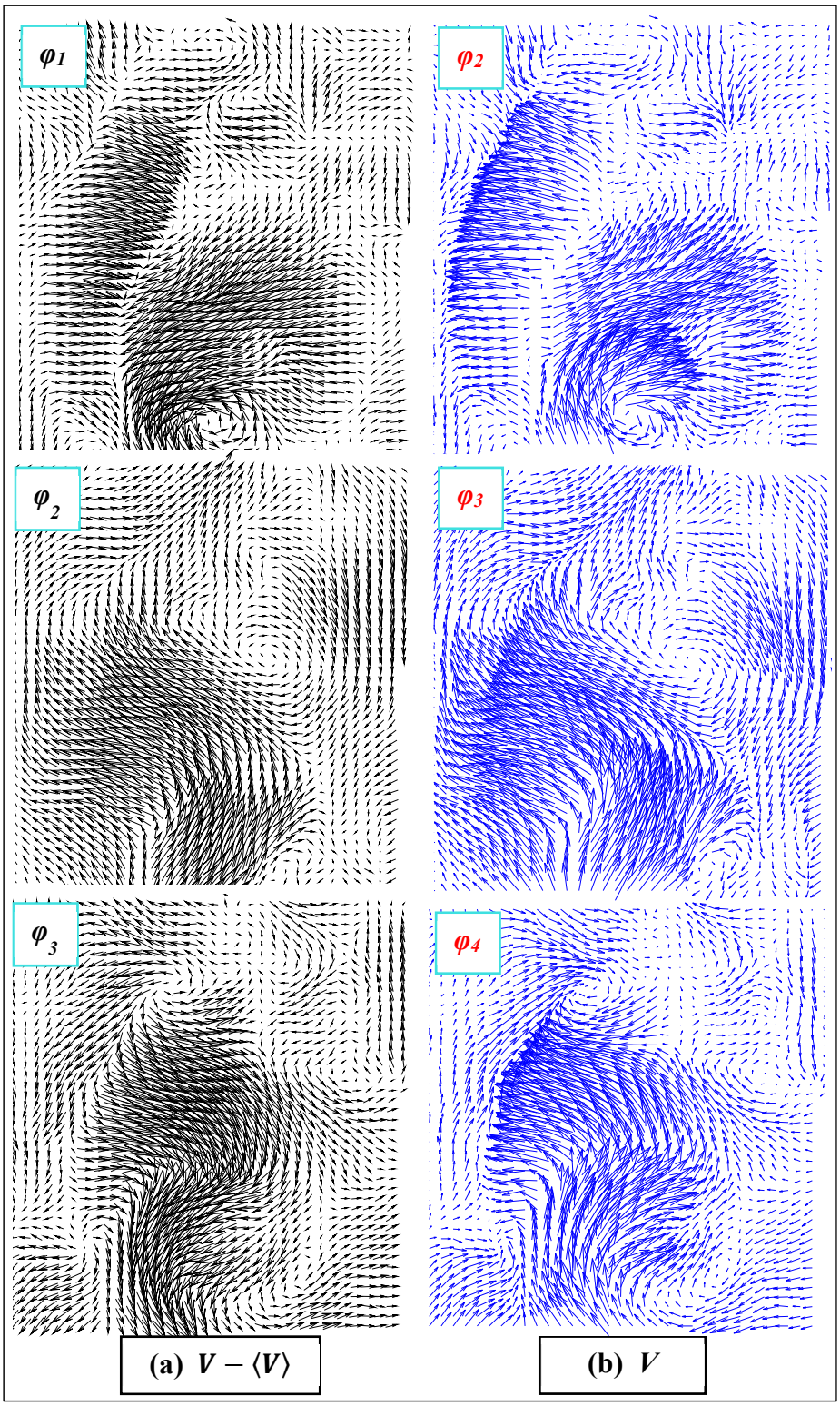


Figure 4.25: POD modes (a) after subtracting the ensemble average, $V - \langle V \rangle$, (b) without subtracting the ensemble average, $V$

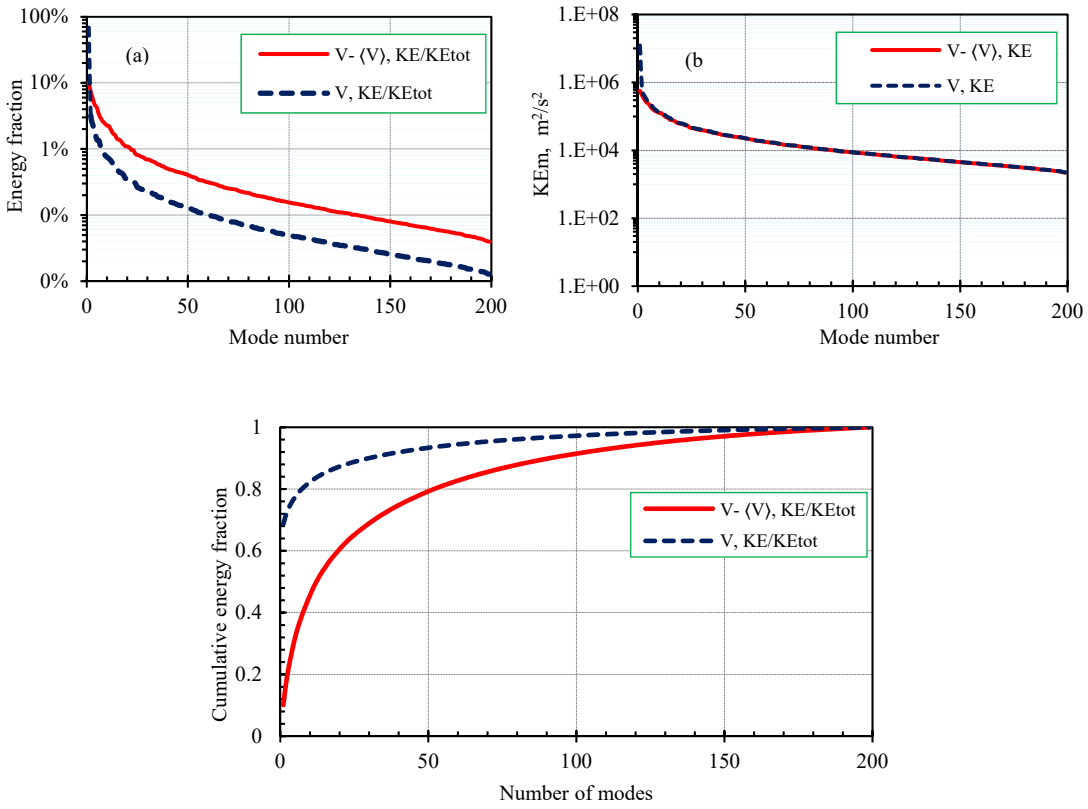


Figure 4.26: Energy distribution curves for V and V- ⟨V⟩ cases, (a) energy-fraction, (b) absolute energy and (c) cumulative energy

### 4.4.2 Evaluation of the Effect of Valve Lift using Phase-Invariant POD

It is significantly important to quantitatively understand how the in-cylinder flow varied and evolved at different valve lifts. Therefore, a large dataset of 5000 velocity vector fields (snapshots) with the same grid size (same number of vectors) from different valve lifts from 1 mm to 10 mm (500 snapshots per valve lift) were arranged to be in one input file. The data was then analysed by using phase-invariant POD to extract the most energetic and organized coherent structures. In this manner, the POD modes could be used to describe the flow structures at any valve lift while their corresponding coefficients could be used to demonstrate the flow evolution.

*4.4.2.1 POD Energy Spectra*

Figure 4.27 presents the energy fraction captured by the first 20 POD modes in order to determine the contribution of each mode to the original flow field. It can be seen that the first three modes together extracted about 74 % of the total kinetic energy from all 5000 input velocity vector fields. The first mode alone contained 44.5 % of the total energy and the second mode contained 18.2 %. As shown in the energy graph, the energy level decreased at higher order modes showing the presence of small-scale structures which may not contribute much in the dynamics of the flow. Subsequently, only the first three POD modes of the flow patterns are discussed in this section.

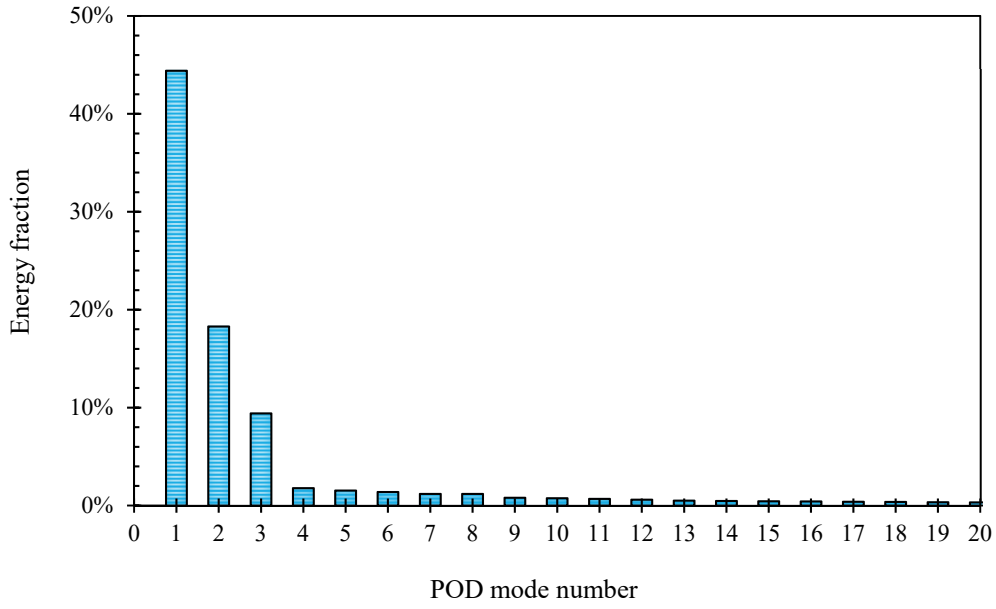


Figure 4.27: Energy fraction captured by first 20 proper orthogonal decomposition modes

*4.4.2.2 POD Mode Structures and their Corresponding Coefficients*

Figure 4.28 (a) shows the flow patterns of the first POD mode and its corresponding coefficients at different valve lifts. As can be seen from the figure, each POD mode contained a particular physical flow structure, while the magnitude of the time-dependent coefficients for a specific POD mode illustrated to what extent this mode was dominant for every snapshot. The first mode captured the two intake air jets coming

into the cylinder through the right and left sides of the intake valves, as emphasised by the arrows. It can be also noticed from the figure that, the difference in the intake jet intensity between the right and left sides and how the left side was more dominant. The left intake jet was stronger than the right. This was attributed to the fact that; the large-scale tumbling motion is generally achieved firstly by restricting the flow rate on the outer side of the intake valves (right side) and using straight ports oriented in such a way that most of the annular jet exiting the intake valves is directed towards the exhaust side. Two observations were extracted from Figure 4.28 (b); firstly, the positive values of all coefficients were an indication that the flow structures captured by this mode were in the same direction as the original velocity vector fields. Second, when comparing the coefficients at different valve lifts, it was clear that the coefficients increased with increasing the valve lift reaching their maximum values at valve lift 7 mm then started to decrease again at higher valve lifts. This was expected as the intensity of the intake jet increased with increasing the valve lift. The reductions in coefficients at high valve lifts 8mm, 9 mm and 10 mm were attributed to the formation of tumble motion and these valve lifts no longer had these jet-like structures.

Figure 4.29 (a) displays the flow patterns of the second POD mode and its corresponding coefficients at different valve lifts. The second POD mode captured a strong, counter-clockwise, rotating coherent structure in the lower half of the cylinder, indicating a strong positive tumble motion, as highlighted by the dashed circle. This was reasonable as at high valve lifts the left side jet interacted with the left cylinder wall then the flat piston at the bottom of the cylinder leading finally to the formation of tumble motion. Moreover, it is clear from Figure 4.29 (b) that the high valve lifts 9 mm and 10 mm were the only contributors to this flow structures. On the other hand, the coefficients remained nearly zero for the other valve lifts indicating that these valve lifts did not possess this rotating flow structures. Moreover, the rapid increase of mode 2 coefficient after valve lift 7 mm indicated that the energy contained in the intake-jet-like structure was transferred into the tumbling motion at high valve lifts.

Figure 4.30 (a) shows the flow patterns of the third POD mode and its coefficients at different valve lifts. Mode 3 mainly extracted vortical structures in the lower and upper half of the cylinder. When revising the ensemble average velocity vector fields

presented before, one could notice that these flow patterns were found only in the valve lift 8 mm, 9 mm and 10 mm cases and are confirmed here by the values of coefficients at these valve lifts.

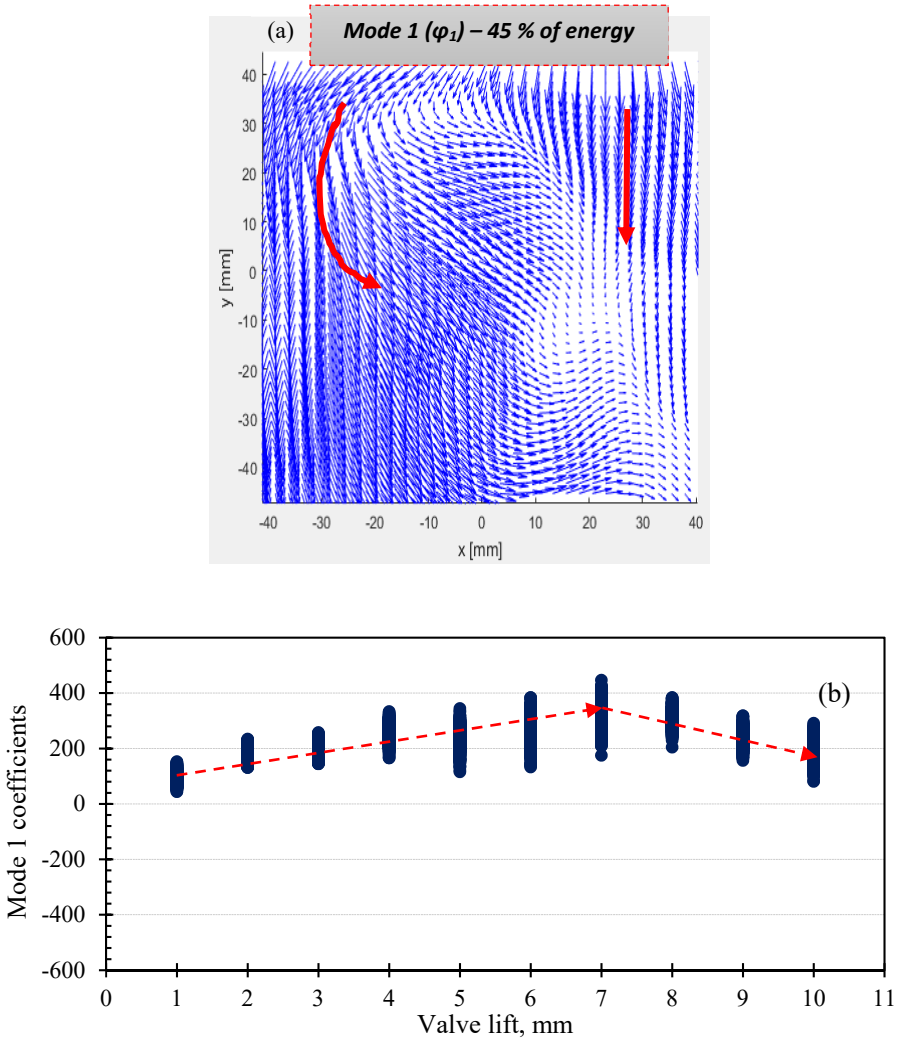


Figure 4.28: Flow patterns of the first POD mode and its corresponding coefficients at different valve lifts

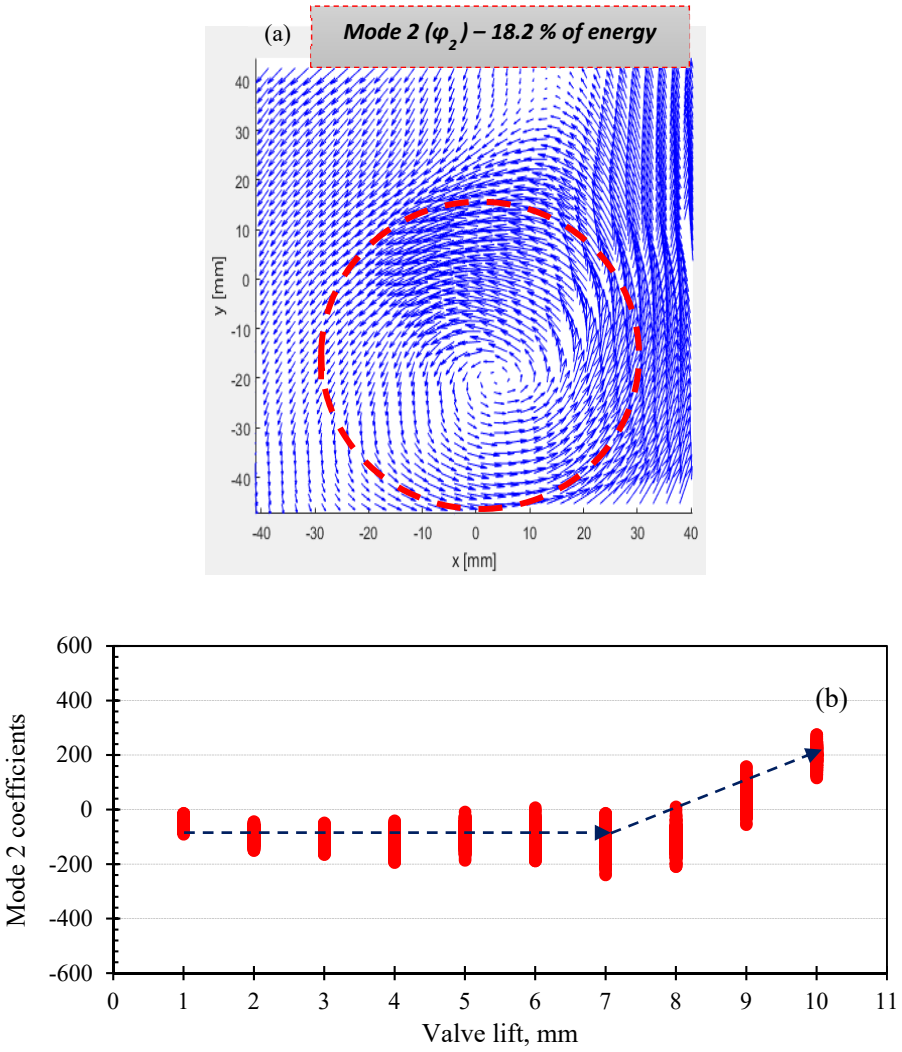


Figure 4.29: Flow patterns of the second POD mode and its corresponding coefficients at different valve lifts

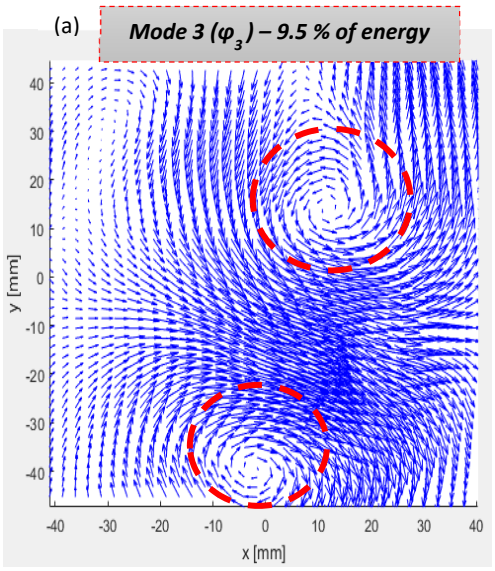

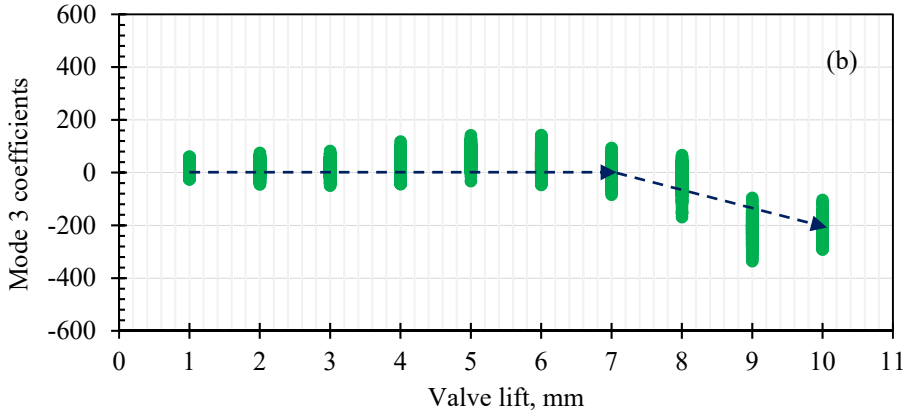


Figure 4.30: Flow patterns of the third POD mode and its corresponding coefficients at different valve lifts

In order to characterize the influence of pressure difference on flow structures, separate data sets at different valve lifts for different pressure differences were acquired in order to perform phase-dependent POD. Secondly, three data set at valve lift 10 mm for three pressure differences were combined into a single file to implement phase-invariant POD. Consequently, in this case, a single set of POD modes was created, thereby their corresponding coefficients or energies could be used to demonstrate the equivalency of these three data sets. However, for all previous cases, all data sets had the same grid size in order to create comparable modes.

### 4.4.3 Evaluation of the Effect of Pressure Difference using Phase-Dependent POD

#### *4.4.3.1 Ensemble Average versus Phase Dependent POD Modes Structure*

Figure 4.31 depicts mode 1 and mode 2 flow patterns at valve lift 10 mm for different pressure differences 300, 450 and 600 mm$H_2O$. It can be seen from the Figure, for all cases, that the flow patterns of the first mode were almost identical to the flow patterns of the ensemble average shown in section 4.3.3. This was not surprizing as the flow inside an engine cylinder under steady-state conditions could be classified as directed flow where the flow patterns of every snapshot appeared similar to the flow patterns of the ensemble average. However, one significant question remained, whether the kinetic

energy captured by the first mode was equivalent to that contained in the ensemble average or not.

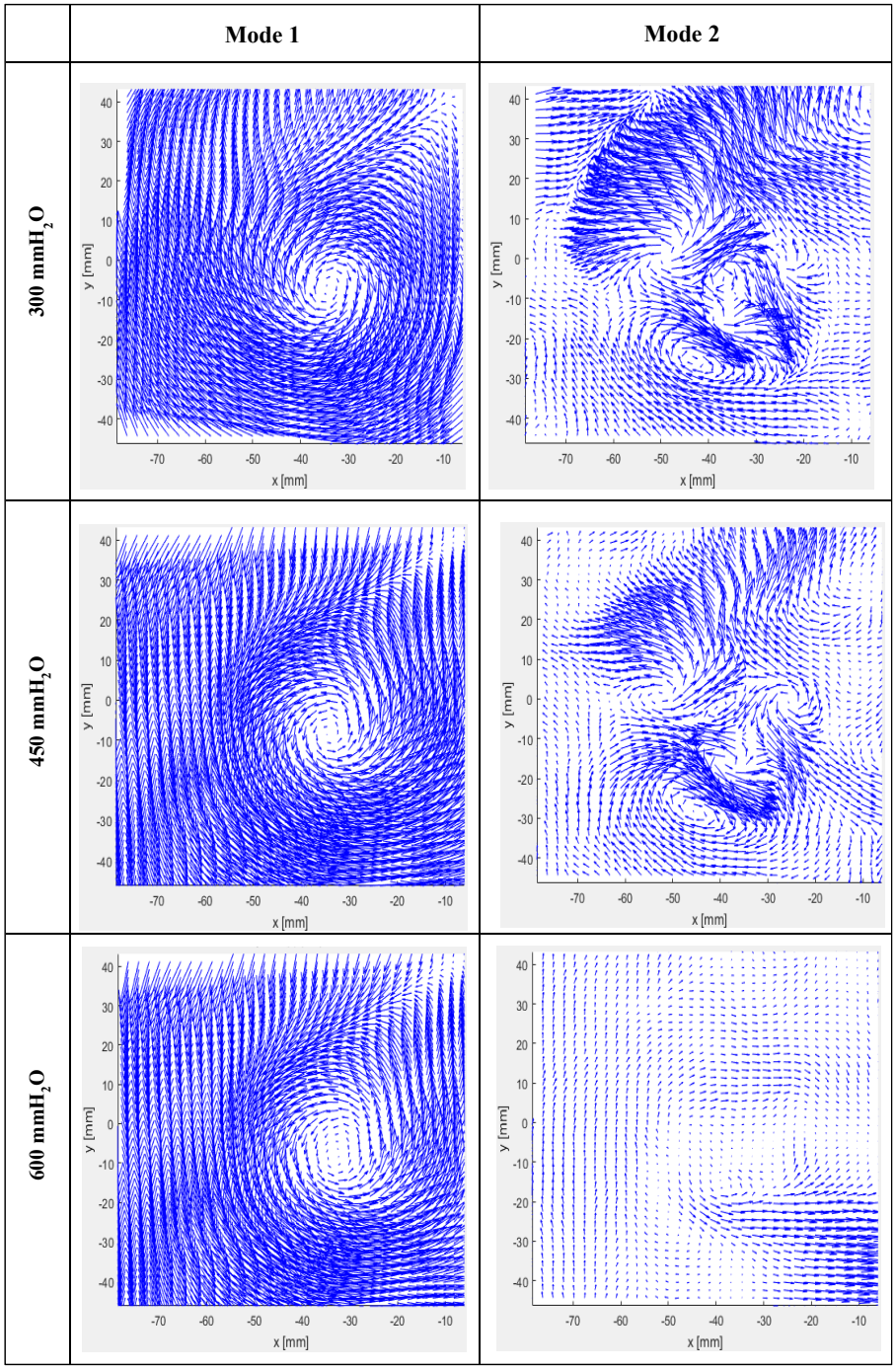


Figure 4.31: Ensemble average versus mode 1 and mode 2 at valve lift 10 mm for different pressure differences

Mode 1 kinetic energy (KE1) was calculated from the coefficients $(\frac{1}{2}(C_1^{(k)})^2)$ and divided by $K$=1000 to provide the ensemble average value. It was found that, the kinetic energy captured by mode 1 was almost equal to the kinetic energy contained in the ensemble average. For instance, Mode 1 kinetic energies were 280263 $m^2/s^2$, 395399 $m^2/s^2$ and 468565 $m^2/s^2$ while the kinetic energies contained in the ensemble average were 279680 $m^2/s^2$, 394767 $m^2/s^2$ and 467375 $m^2/s^2$ at valve lift 10 mm for pressure difference 300, 450 and 600 $mmH_2O$, respectively. Consequently, the approximate equivalency of both kinetic energy and flow patterns appearance of mode 1 and the ensemble average demonstrated that mode 1 for all pressure differences was an excellent estimate of the ensemble average. It can, therefore, be concluded that the higher modes (between 2 and 1000) represented a good estimation of the fluctuations in the in-cylinder flow structures and captured the relatively insignificant flow structures (see mode 2 in Figure 4.31) and the sum of the kinetic energy contained in these modes represented the kinetic energy of RANS turbulence [135].

#### *4.4.3.2 Energy Fraction of Phase Dependent POD Modes*

Figure 4.32 shows the energy fractions captured by the first 50 phase-dependent POD modes at different valve lifts for different pressure differences. It can be noticed that mode 1 captured 59.5 %, 59.54 % and 60.5 % at valve lift 2mm, 65.3 %, 61 % and 55.9 % at valve lift 5 mm and 86 %, 87 % and 86.4 % at valve lift 10 mm for pressure differences 300 $mmH_2O$, 450 $mmH_2O$ and 600 $mmH_2O$, respectively. This was due to mode 1 resembled the dominant ensemble-averaged of reverse-tumble pattern for valve lift 2 mm and two intake air jets pattern coming through the two sides of the intake valves for valve lift 5mm and strong tumble pattern for valve lift 10 mm which were spatially large-scale structures. It is worth recalling also that the higher values of energy fraction captured by the first POD mode confirmed that the in-cylinder flow was highly organised and highly repeatable in the input snapshots with small snapshot-to-snapshot variations [134, 169]. Taking this note in mind, one can suggest that the flow was more repeatable at high valve lift and high-pressure differences [134]. On the other hand, the higher modes, which represented small scale structures, contained much less energy fraction, for instance, mode 2, mode 3, mode 4 and mode 5 captured 1.4 %, 0.9 %,

0.643 % and 0.642 % of the total energy at valve lift 10 mm for a pressure difference of 600 mmH$_2$O, respectively.

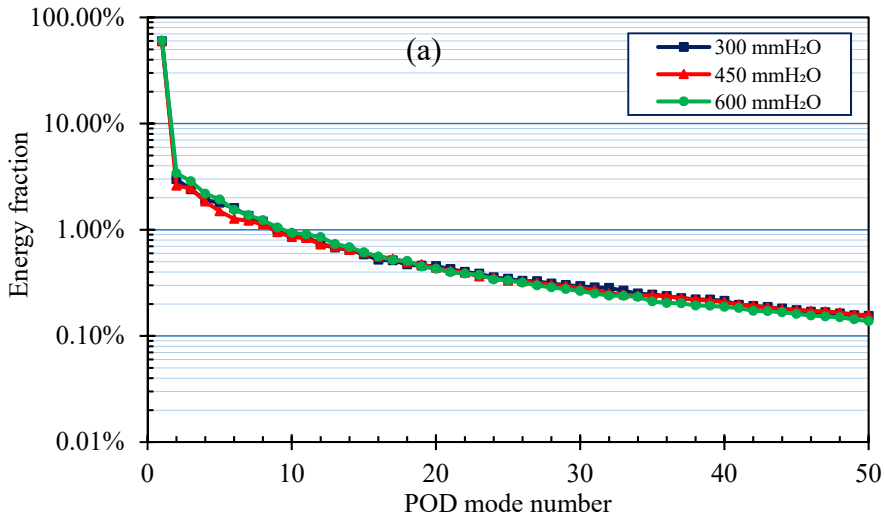


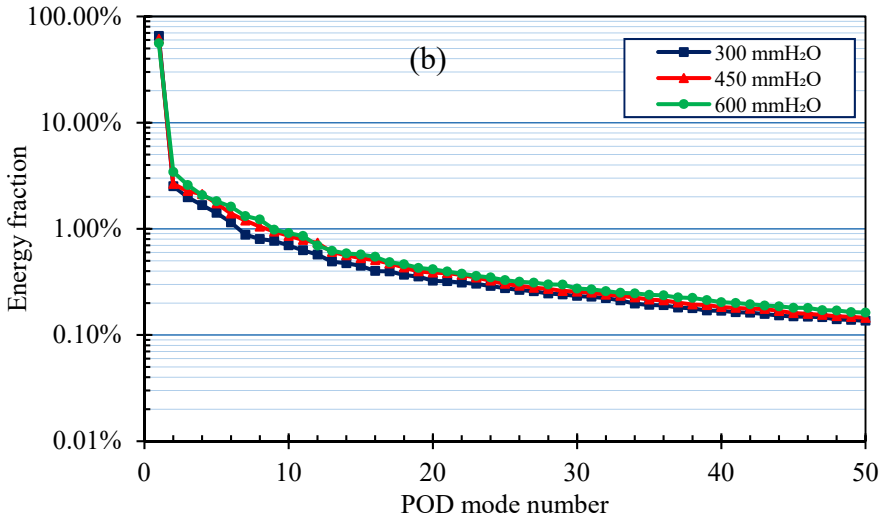

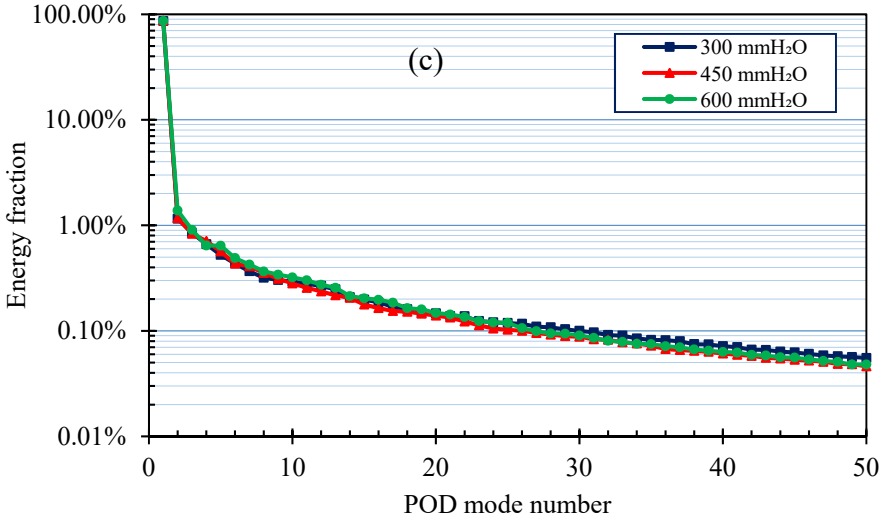


Figure 4.32: Energy fraction captured by the first 50 phase dependent POD modes at different valve lifts for different pressure differences (a) VL- 2mm, (b) VL- 5 mm, (c) VL-10 mm

*4.4.3.3 Phase Dependent POD Mode Coefficients*

Theoretically, the POD modes capture only the spatial pattern of the in-cylinder flow (either jet-like structure or tumble pattern) while the intensities of these modes are captured by their corresponding coefficients which resulted from the projection of POD modes onto the original input snapshots. Figure 4.33 shows mode 1 and mode 2 coefficients at different valve lifts for different pressure differences for all input 1000 snapshots. It is clear from Figure 4.33(a) that there was a good correlation between mode 1 coefficients and the applied pressure difference. For all valve lifts, the higher the pressure difference the higher the magnitude of mode 1 coefficients. For instance, the average mode 1 coefficients were 747, 888 and 966 for 300, 450 and 600 $mmH_2O$ at valve lift 9mm, respectively. Moreover, the coefficients of variation (COV) for mode 1 coefficients at valve lift 2 mm were 9.18 % and 9.95 %, while the COV's of mode 1 coefficients at valve lift 10 mm were 4.56 % and 5.04 % for pressure differences 300 and 600 $mmH_2O$, respectively. This confirmed that the flow was more repeatable at high valve lift conditions. On the other hand, the lower values of mode 2 coefficients (shown in Figure 4.33(b) for all cases compared to mode 1 coefficients reflected the

insignificant contribution of this mode and consequently the higher modes contributions as well.

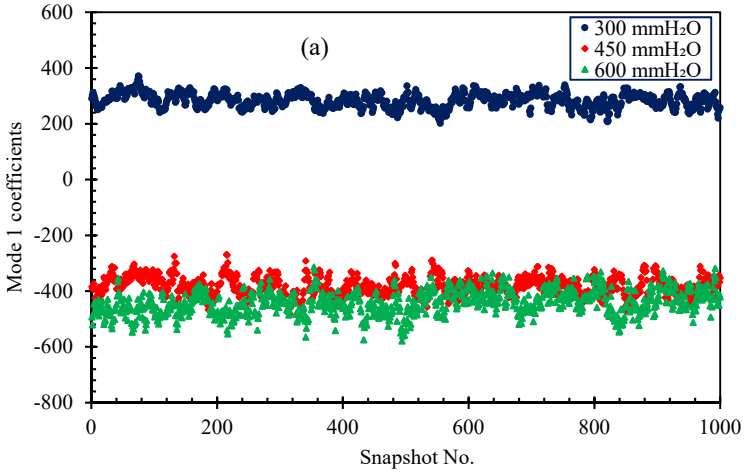


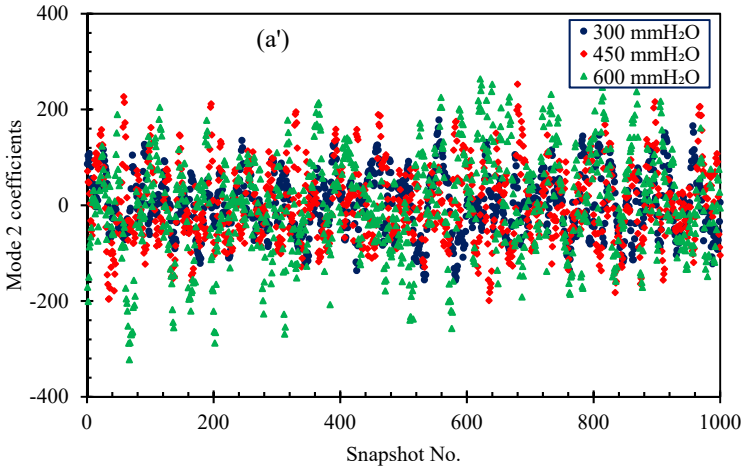


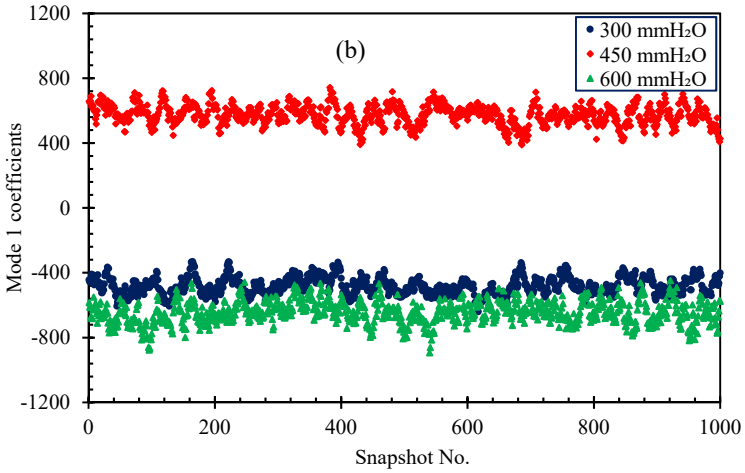

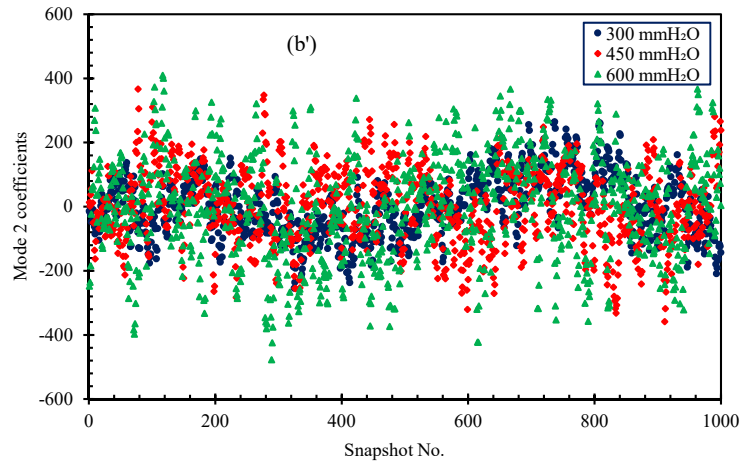


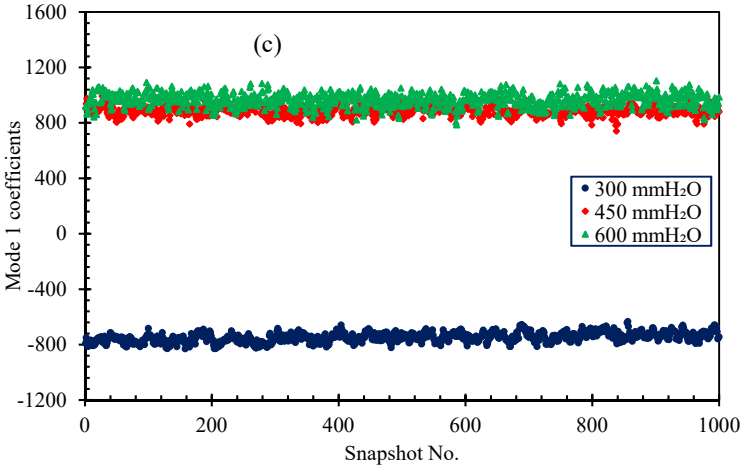


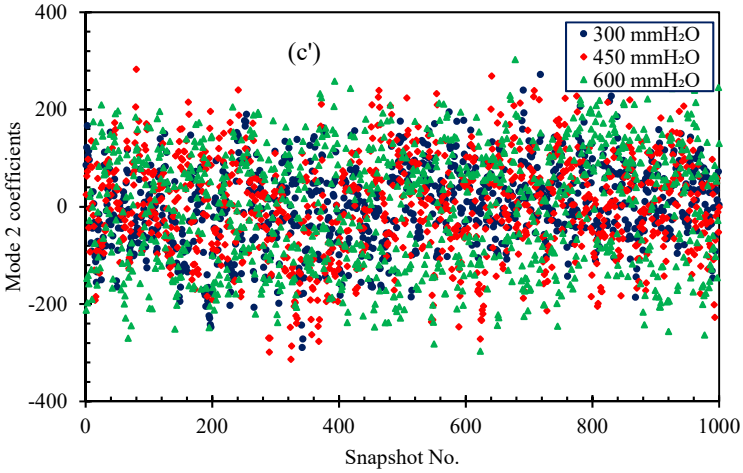


Figure 4.33: Mode 1 and mode 2 coefficients for all snapshots at different valve lifts for different pressure differences (a) VL- 2mm, (b) VL- 5 mm, (c) VL- 10 mm

### 4.4.4 Evaluation of the Effect of Pressure Difference using Phase-Invariant POD

It is worth recalling that POD is considered as a powerful and quantitative tool for the comparison of experimental datasets. Therefore, POD was used here to compare the in-cylinder flow structures evolution and variation at valve lift 10 mm for different pressure differences 300, 450 and 600 mm$H_2O$. A 1000 velocity vector fields from each pressure difference at valve lift 10 mm were arranged in one input file to apply phase invariant POD. Under this scenario, for these 3000 input snapshots, 3000 phase-invariant POD modes and their corresponding coefficients were constructed accordingly.

#### *4.4.4.1 Phase-Invariant POD Modes Spatial Patterns and Energy Fraction*

Figure 4.34 depicts the spatial patterns of the first four phase-invariant POD modes. In order to show to what extent mode 1 was dominant in these different experimental conditions, the values of the average kinetic energy of the first four POD modes were calculated from their corresponding coefficients. It was found that the average kinetic energy contained in mode 1, mode 2, mode 3 and mode 4 were 378,008 $m^2/s^2$, 4,884 $m^2/s^2$, 3,892 $m^2/s^2$ and 3,529 $m^2/s^2$, respectively. This established one important feature of the effect of pressure difference variation on the in-cylinder flow structures. Even though the input snapshots were collected from different cases of pressure differences, mode 1 only was able to extract more than 85 % of the total energy, this quantify the degree of similarity between these datasets as confirmed by the energy fraction curves shown in Figure 4.35. This was also consistent with the fact that, the image structures with repeated patterns could be placed in one mode and the other modes were arranged with decreasing order of kinetic energy [134].

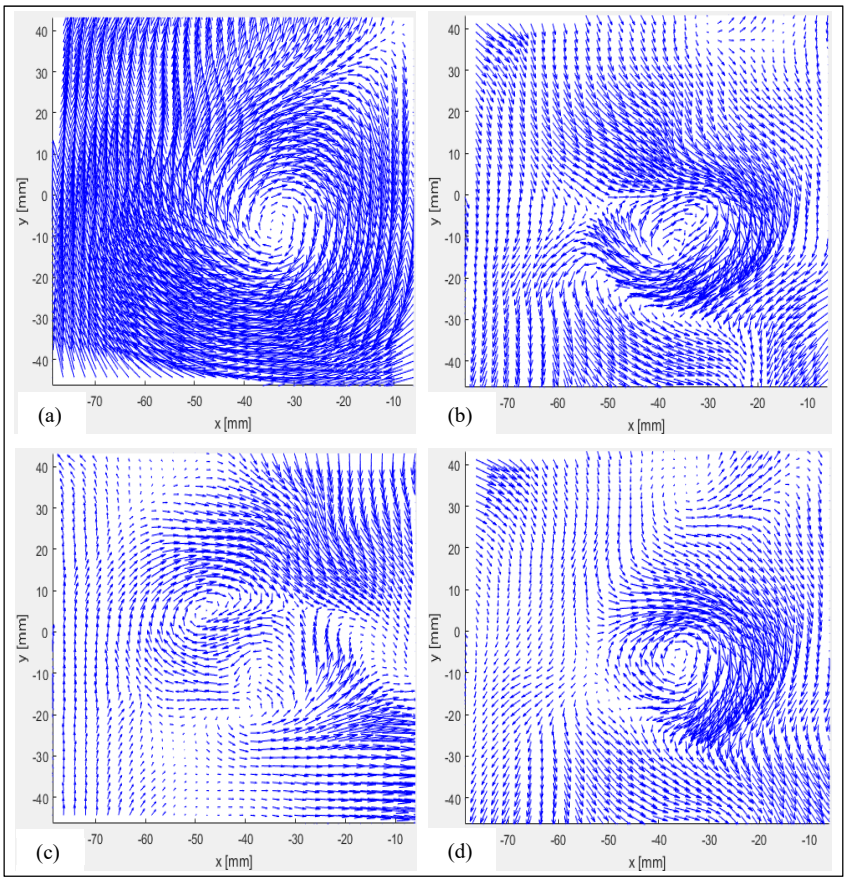


Figure 4.34: The first four phase-invariant POD modes at valve lift 10 mm, (a) mode 1, (b) mode 2, (c) mode 3 and (d) mode 4

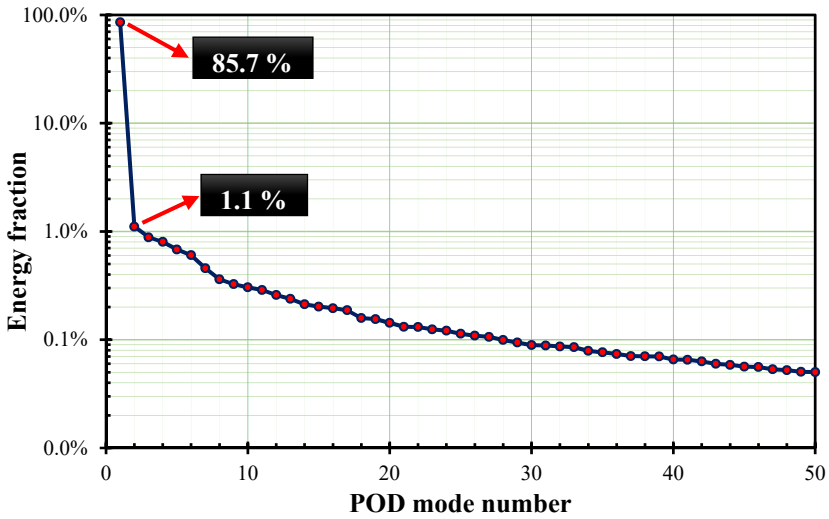


Figure 4.35: The energy fraction captured by the first 50 phase invariant POD modes at valve lift 10 mm

Figure 4.36 depicts the coefficients associated with the first three phase-invariant POD modes versus all 3000 input snapshots. A number of observations can be made from this Figure. First, there was linear fit between mode 1 coefficients and the applied pressure difference. This was confirmed by the higher value of the coefficient of determination $R^2$, shown in Figure 4.37, which represented the goodness of data fit. Theoretically, a perfect fit was achieved if the value of the coefficient of determination approached unity. In the current case, $R^2$ was 0.9674 showing the strong linearity existing between mode 1coefficients and the pressure difference. This indicated that the tumbling motion intensity increased with increasing the pressure difference.

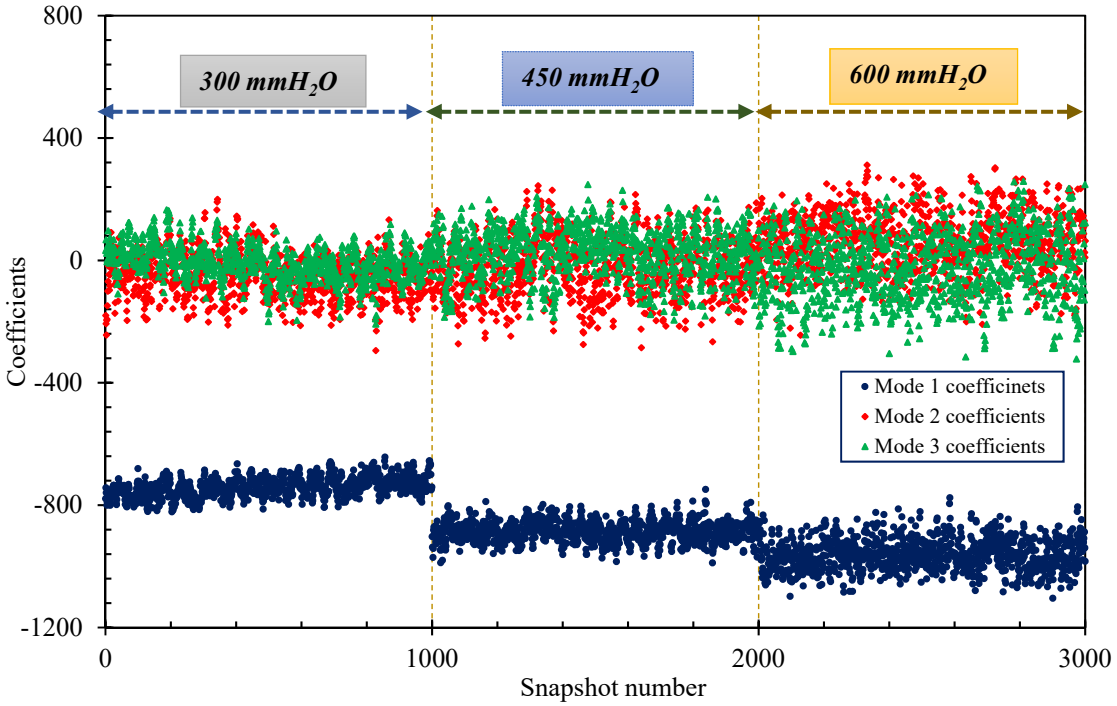


Figure 4.36: Coefficients associated with the first three phase-invariant POD modes at valve lift 10 mm

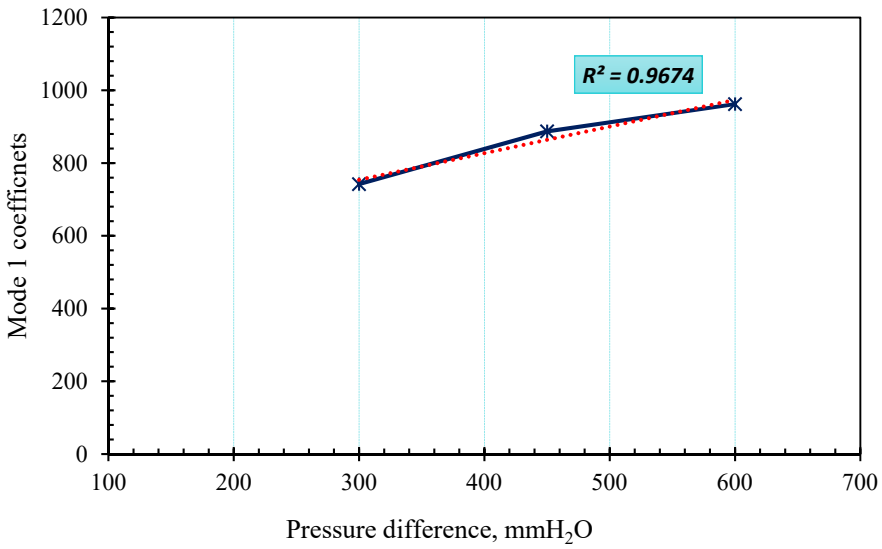


Figure 4.37: Linear fit between average absolute values of mode 1 coefficients and various pressure differences

## 4.5 Air/Spray Interaction

In the following sections, the interaction between high pressure direct fuel injection and the intake-generated tumble motion at different experimental conditions are presented and discussed. These sections include, the characterization of the fuel spray at different injection pressures and a qualitative and quantitative overview of the interaction process at different pressure differences across the air intake valves and fuel different injection pressures.

### 4.5.1 Spray Characteristics (Spray Images and Penetration)

Figure 4.38 depicts the variation of spray formation images with time after the start of injection (SOI) for two injection pressures 32.5 and 35 MPa. These static spray images served as baseline against which the geometrical distortions of the spray under the effect of air flow. It can be observed that the spray plume appeared symmetric around the spray vertical axis with more liquid concentration in the centre around this axis compared to the regions away from the centre of the spray particularly for higher pressure. Moreover, the atomization of fuel droplets around the periphery of the spray

was better for higher pressures. Using these spray images shown in Figure 4.38, for more quantitative information about spray formation, the spray tip penetration was measured. The temporal evolution of spray tip penetration at different injection pressures is shown in Figure 4.39. The average values shown were calculated from three injections. As expected, it can be noticed that increasing the fuel injection pressure led to an increase in the spray tip penetration. This was attributed to the fact that increasing the injection pressure led to an increase in the mass flow rate injected and in the initial liquid velocity and subsequently an increase in the spray momentum therefore, the fuel spray had the ability to propagate more into the surrounding environment [170, 171].

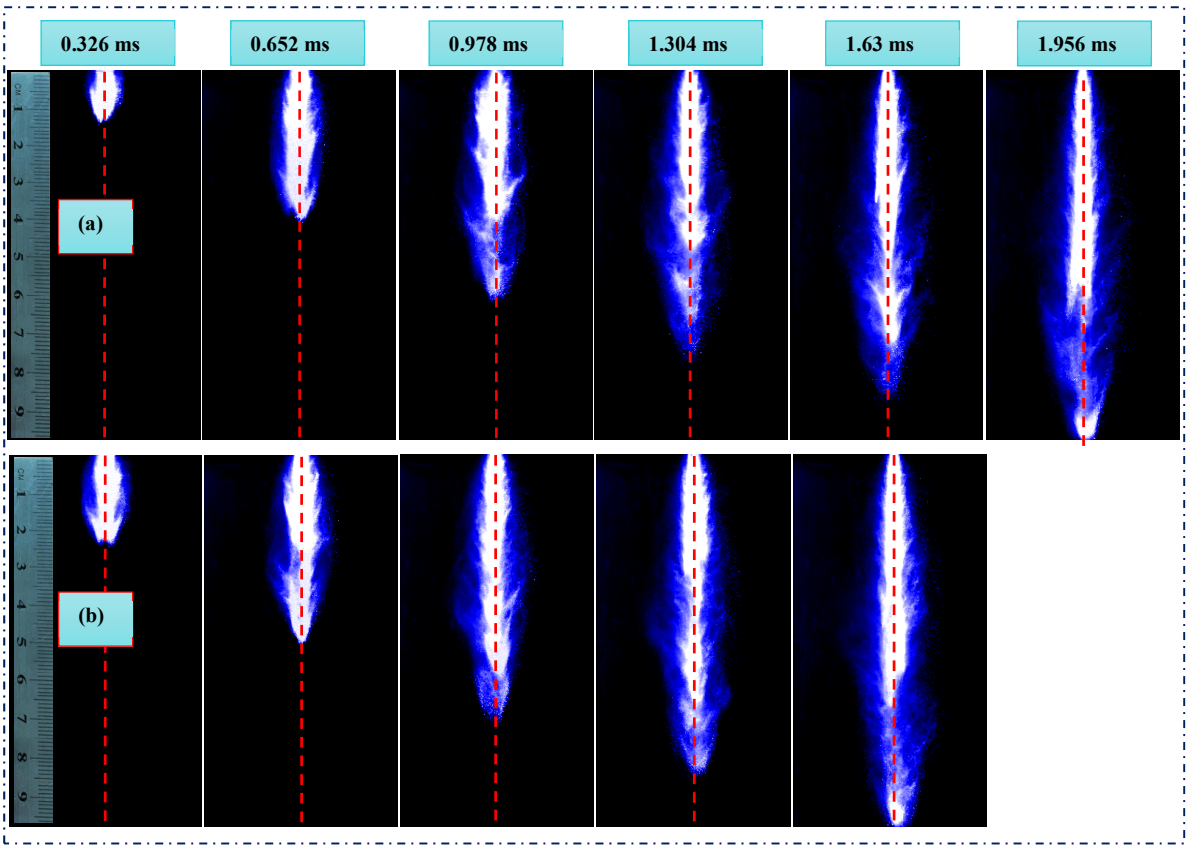


Figure 4.38: Temporal evolution of spray at (a) 32.5 MPa and (b) 35.0 MPa

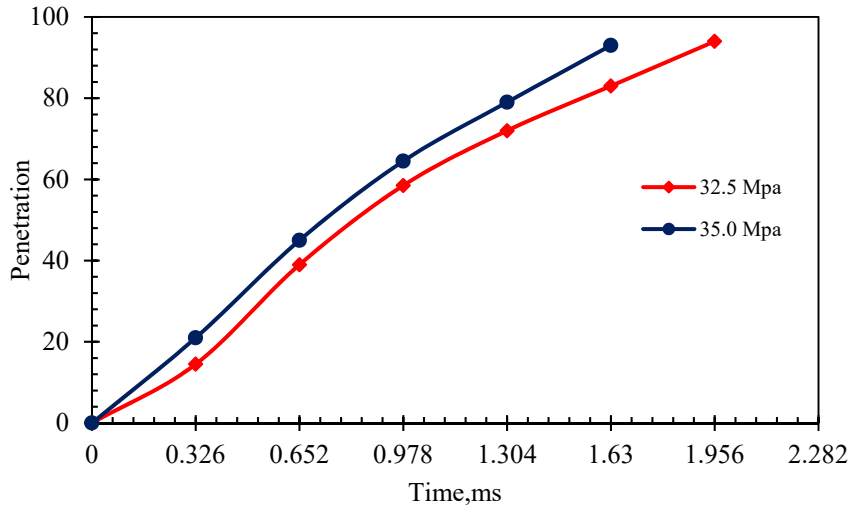


Figure 4.39: The variation of spray tip penetration with time after start of injection at different injection pressures

### 4.5.2 Mie Scattering of Fuel Spray under the Effect of Air Motion

A temporal sequence of the Mie scattering of the fuel spray development under the effect of air flow at different measurement times after the start of injection at valve lift 10 mm for different air pressure differences 150, 300 and 450 mm$H_2O$ is illustrated in Figure 4.40. The aim of this figure was to qualitatively show how the fuel spray was affected by the in-cylinder air motion at different experimental conditions and to chronicle the evolution of spray event which was expected to be used to interpret the results. With such high valve lift, the air momentum was speculated to be high and subsequently the in-cylinder air flow could interact strongly with the developing fuel spray. This interaction was manifested in geometric differences between the spray trajectory observed in two cases, with and without in-cylinder air motion. To better visualize this, the spray plume centreline from the static injection conditions (without air motion) were overlaid as dashed red lines over the subsequent spray images under the effect of air motion. As illustrated before, increasing the pressure difference across the intake valves led to an increase in air flow rate into the cylinder and subsequently an increase in air velocities and more expected momentum exchange between the air flow and the fuel spray plume. Comparing Figure 4.40 (a), (b) and (c), the effect of pressure difference (subsequently engine speed) on spray development could be

recognized. As a general view, for low pressure difference at 150 mm $H_2O$ of (Figure 4.40 (a)), the impact of the in-cylinder flow on the spray was small particularly at the onset of the injection event. The tumble momentum at this low-pressure difference (speed) was not high enough to notably affect the high-momentum spray trajectory. However, at the higher-pressure difference of 450 mm$H_2O$ (Figure 4.40 (c)), the effect of the in-cylinder tumble flow on the spray was quite prominent. A number of detailed observations of special interest were extracted from this Figure. The first observation was that, for all cases of pressure differences, the spray plume had enough initial momentum to propagate through the air flow till around 2 ms after the start of injection (the middle of injection duration). However, it was noteworthy that during this time, the spray plume appeared asymmetric with the observation that the higher the pressure difference, the higher the level of asymmetry. This asymmetric fuel spray distortion was mainly concentrated towards the left-hand side of the spray (the exhaust side). This was attributed to the concept of the tumbling-motion generation where the intake port task was to direct a significant amount of air flow towards the exhaust side of the cylinder. The second observation was that, once the spray plume approached the bottom of the cylinder, the generated tumbling vortex at this valve lift drove the tail of the spray away from the vertical position towards the counter-clock wise direction (rolling up effect). This was very clear particularly at pressure difference of 450 mm$H_2O$ where the strongest tumbling vortex was generated inside the cylinder. The third observation was that, by the second half of the injection event, the spray plume started to lose its momentum and the in-cylinder air flow momentum became more significant to entrain more of the fuel spray. Moreover, shortly after the end of injection (EOI) at 4 ms, the fuel droplets distribution was totally dependent on the in-cylinder tumbling vortex. Furthermore, the complete time for fuel spray to totally follow the in-cylinder motion decreasing as the pressure difference increased. For instance, the fuel spray plume required 7.2 ms, 6.2 ms and 5.9 ms for pressure differences 150, 300 and 450 mm$H_2O$ respectively. It is worth recalling also that, depending on the previous stages of air/spray interaction, one hypothesis was proposed that the intake-generated large-scale tumble flow might be considered as a key parameter to control the fuel propagation, distortion and distribution inside the engine cylinder. Once the fuel droplets tracked the tumbling vortex, the possibility of the momentum exchange between air and spray droplets was

expected to increase which finally might lead to good mixing and prohibiting local areas with too high fuel concentration and hence more soot particulates. Figure 4.41 shows the velocity vector fields of the spray evolution which were overlapped onto the greyscale raw images of the spray under the influence of air motion at valve lift 10 mm for pressure difference of 450 mm$H_2O$ to demonstrate the interaction process in a qualitative way. It was clear that the velocity of the spray propagation was affected by the intake-generated flow. As shown in the sequence of the flow fields, during the initial stage of the injection event, the fuel spray was concentrated in the exhaust side. Then the fuel spray was curled up and compelled to move towards the intake side to follow the counter-clock wise tumble vortex, as demonstrated by the arrows in the figure.

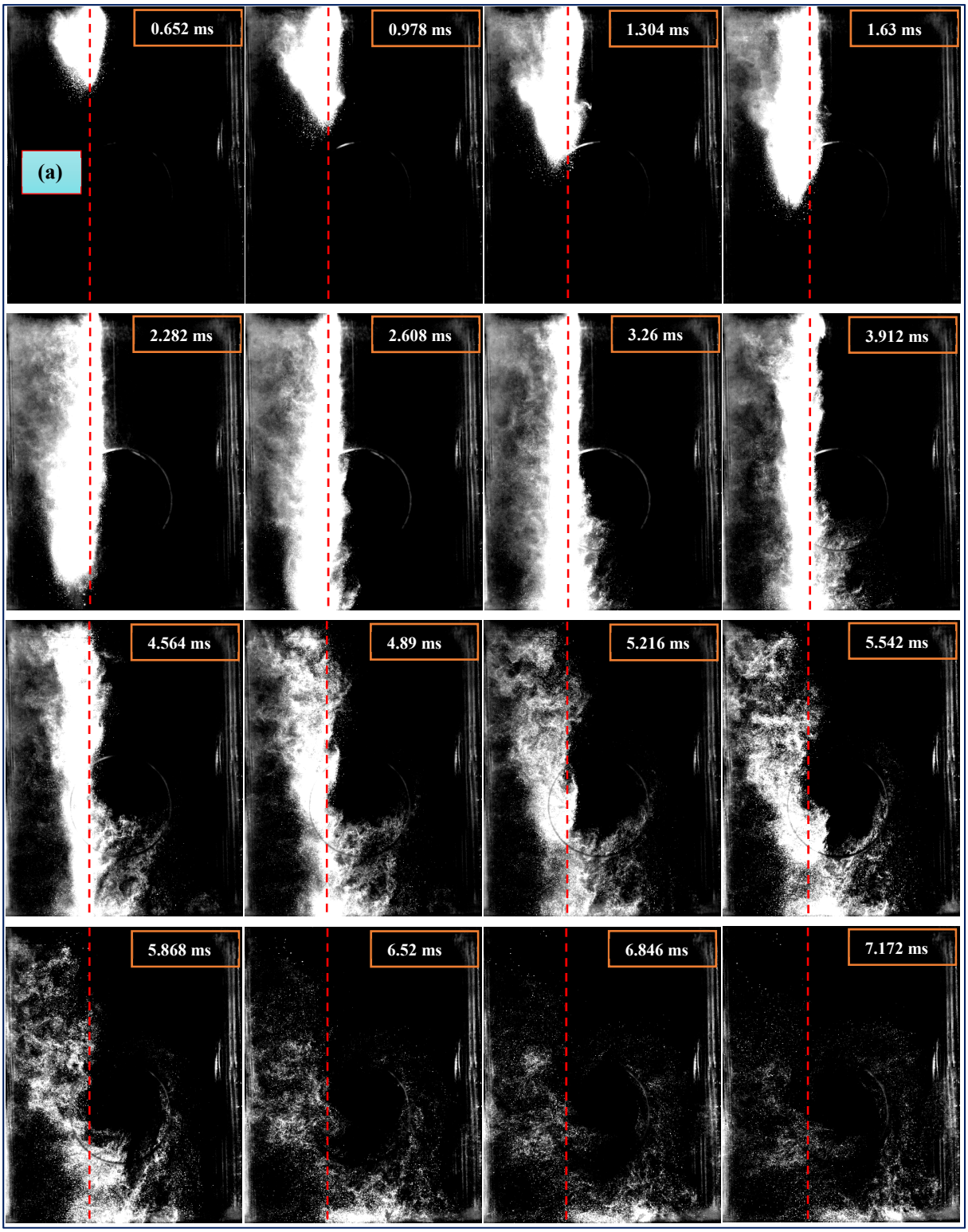
(a)
0.652 ms
0.978 ms
1.304 ms
1.63 ms
2.282 ms
2.608 ms
3.26 ms
3.912 ms
4.564 ms
4.89 ms
5.216 ms
5.542 ms
5.868 ms
6.52 ms
6.846 ms
7.172 ms

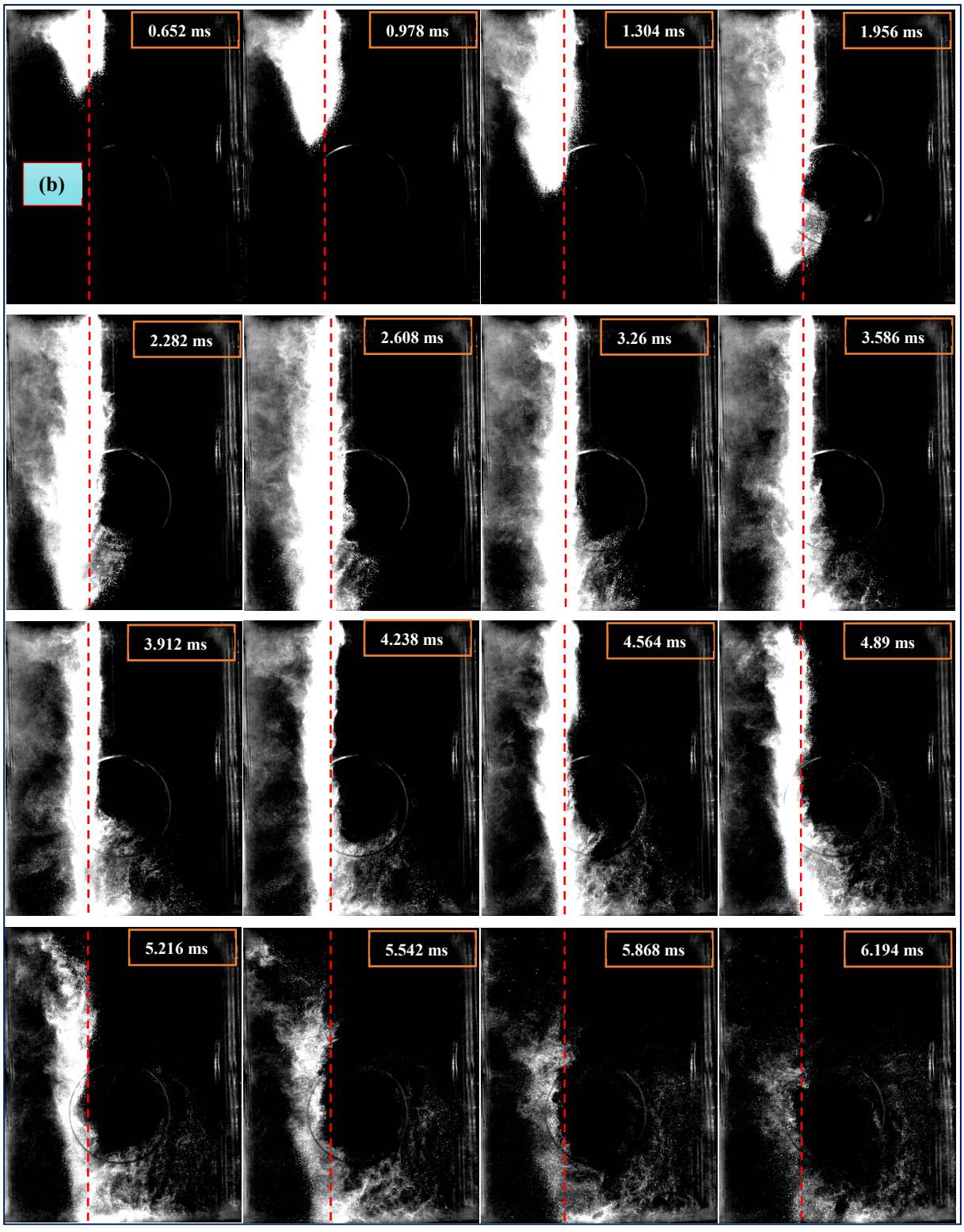
(b)
0.652 ms
0.978 ms
1.304 ms
1.956 ms
2.282 ms
2.608 ms
3.26 ms
3.586 ms
3.912 ms
4.238 ms
4.564 ms
4.89 ms
5.216 ms
5.542 ms
5.868 ms
6.194 ms

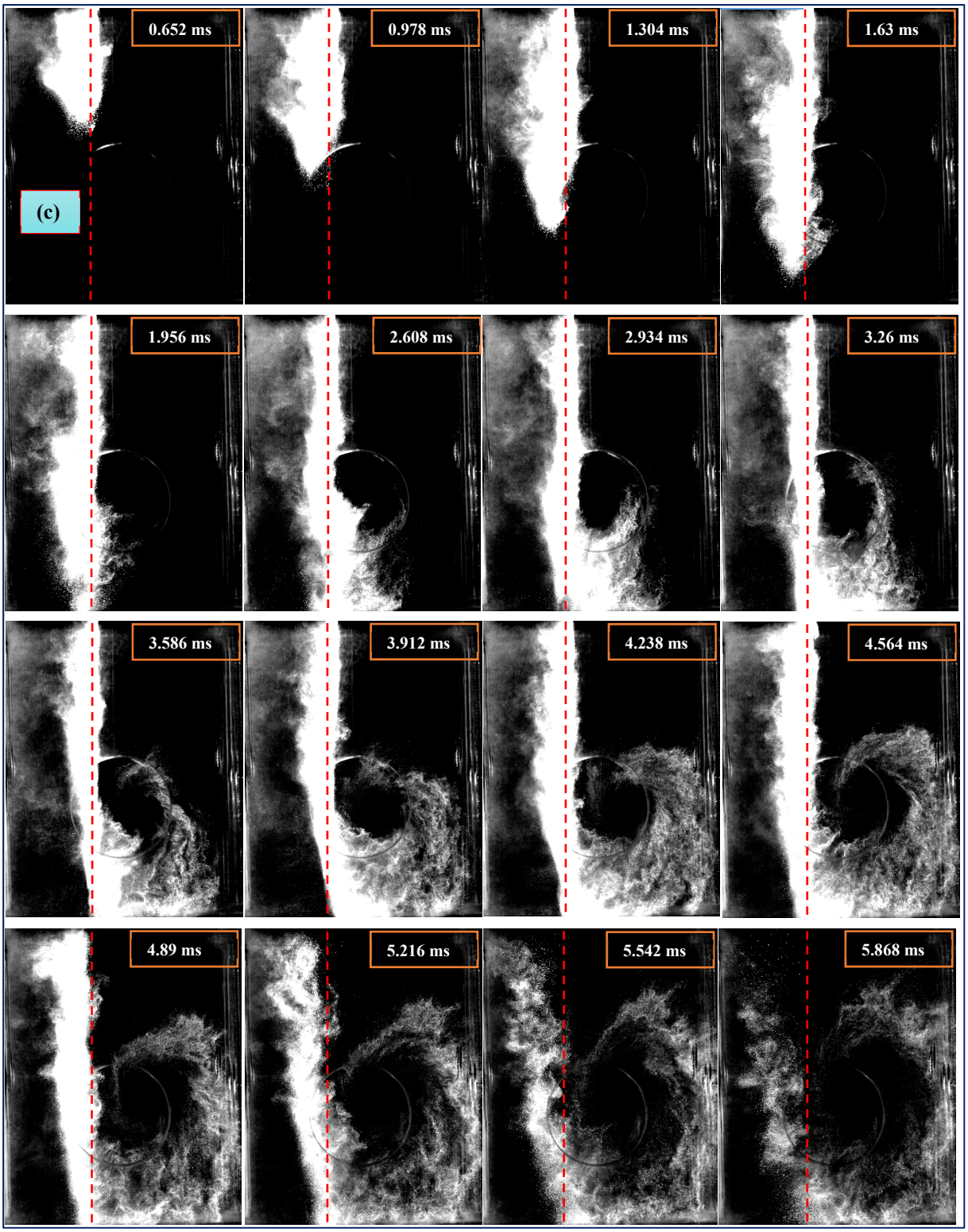


Figure 4.40: Temporal sequence of the Mie scattering of the fuel spray under the effect of air flow at different measurement times after the start of injection at valve lift 10 mm and injection pressure of 32.5 MPa (a) 150 mm$H_2O$, (b) 300 mm$H_2O$ and (c) 450 mm$H_2O$

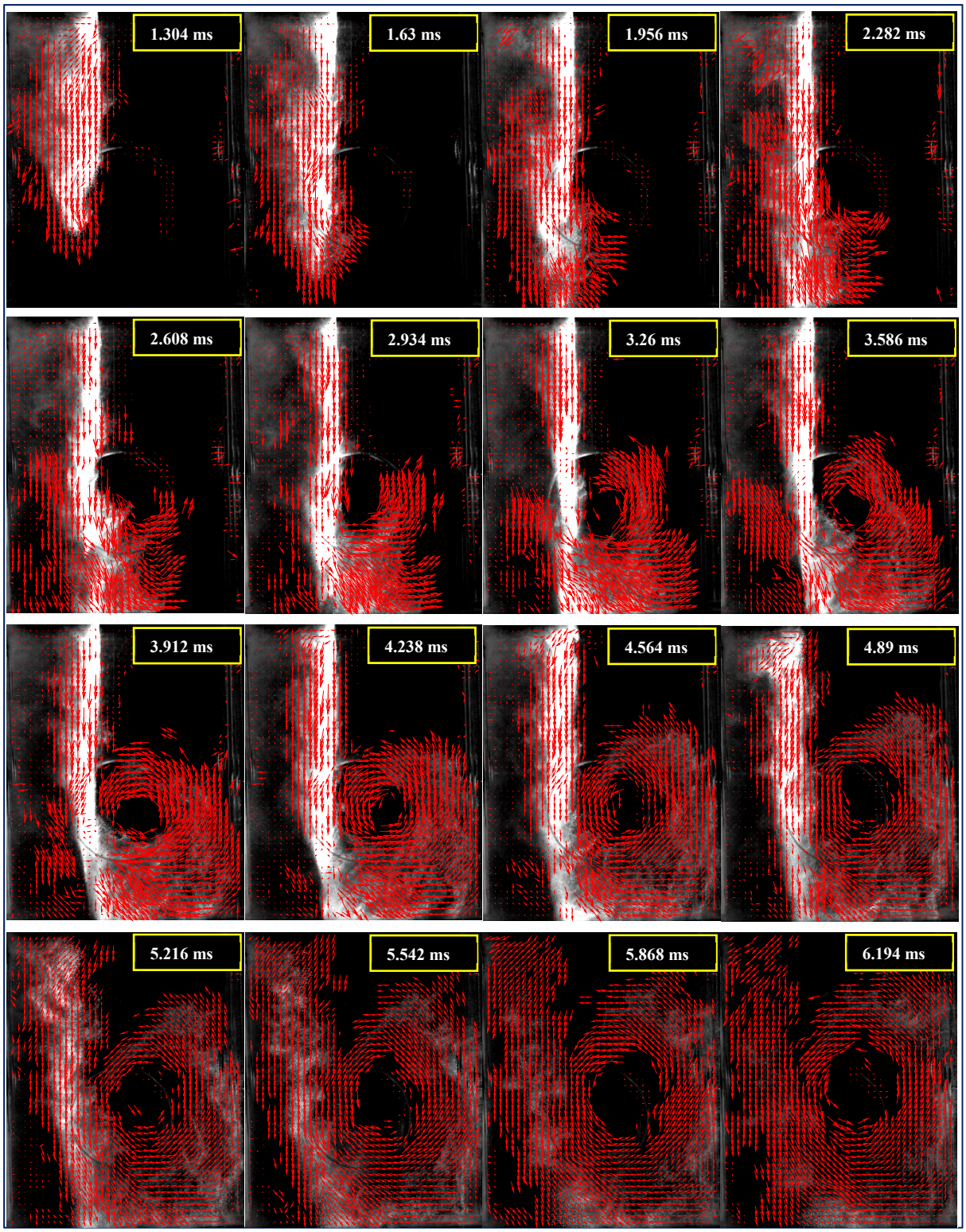


Figure 4.41: Temporal sequence of the velocity vector fields superimposed into Mie scattering of the fuel spray under the effect of air flow at different measurement times after SOI at valve lift 10 mm and injection pressure of 32.5 MPa at 450 mm$H_2O$

In an attempt to study the simultaneous interaction between air and spray, the following sections present the results for air and spray interaction while air was seeded with solid particles and the fuel droplets were used as seeding particles.

### 4.5.3 Air/Spray Instantaneous Velocity Vector Fields

Figure 4.42 depicts the Mie scattering images and their corresponding instantaneous velocity vector fields for air and spray mixture at selected times before, during and after the injection process at valve lift 10 mm for different pressure differences and different injection pressures. At valve lift 10 mm (at the time of maximum valve lift), the tumble vortex was fully developed and covered nearly the whole cylinder volume. The local flow direction was represented by the velocity vectors, whilst the velocity magnitude of the two in-plane velocity components was represented by the colour scale. The aim of this figure was to chronicle the spatial and temporal evolution of air/spray mixture and their interaction. As a general view to the figure, it was clear that, PIV did not provide velocity information in some regions at the left-hand side of the spray plume early during the injection event. This was attributed to the fact that the laser sheet could not pass through the dense spray plume because of its initial momentum and droplets cohesion. By the time, because of the interaction between spray and air flow, the laser sheet could pass and subsequently the velocity information became available in both sides of the spray plume. Image analysis was divided into four sections, before injection event, at 1.304 ms ASOI and at 4.564 ms ASOI and after injection. The first image for all cases (air flow prior to injection event) showed the counter clock-wise tumble vortex which dominated the whole cylinder at valve lift 10 mm. As illustrated before in sections 4.3.3.1 and 4.3.3.2, the effect of the pressure difference on the flow structures was negligible as the vortices formed preserved their shape for the same valve lift at different pressure differences. The only change was that, the vortex strength increased with increasing the pressure difference. Images at 1.304 ms ASOI showed a fuel-rich spray plume penetrating through the in-cylinder flow at high velocities in the spray center reaching about 55 m/s, 56 m/s, 57 m/s and 56 m/sec for 32.5 MPa, 35.0 MPa (at 300 mm$H_2O$) and 32.5 MPa and 35.0 MPa at 450 mm$H_2O$ respectively. Whilst the velocity at the periphery of the spray was low because of the in-cylinder air resistance.

The spray plume was much affected on the left side because of the direction of tumbling motion with centrally concentrated dense liquid and good atomization on the periphery of the spray plume particularly at higher injection pressure. By 4.564 ms ASOI (shortly after the end of injection-EOI), the liquid fuel injection ended and the fuel droplets were dispersed at the tail of spray plume while at the upper side of the spray, because of initial momentum, the droplets were still agglomerated. Since the intake generated tumble motion was anticlockwise, the right side of the spray plume easily followed the tumble vortex. Moreover, it was noticed that the combination of high injection pressure and high-pressure difference led to good atomization and better droplets dispersion as can be seen for 35.0 MPa injection pressure and pressure difference of 450 mm$H_2O$ case. At higher pressure difference across the air intake valves (equivalent to increasing the engine speed), the in-cylinder flow became sufficiently strong to impact on the fuel spray [35]. It was noticed also that (this was not depicted in the figures) the higher the pressure difference, the higher the left cylinder wall wetting (exhaust side), however, at the same time the lower the piston wall wetting as the strong vortex generated at high pressure difference drove the tail of the spray plume away from the piston surface. This was consistent with the work of Yunqing *et al.* [172] and Wei Zeng *et al.* [29]. After Injection, by 5.542 ms ASOI, the air entrainment into the fuel jet was fully established as a significant amount of fuel was dispersed resulting in a more uniform fuel distribution. The counter-clock wise tumble vortex disrupted by the injection event was then retained, to some degree, for a few milliseconds after the end of injection. Moreover, the velocity magnitude decreased to values similar to those measured before the injection event.

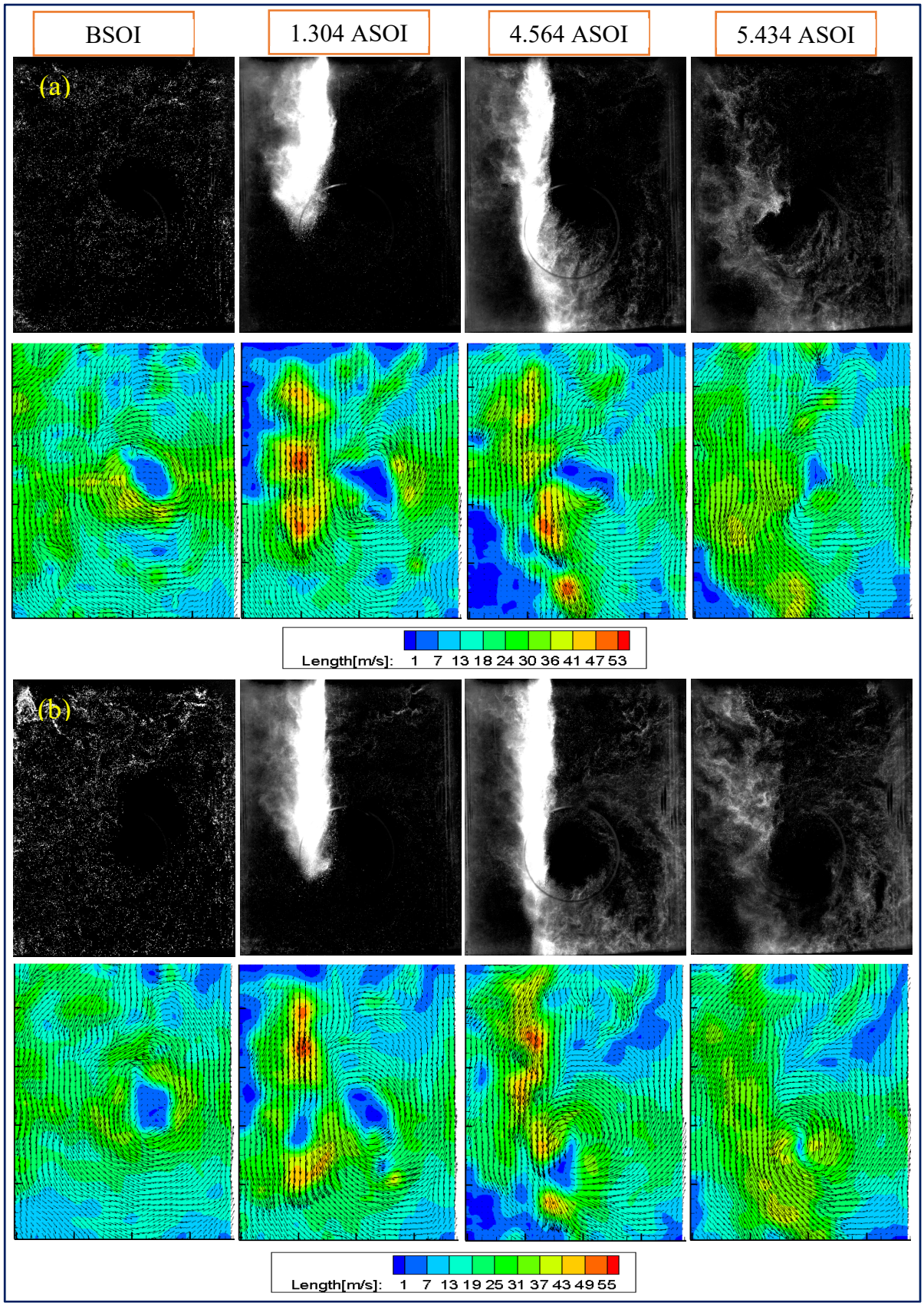
BSOI
1.304 ASOI
4.564 ASOI
5.434 ASOI
(a)
Length[m/s]: 1 7 13 18 24 30 36 41 47 53
(b)
Length[m/s]: 1 7 13 19 25 31 37 43 49 55

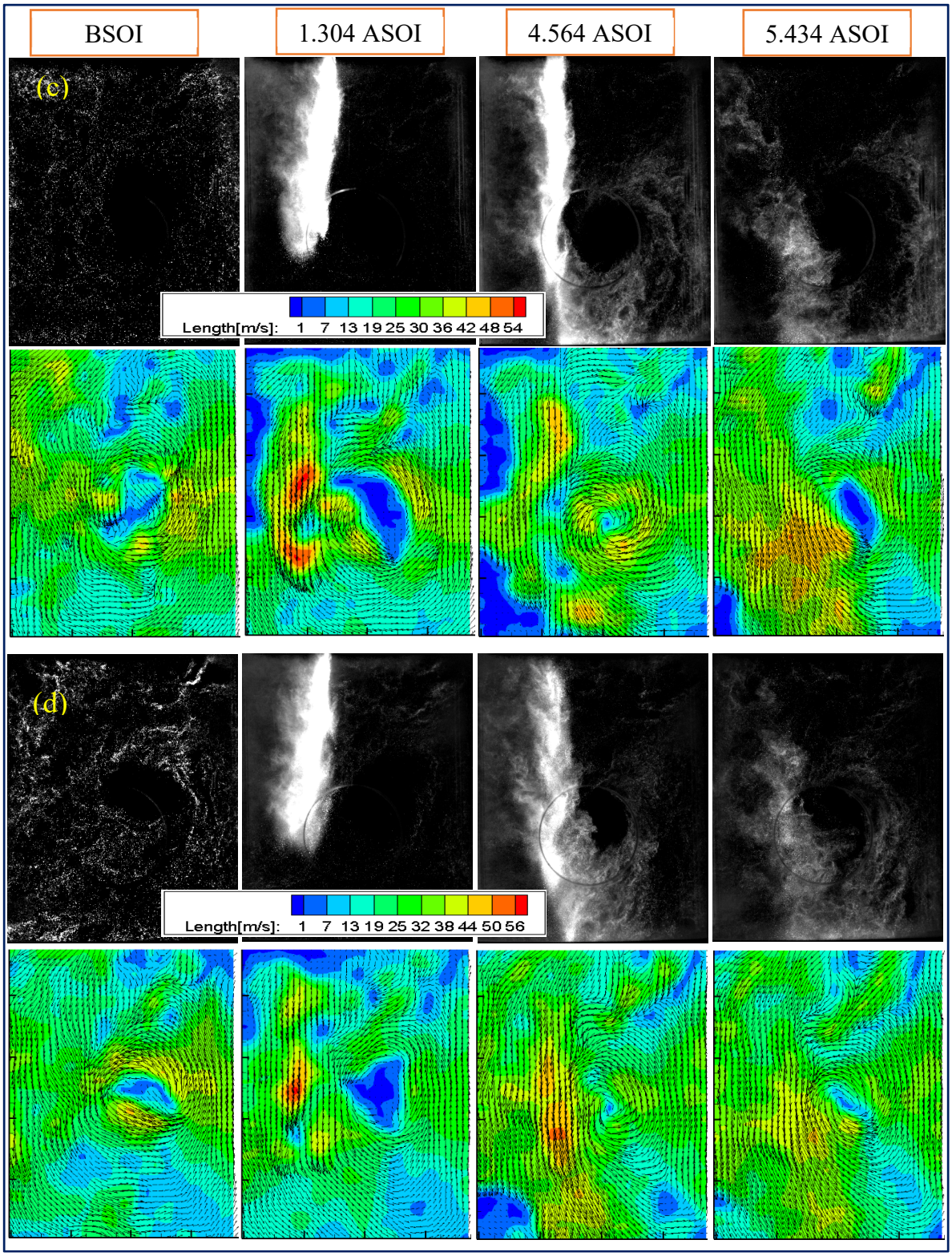


Figure 4.42: Instantaneous Mie scattering images and their corresponding velocity vector fields at selected times at valve lift 10 mm, (a) 32.5 MPa - 300 mm$H_2O$, (b) 35.0 MPa - 300 mm$H_2O$, (c) 32.5 MPa - 450 mm$H_2O$, and (d) 35.0 MPa - 450 mm$H_2O$

### 4.5.4 Air/Spray Momentum Exchange

In addition to the intake-induced bulk air motion, another significant factor was addressed; the spray-induced flow field and its influence on the in-cylinder flow field. This was addressed through comparing the values of the maximum kinetic energy generated inside the cylinder before, during and after the injection event. The kinetic energy was considered as a key parameter which might be used to reveal the momentum exchange process between the high injection fuel pressure and the in-cylinder tumble motion [30]. Additionally, in order to move the rich fuel concentrated in the spray core to mix with the air inside the cylinder, the presence of the in-cylinder velocity was essential [173].

Figure 4.43 shows the maximum kinetic energy relative to the time after the start of injection at different injection pressures and different pressure differences. As can be seen from the figure, after the start of injection the maximum kinetic energy inside the cylinder increased linearly. This might be attributed to the fact that the momentum generated by the high-pressure jet spray was partially transferred to the surrounding air, which increased the kinetic energy of the charge soon after the fuel was injected. It was noticeable that, even though the spray momentum was the same for the same injection pressure, the magnitude of the K.E was different for different cases of air pressure differences and subsequently the in-cylinder motion strength. Initially the maximum KE increased by 82 %, 96 %, 54 % and 63 % till 1.304 msec ASOI for 32.5 MPa, 35.0 MPa (at 300 $mmH_2O$) and 32.5 MPa and 35.0 MPa (at 450 $mmH_2O$) respectively. However, from 1.304 msec to 4.564 msec ASOI, the max KE decreased by 7.5 %, 8.5 %, 15 % and 19.7 % for 32.5 MPa, 35.0 MPa (at 300 $mmH_2O$) and 32.5 MPa and 35.0 MPa (at 450 $mmH_2O$) respectively, indicating more momentum exchange between the in-cylinder tumble motion and the fuel spray, particularly under high pressure difference and high injection pressure conditions. This high momentum exchange was expected to increase the dispersion and the distribution of fuel droplets by the large-scale tumble vortex to all positions inside the cylinder, making spray droplets and air mix better and avoiding any local areas with too high concentration of fuel droplets and hence reduce the HC emissions.

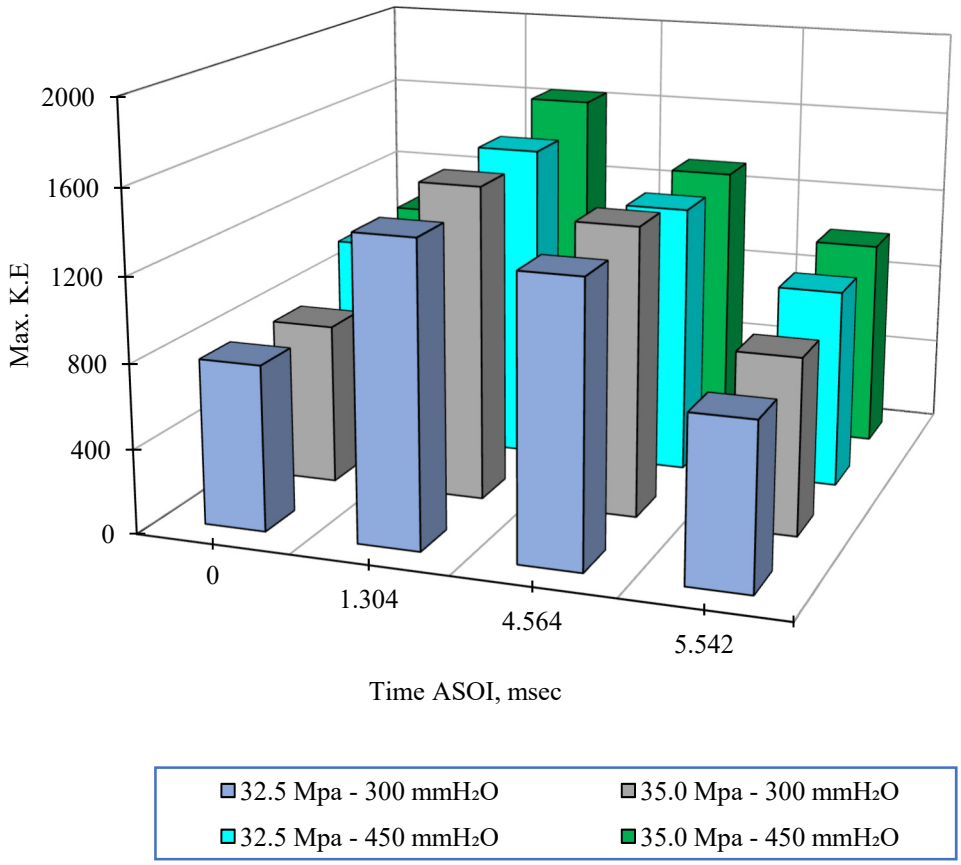


Figure 4.43: Variation of max. K.E with time after start of injection for different pressure differences and different injection pressures

# CHAPTER 5

# CONCLUSIONS AND RECOMMENDATION

## 5.1 Conclusions

The behaviour of the flow in the cylinder of a GDI engine was investigated and characterized using a number of experimental techniques on a steady-state experimental rig. Firstly, 'traditional' measurements of integral parameters such as air volume flow rate, flow coefficient, discharge coefficient, and tumble ratio were carried out. These measurements were aimed at confirming the accuracy and level of correlation between the test rig at UTP and that at Ricardo before the detailed investigation of the flow characteristics. The tumble ratio was calculated from readings of an FEV paddle wheel anemometer while those of Ricardo were based on an impulse torque meter. The results showed a good level of agreement between both rigs in terms of air volume flow rate, flow coefficient and discharge coefficient. Although there was an acceptable level of agreement in the measured non-dimensional rig-tumble between the two rigs, noticeable differences could be detected which were mainly due to the absence of a piston in the case of the Ricardo test rig. 2D-2C planar high-speed time-resolved particle image velocimetry measurements of full field velocity vector maps were carried out at the mid-cylinder tumble plane and in order to validate the Ricardo's CFD VECTIS simulation. The CFD results correlated well with the PIV measurements giving confidence in the CFD calculations. The tumble ratio was calculated from the PIV velocity vector maps using two methods; momentum integral and vorticity and both showed good agreement with direct paddle wheel and torque meter measurements thus confirming the correct set up of the PIV set up.

The flow rig was modified to provide complete optical access in order to investigate detailed characteristics of in-cylinder flow structure using a novel 2D-3C stereoscopic

time-resolved high-speed particle image velocimetry. Several experimental conditions were considered and examined. First, the effect of valve lift on the in-cylinder flow was investigated at the plane of symmetry. The analysis of the ensemble average velocity vector fields of 1000 instantaneous velocity vector fields at different valve lifts revealed that, the incoming air into the cylinder through the intake valves formed two separate jets; the intake side jet and the exhaust side jet. At high valve lifts, a significant amount of air was directed towards the exhaust side then interacted with the combustion chamber walls and the cylinder liner and finally with the flat piston located at the bottom of the cylinder. This led to the formation of a counter clock-wise tumble vortex which dominated the whole cylinder volume at valve lift 10 mm. Moreover, increasing the valve lift led to higher flow rates inside the cylinder with high mean and fluctuating velocities which in-turn increased the strength of the air motion and therefore enhanced the turbulent kinetic energy (TKE) and tumble ratio (TR). Second, the effect of measurement plane was investigated considering three vertical tumble planes; the mid-cylinder plane, the mid-injector plane and the mid-intake valve plane. The results showed that, the location of the vortex center in the different tumble planes did not vary greatly across the cylinder volume at high valve lifts which in turn indicated a uniform overall three-dimensional shape of the tumbling pattern. A far more effective tumble pattern was observed with higher velocity magnitudes and flow structures closer to solid body rotation at valve lift 10 mm for all tumble positions. The higher velocities generated at the mid-valve plane improved the overall air motion inside the cylinder in terms of higher TKE and tumble ratios compared to the other planes. Third, the effect of pressure difference across the intake valves was investigated considering three pressure differences 300, 450 and 600 mm$H_2O$. Averaged velocity vector fields obtained in the mid-cylinder plane were analysed in order to understand the in-cylinder flow behaviour. The results revealed that, the effect of the pressure difference on the flow structure and tumble ratio was negligible compared to the effect of valve lift. The vortices formed preserved their shape at the same valve lift for different pressure differences. The only change was that the vortex strength increased with increasing the pressure difference. This indicated consistent flow structures within the cylinder for all engine speeds.

The Proper Orthogonal Decomposition (POD) method was used for the analysis of the variation and evolution of the measured PIV air flow. Each POD mode contained a particular spatial flow structure, while the magnitude of the time-dependent coefficients for a specific POD mode illustrated to what extent this mode was dominant for every snapshot. An innovative technique of combining synthetic velocity field datasets and the actual engine flow fields was used, in order to solve the well documented difficulties of applying POD methods to such complex flows. Further, two types of POD, namely phase-dependent and phase-invariant, were implemented on the acquired 2D-3C PIV velocity vector fields at different experimental conditions. The application of phase-invariant at different valve lifts from 1 mm to 10 mm revealed how the in-cylinder flow varied and evolved. The POD energy spectra showed that the first three modes together extracted about 74 % of the total kinetic energy from all 5000 input velocity vector fields. The first mode captured the two intake air jets coming into the cylinder through the right and left sides of the intake valves and showed that the right-side jet was weaker than the left one because of the concept of tumbling motion generation. While the second and third modes captured the tumble motion generated at high valve lifts. Moreover, the phase-invariant POD analysis was extended to quantitatively evaluate the effect of the pressure difference on the in-cylinder flow behaviour. The results revealed that, even though the input snapshots were collected from different cases of pressure differences, mode 1 only was able to extract more than 85 % of total energy, indicating a high degree of similarity between these datasets and illustrated the insignificant effect of pressure difference on in-cylinder flow structures. Regardless of the applied pressure difference, the in-cylinder flow patterns did not change, however, the level of the turbulence kinetic energy increased as the pressure difference increased. This was very clear from the strong linearity existing between mode 1 coefficients and the applied pressure difference. In addition, mode 1 coefficients showed high coefficients of variation (COV) at high pressure differences. For instance, the COV of mode 1 coefficients was 4.42 % and 5.38 % for 300 and 600 mm$H_2O$ at valve lift 10 mm, respectively. This illustrated, in a quantitative manner, that there was larger snapshot-to-snapshot variation at high pressure difference than at lower ones. This was attributed to the fact that higher pressure differences resulted in more air coming into the cylinder with higher velocities and subsequently more turbulence.

The interaction between the air motion and the fuel spray and hence the spatial and temporal evolution of the air/fuel mixture was investigated by means of simultaneous PIV and high-speed Shadowgraph. The effects of injection pressure and pressure difference across the air intake valves on the interaction process were investigated at valve lift 10 mm where the tumble vortex was fully developed. The results revealed that for the centrally mounted injector position, the intake generated tumble motion affected the trajectory of the injected spray significantly by diverting the spray plume towards the cylinder wall (exhaust side) particularly at high pressure differences. Further, the spray plume exhibited shorter penetrations under the effect of air flow than those shown under static injection conditions. This was attributed to the momentum exchange that occurred between the in-cylinder flow and the spray. This momentum exchange increased with the increase in the pressure difference across the intake valves. This, in turn, improved the breakup of the fuel spray and hence the mixing process resulting in a more homogeneous charge.

## 5.2 Contribution of the Present Work

The major contribution of this study is summarized as follows:

- The introduction of high-speed time-resolved stereoscopic PIV to an engine flow field on a flow rig which allowed the recording of all three velocity components within different measuring vertical tumble planes. Comprehensive investigations were conducted on the main factors that affect the flow behaviour inside a cylinder of modern GDI engines.

- The acquired steady-state measurements are a good source to validate the numerical tools as Reynolds-averaged Navier-Stokes (RANS) and large-eddy simulations (LES) without the added complexity of cycle-to-cycle variability which occur in real engine operation.

- The combination of the steady-state flow rig, the high-speed time-resolved particle image velocimetry (PIV) and the powerful statistical analysis proper

orthogonal decomposition (POD) technique offered a new insight into in-cylinder flows and can be utilized as new engine research tool.

- The data on the spray-flow interaction provides an important insight into the mixture preparation process in GDI engines and helps in the design optimisation of these engines.

### 5.3 Recommendations for Future Works

The following are some thoughts that would be of interest for future work:

- The flow structures captured within this set-up could also be compared to the flow structures captured within motored optical engines. This is speculated to confirm the suitability of steady flow laser-based testing as a method for future engine design.

- Although good expertise has been gained in the understanding of the intake generated flow topology for pure tumble engines, many modern cylinder heads tend to produce a mixture of both swirl and tumble. More work is therefore necessary in this direction.

- The air/spray interaction measurements can be extended to use two-phase stereoscopic PIV relying on a dual camera scope and image intensifier. The DaulScope provides separate imaging visualization of liquid phase and gas phase. This is speculated to add more quantitative information about the air and fuel distribution inside the engine cylinder.

LIST OF PUBLICATIONS

| | JOURNAL | STATUS | INDEXING |
|---|---|---|---|
| 1 | **Mohammed El-Adawy**, M. R. Heikal, A. Rashid A. Aziz, M. I. Siddiqui, and Hasanain A. Abdul Wahhab. "Experimental study on an IC engine in-cylinder flow using different steady-state flow benches." Alexandria Engineering Journal" 56, no. 4 (2017): 727-736. | 2017, Published | ISI |
| 2 | **Mohammed El-Adawy**, Morgan R. Heikal, A. Rashid A Aziz, Muhammad I. Siddiqui, and Shahzad Munir. "Characterization of the Inlet Port Flow under Steady-State Conditions Using PIV and POD." Energies" 10, no. 12 (2017): 1950. | 2017, Published | ISI, IF:2.676 |
| 3 | **Mohammed El-Adawy**, M. R. Heikal, A. Rashid A. Aziz, S. Munir, and M. I. Siddiqui. "Effect of Boost Pressure on the In-Cylinder Tumble-Motion of GDI Engine under Steady-State Conditions using Stereoscopic-PIV." Journal of Applied Fluid Mechanics 11, no. 3 (2018): 733-742. | 2018, Published | ISI, IF:1.1 |
| 4 | **Mohammed El-Adawy**, Morgan Heikal, A. rashid A. Aziz, Ibrahim Adam, Mhadi Ismael, Mohammed Babiker, Masri Baharom, and Ezrann Abidin. "On the Application of Proper Orthogonal Decomposition (POD) for In-Cylinder Flow Analysis." Energies 11, no. 9 (2018): 2261. | 2018, Published | ISI, IF:2.676 |
| 5 | **Mohammed El-Adawy**, M. Heikal, A. Rashid. A. Aziz" Experimental Investigation of the In-Cylinder Tumble Motion inside GDI cylinder at Different Planes under Steady-State Condition using Stereoscopic-PIV," Journal of Applied Fluid Mechanics, 2019. | 2018, Published | ISI, IF:1.1 |

| | | | |
|---|---|---|---|
| 6 | **Mohammed El-Adawy**, M. Heikal, A. Rashid. A. Aziz" Stereoscopic Particle Image Velocimetry Measurements and Proper Orthogonal decomposition Analysis of the In-Cylinder Flow of Gasoline Direct Injection Engine," Journal of Energy Resources Technology, DOI: 10.1115/1.4042068, 2018. | 2018, Published | ISI, IF:2.2 |
| 7 | **Mohammed El-Adawy**, M. Heikal, A. Rashid. A. Aziz" On the Application of High-Speed Time-Resolved Particle Image Velocimetry (PIV) for Air/Spray Interaction Analysis," International Journal of Multiphase Flow, 2019. | 2019, Under Review | ISI, IF:2.6 |
| 8 | **Mohammed El-Adawy**, M. Heikal, A. Rashid. A. Aziz, Nick Tiney, Mullineux James" Particle Image Velocimetry-Ricardo VECTIS CFD Validation," Journal of Energy Resources Technology, 2019. | 2019, Under Review | ISI, IF:2.2 |

| | **CONFERENCE** | **STATUS** | **INDEXING** |
|---|---|---|---|
| 1 | **Mohammed El-Adawy**, M. Heikal, A. Rashid. A. Aziz, " Tumble Motion Evolution for GDI Engine Using Particle Image Velocimetry (PIV) ", Journal of Mechanical Engineering, Vol SI 7 (1), 191-201, 2018. | 2017, Published | Scopus |
| 2 | **Mohammed El-Adawy**, M. Heikal, A. Rashid. A. Aziz, " Characterization of the effect of pressure difference on in-cylinder flow field using proper orthogonal decomposition (POD)," 6th International Conference on Production, Energy and Reliability 2018AIP Conf. Proc. 2035, 040004-1–040004-6; https://doi.org/10.1063/1.5075568. | 2018, Published | Scopus |

# REFERENCES


[1] A. Hasan *et al.*, "Control of harmful hydrocarbon species in the exhaust of modern advanced GDI engines," *Atmospheric Environment* vol. 129, pp. 210-217, 2016.

[2] L. Teodosio, D. Pirrello, F. Berni, V. De Bellis, R. Lanzafame, and A. D'Adamo, "Impact of intake valve strategies on fuel consumption and knock tendency of a spark ignition engine," *Applied Energy,* vol. 216, pp. 91-104, 2018.

[3] H. E. Institute., *Traffic-related air pollution: a critical review of the literature on emissions, exposure, and health effects* (no. 17). Health Effects Institute.Panel on the Health Effects of Traffic-Related Air Pollution, 2010.

[4] T. Berntsen and J. Fuglestvedt, "Global temperature responses to current emissions from the transport sectors," *Proceedings of the National Academy of Sciences* p. pnas. 0804844105, 2008.

[5] H. Zhuang and D. L. Hung, "Characterization of the effect of intake air swirl motion on time-resolved in-cylinder flow field using quadruple proper orthogonal decomposition," *Energy conversion management* vol. 108, pp. 366-376, 2016.

[6] https://www.delphi.com/innovations#emissionstandards-2017-2018, "Passenger Cars & Light Duty Vehicles.."

[7] Z. Zhang, H. Zhang, T. Wang, and M. Jia, "Effects of tumble combined with EGR (exhaust gas recirculation) on the combustion and emissions in a spark ignition engine at part loads," *Energy* vol. 65, pp. 18-24, 2014.

[8] S. Kim, Y. Yan, J. Nouri, and C. Arcoumanis, "Effects of intake flow and coolant temperature on the spatial fuel distribution in a direct-injection gasoline engine by PLIF technique," *Fuel* vol. 106, pp. 737-748, 2013.

[9] F. Brusiani, S. Falfari, and G. Cazzoli, "Tumble motion generation in small gasoline engines: A new methodological approach for the analysis of the influence of the intake duct geometrical parameters," *Energy Procedia* vol. 45, pp. 997-1006, 2014.

[10] S. Buhl *et al.*, "A combined numerical and experimental study of the 3D tumble structure and piston boundary layer development during the intake stroke of a gasoline engine," *Flow, Turbulence Combustion* vol. 98, no. 2, pp. 579-600, 2017.

[11] T. Wang, D. Liu, B. Tan, G. Wang, and Z. Peng, "An investigation into in-cylinder tumble flow characteristics with variable valve lift in a gasoline engine," *Flow, Turbulence Combustion* vol. 94, no. 2, pp. 285-304, 2015.

[12] A. C. Clenci, V. Iorga-Simăn, M. Deligant, P. Podevin, G. Descombes, and R. Niculescu, "A CFD (computational fluid dynamics) study on the effects of operating an engine with low intake valve lift at idle corresponding speed," *Energy* vol. 71, pp. 202-217, 2014.

[13] M. Baratta *et al.*, "Experimental and numerical approaches for the quantification of tumble intensity in high-performance SI engines," *Energy Conversion,* vol. 138, pp. 435-451, 2017.

[14] B. M. Krishna and J. Mallikarjuna, "Effect of engine speed on in-cylinder tumble flows in a motored internal combustion engine—an experimental investigation using particle image velocimetry," *J. Appl. Fluid Mech* vol. 4, no. 1, pp. 1-14, 2011.

[15] K. Bizon, G. Continillo, E. Mancaruso, S. Merola, and B. Vaglieco, "POD-based analysis of combustion images in optically accessible engines," *Combustion flame* vol. 157, no. 4, pp. 632-640, 2010.

[16] B. Peterson and V. Sick, "Simultaneous flow field and fuel concentration imaging at 4.8 kHz in an operating engine," *Applied Physics B* vol. 97, no. 4, p. 887, 2009.

[17] K. Lee, C. Bae, and K. Kang, "The effects of tumble and swirl flows on flame propagation in a four-valve SI engine," *Applied thermal engineering* vol. 27, no. 11-12, pp. 2122-2130, 2007.

[18] J. Fu, G. Zhu, F. Zhou, J. Liu, Y. Xia, and S. Wang, "Experimental investigation on the influences of exhaust gas recirculation coupling with intake tumble on gasoline engine economy and emission performance," *Energy Conversion Management* vol. 127, pp. 424-436, 2016.

[19] J. Rabault, J. A. Vernet, B. Lindgren, and P. H. Alfredsson, "A study using PIV of the intake flow in a diesel engine cylinder," *nternational Journal of Heat Fluid Flow* vol. 62, pp. 56-67, 2016.

[20] P. Saha, G. Biswas, A. Mandal, and S. Sarkar, "Investigation of coherent structures in a turbulent channel with built-in longitudinal vortex generators," *International Journal of Heat Mass Transfer* vol. 104, pp. 178-198, 2017.
[21] R. Antonia, "Conditional sampling in turbulence measurement," *Annual review of fluid mechanics,* vol. 13, no. 1, pp. 131-156, 1981.
[22] R. J. Adrian and P. Moin, "Stochastic estimation of organized turbulent structure: homogeneous shear flow," *Journal of Fluid Mechanics,* vol. 190, pp. 531-559, 1988.
[23] Z. Liu, R. Adrian, and T. Hanratty, "Large-scale modes of turbulent channel flow: transport and structure," *Journal of Fluid Mechanics* vol. 448, pp. 53-80, 2001.
[24] J. Zhou, R. J. Adrian, S. Balachandar, and T. Kendall, "Mechanisms for generating coherent packets of hairpin vortices in channel flow," *Journal of fluid mechanics,* vol. 387, pp. 353-396, 1999.
[25] J. L. Lumley, "The structure of inhomogeneous turbulent flows," *Atmospheric turbulence radio wave propagation* 1967.
[26] F. Zentgraf, E. Baum, B. Böhm, A. Dreizler, and B. Peterson, "On the turbulent flow in piston engines: Coupling of statistical theory quantities and instantaneous turbulence," *Physics of Fluids* vol. 28, no. 4, p. 045108, 2016.
[27] B. Peterson, E. Baum, C.-P. Ding, D. Michaelis, A. Dreizler, and B. Böhm, "Assessment and application of tomographic PIV for the spray-induced flow in an IC engine," *Proceedings of the Combustion Institute* vol. 36, no. 3, pp. 3467-3475, 2017.
[28] J. Bode, J. Schorr, C. Krüger, A. Dreizler, and B. Böhm, "Influence of three-dimensional in-cylinder flows on cycle-to-cycle variations in a fired stratified DISI engine measured by time-resolved dual-plane PIV," *Proceedings of the Combustion Institute* vol. 36, no. 3, pp. 3477-3485, 2017.
[29] W. Zeng, M. Sjöberg, D. L. Reuss, and Z. Hu, "High-speed PIV, spray, combustion luminosity, and infrared fuel-vapor imaging for probing tumble-flow-induced asymmetry of gasoline distribution in a spray-guided stratified-charge DISI engine," *Proceedings of the Combustion Institute* vol. 36, no. 3, pp. 3459-3466, 2017.
[30] X. Zhang, T. Wang, M. Jia, W. Li, L. Cui, and X. Zhang, "The Interactions of In-Cylinder Flow and Fuel Spray in a Gasoline Direct Injection Engine With Variable Tumble," *Journal of Engineering for Gas Turbines Power* vol. 137, no. 7, p. 071507, 2015.
[31] W. Zeng, M. Sjöberg, D. L. Reuss, and Z. Hu, "The role of spray-enhanced swirl flow for combustion stabilization in a stratified-charge DISI engine," *Combustion Flame* vol. 168, pp. 166-185, 2016.
[32] B. Peterson, D. L. Reuss, and V. Sick, "On the ignition and flame development in a spray-guided direct-injection spark-ignition engine," *Combustion Flame* vol. 161, no. 1, pp. 240-255, 2014.
[33] W. Zeng, M. Sjöberg, and D. Reuss, "Using PIV measurements to determine the role of the in-cylinder flow field for stratified DISI engine combustion," *SAE International Journal of Engines,* vol. 7, no. 2, pp. 615-632, 2014.
[34] H. Chen, P. M. Lillo, and V. Sick, "Three-dimensional spray–flow interaction in a spark-ignition direct-injection engine," *International Journal of Engine Research* vol. 17, no. 1, pp. 129-138, 2016.
[35] W. Zeng, M. Sjöberg, and D. L. Reuss, "Combined effects of flow/spray interactions and EGR on combustion variability for a stratified DISI engine," *Proceedings of the Combustion Institute* vol. 35, no. 3, pp. 2907-2914, 2015.
[36] F. Zentgraf, E. Baum, B. Böhm, A. Dreizler, and B. Peterson, "On the turbulent flow in piston engines: Coupling of statistical theory quantities and instantaneous turbulence," *Physics of Fluids,* vol. 28, no. 4, p. 045108, 2016.
[37] T. Justham, S. Jarvis, A. Clarke, C. Garner, G. Hargrave, and N. Halliwell, "Simultaneous study of intake and in-cylinder IC engine flow fields to provide an insight into intake induced cyclic variations," in *Journal of Physics: Conference Series*, 2006, vol. 45, no. 1, p. 146: IOP Publishing.
[38] N. Ozdor, M. Dulger, and E. Sher, "Cyclic variability in spark ignition engines a literature survey," *SAE transactions,* pp. 1514-1552, 1994.
[39] H. Chen, D. L. Reuss, and V. Sick, "On the use and interpretation of proper orthogonal decomposition of in-cylinder engine flows," *Measurement Science Technology* vol. 23, no. 8, p. 085302, 2012.

[40] C. Pera, V. Knop, and J. Reveillon, "Influence of flow and ignition fluctuations on cycle-to-cycle variations in early flame kernel growth," *Proceedings of the Combustion Institute* vol. 35, no. 3, pp. 2897-2905, 2015.
[41] R. Stiehl, J. Schorr, C. Krüger, A. Dreizler, and B. Böhm, "In-cylinder flow and fuel spray interactions in a stratified spray-guided gasoline engine investigated by high-speed laser imaging techniques," *Flow, turbulence combustion* vol. 91, no. 3, pp. 431-450, 2013.
[42] B. Peterson, D. L. Reuss, and V. Sick, "High-speed imaging analysis of misfires in a spray-guided direct injection engine," *Proceedings of the Combustion Institute* vol. 33, no. 2, pp. 3089-3096, 2011.
[43] R. Stiehl, J. Bode, J. Schorr, C. Krüger, A. Dreizler, and B. Böhm, "Influence of intake geometry variations on in-cylinder flow and flow–spray interactions in a stratified direct-injection spark-ignition engine captured by time-resolved particle image velocimetry," *International Journal of Engine Research,* vol. 17, no. 9, pp. 983-997, 2016.
[44] S. Müller, B. Böhm, M. Gleißner, R. Grzeszik, S. Arndt, and A. Dreizler, "Flow field measurements in an optically accessible, direct-injection spray-guided internal combustion engine using high-speed PIV," *Experiments in fluids* vol. 48, no. 2, pp. 281-290, 2010.
[45] https://ricardo.com/.
[46] F. Zhao, M.-C. Lai, and D. L. Harrington, "Automotive spark-ignited direct-injection gasoline engines," *Progress in energy combustion science* vol. 25, no. 5, pp. 437-562, 1999.
[47] J. D. Smith and V. Sick, "A multi-variable high-speed imaging study of ignition instabilities in a spray-guided direct-injected spark-ignition engine," SAE Technical Paper0148-7191, 2006.
[48] T. Kim, J. Song, J. Park, and S. Park, "Numerical and experimental study on effects of fuel injection timings on combustion and emission characteristics of a direct-injection spark-ignition gasoline engine with a 50 MPa fuel injection system," *Applied Thermal Engineering,* 2018.
[49] S. Chincholkar and J. Suryawanshi, "Gasoline Direct Injection: An Efficient Technology," *Energy Procedia* vol. 90, pp. 666-672, 2016.
[50] B. Harshavardhan and J. Mallikarjuna, "Effect of piston shape on in-cylinder flows and air–fuel interaction in a direct injection spark ignition engine–A CFD analysis," *Energy* vol. 81, pp. 361-372, 2015.
[51] A. C. Alkidas and S. H. El Tahry, "Contributors to the fuel economy advantage of DISI engines over PFI engines," SAE Technical Paper0148-7191, 2003.
[52] T. Kume, Y. Iwamoto, K. Iida, M. Murakami, K. Akishino, and H. Ando, "Combustion control technologies for direct injection SI engine," SAE technical paper0148-7191, 1996.
[53] Z. Zheng, C. Liu, X. Tian, and X. Zhang, "Numerical study of the effect of piston top contour on GDI engine performance under catalyst heating mode," *Fuel,* vol. 157, pp. 64-72, 2015.
[54] R. Ortmann, S. Arndt, J. Raimann, R. Grzeszik, and G. Würfel, "Methods and analysis of fuel injection, mixture preparation and charge stratification in different direct injected SI engines," SAE Technical Paper0148-7191, 2001.
[55] S. Stefan, "Optical Diagnostics on FSI Transparent Engine," in *FISITA World Automotive Congress, Barcelona*, 2004, pp. 23-27.
[56] K. Kawajiri, T. Yonezawa, H. Ohuchi, M. Sumida, and H. Katashiba, "Study of interaction between spray and air motion, and spray wall impingement," SAE Technical Paper0148-7191, 2002.
[57] J. T. Kashdan, S. Mendez, and G. Bruneaux, "On the origin of unburned hydrocarbon emissions in a wall guided, low NOx diesel combustion system," *SAE Transactions* pp. 234-257, 2007.
[58] H. Kubach, J. Gindele, and U. Spicher, "Investigations of mixture formation and combustion in gasoline direct injection engines," SAE Technical Paper0148-7191, 2001.
[59] H. Baecker, A. Kaufmann, and M. Tichy, "Experimental and simulative investigation on stratification potential of spray-guided GDI combustion systems," SAE Technical Paper0148-7191, 2007.
[60] S. Soid and Z. Zainal, "Spray and combustion characterization for internal combustion engines using optical measuring techniques–A review," *Energy* vol. 36, no. 2, pp. 724-741, 2011.
[61] C. Wang, H. Xu, J. M. Herreros, J. Wang, and R. Cracknell, "Impact of fuel and injection system on particle emissions from a GDI engine," *Applied Energy* vol. 132, pp. 178-191, 2014.
[62] A. R. G. S. Raj and V. Mallikarjuna, "Energy efficient piston configuration for effective air motion–A CFD study," *Applied Energy* vol. 102, pp. 347-354, 2013.
[63] J. B. Heywood, "Internal combustion engine fundamentals," 1988.

[64] M. Faure, M. Heikel, and N. Jackson, "Three-dimensional in-cylinder flow maps using two-dimensional PIV system," in *IMECHE CONFERENCE TRANSACTIONS*, 1996, vol. 3, pp. 147-156: MECHANICAL ENGINEERING PUBLICATIONS.

[65] S. Bari and I. Saad, "CFD modelling of the effect of guide vane swirl and tumble device to generate better in-cylinder air flow in a CI engine fuelled by biodiesel," *Computers Fluids* vol. 84, pp. 262-269, 2013.

[66] J. Martins, B. S. Ribeiro, and S. Teixeira, "In-cylinder swirl analysis of different strategies on over-expanded cyclies," 2009.

[67] T. Wang, W. Li, M. Jia, D. Liu, W. Qin, and X. Zhang, "Large-eddy simulation of in-cylinder flow in a DISI engine with charge motion control valve: Proper orthogonal decomposition analysis and cyclic variation," *Applied Thermal Engineering* vol. 75, pp. 561-574, 2015.

[68] Y. Li, H. Zhao, Z. Peng, and N. Ladommatos, "Analysis of tumble and swirl motions in a four-valve SI engine," SAE Technical Paper0148-7191, 2001.

[69] R. Szengel, H. Middendorf, E. Pott, J. Theobald, T. Etzrodt, and R. Krebs, "The TSI with 88 kW-the expansion of the Volkswagen family of fuel-efficient gasoline engines," *FORTSCHRITT BERICHTE-VDI REIHE 12 VERKEHRSTECHNIK FAHRZEUGTECHNIK* vol. 639, no. 2, p. 113, 2007.

[70] A. S. Krishna, J. Mallikarjuna, and D. Kumar, "Effect of engine parameters on in-cylinder flows in a two-stroke gasoline direct injection engine," *Applied energy* vol. 176, pp. 282-294, 2016.

[71] H. Xu, "Some critical technical issues on the steady flow testing of cylinder heads," SAE Technical Paper0148-7191, 2001.

[72] S. Binjuwair, "Characterisation of flow structures inside an engine cylinder under steady state condition," © Saud Binjuwair, 2013.

[73] J. Ricardo, "Steady state flowbench port performance measurement and analysis techniques," *Report DP93/* 1993.

[74] D. Liu, M. Jia, T. Wang, P. Zhao, S. Jin, and S. Liu, "Insights into the development of the tumble motion using the direct and indirect steady-flow test methods," *Proceedings of the Institution of Mechanical Engineers, Part D: Journal of Automobile Engineering,* vol. 228, no. 13, pp. 1530-1546, 2014.

[75] C. Arcoumanis, J. Nouri, H. Xu, and R. Stone, "Analysis of the Steady Flow Characteristics of Tumble-Generating Four-Valve Cylinder Heads," *Opt. Diagnost. Eng,* vol. 2, no. 2, pp. 71-83, 1997.

[76] A. K. Agarwal, S. Gadekar, and A. P. Singh, "In-Cylinder Flow Evolution Using Tomographic Particle Imaging Velocimetry in an Internal Combustion Engine," *Journal of Energy Resources Technology,* vol. 140, no. 1, p. 012207, 2018.

[77] P. Stansfield, G. Wigley, T. Justham, J. Catto, and G. Pitcher, "PIV analysis of in-cylinder flow structures over a range of realistic engine speeds," *Experiments in fluids,* vol. 43, no. 1, pp. 135-146, 2007.

[78] P. A. Stansfield *et al.*, "Unthrottled engine operation using variable valve actuation: the impact on the flow field, mixing and combustion," SAE Technical Paper0148-7191, 2007.

[79] J. E. Rimmer, "An optical investigation into the effect of fuel spray, turbulent flow and flame propagation on DISI engine performance," © JET Rimmer, 2011.

[80] A. C. Yunus and J. M. Cimbala, "Fluid mechanics fundamentals and applications," *International Edition, McGraw Hill Publication* vol. 185201, 2006.

[81] Y. Yeh and H. Cummins, "Localized fluid flow measurements with an He–Ne laser spectrometer," *Applied Physics Letters* vol. 4, no. 10, pp. 176-178, 1964.

[82] W. Kim, K. Huth, J. Lee, and K. Kang, "Numerical simulation of intake and compression flow in a four-valve pent-roof spark ignition engine and validation with LDV data," *Proceedings of the Institution of Mechanical Engineers, Part D: Journal of Automobile Engineering* vol. 214, no. 4, pp. 361-372, 2000.

[83] Y.-f. Li, S.-l. Liu, S. Shi, M. Feng, and X. Sui, "An investigation of in-cylinder tumbling motion in a four-valve spark ignition engine," *Proceedings of the Institution of Mechanical Engineers, Part D: Journal of Automobile Engineering* vol. 215, no. 2, pp. 273-284, 2001.

[84] A. Bicen, C. Vafidis, and J. Whitelaw, "Steady and unsteady airflow through the intake valve of a reciprocating engine," *Journal of Fluids Engineering,* vol. 107, no. 3, pp. 413-420, 1985.

[85] C. J. Pickering and N. A. Halliwell, "Speckle photography in fluid flows: signal recovery with two-step processing," *Applied optics,* vol. 23, no. 8, pp. 1128-1129, 1984.

[86] R. J. Adrian, "Scattering particle characteristics and their effect on pulsed laser measurements of fluid flow: speckle velocimetry vs particle image velocimetry," *Applied optics,* vol. 23, no. 11, pp. 1690-1691, 1984.
[87] M. Raffel, C. E. Willert, and J. Kompenhans, *Particle image velocimetry: a practical guide*. Springer Science & Business Media, 2007.
[88] R. J. Adrian and J. Westerweel, *Particle image velocimetry* (no. 30). Cambridge University Press, 2011.
[89] M. Buschbeck, N. Bittner, T. Halfmann, and S. Arndt, "Dependence of combustion dynamics in a gasoline engine upon the in-cylinder flow field, determined by high-speed PIV," *Experiments in fluids* vol. 53, no. 6, pp. 1701-1712, 2012.
[90] I. Bücker, D.-C. Karhoff, M. Klaas, and W. Schröder, "Stereoscopic multi-planar PIV measurements of in-cylinder tumbling flow," *Experiments in fluids,* vol. 53, no. 6, pp. 1993-2009, 2012.
[91] R. Goldstein, *Fluid mechanics measurements*. Routledge, 2017.
[92] H.-E. Albrecht, N. Damaschke, M. Borys, and C. Tropea, *Laser Doppler and phase Doppler measurement techniques*. Springer Science & Business Media, 2013.
[93] D. L. Reuss, R. J. Adrian, C. C. Landreth, D. T. French, and T. D. Fansler, "Instantaneous planar measurements of velocity and large-scale vorticity and strain rate in an engine using particle-image velocimetry," SAE Technical Paper0148-7191, 1989.
[94] H. Chen, H. Zhuang, D. Reuss, and V. Sick, "Influence of Early and Late Fuel Injection on Air Flow Structure and Kinetic Energy in an Optical SIDI Engine," 2018.
[95] J. Bode, J. Schorr, C. Krüger, A. Dreizler, and B. Böhm, "Influence of the in-cylinder flow on cycle-to-cycle variations in lean combustion DISI engines measured by high-speed scanning-PIV," *Proceedings of the Combustion Institute* 2018.
[96] F. Brusiani, S. Falfari, and G. Cazzoli, "Tumble motion generation in small gasoline engines: A new methodological approach for the analysis of the influence of the intake duct geometrical parameters," *Energy Procedia,* vol. 45, pp. 997-1006, 2014.
[97] M. Kim, S. Lee, and W. Kim, "Tumble flow measurements using three different methods and its effects on fuel economy and emissions," in *ASME 2006 Internal Combustion Engine Division Spring Technical Conference*, 2006, pp. 267-277: American Society of Mechanical Engineers.
[98] F. Millo, S. Luisi, F. Borean, and A. Stroppiana, "Numerical and experimental investigation on combustion characteristics of a spark ignition engine with an early intake valve closing load control," *Fuel* vol. 121, pp. 298-310, 2014.
[99] F. Payri, J. Benajes, X. Margot, and A. Gil, "CFD modeling of the in-cylinder flow in direct-injection Diesel engines," *Computers fluids* vol. 33, no. 8, pp. 995-1021, 2004.
[100] S. Falfari, F. Brusiani, and P. Pelloni, "3D CFD analysis of the influence of some geometrical engine parameters on small PFI engine performances–the effects on the tumble motion and the mean turbulent intensity distribution," *Energy Procedia* vol. 45, pp. 701-710, 2014.
[101] W. Zeng, S. Keum, T.-W. Kuo, and V. Sick, "Role of large scale flow features on cycle-to-cycle variations of spark-ignited flame-initiation and its transition to turbulent combustion," *Proceedings of the Combustion Institute* 2018.
[102] Y. Li, H. Zhao, B. Leach, T. Ma, and N. Ladommatos, "Characterization of an in-cylinder flow structure in a high-tumble spark ignition engine," *International Journal of Engine Research* vol. 5, no. 5, pp. 375-400, 2004.
[103] C. A. Gomes, R. B. R. da Costa, R. L. Franco, R. M. Valle, and R. Huebner, "PIV Measurements of In-Cylinder Tumble Flow in a Motored Single Cylinder Optical Research Engine," SAE Technical Paper0148-7191, 2015.
[104] R. B. R. da Costa, R. M. Braga, C. A. G. Júnior, R. M. Valle, and R. Huebner, "PIV measurements and numerical analysis of in-cylinder tumble flow in a motored engine," *Journal of the Brazilian Society of Mechanical Sciences Engineering* vol. 39, no. 10, pp. 3931-3945, 2017.
[105] B. M. Krishna and J. Mallikarjuna, "Comparative study of in-cylinder tumble flows in an internal combustion engine using different piston shapes—an insight using particle image velocimetry," *Experiments in fluids* vol. 48, no. 5, pp. 863-874, 2010.
[106] J. M. Mallikarjuna, "Effect of Manifold Orientation on Non-Reacting In-Cylinder Tumble Flows in an IC Engine with Pentroof Piston-An Investigation Using PIV," *SAE International Journal of Materials Manufacturing* vol. 3, no. 1, pp. 597-607, 2010.

[107] J. Dannemann, K. Pielhop, M. Klaas, and W. Schröder, "Cycle resolved multi-planar flow measurements in a four-valve combustion engine," *Experiments in fluids* vol. 50, no. 4, pp. 961-976, 2011.
[108] M. Zhang, M. Xu, and D. L. Hung, "Simultaneous two-phase flow measurement of spray mixing process by means of high-speed two-color PIV," *Measurement Science Technology* vol. 25, no. 9, p. 095204, 2014.
[109] G. Pitcher, S. Binjuwair, T. Picton-Turbervill, A. Wood, G. Wigley, and D. Hollis, "LDA and PIV Analyses and Comparison of In-Cylinder Flow Structures under Steady Flow Conditions," in *15th Int. Symp on Application of Laser Techniques to Fluid Mechanics, Lisbon*, 2010.
[110] S. Binjuwair, S. Ibrahim, G. Wigley, and G. Pitcher, "In-Cylinder Flow Structure Analysis by Particle Image Velocimetry Under Steady State Condition," SAE Technical Paper0148-7191, 2012.
[111] B. M. Krishna and J. Mallikarjuna, "Characterization of flow through the intake valve of a single cylinder engine using particle image velocimetry," 2010.
[112] G. Pitcher, "An investigation and comparison between standard steady flow measurements and those in a motored engine," © Graham Pitcher, 2013.
[113] B. Khalighi, "Multidimensional in-cylinder flow calculations and flow visualization in a motored engine," *Journal of fluids engineering* vol. 117, no. 2, pp. 282-288, 1995.
[114] B. Khalighi, S. El Tahry, D. Haworth, and M. Huebler, "Computation and measurement of flow and combustion in a four-valve engine with intake variations," *SAE transactions* pp. 611-644, 1995.
[115] S. Bari and I. Saad, "CFD modelling of the effect of guide vane swirl and tumble device to generate better in-cylinder air flow in a CI engine fuelled by biodiesel," *Computers Fluids* vol. 84, pp. 262-269, 2013.
[116] B. Harshavardhan and J. Mallikarjuna, "Effect of Combustion Chamber Shape on In-Cylinder Flow and Air-Fuel Interaction in a Direct Injection Spark Ignition Engine-A CFD Analysis," SAE Technical Paper0148-7191, 2015.
[117] Z. Zheng, H. Liu, and X. Tian, "Effects of throat area and inlet area of intake port on mixture formation of gasoline direct injection engines," *Proceedings of the Institution of Mechanical Engineers, Part D: Journal of Automobile Engineering* p. 0954407018762587, 2018.
[118] W. Qin, M. Xie, M. Jia, T. Wang, and D. Liu, "Large eddy simulation of in-cylinder turbulent flows in a DISI gasoline engine," *Applied Mathematical Modelling* vol. 38, no. 24, pp. 5967-5985, 2014.
[119] C. Catellani, G. Cazzoli, S. Falfari, C. Forte, and G. M. Bianchi, "Large Eddy simulation of a steady flow test bench using OpenFOAM®," *Energy Procedia,* vol. 101, pp. 622-629, 2016.
[120] X. Yang and T.-W. Kuo, "Correlation of CCV Between In-Cylinder Swirl Ratio and Polar Velocity Profile in Valve Seat Region Using LES Under Motored Engine Condition," *Oil Gas Sciences Technology–Revue d'IFP Energies nouvelles* vol. 72, no. 6, p. 38, 2017.
[121] H. Kahila *et al.*, "Large-eddy simulation on the influence of injection pressure in reacting Spray A," *Combustion Flame* vol. 191, pp. 142-159, 2018.
[122] A. Montorfano *et al.*, "Comparison of direct and large eddy simulations of the turbulent flow in a valve/piston assembly," *Flow, Turbulence Combustion* vol. 95, no. 2-3, pp. 461-480, 2015.
[123] M. Schmitt, C. E. Frouzakis, A. G. Tomboulides, Y. M. Wright, and K. Boulouchos, "Direct numerical simulation of multiple cycles in a valve/piston assembly," *Physics of Fluids* vol. 26, no. 3, p. 035105, 2014.
[124] A. Banaeizadeh, A. Afshari, H. Schock, F. Jaberi, and M. Transfer, "Large-eddy simulations of turbulent flows in internal combustion engines," *International Journal of Heat,* vol. 60, pp. 781-796, 2013.
[125] S. K. Robinson, "Coherent motions in the turbulent boundary layer," *Annual Review of Fluid Mechanics* vol. 23, no. 1, pp. 601-639, 1991.
[126] R. Adrian, K. Christensen, and Z.-C. Liu, "Analysis and interpretation of instantaneous turbulent velocity fields," *Experiments in fluids,* vol. 29, no. 3, pp. 275-290, 2000.
[127] S. Mallat, *A wavelet tour of signal processing*. Elsevier, 1999.
[128] H. Chen, D. L. Reuss, D. L. Hung, and V. Sick, "A practical guide for using proper orthogonal decomposition in engine research," *International Journal of Engine Research* vol. 14, no. 4, pp. 307-319, 2013.
[129] L. Sirovich, "Turbulence and the dynamics of coherent structures. I. Coherent structures," *Quarterly of applied mathematics,* vol. 45, no. 3, pp. 561-571, 1987.

[130] G. Berkooz, P. Holmes, and J. L. Lumley, "The proper orthogonal decomposition in the analysis of turbulent flows," *Annual review of fluid mechanics,* vol. 25, no. 1, pp. 539-575, 1993.
[131] H. P. Bakewell Jr and J. L. Lumley, "Viscous sublayer and adjacent wall region in turbulent pipe flow," *The Physics of Fluids,* vol. 10, no. 9, pp. 1880-1889, 1967.
[132] V. Sick, M. C. Drake, and T. D. Fansler, "High-speed imaging for direct-injection gasoline engine research and development," *Experiments in fluids* vol. 49, no. 4, pp. 937-947, 2010.
[133] V. Sick, "High speed imaging in fundamental and applied combustion research," *Proceedings of the Combustion Institute* vol. 34, no. 2, pp. 3509-3530, 2013.
[134] H. Chen, D. Hung, M. Xu, and J. Zhong, "Analyzing the cycle-to-cycle variations of pulsing spray characteristics by means of the proper orthogonal decomposition," *Atomization Sprays* vol. 23, no. 7, 2013.
[135] H. Chen, D. L. Hung, M. Xu, H. Zhuang, and J. Yang, "Proper orthogonal decomposition analysis of fuel spray structure variation in a spark-ignition direct-injection optical engine," *Experiments in fluids* vol. 55, no. 4, p. 1703, 2014.
[136] H. ZHUANG, D. L. HUNG, M. XU, and H. CHEN, "Analysis of spray structure and penetration variations using proper orthogonal decomposition," in *The 16th Conference of ILASS-Asia*, 2013, vol. 22, pp. 158-63.
[137] H. Zhuang, D. L. Hung, and H. Chen, "Study of time-resolved vortex structure of in-cylinder engine flow fields using proper orthogonal decomposition technique," *Journal of Engineering for Gas Turbines Power* vol. 137, no. 8, p. 082604, 2015.
[138] H. Zhuang, D. L. Hung, J. Yang, and S. Tian, "Investigation of Swirl Ratio Impact on In-Cylinder Flow in an SIDI Optical Engine," *Journal of Engineering for Gas Turbines Power* vol. 138, no. 8, p. 081505, 2016.
[139] M. Fogleman, J. Lumley, D. Rempfer, and D. Haworth, "Application of the proper orthogonal decomposition to datasets of internal combustion engine flows," *Journal of Turbulence,* vol. 5, no. 23, pp. 1-3, 2004.
[140] K. Liu, D. C. Haworth, X. Yang, and V. Gopalakrishnan, "Large-eddy simulation of motored flow in a two-valve piston engine: POD analysis and cycle-to-cycle variations," *Flow, turbulence combustion* vol. 91, no. 2, pp. 373-403, 2013.
[141] P. Abraham *et al.*, "Evaluating large-eddy simulation (LES) and high-speed particle image velocimetry (PIV) with phase-invariant proper orthogonal decomposition (POD)," vol. 69, no. 1, pp. 41-59, 2014.
[142] H. Chen, M. Xu, and D. L. Hung, "Analyzing in-cylinder flow evolution and variations in a spark-ignition direct-injection engine using phase-invariant proper orthogonal decomposition technique," SAE Technical Paper0148-7191, 2014.
[143] S. G. Tuttle, C. D. Carter, and K.-Y. Hsu, "Particle image velocimetry in a nonreacting and reacting high-speed cavity," *Journal of Propulsion Power* vol. 30, no. 3, pp. 576-591, 2014.
[144] F. Chen, H. Liu, Z. Yang, and H. Hu, "Tracking characteristics of tracer particles for PIV measurements in supersonic flows," *Chinese Journal of Aeronautics,* vol. 30, no. 2, pp. 577-585, 2017.
[145] F. Chen and H. Liu, "Particle image velocimetry for combustion measurements: Applications and developments," *Chinese Journal of Aeronautics,* 2018.
[146] J. Rabault, "PIV Investigation of the Intake Flow in a Parallel Valves Diesel Engine Cylinder," ed, 2015.
[147] L. E. J. C. Drain, Sussex, England and W.-I. New York, . 250 p., "The laser doppler techniques," 1980.
[148] H. Tennekes, J. L. Lumley, and J. Lumley, *A first course in turbulence*. MIT press, 1972.
[149] R. J. Adrian, "Particle-imaging techniques for experimental fluid mechanics," *Annual review of fluid mechanics,* vol. 23, no. 1, pp. 261-304, 1991.
[150] https://www.dantecdynamics.com/.
[151] https://www.lavision.de/en/.
[152] H. W. Coleman and W. G. Steele, *Experimentation, validation, and uncertainty analysis for engineers*. John Wiley & Sons, 2018.
[153] M. Megerle, V. Sick, and D. L. Reuss, "Measurement of digital particle image velocimetry precision using electro-optically created particle-image displacements," *Measurement Science Technology* vol. 13, no. 7, p. 997, 2002.
[154] R. D. Keane and R. J. Adrian, "Optimization of particle image velocimeters. I. Double pulsed systems," *Measurement science technology* vol. 1, no. 11, p. 1202, 1990.

[155] J. Westerweel, "Fundamentals of digital particle image velocimetry," *Measurement science technology* vol. 8, no. 12, p. 1379, 1997.
[156] A. Sciacchitano, B. Wieneke, and F. Scarano, "PIV uncertainty quantification by image matching," *Measurement Science Technology* vol. 24, no. 4, p. 045302, 2013.
[157] D. C. J. A. o. V. Bjorkquist, "Particle Image Velocimetry," vol. 313, 1993.
[158] D. L. Reuss, "Cyclic variability of large-scale turbulent structures in directed and undirected IC engine flows," *SAE transactions,* pp. 128-145, 2000.
[159] P. Druault, P. Guibert, and F. Alizon, "Use of proper orthogonal decomposition for time interpolation from PIV data," *Experiments in fluids* vol. 39, no. 6, pp. 1009-1023, 2005.
[160] R. Huang, C. Huang, S. Chang, H. Yang, T. Lin, and W. Hsu, "Topological flow evolutions in cylinder of a motored engine during intake and compression strokes," *Journal of Fluids Structures* vol. 20, no. 1, pp. 105-127, 2005.
[161] P. Holmes, J. L. Lumley, G. Berkooz, and C. W. Rowley, *Turbulence, coherent structures, dynamical systems and symmetry*. Cambridge university press, 2012.
[162] W. Cazemier, R. Verstappen, and A. Veldman, "Proper orthogonal decomposition and low-dimensional models for driven cavity flows," *Physics of fluids,* vol. 10, no. 7, pp. 1685-1699, 1998.
[163] J. Whitelaw and H. Xu, "Cyclic variations in a lean-burn spark ignition engine without and with swirl," *SAE transactions* pp. 1202-1220, 1995.
[164] J. L. Lumley, *Engines: an introduction*. Cambridge University Press, 1999.
[165] A. K. Agarwal, S. Gadekar, and A. P. Singh, "In-Cylinder Flow Evolution Using Tomographic Particle Imaging Velocimetry in an Internal Combustion Engine," *Journal of Energy Resources Technology* vol. 140, no. 1, p. 012207, 2018.
[166] B. Khalighi, "Study of the intake tumble motion by flow visualization and particle tracking velocimetry," *Experiments in Fluids* vol. 10, no. 4, pp. 230-236, 1991.
[167] M. Söder, "Creation and destruction of in-cylinder flows: Large eddy simulations of the intake and the compression strokes," KTH Royal Institute of Technology, 2015.
[168] J. Vernet, "Detailed study of steady incylinder flow and turbulence using stereo-PIV," ed, 2012.
[169] S. Tanov, B. Johansson, M. Izadi Najafabadi, and H. Wang, "Analyzing Of In-Cylinder Flow Structures And Cyclic Variations Of Partially Premix Combustion In A Light Duty Engine," in *FISITA 2016 World Automotive Congress, F2016-ESYF-005*, 2016.
[170] W.-M. Ren and J. Nally, "Computations of hollow-cone sprays from a pressure-swirl injector," SAE Technical Paper0148-7191, 1998.
[171] A. Arbeau, R. Bazile, G. Charnay, and P. Gastaldi, "A new application of the particle image velocimetry (PIV) to the air entrainment in gasoline direct injection sprays," SAE Technical Paper0148-7191, 2004.
[172] Y. Liu, Y. Shen, Y. You, and F. Zhao, "Numerical simulation on spray atomization and fuel-air mixing process in a gasoline direct injection engine," SAE Technical Paper0148-7191, 2012.
[173] S. Bari, I. Saad, and Fluids, "CFD modelling of the effect of guide vane swirl and tumble device to generate better in-cylinder air flow in a CI engine fuelled by biodiesel," *Computers Fluids* vol. 84, pp. 262-269, 2013.

APPENDIX A

PROCESSED DATA AND RESULTS FOR BOTH FEV AND RICARDO FLOW RIGS

Table A1: Ricardo processed results

| **RICARDO PROCESSED RESULTS** | | | | | | | |
|---|---|---|---|---|---|---|---|
| **Valve Lift** | | **Port ΔP $mmH_2O$** | **Air Flow Rate $m^3/s$** | **SM Torque Nm $\times 10e\text{-}^3$** | **Flow Coefficient $C_f$** | **Discharge Coefficient $C_d$** | **Non-Dim Rig Tumble** |
| **Test [mm]** | **Non-Dim L/D** | | | | | | |
| 0 | 0 | 600 | 0 | 0 | 0 | 1 | 0 |
| 1 | 0.030 | 600 | 0.0151 | 0.00 | 0.088 | 1.032 | 0.000 |
| 2 | 0.059 | 600 | 0.0305 | -1.45 | 0.178 | 1.030 | -0.034 |
| 3 | 0.089 | 600 | 0.0454 | 03.73 | 0.264 | 1.005 | -0.058 |
| 4 | 0.119 | 600 | 0.0585 | 2.49 | 0.341 | 0.958 | 0.030 |
| 5 | 0.148 | 600 | 0.713 | 13.26 | 0.414 | 0.919 | 0.132 |
| 6 | 0.178 | 600 | 0.0832 | 25.89 | 0.484 | 0.882 | 0.221 |
| 7 | 0.208 | 600 | 0.0932 | 37.49 | 0.541 | 0.834 | 0.286 |
| 8 | 0.237 | 600 | 0.0999 | 54.27 | 0.579 | 0.771 | 0.386 |
| 9 | 0.267 | 600 | 0.1039 | 69.60 | 0.602 | 0.703 | 0.476 |

Table A2: FEV processed test data

| FEV PROCESSED TEST DATA | | | | | | | | |
|---|---|---|---|---|---|---|---|---|
| Valve Lift | | Port ΔP $mmH_2O$ | $A_{seat}$ $m^2$ | $A_V$ $m^2$ | $\rho_s$ $kg/m^3$ | Cs m/sec | $m^o_{theor.}$ $m^3/hr.$ | $R_{MFL}$ RPS |
| Test [mm] | Non-Dim L/D | | | | | | | |
| 0 | 0 | 600 | 0 | 0 | 0 | 0 | 1 | 0 |
| 1 | 0.030 | 600 | 0.0017 | 0.0001 | 0.00 | 0.088 | 1.032 | -5.14 |
| 2 | 0.059 | 600 | 0.0017 | 0.0003 | -1.45 | 0.178 | 1.030 | -8.48 |
| 3 | 0.089 | 600 | 0.0017 | 0.0004 | 03.73 | 0.264 | 1.005 | -9 |
| 4 | 0.119 | 600 | 0.0017 | 0.0006 | 2.49 | 0.341 | 0.958 | -5.67 |
| 5 | 0.148 | 600 | 0.0017 | 0.0008 | 13.26 | 0.414 | 0.919 | -1.52 |
| 6 | 0.178 | 600 | 0.0017 | 0.0009 | 25.89 | 0.484 | 0.882 | 3.4 |
| 7 | 0.208 | 600 | 0.0017 | 0.0011 | 37.49 | 0.541 | 0.834 | 12.15 |
| 8 | 0.237 | 600 | 0.0017 | 0.0013 | 54.27 | 0.579 | 0.771 | 19.18 |
| 9 | 0.267 | 600 | 0.0017 | 0.0015 | 69.60 | 0.602 | 0.703 | 36.06 |

Table A3: FEV processed test results

| FEV PROCESSED TEST RESULTS | | | | | | |
|---|---|---|---|---|---|---|
| Valve Lift | | Port ΔP $mmH_2O$ | Air Flow Rate $m^3/hr.$ | Flow Coefficient $C_f$ | Discharge Coefficient $C_d$ | Non-Dim Rig Tumble |
| Test [mm] | Non-Dim L/D | | | | | |
| 0 | 0 | 600 | 0 | 0 | 1 | 0 |
| 1 | 0.030 | 600 | 60 | 0.103 | 1.086 | -0.022 |
| 2 | 0.059 | 600 | 119.36 | 0.191 | 1.064 | -0.077 |
| 3 | 0.089 | 600 | 175.93 | 0.282 | 1.031 | -0.088 |
| 4 | 0.119 | 600 | 224.25 | 0.360 | 0.972 | -0.062 |
| 5 | 0.148 | 600 | 263.94 | 0.424 | 0.902 | -0.018 |
| 6 | 0.178 | 600 | 296.7 | 0.477 | 0.834 | 0.044 |
| 7 | 0.208 | 600 | 318.48 | 0.512 | 0.757 | 0.179 |
| 8 | 0.237 | 600 | 337.58 | 0.542 | 0.692 | 0.320 |
| 9 | 0.267 | 600 | 345.88 | 0.556 | 0.622 | 0.688 |

APPENDIX B

STEREOSCOPIC PIV PROCESSING

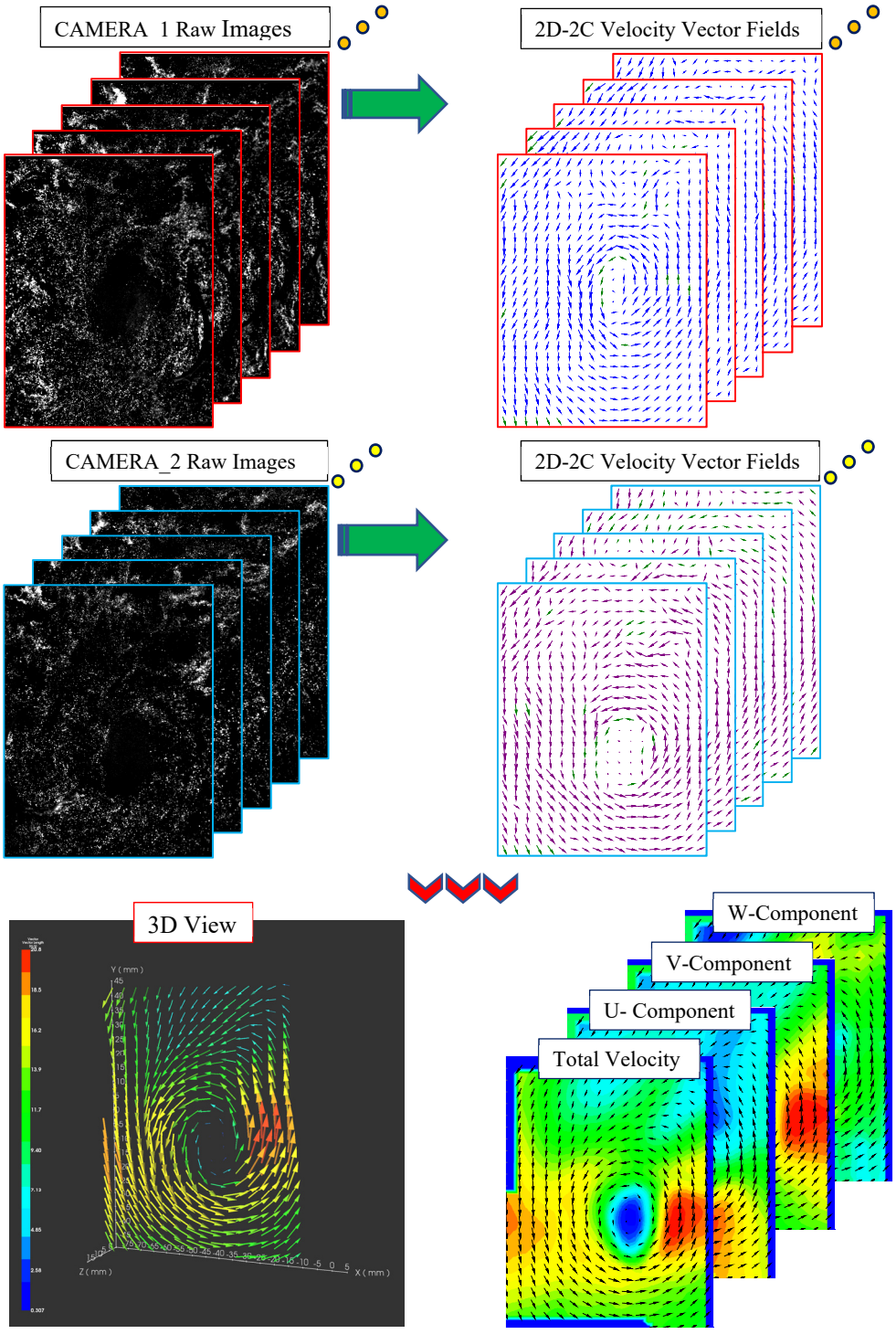


Figure B1: Vectors calculation process for stereoscopic PIV

# APPENDIX C

## POD MATLAB CODE

```
% read PIV data
clc
close all
clear all;
directory= 'POD3DVL9P600\';
files = dir(fullfile(directory, '*.txt'))
ns=length(files);
% number of samples
for n=1:ns;
disp(n);
fid=fopen([directory files(n).name]);
tmp=textscan(fid,'%s',6,'Delimiter','\n');
my_data = fscanf(fid,'%f',[5,inf]);
my_data=my_data';
x1=my_data(:,1);
size(x1)
y1=my_data(:,2);
u1=my_data(:,3);
v1=my_data(:,4);
w1=my_data(:,5);
M=34;
N=46;
x = reshape(x1,M,N);
y = reshape(y1,M,N);
u(:,:,n)=reshape(u1,M,N);
v(:,:,n)=reshape(v1,M,N);
w(:,:,n)=reshape(w1,M,N);
fclose(fid);
end
% Do POD analysis
close all
[nx,nj,ns]=size(u);
xmin=min(x(:));
xmax=max(x(:));
ymin=min(y(:));
ymax=max(y(:));
Um=mean(u,3);
Vm=mean(v,3);
Wm=mean(w,3);
Uf=u-repmat(Um,[1 1 ns]);
Vf=v-repmat(Vm,[1 1 ns]);
Wf=w-repmat(Wm,[1 1 ns]);
% end
% create matrix for all fluctuating velocity components for each
snapshot in a column
%
Uall=[reshape(Uf,nx*nj,ns);reshape(Vf,nx*nj,ns);reshape(Wf,nx*nj,ns];
Uall=[reshape(u,nx*nj,ns);reshape(v,nx*nj,ns);reshape(w,nx*nj,ns)];
% Do POD analysis
R=Uall'*Uall;          % Autocovariance matrix
[eV,D]=eig(R);         % solve: V is eigenvectors, D is eigenvalues
in diagonal matrix
```

```
[L,I]=sort(diag(D));   % sort eigenvalues in ascending order - I is
sorted index vector
for i=1:length(D)
eValue(length(D)+1-i)=L(i);       % Eigenvalues sorted in descending
order
eVec(:,length(D)+1-i)=eV(:,I(i)); % Eigenvectors sorted in the same
order
end;
eValue(length(eValue))=0;   % last eigenvalue should be zero - ensure
this to avoid problems
C=sum(eValue);
menergy=eValue(1:ns)/sum(eValue);
% calculate and plot the first m modes
m=50;
for i=1:m
tmpe=Uall*eVec(:,i);          % find mode m
phi(:,i)=tmpe/norm(tmpe);  % normalize mode
end;
clear tmpe;
a=phi'*Uall;   %calculate reconstruction coefficient
% a=phi'*Uall;
phiU=reshape(phi(1:nx*nj,:),nx,nj,m);            % extract U part of
modes
phiV=reshape(phi(nx*nj+1:2*nx*nj,:),nx,nj,m);    % extract V part of
modes
scale=1600;
for i=1:20
figure(i);
shading interp
axis tight
hold on;
quiver(x,y,phiU(:,:,i),phiV(:,:,i),4.7,'color', 'blue');
axis([xmin xmax ymin ymax]);
xlabel('x [mm]');
ylabel('y [mm]');
title(['POD mode no. ' num2str(i)]);
end
figure(i+1);
%plot(eValue(1:100)/sum(eValue))
bar(menergy,'r');
title('cumulative energy of POD modes')
xlabel('mode no.')
ylabel('relative energy')
axis tight
% reconstruct a snapshot
isnap = 1;
figure(i+2)
Urecon = Um;
Vrecon = Vm;
for i = 1:10
Urecon = Urecon+a(i,isnap)*phiU(:,:,i);
Vrecon = Vrecon+a(i,isnap)*phiV(:,:,i);
end
quiver(x,y,Urecon(:,:),Vrecon(:,:), 3.7, 'color','blue')
axis equal
xlabel('x [mm]')
ylabel('y [mm]')
title('Reconstruction')
end
```